Characterisation and aerodynamic impact of leading-edge vortices on propeller blades

Ye-Bonne Koyama

université PARIS-SACLAY

ÉCOLE POLYTECHNIQUE
UNIVERSITÉ PARIS-SACLAY

NNT : 2018SACLX021

THÈSE DE DOCTORAT
DE
L'UNIVERSITÉ PARIS-SACLAY
PRÉPARÉE À
L'ÉCOLE POLYTECHNIQUE

ÉCOLE DOCTORALE N° 579
Sciences mécaniques et énergétiques, matériaux et géosciences

Spécialité de doctorat : Mécanique des fluides

Par

Ye-Bonne KOYAMA MALDONADO

Characterisation and aerodynamic impact of leading-edge vortices on propeller blades

Thèse présentée et soutenue à Meudon, le 4 avril 2018

Composition du Jury :

M Clément DEJEU	Ingénieur, Safran Aircraft Engines	Encadrant, Invité
M Grégory DELATTRE	Ingénieur de recherche, ONERA	Co-directeur de thèse
M Ivan DELBENDE	Maître de conférences, Sorbonne Université	Examinateur
M Georges GEROLYMOS	Professeur, Sorbonne Université	Examinateur
M Ismet GURSUL	Professeur, University of Bath	Rapporteur
M Serge HUBERSON	Professeur, Université de Poitiers	Rapporteur
M Laurent JACQUIN	Professeur, Ecole Polytechnique	Directeur de thèse
Mme Isabelle TRÉBINJAC	Professeur, École Centrale de Lyon	Présidente du jury

À mon grand-père,
qui m'a initiée à la science

À mon frère Akinori,
qui m'expliquait à cinq ans comment fonctionne une hélice

竹とんぼ *(Taketombo), Japanese traditional toy made of bamboo*

Remerciements

Je tiens à remercier tout particulièrement mon directeur de thèse, Laurent Jacquin, pour tout ce qu'il m'a appris en mécanique des fluides, pour sa passion et son ouverture d'esprit qui sont une source inépuisable d'inspiration. Un grand merci également à mon encadrant Grégory Delattre, pour ses conseils ciblés et toujours pertinents, sa réactivité, et sa bonne humeur. Je crois que tu as bien compris ma façon de fonctionner, et j'en retiens un encadrement très efficace. Merci à tous deux de m'avoir fait réfléchir et d'être toujours restés impliqués et disponibles.

Merci à Safran Aircraft Engines de m'avoir fait confiance et d'avoir financé cette thèse. Je remercie notamment Clément Dejeu de son suivi, et de son accueil chaleureux lorsque je me rendais à Villaroche. Merci à Laurence V. et à toute l'équipe YHKR1 pour l'intérêt qu'il ont témoigné à mon travail.

Merci beaucoup à tous les membres de mon jury d'avoir pris le temps d'examiner mes travaux, et d'avoir fait le déplacement le jour de ma soutenance malgré les difficultés d'accès en temps de grève.

Je voudrais aussi exprimer ma grande reconnaissance à l'ONERA pour m'avoir accueillie durant ces trois années. J'ai pris beaucoup de plaisir à travailler dans ce cadre boisé de Meudon, qui a vu passer plus d'un siècle d'histoire de l'aéronautique ! J'ai eu la chance d'interagir avec un grand nombre de collègues et cela a été extrêmement enrichissant, techniquement mais aussi humainement.

Je remercie vivement toute l'équipe "expérimentale", sans qui je ne serais pas allée bien loin. Merci aux collègues mécaniciens Jean-Marc, Yves C., Gilles P. toujours prêts à aider, malgré mes nombreuses sollicitations. Merci François pour la conception de la veine optique, qui a été un élément incontournable de mes expériences. Merci aux lasermen, Gilles L., Robert, Didier S. et particulièrement Cédric I. avec qui j'ai fait la plupart de mes essais PIV, toujours dans la joie et la boonne humeur ! Merci à Yves L.S. et Philippe G. côté logiciel, pour leur disponibilité et leur grande gentillesse. Merci Philippe et Michel pour m'avoir assistée durant la période délicate du redémarrage et de la requalification de la soufflerie. Merci Jean-Pierre pour le réglage de la balance, pour la délicieuse boîte de chocolat, et pour être souvent passé prendre des nouvelles dans mon bureau. Merci Pascal M. pour la bouillie et le précieux coup de main lors des pesées, et pour la relecture des chapitres expérimentaux. Merci à Vincent et à Benjamin L. pour leurs conseils. Merci à tous ceux avec qui j'ai travaillé un peu moins directement mais qui ont contribué à rendre mon passage à l'ONERA inoubliable. Merci à Claire et Dominique, pour la petite touche féminine et les discussions rafraîchissantes.

Merci à tous les doctorants, ex-doctorants, post-docs pour tous les bons moments passés ensemble, qui ont beaucoup égayé mon séjour à l'ONERA: Adam, Romain, Juan, Samir, Robin, Toni, Niccolo, Navrose, Colin, Benjamin G., Ilias, Cédric U., Carlos, Denis, Lucas, Leopold, Benjamin D., Anthony, Arnold, Johann, Quentin, Luis, Tobias, Catherine, et une mention spéciale pour Jean-Lou qui m'a pris de superbes photos dans les souffleries.

Merci beaucoup à la fine équipe des 4 fantastiques, que nous formions avec Holly, Damien et Nicolas, pour tous les fous rires. Si j'ai pu progresser un peu dans la compréhension du second degré, c'est à vous que je le dois. Un immense merci à tous ceux avec qui j'ai partagé un bureau:

Damien et Nicolas, Holly, puis Jahnavi. Vous m'avez aidée à entretenir ma motivation, au fil des hauts et des bas de la thèse.

Merci beaucoup Kazu, c'était inspirant que nous nous soyons retrouvées à faire une thèse au même moment, ce qui nous a permis de bien nous comprendre ! Merci pour les textos réguliers et les conversations revigorantes. Merci à tous mes nombreux amis, qui m'ont bien entourée et m'ont permis de bien décompresser durant toute cette période.

Je remercie du fond du coeur mes parents, mes frères et soeurs, Mits & Chwan, Take, et Aki; ma belle famille, ma famille de France et du Japon, Jung-jae & Hwayeon. C'est grâce au soutien inconditionnel et aux encouragements que vous m'avez apportés tout au long de mes études que j'ai pu arriver jusque là. Merci encore Otosan, Okasan, Mits, Junko-san, et Jordane: votre présence le jour de ma soutenance m'a apporté beaucoup de joie et de sérénité.

Enfin, merci infiniment Thierry. Tu as été au plus près de moi durant ces trois années et tu as toujours cru en moi. Merci de ton écoute et de tes conseils pratiques dans les moments difficiles, et surtout, merci de m'encourager constamment à donner le meilleur de moi-même.

Table of Contents

List of Figures

List of Tables

Nomenclature

Greek letters

α	angle of attack	
α_0	zero lift incidence	
β	angle between inflow velocity and direction of rotation	
γ	perfect gas constant	1.4
Γ	circulation	
Δf	frequency resolution of the spectra	
ϵ	orientation of model blade root with respect to the test-section window	
Θ	twist angle	
θ	angle between vortex mid-line and PIV plane	
ν	air kinematic viscosity	
ρ	air density	
σ	thrust ratio between the upstream and downstream row propellers	
σ'	blade solidity	$\frac{B\,c}{2\,\pi\,r}$
τ, C_T	thrust coefficient	$\frac{F_x}{\rho n^2 D^4}$
ϕ	sweep angle	
χ	power coefficient	$\frac{P}{\rho n^3 D^5}$
Ψ	pitch angle	
Ω	rotational speed in $rad.s^{-1}$	
ω	vorticity field	
$\widetilde{\omega}$	dimensionless vorticity field	$\frac{\omega\,c_{tip}}{W_{tip}}$

Roman letters

AR	aspect ratio	

a	axial induction factor
a'	tangential induction factor
B	number of blades on a propeller
$BEMT$	Blade Element Momentum Theory
c	chord of the wing
C	torque
C_C	torque coefficient
CL	lift coefficient
CD	drag coefficient
CD_i	induced drag coefficient
Cp	pressure coefficient
D	rotor diameter
$D0, D1, D2, D3$	detachment points
Eu	Euler number
$\vec{e_x}, \vec{e_y}, \vec{e_z}$	Normalised unit vectors
F_x, T	thrust
f_{ce}	Centrifugal force density
f_{co}	Coriolis force density
f_{hw}	hot wire acquisition frequency
f_{PIV}	TR-PIV acquisition frequency
$\vec{f_v}$	Wall friction vector
J	advance ratio $\frac{U_{\inf}}{\Omega D}$
Ki	Polhamus induced drag coefficient
Kp	Polhamus potential coefficient
Kv	Polhamus vortex coefficient

L	Lift	
LEV	Leading-edge vortex	
M	Mach number	
n	rotational speed in Hz	$\frac{\Omega}{2\pi}$
Nh	height of the interrogation window used for PIV reconstruction	
Nl	length of the interrogation window used for PIV reconstruction	
Np	potential part of the forces normal to the profile	
Nt	vortex part of the forces normal to the profile	
p	pressure at the wing surface	
p_0	total pressure	
PIV	Particle Image Velocimetry	
POD	Proper Orthogonal Decomposition	
R	semi-span for a Delta wing, span for a non-Delta fixed wing, blade tip radius for a rotating wing	
r	radius of a given section (with respect to the axis of rotation), or spanwise position	
r_0	spanwise position corresponding to the onset of the LEV	
$R1, R2, R3$	reattachment points	
r_{disp}	dispersion radius	
Re	Reynolds number	
Re_{exp}	Reynolds number in the experiment	$\frac{U_{\inf} c}{\nu}$
Re_{prop}	Reynolds number for a rotating propeller based on relative speed	$\frac{W c}{\nu}$
Ro	Rossby number	
s	coordinate materialising the LEV radius	
St	Strouhal number	
T, F_x	thrust	
T_0	total temperature	

TR-PIV Time-Resolved Particle Image Velocimetry

U, u, v, w velocity field

u' velocity fluctuation field

$W(r)$ relative speed at spanwise position r $\sqrt{U_{\text{inf}}^2 + (\Omega r)^2}$

w_i downwash induced velocity

x_m, y_m coordinates of the point of maximal absolute vorticity in the shear layer

Subscripts

ad advance value

$airfoil$ value at the airfoil level

ave average value

$core$ core value

inf freestream value

p potential part or non-vortex part

rot value expressed in rotating frame

tip tip value

TO take-off value

tot total value

v vortex part

x streamwise value

y vertical value

z spanwise value (normal to the PIV planes)

Introduction

Context

The aeronautical industry has agreed on challenging objectives in terms of emissions and noise reduction, supported by the Clean Sky European program. The environmental goals set by the Advisory Concil for Aeronautics Research in Europe (ACARE) to be reached in 2020 include 50% reduction of CO2 emissions, 80% reduction of NOx emissions and 50% reduction of external noise with respect to their levels in 2000. Responding to this call for more sustainable and green aviation, the envisioned new engine architectures will rely on larger bypass ratios.

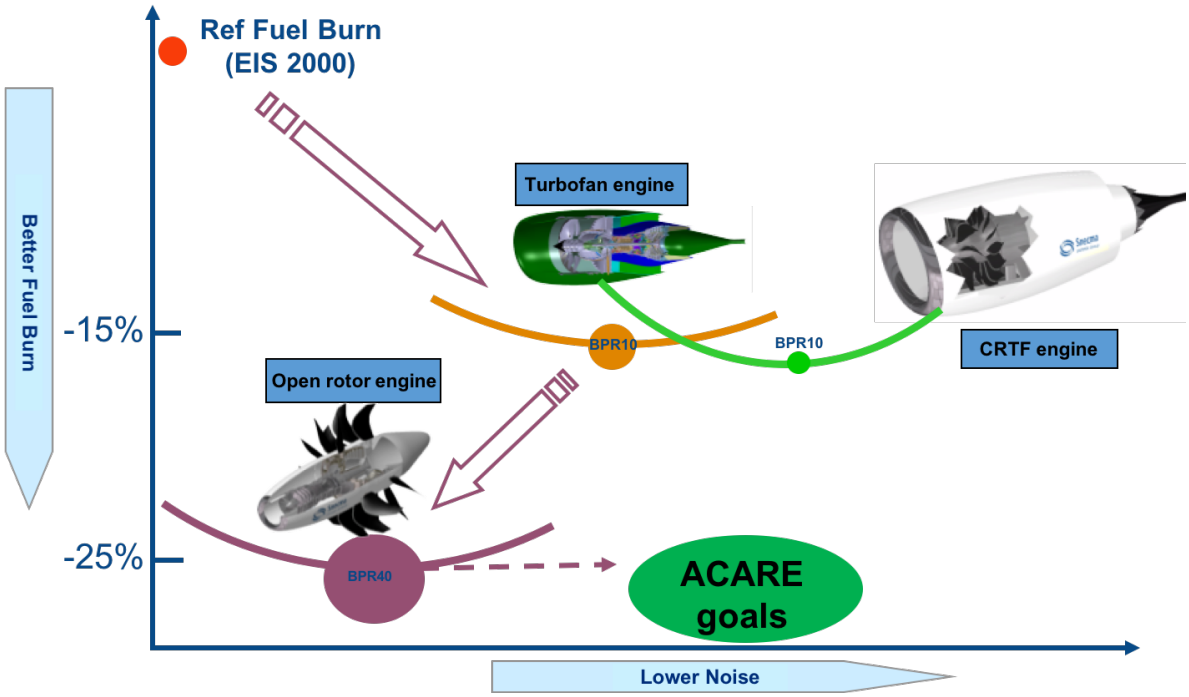

Figure 0.1. *Engine architectures with respect to noise level and fuel burn. From ICAS 2010 presentation, Jérôme Talbotec, Safran*

In this context, propellers have aroused renewed interest, and are the scope of this study. Among the concepts under development are counter-rotating transonic propellers (see Figure 0.2), also called Counter-Rotating Open Rotor (CROR). As the name suggests, this engine consists of two counter-rotating propellers mounted on the same shaft. Figure 0.1 indicates that the Open Rotor's high bypass ratio (30-40 with respect to 10 for the LEAP engine) would enable to reduce fuel consumption by 25% with respect to traditional turbofans at relatively low speeds (corresponding to short and medium-haul flights). In terms of acoustics however, the Open Rotor technology is less competitive. Indeed, acoustic waves are unconstrained and free to travel due to the absence of the carter. In addition to its high bypass ratio, one particularity of the Open Rotor is that the downstream blade row retrieves the swirled flow exiting the first blade row. Due to the beneficial mutual induced velocities, the overall efficiency is higher than that of two single propellers [Beaumier, 2014]. The following study is based on the HTC5

propeller geometry, designed at ONERA for CRORs [Gardarein, 1991], because it is a public geometry, whose form laws and circulation distribution are generic.

Figure 0.2. *The Safran Counter Rotating Open Rotor*

Propeller blade aerodynamics

As far as propeller blades are concerned, one of the major challenges is to design the blade geometry and choose its operating parameters, based on aerodynamic and acoustic constraints:

- achieving a sufficient thrust at take-off
- achieving the best cruise efficiency
- noise level abiding by the acoustic specifications

Satisfying those aero-acoustic constraints implies a trade-off in the design process. This kind of problem can be solved using multi-objective RANS-based surrogate optimisation strategies [Lepot et al., 2011], and lead to the definition of various geometries located on a Pareto front with respect to acoustic and aerodynamic criteria. The trade-off even applies from a purely aerodynamic point of view, because the blade must function over different flight regimes. In order to guarantee a high efficiency in cruise, propeller blades typically have thin and low-cambered profiles reducing profile drag. The most radially outward sections, which operate in the transonic regime, are swept to prevent the appearance of shocks. Consequently, in take-off conditions, the blade profiles must work at high incidence in order to generate the required thrust. Thus, the flow can easily detach at the leading-edge. Figure 0.3 features the friction lines on the HTC5 Open Rotor front blade at take-off. Flow separation occurs between the apex (foremost point on the leading-edge) and the tip. The flow reattaches to the profile further downstream. The recirculating friction lines between the leading-edge and the reattachment line indicate that a conical vortex structure is formed at the leading-edge. This structure can be found on several geometries of propeller blades [Vaczy and Cormick, 1987, Vion, 2013, Zachariadis et al., 2013]. Even though [Zachariadis et al., 2013] showed that increasing the rotation speed and repitching the blade enabled to reduce the size of the leading-edge vortex (LEV) at iso-thrust, the suppression of the vortex was not reached in the range of applicable parameters, which shows that this structure is often present at take-off. Therefore it is worth understanding what influence this leading-edge vortex may have on acoustic and aerodynamic performance at take-off.

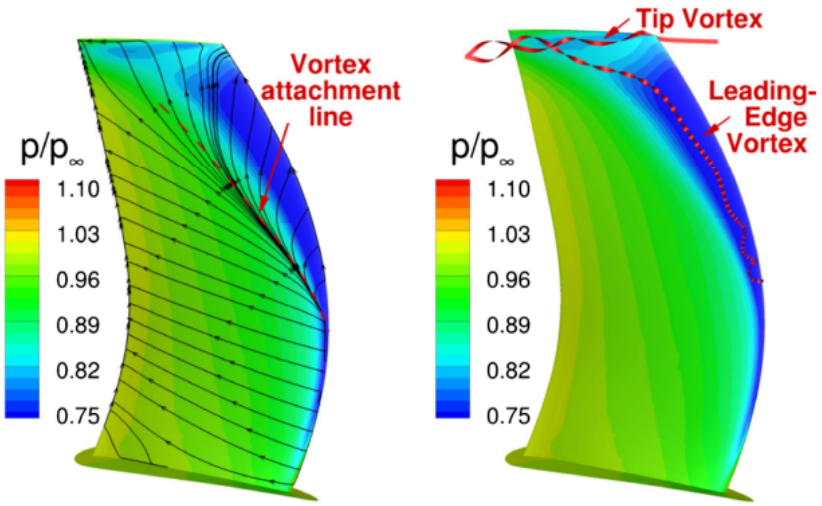

Figure 0.3. *HTC5 front blade suction-side wall pressure, with wall friction lines or streamlines seeded near tip and leading-edge vortex cores rendered by Frenet ribbons. Figure 4 from [Delattre and Falissard, 2015]*

LEV impact on the acoustic properties of a CROR configuration

As will be detailed in this paragraph, the leading-edge vortex characteristics greatly influence those of the vortex shed in the wake, and consequently the interaction noise in a CROR configuration. The interaction noise is caused by the induced effects created by one rotor on the other, including the front blades' tip vortices and wake impacting the downstream rotor. When struck by those structures, the downstream blades are subject to important incidence and loading fluctuations. The fluctuating pressure field gives rise to the propagation of acoustic waves. This is the main source of noise on CRORs [Hanson, 1985].

The work of [Simonich et al., 1990] suggests that the characteristics of the shed vortex are greatly influenced by those of the leading-edge vortex. The authors performed an experiment on a rotor placed in the wake of a non-rotating swept wing. Figure 0.4 presents the two tested configurations. On the one hand, the forward swept wing generates two vortices : the tip vortex and a LEV propagating towards the wing foot. On the other hand, the aft swept wing creates a LEV which mixes with the tip vortex before it is shed in the wake. Those two configurations have the same loading.

The overall sound pressure level is found to be 10 dB lower in the case of the forward swept wing. The article provides two explanations. First, in the forward swept case, the LEV impacts the rotor at its root where rotation velocities are lower. Secondly, it suggests that the tip vortex of the forward swept vane will generate less interaction noise because it is less diffuse, has a smaller radius and a lower axial velocity deficit compared to the vortex shed in the wake of the aft swept vane.

The article interestingly notes that the vortex shed by the aft swept vane is actually quite diffuse, turbulent and with a large core velocity deficit, just like the leading-edge vortex of the forward swept vane, but unlike its tip vortex. This suggests that in merging with the tip vortex, the LEV greatly influences the characteristics of the shed vortex.

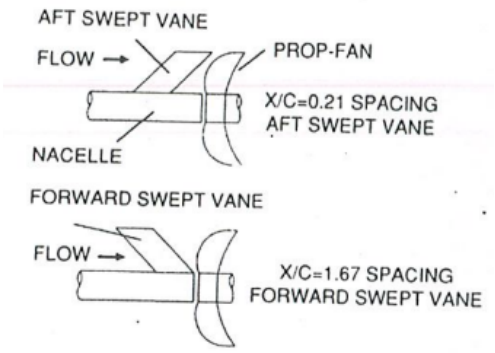

Figure 0.4. *Sketch of the experiment of [Simonich et al., 1990]*

The conclusions of the PhD thesis of [Vion, 2013] support the fact that it is best to act at the leading-edge in order to modify the wake characteristics. Although trailing edge modifications were attempted, a protrusion added at the leading-edge was found to be much more efficient at modifying the wake structure and reducing noise. This protrusion enabled to split the LEV such that two vortices of lower circulation and axial velocity deficit were shed into the wake.

The study of [Delattre and Falissard, 2014] elaborates on the hypothesis of [Simonich et al., 1990], that the noise level decreases with the velocity deficit on the axis of the vortex impacting the downstream rotor. The article modifies the torque ratio between the two rotors, keeping total thrust constant. When the upstream rotor is less loaded, the axial velocity deficit in the shed vortex decreases and so does the sound pressure level.

Those studies seem to show the potential of acting on the front blade leading-edge to improve the acoustic performance of the CROR.

Objectives and approach of the thesis

Past studies hint that understanding the leading-edge vortex flow on propeller blades could be a key to achieve the best aeroacoustic compromise, that is, blade geometries with improved aeroacoustics at take-off and a preserved behaviour in cruise. In this framework, the present thesis adopts a purely aerodynamic perspective. Indeed, this work is based on the observation that the leading-edge vortex flows forming on propeller blades look qualitatively similar to Delta wing leading-edge vortices. On Delta wings, leading-edge vortices (LEVs) are known to contribute to lift. However this contribution is at the expense of an increase in drag, thus a decrease in efficiency.

In this context, **the aim of this study is to explore the probable impact of the LEV on lift at take-off in order to reconsider propeller blade designs.**

The first step in this process was to perform a literature survey on leading-edge vortex flows presented in **chapter 1**. The flow topology and the concept of vortex lift as described in earlier studies on Delta wings are discussed in order to provide a base for comparison with transonic propeller blade LEVs. The review revealed that LEV topology, hence their contribution to lift, are sensitive to the Reynolds number and the shape parameters of the wing. In order

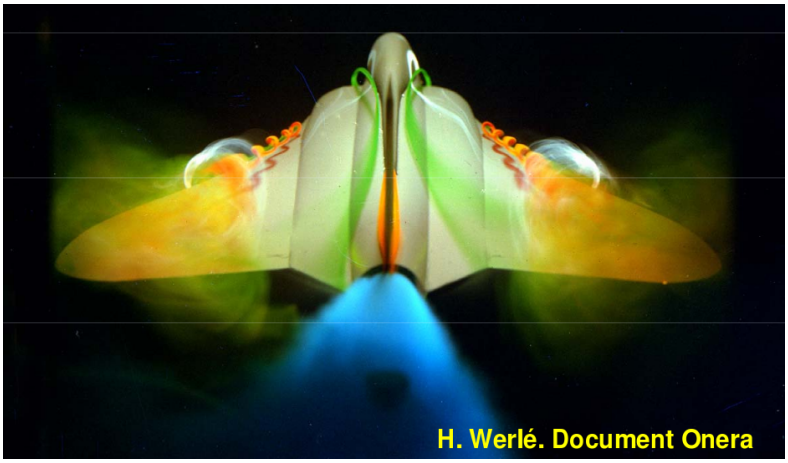

Figure 0.5. *Hydrodynamic tunnel visualisation of the flow on a plane with Delta wings, by [Werlé, 1960a]*

to investigate the effect of rotation on the characteristics and the aerodynamic impact of LEVs, more recent studies dealing with LEVs on insect wings were considered. Those studies highlighted that LEV formation on rotating wings was influenced by specific mechanisms due to wing rotation. In a nutshell, previous works on LEVs dealt either with fixed swept wings at high Reynolds number ($Re \approx 10^7$) or rotating wings at low Reynolds numbers ($Re \leq 10^4$).

Although LEVs on propeller blades were observed through friction lines, no experimental characterisation of their core had ever been performed, while the ability of RANS calculations to accurately reproduce flow separation and reattachment in this configuration still remains to be proven. The sensitivity of the LEV to the Reynolds number, to the shape parameters of the wing, and to the presence of rotation legitimised the necessity to characterise the leading-edge vortex flow occurring on propeller blades ($Re \geq 10^5$).

The next step was to characterise the leading-edge vortex flow on propeller blades, in order to determine how it would fit in the global picture of LEVs. For this purpose, an experiment was set using the model blade developed in the PhD thesis of [Vion, 2013]. This model blade was designed to be representative of the behaviour of the HTC5 front blade, even though it was not rotating. Instead of investigating the wake of this blade as Laurence Vion did in her thesis, three cut planes inside the LEV were performed using Time Resolved Particle Image Velocimetry (TR-PIV). The experiments were carried out in the S2L subsonic wind tunnel at ONERA Meudon. Numerical simulations were carried out for comparison with experimental results. **Chapter 2** describes in detail the experimental and numerical tools and methods used in this thesis.

Chapter 3 presents the choice of the testing parameters in order to reproduce the experimental configuration of [Vion, 2013]. This implied to characterise the flow in the empty S2L wind tunnel, which was displaced and renovated since then. The influence of the new surroundings on the flow in the test section had to be verified, all the more so as it is an open wind tunnel. It was also necessary to qualify the new test section built to facilitate optical access for PIV. For this purpose, soundings of the average velocity, the turbulence level and the boundary layer thickness were performed. Then, the objective was to examine the sensitivity of the flow around the model blade to various positioning parameters. This study was especially motivated by the use of a new test section, and the placement of the blade further downstream

compared to Laurence Vion's experiments. Indeed, [Vion, 2013] showed that the model blade was representative of the rotating configuration for a given incidence in the wind tunnel, which was sensitive to blockage effects. Thus it was important to get as close as possible to the experimental conditions of Laurence Vion, and estimate any discrepancies with her configuration. This step was performed using static pressure probes embedded in the model blade, force balance measurements and a PIV plane in the wake to compare the characteristics of the shed vortex to those measured by [Vion, 2013].

Once the testing configuration was established, the LEV core could be characterised. This step is presented in **chapter 4**. Laser tomoscopy first revealed that the LEV on the model blade was a very near wall structure. This, in addition to its pronounced three dimensional characteristics, could easily lead to PIV reconstruction bias and errors, and requested to verify the reliability of PIV reconstruction and choose carefully the reconstruction parameters. A RANS simulation of the experimental setup was performed in order to evaluate the ability of RANS calculations to reproduce the three dimensional detachment and reattachment characterising the LEV. The LEV characteristic dimensions and core velocity were defined and used to compare experimental and numerical flow fields. Both experimental and numerical results showed that the LEV had an elongated core and axial core velocities in the order of 50% of the inflow velocity. An analysis of the time-resolved behaviour using TR-PIV instantaneous images and hot wire measurements in the LEV was carried out in order to determine if any instability mechanisms were present. This revealed that Kelvin-Helmholtz instabilities existed in the shear layer, but were a wide-band phenomenon, quickly transitioning to turbulence when the flow reattached. The absence of a "strong" instability mechanism supported the fact that RANS results were in reasonable agreement with experimental ones. The LEV topology investigated experimentally looked qualitatively similar to LEVs on non-slender Delta wings at low incidence. This may indicate that the LEV contributes to lift on the HTC5 blade, though not as much as may a round, "jet-like" LEV like those on slender Delta wings.

This hypothesis is verified in **chapter 5**. It is not straightforward to single out the contribution of the vortex from total lift, and this has rarely been attempted in the past, except on the Delta wing case. Now with the reliability of RANS calculations established, a post-processing method was developed to evaluate the spanwise vortex lift distribution on the HTC5 blade, using RANS wall pressure fields. This method was evaluated based on comparisons with existing vortex lift definitions and validated on the Delta wing case. Applying this method on the HTC5 model blade showed that the LEV contributed to lift, but that this contribution remained limited compared to that which can be achieved on slender Delta wings at high incidence. Hence the aim was to examine if it was interesting to enhance vortex lift at take-off, and if this could be achieved at a reasonable cost in efficiency.

The initial idea was to perform a parametric study, varying the blade shape and functioning parameters (pitch, rotation velocity) to determine the impact on LEV topology and blade aerodynamic performance. However, due to the strong coupling of the physical mechanisms involved around the blade, it was difficult to distinguish the influence of one given parameter, which would act on several physical mechanisms, and to anticipate which mechanism would prevail on the others. In order to elucidate the dependency of vortex lift to blade geometry and functioning parameters, it was decided to design a vortex lift model, compatible with a 1D load calculation method such as the Blade Element Momentum Theory (BEMT). This part is presented in **chapter 6**. The 1D vortex lift model is inspired by the estimations for spanwise vortex lift extracted from RANS calculations (using the tool developed in chapter 5), and by the leading-edge suction analogy of [Polhamus, 1966], which deduces the forces obtained in the presence of a LEV from those obtained by potential calculations at lower incidence, without

LEV. The 1D model is tested on Delta wings, the model HTC5 blade, and the rotating HTC5 blade.

Chapter 7 focuses on proposing concepts which could benefit from an increased vortex lift at take-off using RANS calculations. The corresponding vortex lift is monitored using the method developed in chapter 5. RANS calculations are performed on single propellers with 4 blades (no downstream propeller), because this configuration enables to limit the effect of mutually induced velocities in order to focus on the impact of the LEV on a given blade. Meanwhile it simplifies the calculation procedure, allowing the use of periodic boundary conditions instead of chorochronic ones. The reference case is the HTC5 front blade geometry, but in the 4 blade propeller configuration. Varying the pitch, rotation velocity and sweep, cases reaching the target thrust at take-off for various levels of vortex lift are compared. Finally, a blade geometry is proposed, which relies on vortex lift to generate the thrust at take-off in spite of a surface reduction in the order of 30% compared to the HTC5 case.

1

Literature review on the leading-edge vortex

1.1. Leading-edge vortices on Delta wings

The development of the Delta wing concept is very interesting from a historical point of view, as it constituted a completely new approach to aerodynamic design [Maltby, 1968]. According to [Anderson, 2007], first investigations on Delta wings date back as far as the work of Alexander Lippisch in the 1930s. Until then, classical aircraft design (for incompressible flow at subsonic speeds) relied on high aspect ratio wings. In order to produce lift with minimum drag, the shape of those wings was optimised to avoid flow separation. However, with the development of transonic, supersonic and hypersonic aircrafts, compressibility effects led to a new source of drag, called wave drag. Increasing the sweep was found to mitigate those effects. Thus the need to reduce cruise wave drag led to the development of slender, sharp-edged wing concepts: the first Delta wings. However, at lower speeds, those designs led the flow to separate along the entire leading-edges, and roll up into spiral leading-edge vortices (LEVs). Those LEVs were found to be stable over a wide range of attitudes. In addition, the research community became rapidly aware that the LEVs contributed to lift, eliminating the need for high lift devices at take-off [Polhamus, 1971]. For the first time, a departure from the "attached flow" concept was witnessed, in order to reduce cruise wave drag and increase manoeuvrability, but at the expense of decreased lift-to-drag ratio at low speeds.

Several supersonic military (Convair F-102A) and civil (French-British Concorde) projects fuelled research on Delta wing leading-edge vortices over a wide range of subjects, which will be classified into three main categories : investigation of the flow topology, identification and modelling of vortex lift, and unsteady behaviour.

1.1.1. Flow topology and influencing parameters

For the reasons stated above, the first investigated Delta wings were slender (sweep $\phi \geq 65$ degrees), to mitigate compressibility effects, and had sharp-edges in order to fix flow separation at the leading-edges. The flow topology on those wings will be described first as a reference case, then the impact of the main influencing parameters will be presented.

1.1.1.1. Slender sharp-edged Delta wings

Among the first studies characterising Delta wing LEVs are the experimental visualisations of Roy [Roy, 1956] and Werlé [Werlé, 1957, Werlé, 1959, Werlé, 1960b, Werlé, 1960a], over high sweep sharp-edged Delta wings.

At a sufficient incidence, the flow on such wings is characterised by two symmetric leading-edge vortices, originating from the apex (foremost point of the wing, on the symmetry axis), rolling up as spirals and propagating along the leading-edge (see figure 1.1). The flow pattern on slender, sharp-edge Delta wings consists in three rotational zones : the primary leading-edge vortex, its shear layer, and a secondary counter-rotating vortex [Mitchell and Molton, 2002]. This secondary vortex is due to the interaction of the main LEV with the boundary layer on the suction side [Riou, 2009]. [Furman and Breitsamter, 2013] argues that its formation depends on the laminar or turbulent character of the boundary layer.

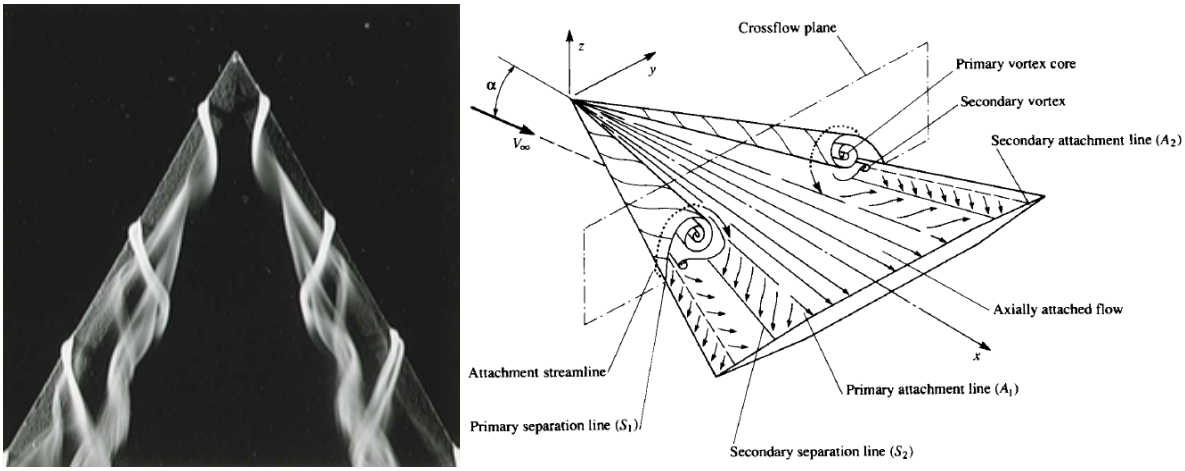

(a) (b)

Figure 1.1. *(a) Visualisation of the LEVs on a 75 degrees sweep Delta wing at an incidence of 16 degrees in a hydrodynamic tunnel, through coloured emissions. Source: [Werlé, 1957]. (b) Schematic view of the flow over a slender sharp-edge Delta wing. Source: [Anderson, 2007]*

As the incidence increases, [Werlé, 1957] showed that the LEVs grow in size, but also in strength, and become more rounded (see figure 1.2). With incidence, [Zohar and Er-El, 1988] also noted that the core of the LEV moved further towards the symmetry plane, and [Pashilkar, 2002] remarked that it also lifted further from the wing surface.

The LEV can be decomposed in two regions depicted on figure 1.3: a viscous subcore, surrounded by a rotational and non viscous zone [Earnshaw, 1961, Nelson and Pelletier, 2003]. The viscous subcore is characterised by the maximal tangential velocity, which can amount to two times the inflow velocity U_{inf}, but also by a strong acceleration of the axial flow. According to experimental [Payne et al., 1986, Mitchell and Molton, 2002, Renac, 2004] and numerical [Ol and Gharib, 2003] studies, the ratio of the axial flow over U_{inf} can reach values close to 3. [Werlé, 1960b] measured that core velocities increased with the angle of attack, and varied along with LEV propagation.

The intensity of the LEVs is evaluated in [Renac, 2004] using an analytical method to determine their circulation. Under the assumption of slenderness, the Delta wing is replaced by a vorticity sheet analogous to Prandtl's lifting line, oriented along the Delta wing symmetry plane. Its

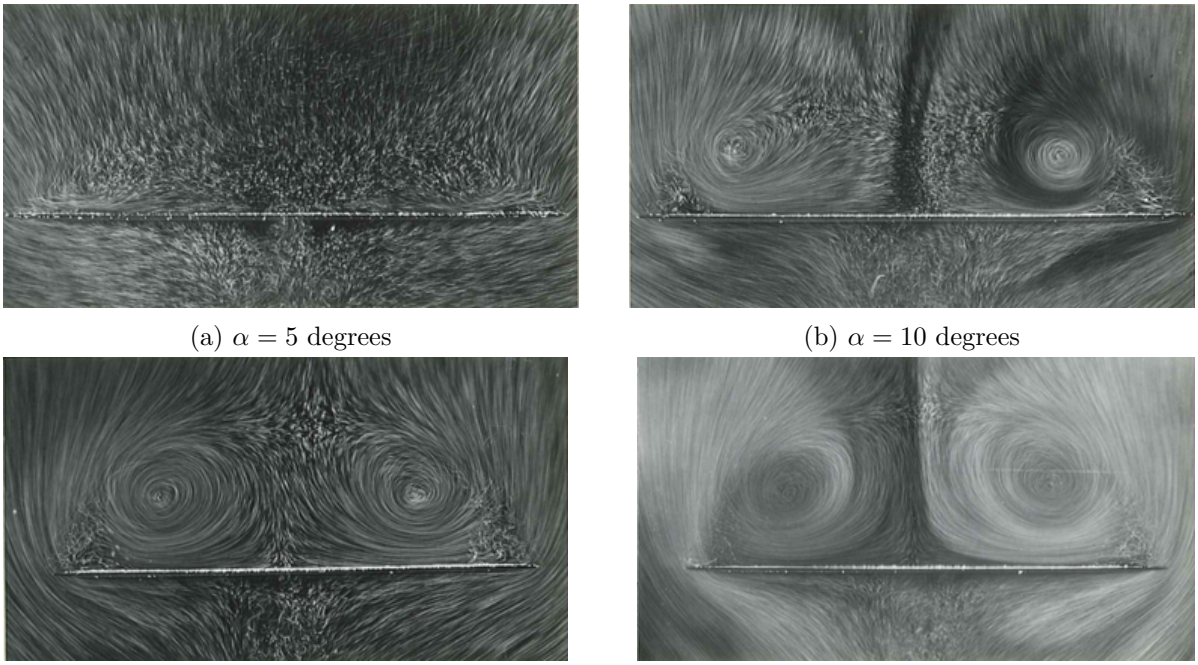

(a) $\alpha = 5$ degrees

(b) $\alpha = 10$ degrees

(c) $\alpha = 15$ degrees

(d) $\alpha = 20$ degrees

Figure 1.2. *Visualisation of the LEVs on a plane normal to the surface of a 75 degrees sweep Delta wing at various angles of attack using air bubbles in a hydrodynamic tunnel. Source: [Werlé, 1957]*

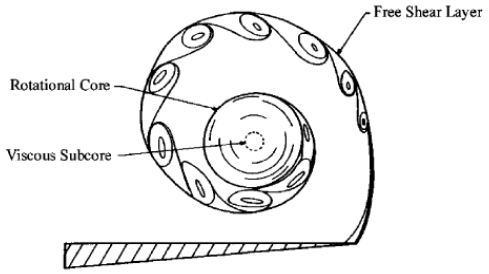

Figure 1.3. *Three regions within a LEV. Source: [Nelson and Pelletier, 2003]*

magnitude at a given position x along the line corresponds to the tangential velocity jump. In order to calculate this quantity, the velocity potential at position x is evaluated using slender wing theory. The wing section at position x is thus modelled by a flat plate oriented perpendicularly to the inflow $U_{inf}\, sin\alpha$, with a Kutta condition at each end. Integrating the vorticity distribution along x gives :

$$\frac{\Gamma(x)}{R(x)\, U_{inf}} = \frac{2\, sin\alpha\, x}{R(x)\, tan\phi}$$

where $R(x)$ is the span at position x, and α the incidence. Thus, the intensity of the LEV increases with the incidence and the inflow velocity, and decreases with sweep. As it progresses toward the tip, the circulation of the LEV increases, hence the depression along its axis. This leads to an increase in axial velocity.

Vortex breakdown. During its progression along the leading-edge, the LEV can experience numerous instabilities which may lead to vortex bursting, or vortex breakdown. This

phenomenon corresponds to a sudden decrease in axial velocity along with an increase in turbulent kinetic energy, and an expansion of the LEV cone. A stagnation point along the LEV axis may appear.

[Werlé, 1960a] established that the vortex bursting location moved closer to the apex when the incidence increased (see figure 1.4), but also when the inflow Reynolds number increased. The main parameters influencing vortex bursting are the adverse pressure gradient [Leuchter and Solignac, 1983] and the initial Swirl number [Solignac and Leuchter, 1983] (meaning the Swirl number before vortex bursting), corresponding to the ratio of tangential velocity over axial velocity along the vortex core. According to [Harvey, 1962] and [Benjamin, 1967], vortex breakdown consists in the transition between two conjugate states of an axisymmetric rotating flow. Indeed, rotating flows are characterised by the propagation of Kelvin waves, which are triggered by small perturbations of a stationary base flow in solid rotation. Vortex bursting corresponds to a change in the direction of propagation of those waves.

The location of vortex bursting can be determined using the initial Swirl number $S = \frac{\Gamma_i}{s_{max,i} U_{core,i}}$ where Γ_i is the initial circulation of the LEV and $s_{max,i}$ its initial radius. According to [Pagan, 1989] ths initial Swirl number should be between 1.3 and 1.4 to trigger vortex breakdown. Another criterion is based on the sign of the scalar product between the velocity and vorticity vectors in the LEV core [Hoeijmakers, 1992]. This latter criterion is derived from the Crocco relationship : for a non viscous fluid, in permanent flow and without energy dissipation, the velocity and vorticity vectors are parallel. Vortex bursting corresponds to the point where the sign of their scalar product changes.

[Lambourne and Bryer, 1961] described two forms of vortex bursting : a bubble form, caused by the recirculation downstream of the stagnation point, or a spiral form, due to the instability of the bubble form. The second form is generally obtained at lower incidences compared to the first. Figure 1.5 presents a scheme of the spiral vortex bursting. When vortex breakdown occurs over the wing surface (instead of occurring in the wake), [Lawford and Beauchamp, 1961] notices an increase in the power density of pressure fluctuations, accompanied by a rise in low frequency fluctuations of the normal force.

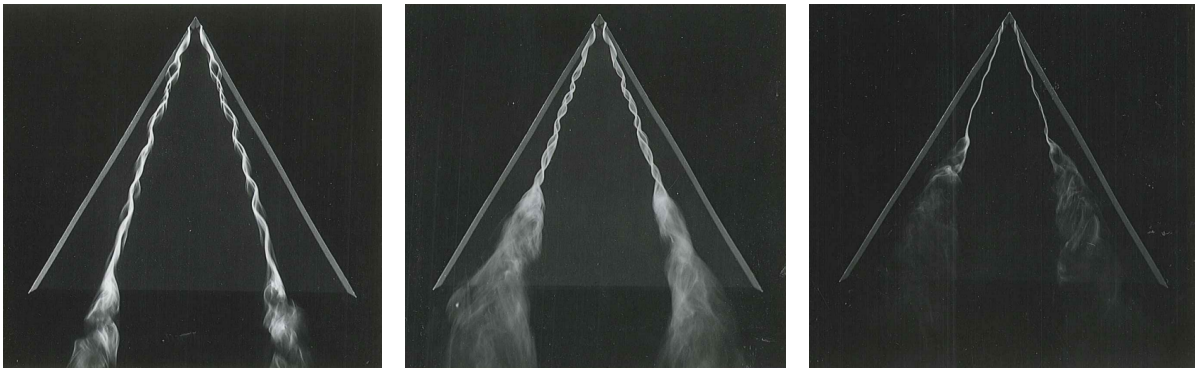

(a) $\alpha = 12$ degrees (b) $\alpha = 16$ degrees (c) $\alpha = 20$ degrees

Figure 1.4. *Visualisation of LEV breakdown at various angles of attack on a 75 degrees sweep Delta wing in a hydrodynamic tunnel, through coloured emissions. Source: [Werlé, 1959]*

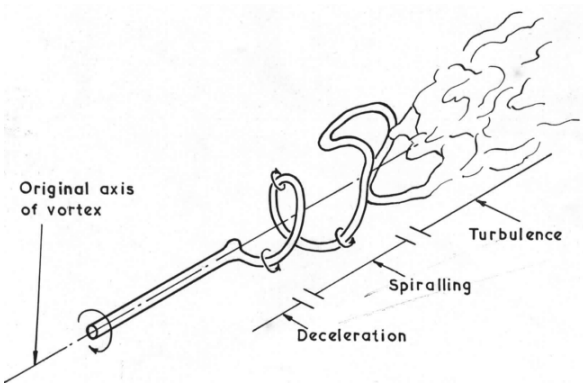

Figure 1.5. *Scheme of spiral vortex bursting. Source: [Lambourne and Bryer, 1961]*

1.1.1.2. Parametric variations

Among the main influencing parameters on LEV shape, core velocity and vortex bursting are the leading-edge radius, the Delta wing sweep and the Reynolds number.

For a sharp leading-edge, LEV formation is fixed at the leading-edge. Studies of [Gursul et al., 2005] indicate that separation and reattachment may be delayed on a more rounded leading-edge. [Werlé, 1961] visualised the influence of the leading-edge thickness and radius and concluded that the LEV flattened when those two parameters increased. Because it is then closer to the wing surface, the secondary counter-rotating vortex causes the sheet of the primary LEV to stretch and separate into two zones of high vorticity which form co-rotating vortices. As [Gordnier and Visbal, 2003] indicates, this phenomenon is highly dependent on the Reynolds number.

The study of [Ramesh et al., 2012] on fixed airfoils offers further insight into flow separation mechanisms, depending on the Reynolds number, the incidence and the leading-edge radius. Knowing that the flow will detach above a critical value of the adverse pressure gradient, the article uses a variable to estimate the related suction peak. This variable, called the "Leading-Edge Suction Parameter" (LESP) is defined as the velocity of the flow bypassing the leading-edge $LESP = U_{LE}$. This is consistent with the work of [Evans and Mort, 1959], which showed that U_{LE} was related to the leading-edge suction peak. [Ramesh et al., 2012] defines the "critical LESP", $LESP_{crit}$, as the value of the $LESP$ at the incidence corresponding to the onset of flow separation. The authors show that the critical LESP only depends on the profile geometry and the inflow Reynolds number. Their previous study [Ramesh and Gopalarathnam, 2011] also stresses that $LESP_{crit}$ does not depend on time for unsteady motions. In order to evaluate the $LESP_{crit}$ for a given airfoil and Reynolds number, the incidence is increased gradually. Once the skin friction turns negative at the leading-edge, the $LESP$ at the incidence corresponding to the maximal leading-edge pressure coefficient (in absolute value) is defined as $LESP_{crit}$. Figure 1.6 presents the evolution of the critical LESP with respect to the inflow Reynolds number, for airfoils with different leading-edge radii. The curve shows that there is a minimal value of $LESP_{crit}$, meaning that there is a value of the Reynolds number most facilitating flow separation.

The Delta wing sweep strongly influences LEV topology and their sensitivity to other parameters. [Ol and Gharib, 2003] notes that the LEV is closer to the surface when the sweep decreases at a fixed incidence. Thus the formation of co-rotating vortices was also reported

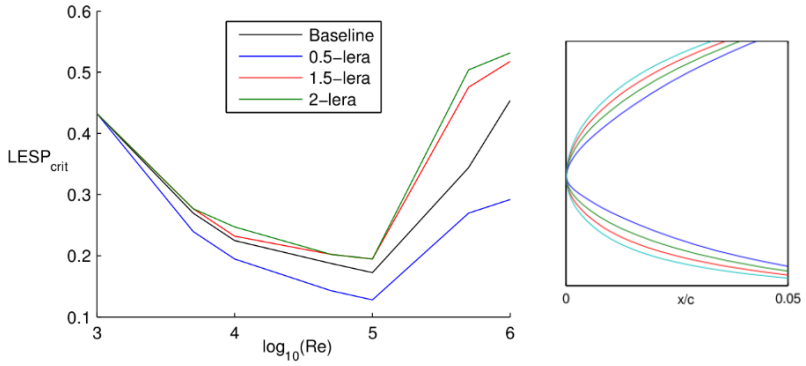

Figure 1.6. *Critical Leading-Edge Suction Parameter ($LESP_{crit}$) variation with the inflow Reynolds number, for airfoils with various leading-edge radii. Source: [Ramesh et al., 2012]*

on non slender Delta wings ($\phi \leq 60$ degrees). At low Reynolds numbers, or low incidence, the velocity profiles in the LEV core exhibit a slight velocity deficit. Also, the core is found to be more unsteady. In addition, Figures 1.7 and 1.8 show that the velocity and vorticity profiles along the axis of the LEV are particularly sensitive to the Reynolds number and the angle of attack in the case of non-slender wings [Gordnier and Visbal, 2005, Gordnier and Visbal, 2003, Gordnier and Visbal, 2006, Gordnier et al., 2009].

The sweep also influences vortex bursting. The vortex bursts closer to the apex on non-slender wings [Gursul et al., 2005]. The higher the sweep, the higher the incidence corresponding to the first occurrence of vortex bursting.

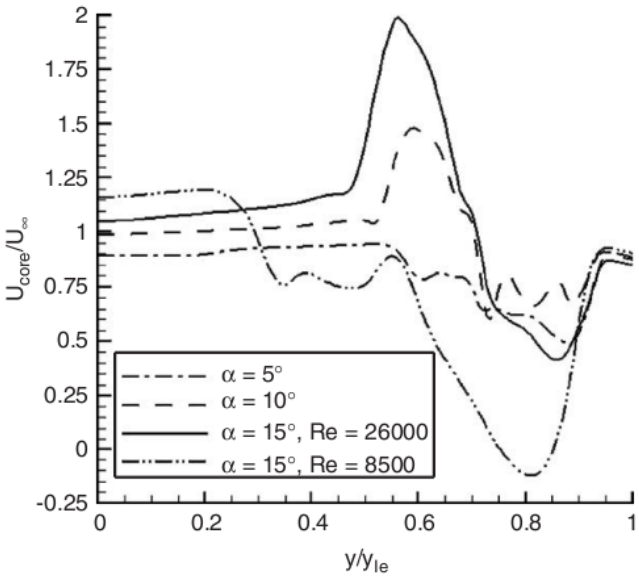

Figure 1.7. *Axial velocity profile in the LEV core for a Delta wing of 50 degrees sweep, at x/c=0.3. Source: [Gursul et al., 2005]*

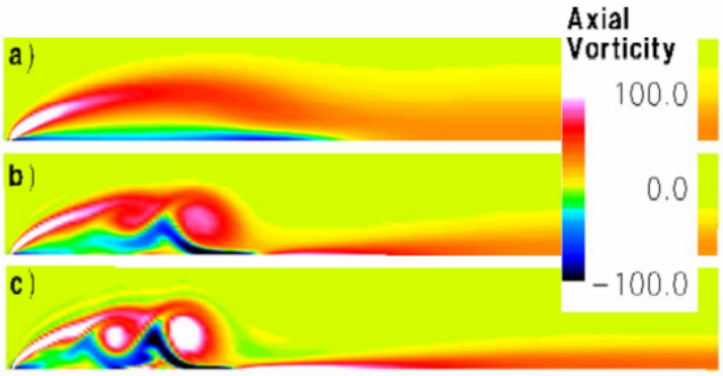

Figure 1.8. *Axial vorticity fields showing the influence of the Reynolds number on the topology of the LEVs on a 50 degrees swept Delta wing. (a) $Re = 10^4$, (b) $Re = 2 \times 10^4$, (c) $Re = 5 \times 10^4$. Source: [Gordnier and Visbal, 2003]*

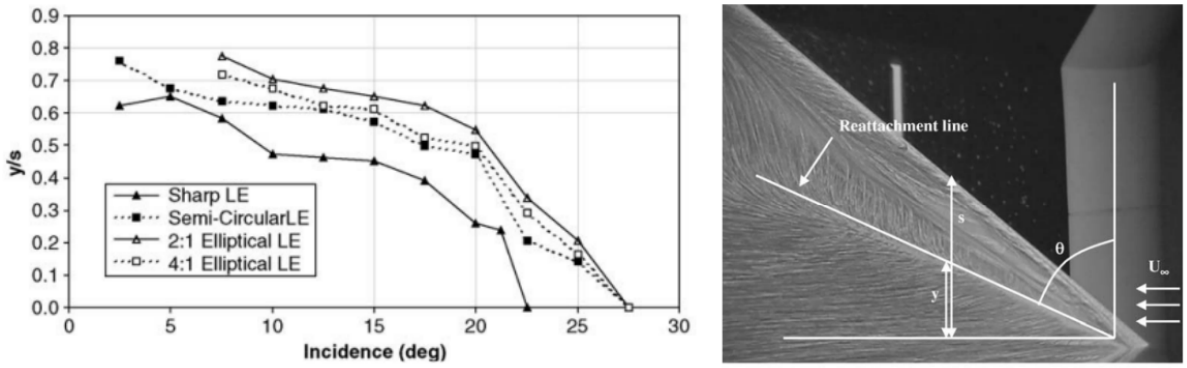

Figure 1.9. *Position of the primary LEV reattachment line depending on leading-edge curvature. Source: [Gursul et al., 2005]*

In a nutshell, while high sweep or slender ($\phi \geq 65$ degrees) Delta wings give rise to nearly circular and jet-like vortices, low sweep Delta wing vortices for the same incidence are more elongated, closer to the blade surface, and are more prone to a wake-like profile [Gursul et al., 2005]. Increased leading-edge radius and airfoil thickness similarly tend to flatten the LEV. Also, the sensitivity of the LEV topology to the inflow Reynolds number is increased for rounded leading-edges and non-slender Delta wings.

After describing Delta wing LEVs' topology and their influencing parameters, the following paragraph focuses on the LEV's impact on the aerodynamics.

1.1.2. Identification and modelling of vortex lift

Several studies [Hill, 1957, Wentz, 1968, Manie et al., 1978b] have shown that Delta wing LEVs enhance depression on the suction side, thus contributing to lift. This contribution is called "vortex lift". Figure 1.10 pictures the wall pressure distribution on a Delta wing and features very strong depression zones corresponding to the locations of the LEVs.

Although the concept of vortex lift has been referred to in a large number of studies, few authors have attempted to quantify the contribution of a vortex to lift. Indeed, as useful as it

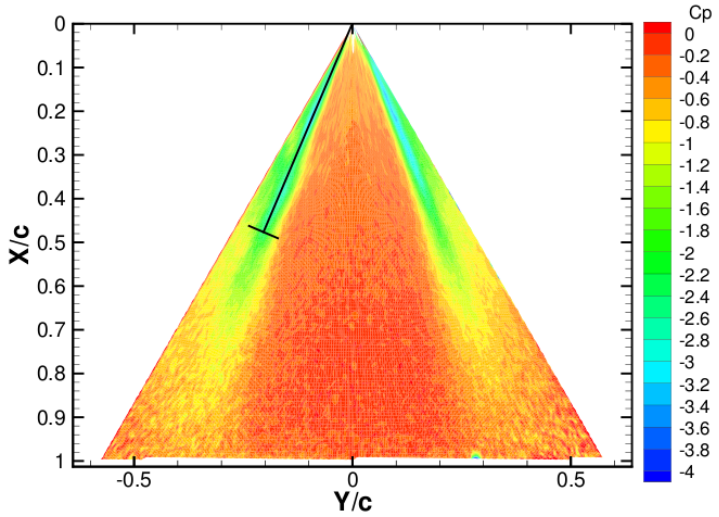

Figure 1.10. *Wall pressure field on a Delta wing, visualised using Pressure Sensitive Paint. Source: [Renac, 2004]*

may be to understand the unfolding physical phenomena, vortex lift is a construct of the mind which is somehow ill-defined. The definition of vortex lift implies that the part of lift created by a leading-edge vortex can be isolated from "total" lift. However, the leading-edge vortex appears due to the shape of the wing, and its incidence, at a given Reynolds number, and one cannot design a "reference case", in the same conditions, without forming a LEV.

At high angle of attack, a significant part of the lift on Delta wings is produced by vortex lift such that stall can be delayed. Figure 1.11a shows that the maximal lift coefficient and the onset of stall are shifted to higher incidences for higher sweeps. In those cases, potential theories based on panel methods were not able to successfully predict lift. Indeed, potential theory is an inviscid theory, unable to capture flow separation at the leading-edge, which gives the aerodynamic loading under the constraint of a fully attached flow. From there stemmed the idea to define vortex lift as the discrepancy of measured lift with potential theory results based on panel methods. This is why the remaining part of lift (or non-vortex lift) has come to be referred to as "potential lift". However we will explain later that this term is inaccurate in some cases, depending on the way vortex lift (thus non-vortex lift) is modelled.

The reference to "potential lift" as opposed to "vortex lift" led some authors [Brown and Michael, 1954, Torres and Mueller, 2004] to identify vortex lift as "non linear lift", the onset of vortex lift being the point where the polar ceases to be linear. Indeed, as the incidence is increased, the lift coefficient polars become non linear (see figure 1.11a and 1.11b). This effect is more visible on figure 1.11b because the data are non-dimensionalised by the sweep.

The first modelling approach for vortex lift follows the work of [Bollay, 1939] for rectangular wings. This work started from the observation that lift versus incidence curves exhibited specific non-linear features for very small aspect ratios (below 1). Because the Prandtl lifting line theory did not hold for those small aspect ratios, and the lifting surface theory, which is essentially linear, did not account for this behaviour, the author resorted to a new modelling approach, which can be viewed as an ancestor to slender wing theory (which will be described in the following paragraph). [Bollay, 1939] considers a wing of infinite chord and finite span, and cuts the wing into small sections along the chordwise directions. Those sections are thus parallel to the span. The modelling consists in assuming that trailing vortices are shed ahead

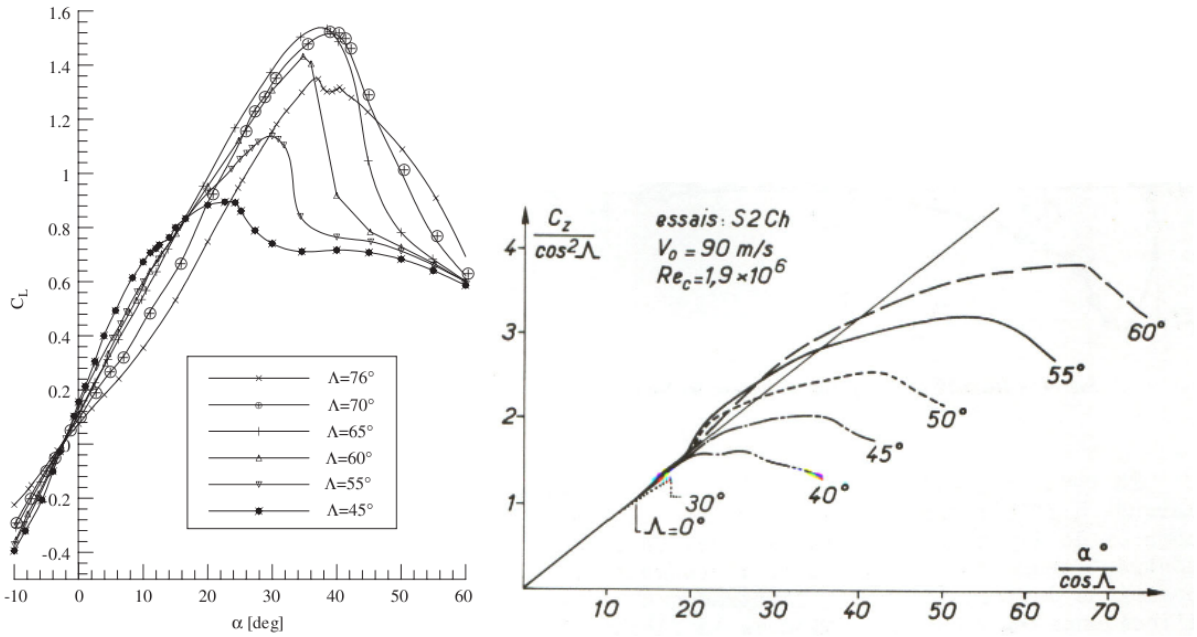

(a) Source: [Earnshaw and Lawford, 1964]

(b) Source: [Manie et al., 1978b]

Figure 1.11. *Lift coefficient with respect to incidence for various sweeps. a: dimensional version. b: version non-dimensionalised by the sweep.*

of the trailing edge, on each side of the sections, forming an array of horseshoe vortices. Those trailing vortices are supposed to be at an angle, relative to the flight direction, equal to one-half the angle of attack. This displacement reduces the downwash induced at the wing surface and thereby requires additional circulation in order to maintain the boundary condition of tangential flow at the wing surface. This additional circulation is assimilated to that caused by the LEV. Later on, [Gersten, 1961] applied this method to arbitrary planforms.

A later approach [Legendre, 1952, Brown and Michael, 1954, Brown and Michael, 1955, Mangler and Smith, 1959] consisted in performing potential calculations while adding a potential line vortex to model the LEV. In order to model the flow around the wing planform, under the assumption of high sweep, the slender wing theory was used, which allowed to simplify the 3D geometry to a series of 2D profiles corresponding to transverse planes, facing the inflow $U_{inf}\, sin\alpha$, with a Kutta condition at each end (see figure 1.12). In addition, the approximation of small thickness (slender body theory) was made. This enabled to simplify the velocity perturbation potential equation, under the assumption of small perturbations, around a thin profile at relatively low angles of attack, for subsonic ($0 \leq M \leq 0.8$) and supersonic ($1.2 \leq M \leq 5$) flows.

The line vortex model was gradually complexified. Following the approach of [Legendre, 1952], [Brown and Michael, 1954, Brown and Michael, 1955] added a feeding sheet of transverse isolated vortices to the line vortex model, enforcing the constraint of zero net force on the vortex plus the feeding sheet. Later, [Mangler and Smith, 1959] added the real spiral vortex sheet form to Browns' model. Those approaches were in reasonable agreement with the experiment for very high sweeps, for subsonic or supersonic flows. However, as [Polhamus, 1971] noted, this approach was not valid for transonic or hypersonic flows (due to the slender body theory assumptions). Furthermore, the [Mangler and Smith, 1959] model relied on heavy calculations.

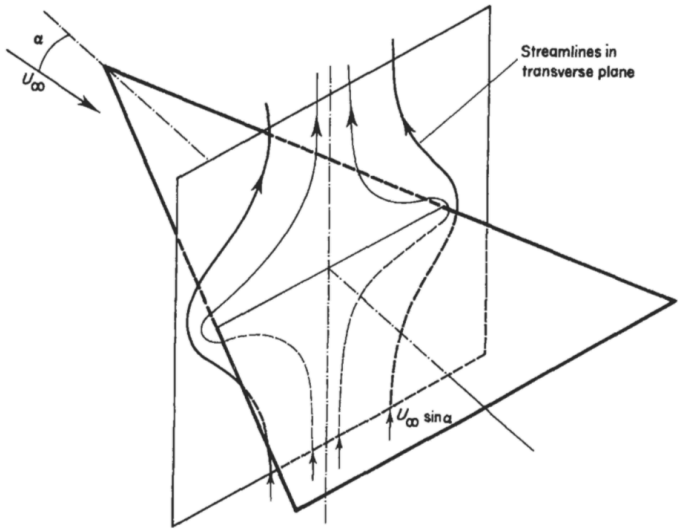

Figure 1.12. *Approximate flow in the transverse plane of a slender delta wing from two-dimensional potential flow theory (slender wing theory). Source: [Houghton and Carpenter, 2003]*

Polhamus [Polhamus, 1966, Polhamus, 1968, Polhamus, 1969, Polhamus, 1971] provided his own identification of vortex lift. The author proposed a semi-empirical theory based on an analogy between vortex induced lift and potential flow leading-edge suction, which is still considered a reference today. The author noticed that the leading-edge suction force on airfoils did not depend on the leading-edge radius, and supposed that this force would simply turn to be normal to the wing surface when the flow detached at the leading-edge. This main hypothesis is referred to as "the leading-edge suction analogy" in the work of Polhamus. Following this reasoning, the author shows that vortex lift can be deduced from potential calculations at low angles of attack, relying on tabulated coefficients Kp and Kv which only depend on the Delta wing sweep.

$$CL_{tot}(\alpha) = CL_p(\alpha) + CL_v(\alpha)$$

$$CL_p(\alpha) = Kp\, cos^2\alpha\, sin\,\alpha$$

$$CL_v(\alpha) = Kv\, cos\,\alpha\, sin^2\alpha$$

where CL_p is refered to as "potential" lift coefficient, CL_v is the vortex lift coefficient, and Kp and Kv are tabulated from whole wing polars at low incidence. This approach provides an analytical reasoning based on potential theory to show that LEVs can contribute to lift and provides a phenomenological argument to separate vortex lift from total lift. As this theory will be referred to later in the manuscript, it will be explained in further detail in part 2.2.1.

This theory improved the representativity compared to past theories, which were only valid for very highly swept wings, due to the slender wing assumption (for instance the theory of [Brown and Michael, 1954] was only tested for Delta wings of sweep $\phi \geq 85$ degrees). The Polhamus theory fit very well with experimental data on thin, sharp-edged, slender delta wings ($\phi \geq 65$ degrees) or derivatives such as high sweep arrow, diamond or double delta wings [Polhamus, 1969]. It applied to subsonic cases, but was also extended to super(hyper)sonic cases in [Polhamus, 1969], taking into account the formation of a Mach cone on the Delta wing.

One of the limitations of the Polhamus theory is that the predicted aerodynamic efforts are more distant from the experimental results when vortex breakdown occurs. In this case, this theory over-estimates lift and under-estimates drag, as illustrated on figure 1.13. Also, it

can be noted that at very high sweeps such that strong interferences appear between the two leading-edge vortices, small discrepancies appear between the Polhamus predictions and the experimental results.

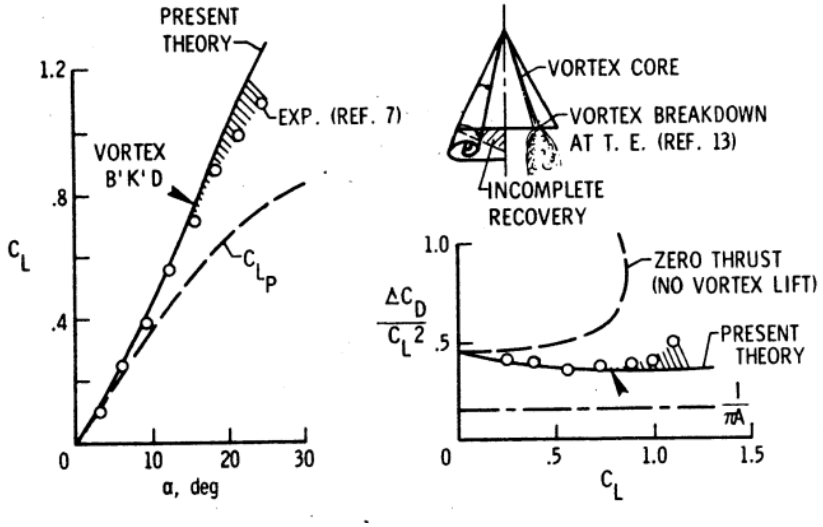

Figure 1.13. *Effect of vortex breakdown on characteristics of a 63 degrees swept Delta wing at M=0. Source: [Polhamus, 1969]*

It is worth noticing that vortex lift definition in the theory of Polhamus does not correspond to that of previous studies. Indeed, as [Hemsch and Luckring, 1989] points out, what Polhamus calls "potential lift" is not linear with respect to the angle of attack, and is therefore different from the result of a potential calculation (see figure 1.14).

This can be discussed using the work of [Saffman and Sheffield, 1977]. In this article, a theoretical study was performed of a free but steady line vortex of circulation γ above a flat plate at an incidence, with a bound circulation Γ, using potential flow theory (in 2D), and discussed the admissible positions of the line vortex. [Saffman and Sheffield, 1977] showed that in this configuration, none of the solutions verified the Kutta condition at the leading-edge. However, the leading-edge suction analogy implicitly considers a Kutta condition at the leading-edge in the presence of a LEV. Indeed, if the leading-edge suction force is oriented normal to the suction side, its projection along the chord direction is zero, which implies that the stagnation point is assumed to be at the leading-edge itself. In other words, if the stagnation point were located on the pressure side, the fluid would apply a suction force in the chord direction as it would circumvent the leading-edge. Therefore, the Polhamus theory is bound to overestimate the ratio of vortex lift to non-vortex lift compared to other vortex lift identification methods, because some part of the potential efforts due to suction at the leading-edge is counted into the vortex lift term. Nonetheless, the leading-edge suction analogy remains a powerful tool, as it predicts total lift coefficients which are in very good agreement with physical data on sharp-edge slender Delta wings.

Further developments of the Polhamus theory include the works of [Lamar, 1974, Lamar, 1975], which extended this theory to rectangular wings, and considered the impact on downstream planforms of a vortex generated in the upstream.

Influence of sweep. Several studies have shown that the sweep not only influences LEV topology but also vortex lift generation. According to [Lee and Ho, 1990], vortex contribution

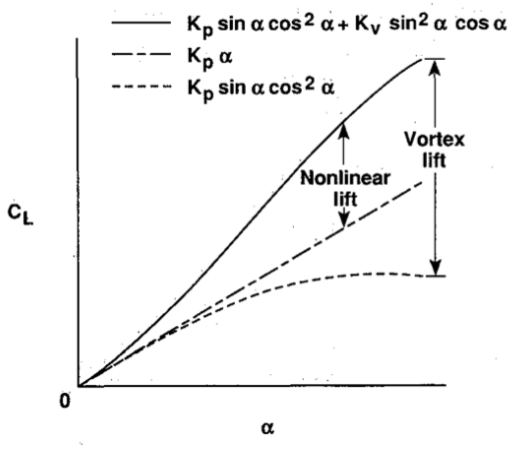

Figure 1.14. *Difference between nonlinear lift and vortex lift as defined by Polhamus. Source: [Hemsch and Luckring, 1989]*

to lift in the case of non slender delta wings is lower with respect to slender wings at the same incidence. [Manie et al., 1978a] even gave a limit in terms of sweep below which vortex lift would not be generated on Delta wings: 40 degrees of sweep.

This dependency of vortex lift on sweep is supported by the experimental work of [Hill, 1957] (in the supersonic regime). This article investigates the sweep dependency of the force normal to the Delta wing surface, and concludes that its non-linear part depends on $\sqrt{M_{inf}^2 - 1}\, cot\phi$, as pictured in figure 1.15. In other words, the normal force coefficient decreased with sweep and increased with the angle of attack. Also, [Wentz and Kohlman, 1971] stated that the leading-edge suction analogy of Polhamus would overpredict vortex lift for wings of moderate sweep. The article justifies that for low sweeps, the LEVs do not stream perpendicular to the trailing edge (while it is nearly the case for high sweeps), thus some part of vortex lift remains unexploited.

As mentioned earlier, the Polhamus theory relies on tabulated coefficients, called Kp and Kv, which depend only on the Delta wing sweep and enable to express "potential" and vortex lift. The PhD thesis of [Renac, 2004] attempted to find the explicit dependency of Kp and Kv on sweep. This was performed using identifications with expressions calculated using the slender wing theory, and led to the following formulas:

$$Kp = \frac{2\pi}{tan\phi},\ Kv = \frac{\pi}{sin\phi}$$

However, figure 1.16 shows that those approximations are only valid for very highly swept wings. Indeed, for lower sweeps, the assumption of 2D flow on transverse planes does not hold anymore. This allows to explain why the Polhamus theory consisted in an improvement compared to previous modelling approaches based on the slender wing theory. However, it also shows that the dependency of vortex lift to sweep has not been clearly explicited yet.

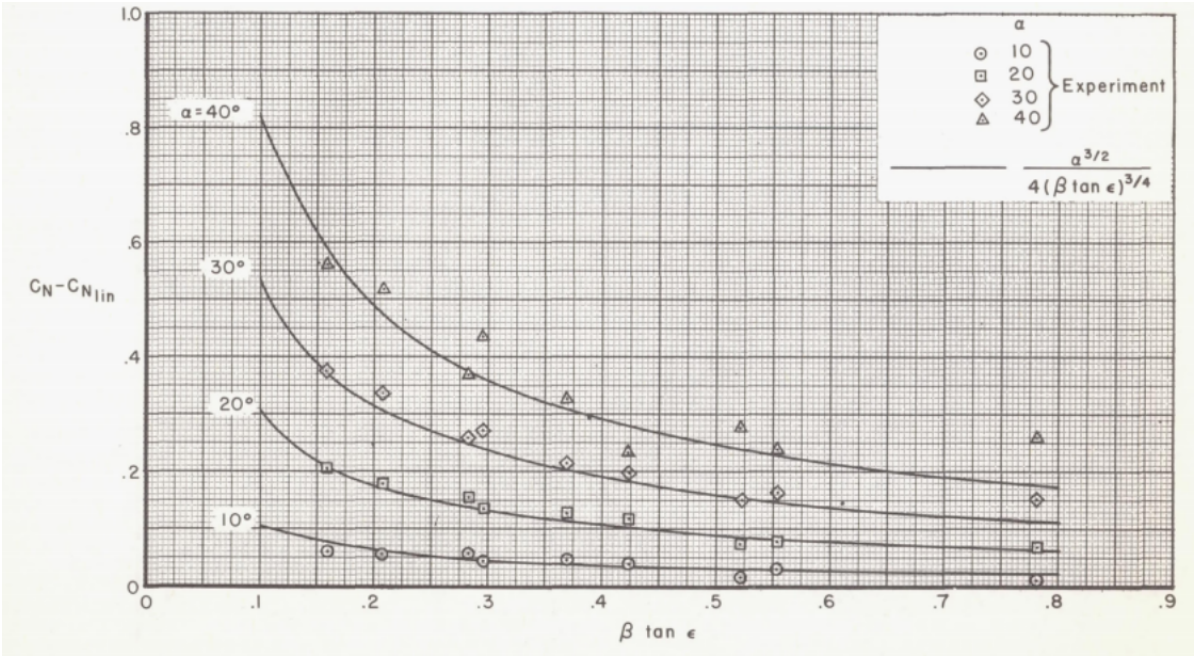

Figure 1.15. *Non-linear part of the normal force coefficient, with respect to sweep. The abscissa* $\beta \tan \epsilon$ *corresponds to* $\sqrt{M_{inf}^2 - 1}\cot\phi$ *in the present nomenclature. Source: [Hill, 1957]*

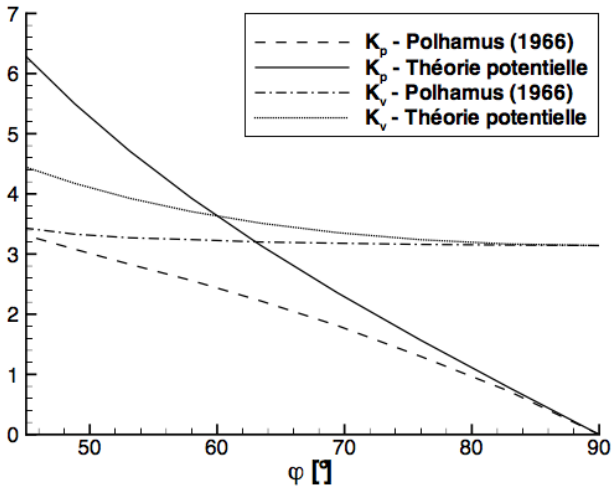

Figure 1.16. *Comparison of Kp and Kv expressions identified through potential calculations using the slender wing theory with the values tabulated by Polhamus. Source: [Renac, 2004]*

In a nutshell, several vortex lift modelling approaches were developed throughout the development of the Delta wing concept. The theory of [Polhamus, 1966], which applies to slender, sharp-edge Delta wings ($\phi \geq 65$ degrees), performs better than models based on the slender wing theory, and is still a reference today. However, this theory was found to overestimate lift on non slender Delta wings, as past studies indicate that vortex lift should decrease with sweep (though no explicit link was made with the change in LEV topology with sweep, and no explicit modelling exists to date). Also, the dependency of the Polhamus coefficients on sweep still remains to be clarified. Finally, this review of vortex lift modelling approaches shows that vortex lift is not a clearly defined concept, as some authors identify it to non-linear lift while others identify it through the leading-edge suction analogy.

1.1.3. Unsteady mechanisms

In view of the Time Resolved PIV which will be performed in this thesis, this part deals with an overview of the unsteady behaviour of Delta wing LEVs.

In the literature, the main driver to characterise the unsteady behaviour of LEVs was to design control strategies. In particular, flow reattachment and vortex breakdown are the two main phenomena determining the effective flow control strategies [Gursul et al., 2007, Riou, 2009]. For instance, the bursting of a LEV above the wing surface can lead to a sudden drop in incidence, especially on slender Delta wings [Wentz and Kohlman, 1971], where vortex lift constitutes the main source of lift. The PhD thesis of [Riou, 2009] presents a vortex breakdown control method based on pulsed jets at frequencies corresponding to natural frequencies in Delta wing LEVs.

First, when the Reynolds number increases, Delta wing LEVs are subject to the development of unsteady rotational structures in the shear layers. This has been observed and their frequency was quantified in [Gordnier and Visbal, 1994]. [Renac, 2004] distinguished various types of instabilities occurring on LEVs on a rounded edge 60 degrees swept Delta wing and on a sharp edge 70 degrees swept Delta wing. The instabilities are identified using both analytical criteria and linear stability analysis on fringe laser velocimetry data fields. Three sources of instabilities were observed, namely : centrifugal instabilities, elliptical instabilities (due to the elliptical form of the velocity contours) and three-dimensional Kelvin Helmholtz instabilities. Figure 1.17 presents a frequential classification of unsteady phenomena observed on highly swept wings.

Some of the modes corresponding to Kelvin Helmholtz instabilities were found to be stationary [Renac, 2004]. Those modes were observed by [Mitchell and Molton, 2002] among others. They consist in stationary vortical structures which are disposed around the LEV in a helical pattern.

[Menke and Gursul, 1997] consider the impact of turbulent unsteady structures found in the shear layers on the dynamics of the LEV. This study showed that the interaction of the LEV with unsteady vortical structures in its shear layer led to a random movement around its axis. The amplitude of the root-mean-square of tangential velocity fluctuations in the LEV was found to reach 50% of the mean tangential velocity. This phenomenon is called vortex wandering.

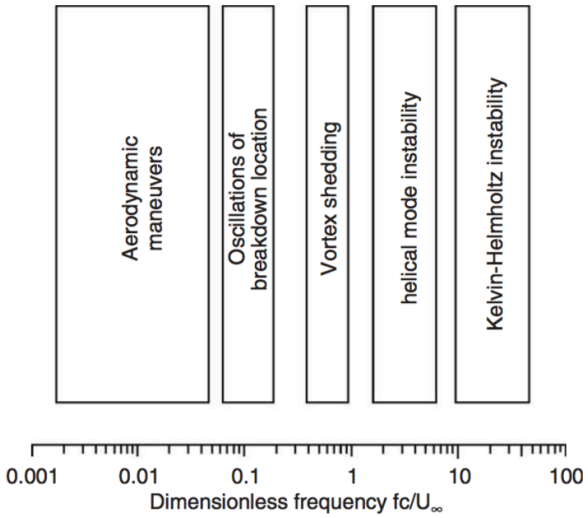

Figure 1.17. *Frequential classification of unsteady phenomena on highly swept wings. Source: [Gursul et al., 2005]*

		Influence on...	Consequence of an increase
Delta wing	Reynolds (Re)	shear layer surrounding the LEV	development of instabilities and small vortical structures
		LEV circulation	increase
	Incidence (α)	LEV circulation	increase
		core velocity along LEV axis	increase (possible vortex breakdown)
		vortex breakdown point	upstream movement towards apex
		normal force coefficient	increase
	Sweep (ϕ)	vortex lift	increase
	Leading-edge radius	LEV position on wing	flattened, closer to surface
		LEV radius	decrease
	initial Swirl number	vortex breakdown point	upstream movement towards apex

Table 1.1. *Parameters influencing Delta wing LEVs*

Table 1.1 summarises the dimensionless parameters' effect on LEV topology and vortex lift on Delta wings. It can be read according to the following example sentence: "an increase of the leading-edge radius will decrease the LEV radius".

1.2. The impact of rotation on leading-edge vortices

Although LEVs were observed in past studies on propeller blades, the ability of the LEV to generate lift was not considered in this context. The approach of [Zachariadis et al., 2013] was mostly to prevent flow separation, while that of [Schülein et al., 2012] was to investigate the role played by the LEV in the laminar / turbulent transition. Moreover, LEVs on propeller blades were mostly observed through RANS calculations, and experiments were limited to friction line visualisations [Schülein et al., 2012, Vion, 2013].

However, LEVs on rotating wings were investigated in the context of the development of Micro Air Vehicles, though at relatively low Reynolds numbers $Re \leq 10^4$. Indeed, LEVs are known to play an important part in the lift of insect wings [Sane, 2003], and have therefore aroused interest in this community. The objective of this part is to present recent studies on rotating wings with a stress on the similarities and differences with Delta wing leading-edge vortices. In particular, the effects of rotation on leading-edge vortex topology, formation and stability mechanisms will be discussed. Comparing fixed and rotating cases is all the more significant as the experimental investigation of the leading-edge vortex on the HTC5 propeller blade is carried out in this thesis using a «fixed» model blade [Vion, 2013].

Just as on Delta wings, flow separation in the leading-edge region creates a structure which transports vorticity along the leading-edge, until it mixes with the tip vortex. The LEVs are also known to be quasi-stationary structures, with a characteristic conical form. This behaviour is reported on various shapes of rotating wings, in different aerodynamic conditions (Reynolds number Re, angle of attack α). For the sake of clarity and homogeneity of the notations, the results of the articles are translated using the frames of reference and nomenclature displayed on figures 1.18 and 1.19.

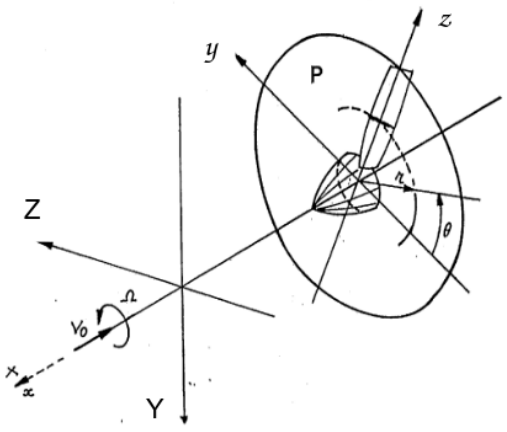

Figure 1.18. *Classical propeller frame of reference. Source: [Bousquet, 2008]*

Influence of the Reynolds number. [Garmann et al., 2013] investigated the influence of the Reynolds number on the LEV topology on a rectangular flat plate rotating around an axis with an angle of attack of 30 degrees. The Reynolds number is defined in this study as $Re = \frac{U_{tip} c_{ave}}{\nu}$, where U_{tip} is the inflow velocity at the tip, c_{ave} the average chord, and ν the air kinematic viscosity. The article considers the following range of Reynolds numbers: $2 \times 10^2 \leq Re \leq 6 \times 10^4$. [Garmann et al., 2013] argues that the simulations have a sufficient resolution in order to correctly model vortex bursting and instabilities in the mixing layer at

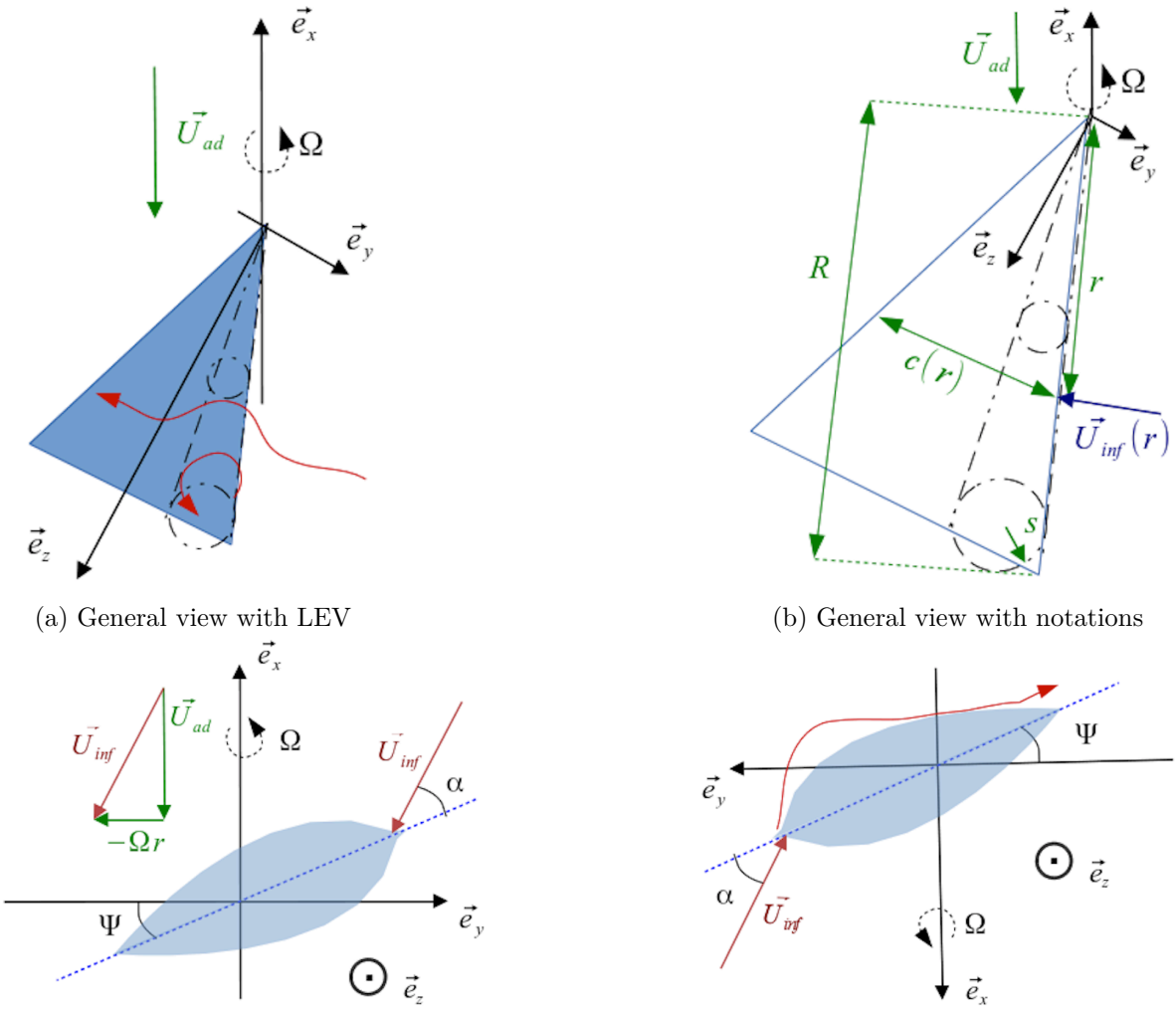

(a) General view with LEV

(b) General view with notations

(c) (x,y) plane view

(d) (x,y) plane view with flow trajectory

Figure 1.19. *Frame of reference $(\vec{e_x}, \vec{e_y}, \vec{e_z})$ attached to the rotating wing, with its characteristic dimensions. $U_{inf}(r)$ is the inflow velocity at position r, R is the wing span, $c(r)$ its chord at position r, U_{ad} the advance velocity, Ω the rotation speed. The red arrows indicate the flow trajectory.*

the edge of the LEV. Indeed, Implicit Large Eddy Simulation guarantees a high resolution as long as the mesh is dense enough, which has been verified in the study. This technique differs from a classical Large Eddy Simulation based on sub-grid scale models, as it solves all scales of the flow like a Direct Numerical Simulation, before applying a low-pass filter to the calculated flow field in order to damp the smallest scales which may not be sufficiently resolved.

The instantaneous and average visualisations of the LEV are presented on figure 1.20. In particular, those simulations enable to observe similar structures to Delta wings at high Reynolds numbers. For a sufficiently high *Re* number, secondary vortices appear as the LEV progresses toward the tip. At high *Re* numbers, thin vorticity filaments surround the LEVs downstream of a given position along the leading-edge. Though small vortical structures start surrounding the LEV as the Reynolds number increases, it is worth noticing that the average flow topology does not seem to be influenced by the Reynolds number. The same trend is observed on the wall pressure distributions in the article. [Ozen and Rockwell, 2012] also supports the fact that the average characteristics of the LEV are relatively independent from the Reynolds number, which mostly influences the unsteady and secondary vortical structures.

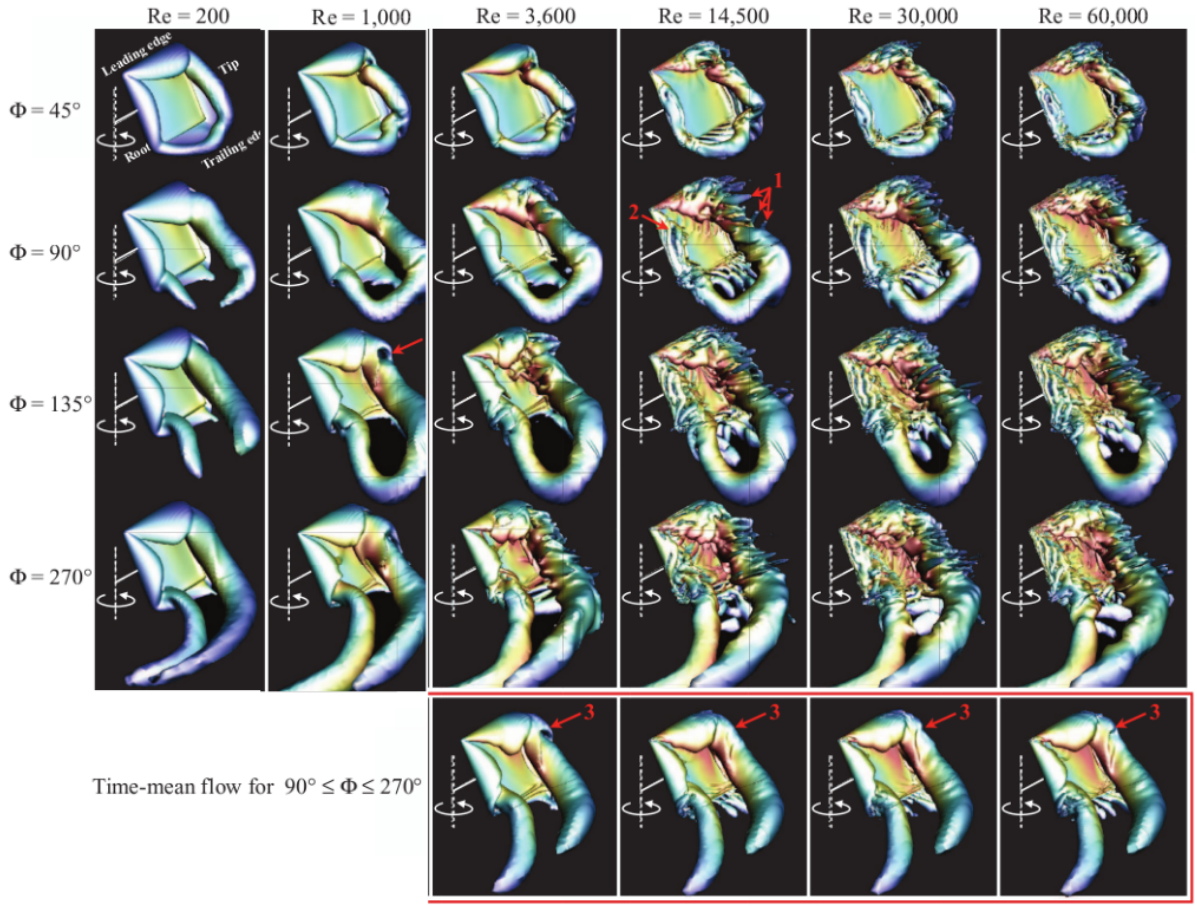

Figure 1.20. *Structure of the LEV for different values of the Reynolds number Re. The incidence of the flat plate is $\alpha = 30$ degrees and its aspect ratio is $AR = 1$. The LEVs are visualised using the Q criterion. ϕ measures the distance travelled by the blade from its initial position $\phi = 0$. Source: [Garmann et al., 2013]*

[Harbig et al., 2013] provides an interesting discussion about the most relevant definition for the Reynolds number in the case of a rotating wing. The authors consider a fly wing geometry and vary the chord for a fixed span, keeping the rotation speed and the advance velocity constant. They notice that increasing the aspect ratio AR produces the same effect as increasing the Reynolds number. This is expected, because the Reynolds number defined previously depends on the average chord. [Harbig et al., 2013] argues that the Reynolds number should be defined based on the span $Re_{span} = \frac{U_{tip}T}{\nu}$, in order to decouple its influence from that of the aspect ratio. Indeed, figure 1.21 shows that the flow topology is very similar for the same Re_{span} ($6 \times 10^2 \leq Re_{span} \leq 8 \times 10^3$), whatever the aspect ratio AR ($1 \leq AR \leq 8$). The justification given by [Harbig et al., 2013] is that the axial velocity component (along the span) plays a greater role than the chordwise component in the propagation of the LEV. This definition of the Reynolds number is valid as long as an axial velocity component is observed, thus for cases with a relatively low root radius and advance parameter $J = \frac{U_{ad}}{T\Omega}$, and sufficiently high angle of attack. This hints that additional parameters such as J influence the development of LEVs on rotating wings.

Finally the work of [Elimelech et al., 2013] shows that different structures are formed depending on the Reynolds number. The author noted on a triangular flat plate rotating at an incidence that a LEV existed for Reynolds numbers in the order of $Re = 200 - 300$, while only a detach-

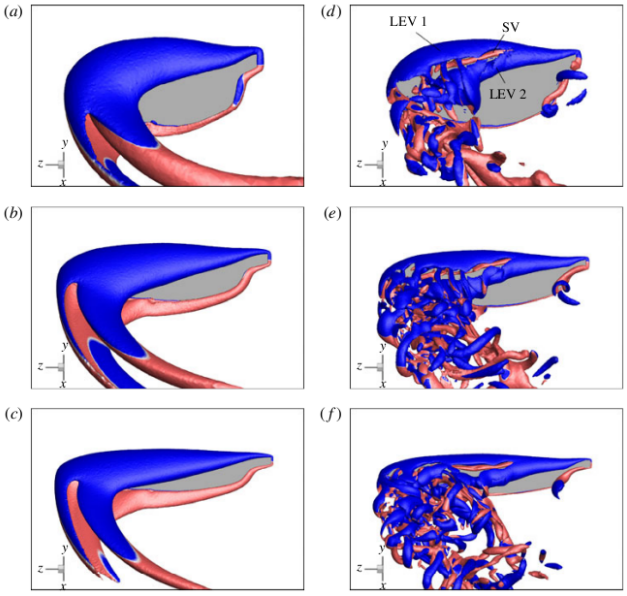

Figure 1.21. *LEVs for different span-based Reynolds numbers $Re_{span} = 613$ (a-c) and $Re_{span} = 7667$ (d-f). The aspect ratios amount to $AR = 2.91$ (a,d), $AR = 5.1$ (b,e), $AR = 7.28$ (c,f). Vortices are visualised using the Q criterion and coloured depending on the sign of their vorticity : positive (red) or negative (blue). Source: [Harbig et al., 2013]*

ment (or separation) bubble was formed at higher Reynolds numbers $Re = 1000$. According to [Elimelech et al., 2013], the distinction between a LEV and a separation bubble lies in the norm of the spanwise vorticity field (see figure 1.22). When the detached flow turns into a LEV, vorticity is maximal at the detachment point: the leading-edge. On the other hand, in the case of a separation bubble, vorticity would be maximal at the reattachment point. In other words, the LEV is a more "open" vortical structure compared to the separation bubble whose core is more shielded from outside flow. In the same train of thought, [Horton, 1968] refers to the low-velocity zone in the core of a separation bubble as a "dead-air" zone.

Influence of the Aspect ratio. Following previous remarks, let us consider the influence of the aspect ratio in the sense that it is decoupled from that of the Reynolds number.

The influence of the aspect ratio on the LEV shape is due to the border effects experienced when the LEV reaches the trailing edge. Then, the LEV interacts with the vorticity field of the pressure side, which reduces the leading-edge suction peak and leads the LEV to lift up from the surface [Garmann and Visbal, 2014].

1.2.1. Comparison of LEV formation and stability mechanisms in fixed and rotating cases

In this section, the term "stability" describes the fact that the leading-edge vortex is attached to the wing, in accordance with the literature. In other words, it is motionless in the wing reference frame.

Comparing LEVs on fixed and rotating wings, an important difference which immediately comes to the mind is that there is no need of sweep to create a LEV on a rotating wing.

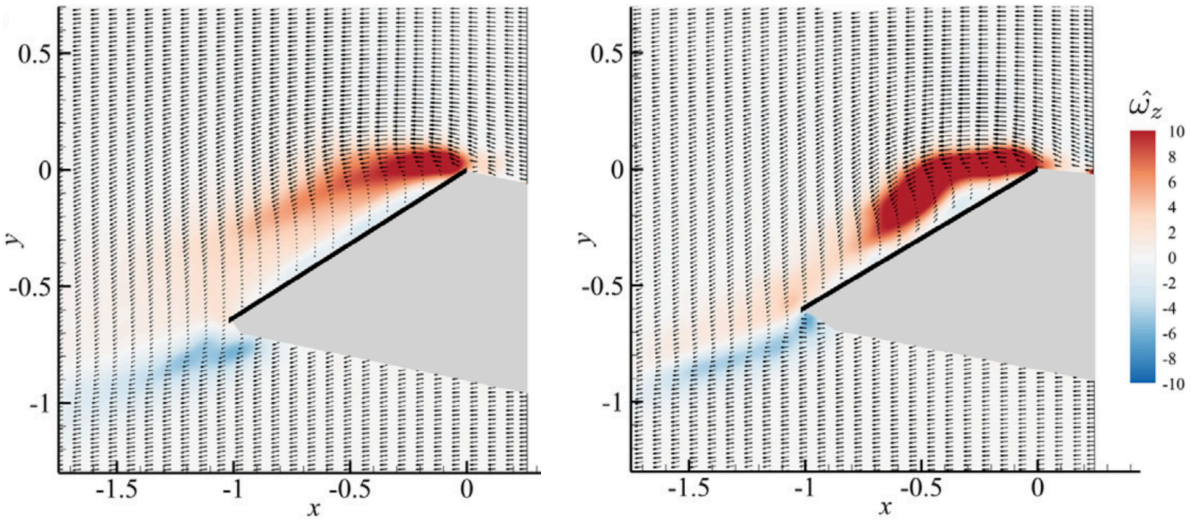

(a) LEV (b) separation bubble

Figure 1.22. *Spanwise vorticity field above a triangular flat blade during accelerated rotation, at same angular position. (a) : $Re = 250$, (b) : $Re = 1000$. Black arrows are representative velocity vectors. Source: [Elimelech et al., 2013]*

The results of [Garmann and Visbal, 2014] on a rotating rectangular flat plate confirm this fact. Moreover, another result highlights the specific role that rotation plays in LEV stability. [Lentink and Dickinson, 2009b] performed several experiments on a fly wing at $Re = 110$ and $Re = 1400$, and observed that the LEV was rapidly released in the wake when the wing was in translation (whatever the sweep in the range of 0 to 60 degrees, and the incidence), while it stayed attached as soon as the wing was rotating. In this case, sweep alone was thus insufficient to create a stable LEV. Therefore several articles [Lentink and Dickinson, 2009b, Usherwood and Ellington, 2002] concluded that specific formation and stability mechanisms (other than the sweep and the induced downwash due to the tip vortex, which were some of the hypotheses in prior work) existed for a wing in rotation. This led the authors to investigate the effects of inertial forces due to rotation: centrifugal and coriolis forces.

Dimensionless version of Navier Stokes equations for generalised flight motion. A former article by the same team [Lentink and Dickinson, 2009a] presents an interesting approach to evaluate the order of magnitude of the centrifugal and coriolis forces with respect to the other terms in Navier-Stokes equation (see equation 1.2). Those orders of magnitude are expressed depending on a large range of parameters modelling various flight types, such as :

- wing form parameters : span R and average chord c_{ave}, thus aspect ratio AR. Sweep is not taken into account.
- parameters describing advance motion : advance velocity U_{ad}, zero slide slip angle, straight trajectory
- parameters describing rotating motion : flapping or rotating frequency f, incidence, and flapping angle (equal to zero for a non-flapping case) $\Phi(t) = \Phi_0 sin(2\pi ft)$.

Those parameters are used to non-dimensionalise Navier-Stokes equations.

$$\rho\,(\frac{\partial\vec{u}}{\partial t}+\vec{u}\cdot\vec{\nabla}u+\vec{\dot{\Omega}}\times\vec{r})=\ -\vec{\nabla}p+\vec{f_{ce}}+\vec{f_{co}}+\nu\Delta\vec{u} \tag{1.1}$$

where $\vec{f_{ce}}=\rho\,\vec{\Omega}\times(\vec{\Omega}\times\vec{r})$ is the centrifugal force density and $\vec{f_{co}}=-2\,\rho\,\vec{\Omega}\times\vec{u}$ is the coriolis force density.

The average velocity at the tip U_{tip} is used as a velocity scale for non-dimensionalisation. In the general case:

$$\frac{\partial\vec{u}}{\partial t}+\vec{u}\cdot\vec{\nabla}u+\frac{1}{J^2+1}(\frac{1}{A^*}\vec{\dot{\Omega}}\times\vec{r}+\frac{1}{AR}\vec{\Omega}\times(\vec{\Omega}\times\vec{r})+\frac{\sqrt{J^2+1}}{AR}2\vec{\Omega}\times\vec{u})=\ -Eu\vec{\nabla}p+\frac{1}{Re}\Delta\vec{u} \tag{1.2}$$

where $A^*=\frac{\Phi_0 R}{c_{ave}}$, $J=\frac{U_{ad}}{4\,\Phi_0\,R\,f}=\frac{\lambda^*}{4A^*}$ is the advance parameter, , $AR=\frac{R}{c}$ is the aspect ratio. $Eu=\frac{p_0}{\rho\,U_{tip}^2}$ is the Euler number. For an incompressible flow, $Eu=1$. For a compressible flow, it can be expressed in function of the Mach number: $Eu=\frac{1}{\gamma M^2}$. The Reynolds number is expressed as $Re=\sqrt{(\frac{U_{ad}c_{ave}}{\nu})^2+(\frac{4\Phi_0 f c_{ave}}{\nu})^2}=\sqrt{Re_{ad}^2+Re_s^2}=\sqrt{J^2+1}\frac{4\Phi_0 f c_{ave}}{\nu}=\sqrt{J^2+1}Re_s$ where Re_{ad} is the Reynolds number associated to the advance velocity and Re_s the stroke / rotation Reynolds number. A^* has a physical interpretation : it represents the amplitude of the wing tip movement.

For a steadily rotating wing (propeller type), this simplifies as (using the classical definition of the advance parameters $J=\frac{U_{ad}}{2\,\pi\,R\,f}$):

$$\frac{\partial\vec{u}}{\partial t}+\vec{u}\cdot\vec{\nabla}u+\frac{1}{J^2+1}(\frac{1}{AR}\vec{\Omega}\times(\vec{\Omega}\times\vec{r})+\frac{\sqrt{J^2+1}}{AR}2\vec{\Omega}\times\vec{u})=\ -Eu\vec{\nabla}p+\frac{1}{Re}\Delta\vec{u} \tag{1.3}$$

It is worth noticing that the magnitude of the forces due to rotation is inversely proportional to the aspect ratio AR. Table 1.2 summarises the dimensionless parameters' effect on LEV topology and vortex lift on rotating wings.

Using the dimensions put forward in the analysis of [Lentink and Dickinson, 2009a], Table 1.3 provides a comparison of the orders of magnitudes of the terms in Navier Stokes equations for various types of flows, along with the characteristic dimensionless parameters. This evaluation clearly shows the impact of the aspect ratio on the magnitude of force densities due to rotation. However, this analysis does not reveal main differences regarding the HTC5 propeller blade at take-off (when a LEV is formed) and in cruise (when it does not appear). A possible explanation is that the incidence of the profiles, as well as Reynolds number and compressibility effects are not accounted for in the approach of [Lentink and Dickinson, 2009a].

Role of rotation forces in stability mechanisms. Generally in the literature [Lentink and Dickinson, 2009a, Garmann and Visbal, 2014] the ratio between inertial and coriolis forces is represented by the Rossby number Ro. Using the scales given by non-dimensionalisation yields $Ro=\sqrt{J^2+1}AR$. [Lentink and Dickinson, 2009b] performed several experiments on a model fly wing in "hovering condition" ($J=0$), using a water tank and air bubble visualisation. The wing was being moved at several Rossby numbers $Ro=AR=2.9,3.6,4.4,\infty$ ($Ro=\infty$ meaning non-rotating motion), Reynolds numbers $110\leq Re\leq 1400$, stroke amplitudes A^*, with or without a reciprocating movement. The authors concluded that a Rossby number

		Influence on...	Consequence of an increase
Rotating wing	Reynolds (Re)	shear layer around LEV	development of instabilities, small vortical structures
	Incidence (α)	vorticity on suction side	increase
		shear layer around lEV	development of instabilities, small vortical structures
		LEV radius	increase
	Aspect Ratio (AR)	LEV propagation	edge effect: LEV interacting with pressure side flow
		centrifugal and Coriolis force densities	decrease in absolute value
		LEV stability	decrease
	Advance parameter (J)	LEV stability	decrease

Table 1.2. *Dimensionless parameters influencing LEVs on rotating wings. This Table can be read according to the following example sentence: "an increase of the Reynolds number will result in the development of instabilities and small vortical structures in the shear layer surrounding the LEV".*

in the order of one or lower seemed to be the main parameter dictating LEV formation and stability. Other studies show that LEVs may also appear on higher aspect ratio wings, but near the hub (as long as the Rossby number based on spanwise position is of order one). According to [Beom-Seok et al., 2002, Tangler, 2004, Lu et al., 2006], this effect is likely responsible for the higher than expected forces found near the hub of high aspect ratio wind turbine blades where local Rossby is less than 3. The work of [Kolomenskiy et al., 2014] also supports the fact that LEVs are stable below a threshold in Rossby number. This study reports numerical simulations of rotating triangular wings (accelerated from rest before reaching a steady state) at $Re = 250$ for various aspect ratios and angles of attack. The article stated that aspect ratios (thus Rossby numbers) below 5.5 led to a stable LEV up to incidences of 70 degrees.

Recall that the Rossby number is linked to rotational accelerations according to equation 1.3. [Lentink and Dickinson, 2009b] explains how this can be translated physically based on an analogy with a purely viscous phenomenon called "Ekman pumping" (or centrifugal pumping). This mechanism is more prominent at low Reynolds numbers, as the Ekman number is $Ek = \frac{Ro}{Re}$. If we think about the flow over a rotating surface as being decomposed into several layers, the first layer (which has the same rotation velocity as the surface) entrains the layers on top through viscosity. Those layers are thus influenced by centrifugal and coriolis forces. The fluid particles are subject to a centrifugal movement and are displaced radially towards the tip, creating a spanwise flow. In order to keep the flow-rate, the fluid is pumped vertically on the rotation axis. In this mechanism, coriolis forces, which are directed in the direction opposite to rotation, contribute to LEV stability by making the flow reattach to the surface (see figure 1.23).

To summarise, it appears that specific mechanisms due to rotation promote LEV stability. These mechanisms are linked to the aspect-ratio and Rossby number. At low Reynolds numbers, the Ekman pumping mechanism has been proposed to explain how rotation would help stabilise LEVs: the centrifugal forces would create a spanwise flow and the coriolis forces would foster flow reattachment. In the following paragraph, studies are presented which elaborate on the role of the spanwise flow.

		Rectangular blade	Fly wing	HTC5 take-off	HTC5 cruise	Wind turbine blade	Helicopter blade	Ekman Pumping	AIPX7 propeller take-off
order of magnitude of force densities	centrifugal	0.13	0.28	0.39	0.33	0.02	0.10	1.00	0.22
	Coriolis	0.13	0.31	0.40	0.36	0.02	0.10	1.00	0.23
	pressure gradient	1.00	1.00	1.00	1.27	1.00	1.00	1.00	1.00
	viscous forces	1.3×10^{-4}	6.2×10^{-3}	3.9×10^{-8}	3.5×10^{-8}	2.4×10^{-8}	1.8×10^{-8}	5.4×10^{-5}	6.3×10^{-8}
characteristic dimensionless numbers	Advance parameter J	0	0.42	0.14	0.47	0	0.01	0	0.137
	Advance Reynolds Re_{ad}	0	6.3×10^{1}	3.6×10^{6}	1.2×10^{7}	0	7.0×10^{5}	0	2.2×10^{6}
	Rotation Reynolds Re_s	8.0×10^{3}	1.5×10^{2}	2.6×10^{7}	2.6×10^{7}	4.2×10^{7}	5.5×10^{7}	1.8×10^{4}	1.6×10^{7}
	Total Reynolds	8.0×10^{3}	1.6×10^{2}	2.6×10^{7}	2.8×10^{7}	4.2×10^{7}	5.5×10^{7}	1.8×10^{4}	1.6×10^{7}
Chosen parameters	Advance velocity (m/s)	0	1	68	225	0	37.5	0	68
	Flapping angular amplitude	0	1	0	0	0	0	0	0
	Rotation or flapping frequency (Hz)	65	200	36	36	6	155	209	35
	Wing radius (m)	5.0×10^{-2}	3.0×10^{-3}	2.13	2.13	30	3	1.5×10^{-2}	2.24
	Aspect ratio	8	3	2.5	2.5	50	10	1	4.4
	Advance Mach number	0	0	0.2	0.75	0	0.11	0	0.2

Table 1.3. *Orders of magnitude of the terms in Navier Stokes equation for various types of flows, evaluated using the analysis of [Lentink and Dickinson, 2009a]*

The role and origin of spanwise flow Spanwise flow has been proposed by several articles to stabilise LEVs ([Maxworthy, 1981], [Ellington et al., 1996]). [Ellington et al., 1996] points out that the spiral LEVs on Delta wings are stabilized by spanwise flow induced by wing sweep, and that it would be quite logical that spanwise flow be similarly critical to the stability of LEVs on rotating wings. Computational studies of [Sun and Wu, 2004] and [Garmann and Visbal, 2014] shed light on the presence of a pressure gradient force in the LEV core, which would generate spanwise flow. [Sun and Wu, 2004] computed the centrifugal and coriolis force density fields on a rotating insect wing with an incidence of 40 degrees, at $Re = 480$. They found an even larger pressure gradient force, concentrated in the LEV, which would also trigger spanwise flow in the LEV. [Garmann and Visbal, 2014] did a similar analysis on a rotating flat plate at an incidence of 60 degrees and $Re = 8000$. Figures 1.24 and 1.25 present respectively the spanwise component and the component normal to the blade of those force densities in a cut plane. In this case, the pressure gradient was an order of magnitude higher than the centrifugal and coriolis force densities in the LEV core. Moreover, figure 1.25 indicates that the coriolis force is oriented upwards, leading [Garmann and Visbal, 2014] to conclude that coriolis forces lead the LEV to lift up from the blade surface.

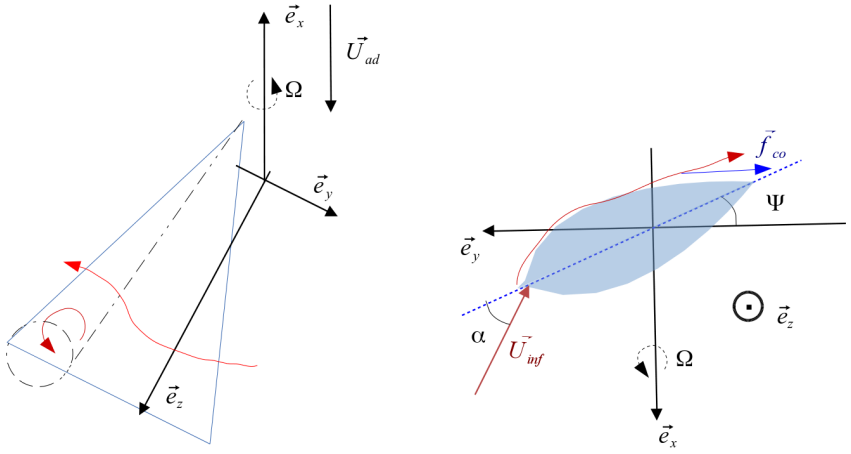

Figure 1.23. *Schematic view of a rotating wing airfoil at high incidence with flow separation, for the approach of [Lindenburg, 2004]*

The study of [Maxworthy, 2007] focuses on understanding the origins of the pressure gradient in the LEV core, through a theoretical analysis on a simplified propeller model (see figure 1.26). A stationary conical LEV is considered, with a perfect fluid assumption. The vorticity field is supposed to be uniform in the LEV and carried only by the spanwise direction $\vec{e_z}$. Cyclostrophic equilibrium in the vortex core (projection of Euler equation along $\vec{e_r}$) writes :

$$\frac{\partial p}{\partial s}(s,r) = \rho \frac{V^2(s,r)}{s}$$

$$p(s,r) = \int_s \rho \frac{V^2(s,r)}{s} + p_a(r)$$

where $p_a(r)$ is the pressure at the vortex periphery. Using relationships due to the conical form of the LEV and the notations on figure 1.26 :

$$\frac{\partial p}{\partial r} = \frac{\partial p_a}{\partial r} - \rho \frac{V_R^2 r}{R^2}(1 - \frac{s_R}{s_{R0}})$$

$p_a(R)$ can be calculated using the Bernoulli theorem on a streamline normal to the leading-edge

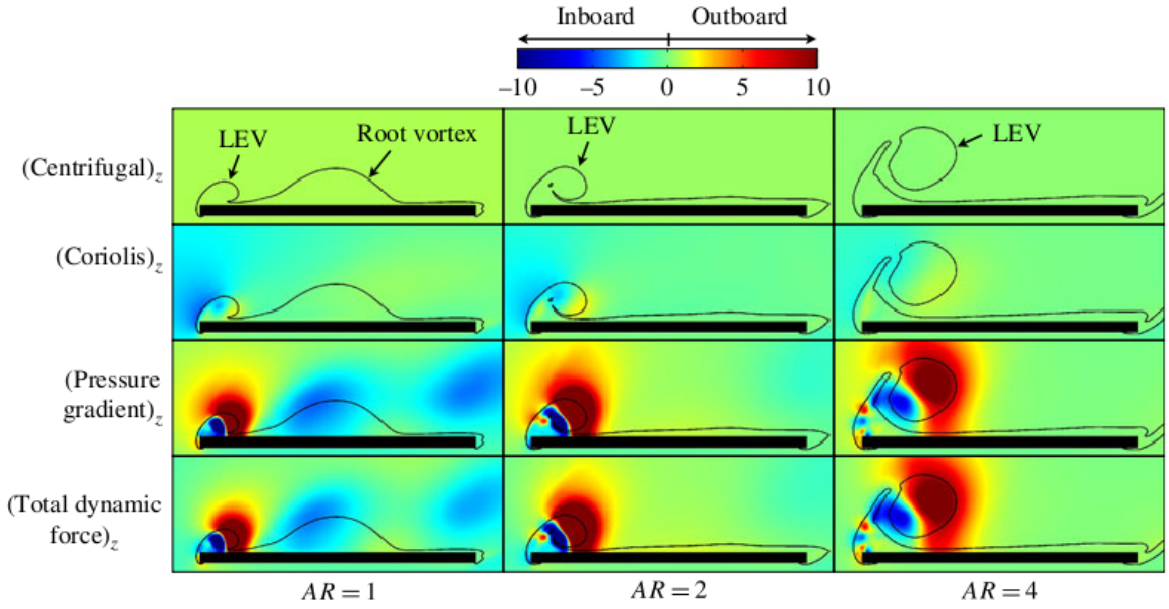

Figure 1.24. *Spanwise components of the coriolis, centrifugal, and pressure gradient force densities, on a cut plane at 25% of span. Source: [Garmann and Visbal, 2014]*

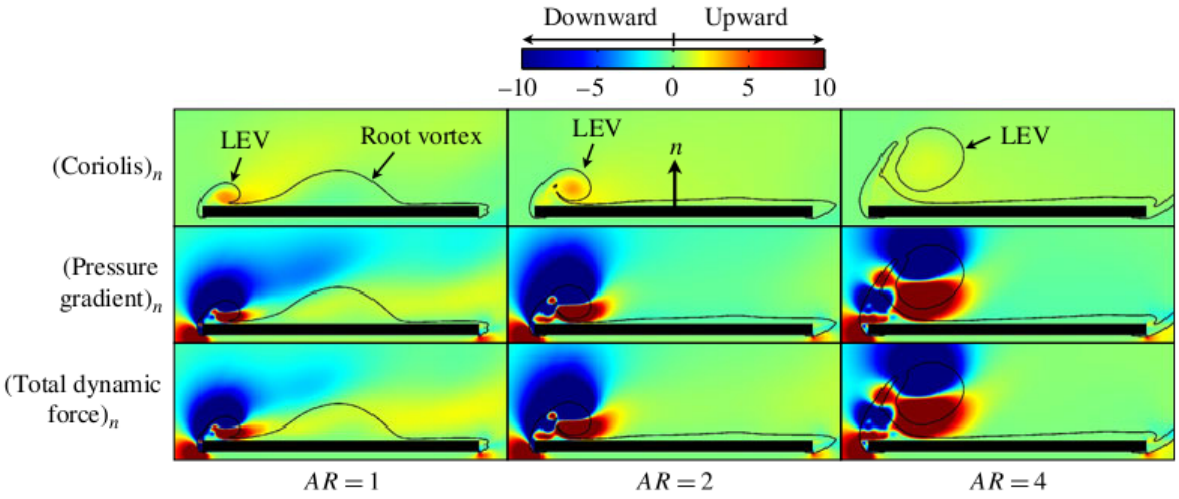

Figure 1.25. *Components normal to the blade of the coriolis, centrifugal, and pressure gradient force densities, on a cut plane at 25% of span. Source: [Garmann and Visbal, 2014]*

and originating in the still flow region (which has not been impacted by the blade).

$$\frac{\partial p_a}{\partial r} = -\rho\Omega^2 r = -\rho\frac{V_R^2 r}{R^2}$$

Finally, the pressure gradient in the LEV can be expressed as :

$$\frac{\partial p}{\partial r} = -\rho\frac{V_R^2 r}{R^2}(1 + (1 - \frac{s_R}{s_{R0}}))$$

The pressure gradient being the sum of two terms, [Maxworthy, 2007] argues that it has two origins. The first one is the conical form of the LEV embodied by $-\rho\frac{V_R^2 r}{R^2}(1 - \frac{s_R}{s_{R0}})$. This

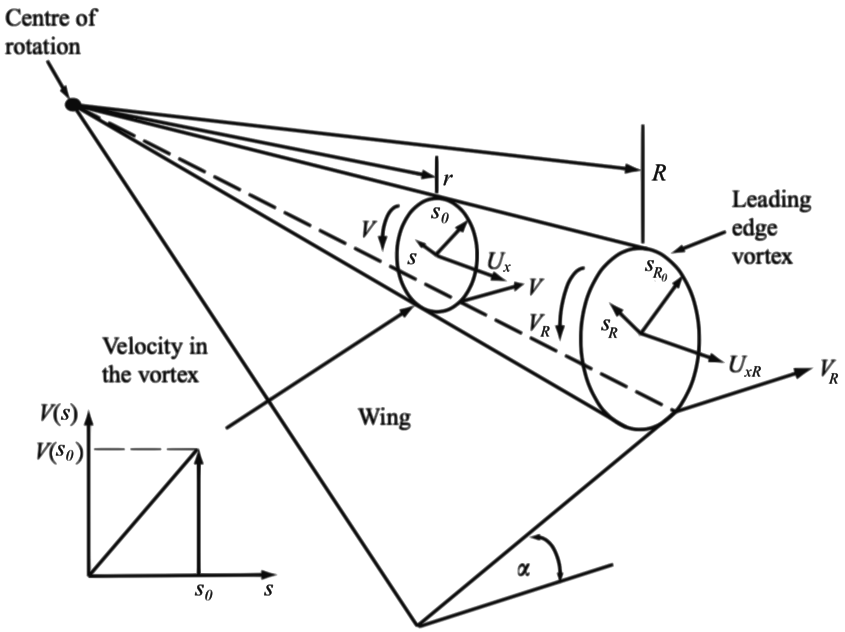

Figure 1.26. *Sketch of the conical LEV studied by [Maxworthy, 2007], with adapted notations. Source: [Maxworthy, 2007]*

mechanism also applies on a fixed blade. The second origin is blade rotation which results in $\frac{\partial p_a}{\partial R} = -\rho \frac{V_R^2 r}{R^2}$.

Spanwise flow is thought to stabilise the LEV because it transports vorticity created at the leading-edge to the tip, thus preventing it from being shed at the trailing-edge [Ellington et al., 1996, Lentink and Dickinson, 2009b]. This hypothesis is tested by [Wojcik and Buchholz, 2014a, Wojcik and Buchholz, 2014b] where a vorticity balance is performed in the LEV in order to evaluate the ratio between spanwise transported vorticity and vorticity created at the leading-edge. The control volume is materialised by three PIV planes in the leading-edge vortex on a rectangular flat plate of aspect ratio 4 rotating at an incidence of 35 degrees (see Figure 1.27). Vorticity production at the leading-edge is evaluated by calculating the vorticity flux along a segment (L_y in figure 1.27): $\beta = \int_{L_y} u_x \omega_z$. Values at 25% ($\beta_1$) and 50% ($\beta_2$) of span are reported. Those values are compared to the vorticity flux transported by the average spanwise core flow in the control volume: $\bar{u_z} \frac{\Gamma_2 - \Gamma_1}{z_2 - z_1}$ (where $\Gamma = \int_{A_z} \omega_Z(x,y) dA_z$ and A_z is the surface corresponding to the LEV in each plane, see Figure 1.27). β_1 and β_2 were found to be between 4 and 7 times higher than the estimated spanwise vorticity flux. Therefore the article concludes that spanwise convection does not provide a sufficient vorticity sink to balance the source substantiated in the leading-edge shear layer. Consequently, the assumption is made that a subsequent part of the vorticity produced at the leading-edge is destroyed through interactions with opposite sign vorticity, in the boundary layers or through interactions with secondary vortices. Spanwise flow alone may not be sufficient to ensure LEV stability, and vorticity dissipation would thus play a non-negligible part.

[Aono et al., 2007] interestingly points out the impact of the Reynolds number on mechanisms creating spanwise flow. On a revolving fruit fly wing at $Re = 134$, the spanwise flow is quite low inside the LEV core, and so is the pressure gradient. However, it is much higher behind the LEV, in the reattached zone, due to centrifugal pumping. On the contrary, on a hawkmoth at Re=6300 a strong spanwise flow and pressure gradient exist in the LEV. [Lentink and Dickinson, 2009b] suggest that, when present, the pressure gradient is more likely to influence

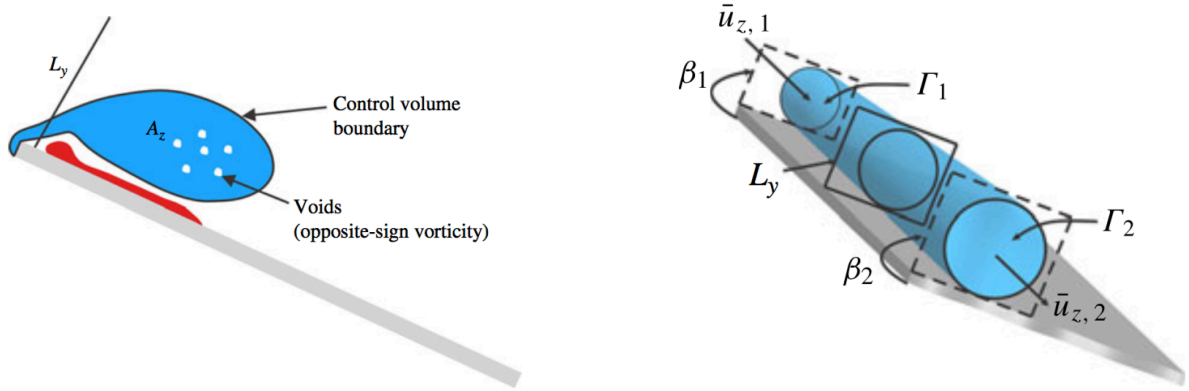

Figure 1.27. *Sketch of the control volume in the study of [Wojcik and Buchholz, 2014b]. Source: [Wojcik and Buchholz, 2014b]*

spanwise flow in the LEV core, while Ekman pumping triggers the spanwise flow in the viscous region aft of the LEV.

LEV formation and stability mechanisms on rotating and flapping wings at very low Reynolds number are still under discussion in the community. Indeed, at very low Reynolds number $150-200 \leq Re \leq 2000$, [Birch and Dickinson, 2001] notices that spanwise flow is not responsible for LEV stability. The conclusion is based on experiments on a model flapping fruitfly wing, with embedded fences. Depending on the position of those fences, they can allow or block spanwise flow, inside and outside the leading-edge vortex. It was found that the LEV was still attached even when spanwise flow was blocked. Moreover, the article notices that the LEV shape does not have a spiral form such as a Delta wing LEV. Therefore the authors rather propose that the downwash induced by the tip vortex and wake stabilises the LEV in this case. [Lim et al., 2009] also suggests that LEV stability on a flapping wing at $Re = 1100$ is not due to the existence of a spanwise velocity profile but to velocity variations along the LEV axis, which cause LEV stretching. However, [Birch and Dickinson, 2001] explain that the precise flow structure of the LEV and the associated stability mechanisms may depend critically on the Reynolds number. Indeed, on a flapping model hawkmoth wing, for $Re \geq 2000$, a spiral vortex is clearly present [Aono et al., 2007, Ellington et al., 1996]. One possible explanation for the difference in flow structure on the smaller fruitfly wing is that the pressure gradient within the vortex core is too small to drive a substantial axial flow. While the literature generally agrees on the role of spanwise flow in stabilising the LEV on rotating wings at "high" Reynolds numbers, the stability mechanisms and LEV topology seem to be very dependent on Reynolds number below a certain threshold ($Re \leq 2 \times 10^3$).

1.2.2. Vortex lift on rotating wings

LEV stability mechanisms were extensively studied in the insect flight literature, because lift enhancement through the LEV plays a subsequent role for flight in this range of Reynolds numbers [Sane, 2003, Ellington et al., 1996]. However, lift enhancement caused by LEVs does not only happen through steady mechanisms.

Some studies dealing with vortex lift on rotating wings (in the context of the development of Micro Air Vehicles) aimed at understanding the impact of flapping flight or reciprocating

motions on lift enhancement. Insects generate higher lift coefficients than fixed wings in steady flow at low Reynolds numbers, which can be explained by the appearance of several unsteady phenomena listed in [Butoescu, 2011]. Among them are the Wagner effect, caused by the formation of a trailing-edge vortex when the wing is quickly accelerated from rest, which accumulates circulation; or the added mass effect, due to the fact that the fluid itself is accelerated around an accelerated wing.

The aim of this paragraph is not to detail the impact of unsteadiness on lift enhancement, but to present the methods employed by those studies to identify vortex lift, or the results which can be applicable in a more general context.

The numerical study of [Slomski and Soleman, 1993] focused on the evolution of lift as the LEV moved away from the airfoil. In the tested range, they found that the lift force increased as the LEV lifted from the airfoil, influencing more of its upper surface. The study of [Ford and Babinsky, 2013] deals with the evaluation of vortex lift on a translated flat plate accelerated from rest in a water tank before reaching a steady state velocity, with the aim of understanding the impact of unsteadiness on the building of lift, on a simpler (non rotating) case. The article is able to distinguish the lift generated by «bound circulation» around the profile from vortex lift and from unsteady non circulatory (added mass) effects, and discusses the link between vortex lift generation and LEV circulation. Bound circulation is calculated by fitting a potential flow model to experimental PIV flow fields, and evaluating the value of the circulation providing the best match on the streamlines. This approach follows the definition of the bound circulation in the theoretical work of [Saffman and Sheffield, 1977]. In the steady state regime, the authors found that bound circulation was small, and most of the circulation was contained in the LEV(s). The lift on the flat plate was explained to originate both in inertial (added mass) effects and the buildup of circulation contained into LEVs.

Nonetheless, [Nabawy and Crowther, 2017] argued that those effects are small with respect to quasi-steady effects. Their recent study questioned the mechanism(s) by which a LEV would increase lift on a steadily revolving wing, and compared the mechanisms put forward in several models from the literature:

- the leading-edge suction analogy [Polhamus, 1966] (see section 1.1.2)
- the "trapped vortex" model (corresponding to the study of [Saffman and Sheffield, 1977]).
- the normal force model, which has been used historically to calculate the lift coefficient on helicopter blades at high angles of attack. This model considers the resulting force to be normal to the wing planform (and therefore the skin friction to be negligible). It consists in multiplying potential flow 3D lift coefficients by a $cos\alpha$ term.

The two first models are referred to as "additional lift" models in the article, because they consider that the LEV adds up to a potential part of lift (though the nature of the potential part in the decomposition of Polhamus was discussed in section 1.1.2). The last model is referred to as an "absence of stall" model. Indeed, in this model, the LEV allows to approximate the potential flow solution at high angles of incidence where the aircraft would stall otherwise. The three models were evaluated with respect to experimental data for various geometrical angles of attack ($0 \leq \alpha \leq 90$ degrees). The normal force model was found to fit more closely to the experiment, which leads the article to conclude that the "absence of stall" mechanism is the most probable explanation for lift enhancement caused by the LEV.

In summary, LEV topology was found to be influenced by the same parameters as on Delta wings. Yet [Lentink and Dickinson, 2009b] also mentions additional parameters, such as the Rossby number, depending on the advance ratio and the blade aspect ratio. A large number of studies [Lentnik et al., 2008, Lentink and Dickinson, 2009a, Lentink and Dickinson, 2009b, Harbig et al., 2013, Garmann et al., 2013, Garmann and Visbal, 2014] highlight the specific effects of rotation on the formation and maintenance of the LEV on rotating wings. Indeed, as the relative velocity varies along the span due to rotation, a spanwise circulation gradient can be created without the need of sweep. This is why a nearly circular LEV can be generated on a rotating flat plate ([Wojcik and Buchholz, 2014b, Garmann et al., 2013, Garmann and Visbal, 2014]). The literature generally agrees on the role of spanwise flow in stabilising the LEV on rotating wings at "high" Reynolds numbers ($Re \geq 2 \times 10^3$). However the mechanisms at lower Reynolds numbers are still unclear: various mechanisms can trigger spanwise flow, and the influence of spanwise flow on LEV stability itself is questioned. At high Reynolds number, the spanwise pressure gradient appears to be the main trigger for spanwise flow in the LEV core, thus LEV generation and stability. Therefore inertial forces due to rotation do not play such a prominent role at high Reynolds numbers as they do at lower Reynolds numbers. In this sense, LEV stability mechanisms on rotating wings at sufficiently high Reynolds number are essentially similar to those on Delta wings, where the pressure gradient is mainly responsible for LEV stability. [Maxworthy, 2007] shows that in this case, rotation induces an additional contribution to the spanwise pressure gradient.

In this framework, the study of [Vion, 2013] provides interesting results on the ability to qualitatively reproduce LEV generation on a propeller blade using a fixed blade with the same dimensionless circulation distribution. This was done by modifying the twist law of the rotating blade to account for a uniform inflow.

[Vion, 2013] found good qualitative agreement between the friction lines obtained from RANS calculations on the rotating case and experimental oil flow visualisation. The circulation of the wake vortex was also compared in the experimental framework and in the rotating framework. The difference between the non-dimensional circulations is in the order of 25%. The vorticity dispersion radii were also used as a means of comparison :

$$r_{disp} = \sqrt{\frac{1}{\Gamma} \int \int_S ((x_S - x_{S,0})^2 + (y_S - y_{S,0})^2) \vec{\omega} \cdot \vec{n} dS}$$

where Γ is the circulation of the vortex, S the surface defined by the set of coordinates (x_S, y_S), $\vec{n}$ the normal vector to S and $(x_{S,0}, y_{S,0})$ the coordinates of the vortex center. The discrepancy between the fixed and rotating frameworks ranged between 23% at one tip chord aft of the blade and 3.5% at five tip chords in the downstream. As rotational effects are not taken into account in the fixed blade experiment, the relatively good representativity of the fixed blade model seems to indicate that the pressure gradient force provided by the circulation distribution is the main driving phenomena in this case. This will be discussed further in chapter 4, while a description of the fixed blade geometry of [Vion, 2013] is performed in chapter 2.

2

Means and methods

This chapter presents a critical analysis of the experimental and numerical tools which were used to perform the TR-PIV experiment, to launch calculations and to model the LEV.

2.1. Experimental devices

2.1.1. The S2L wind tunnel

The experiments were carried out in the S2L subsonic wind tunnel at ONERA. This wind tunnel has a test section of about 1 meter diameter. It is an Eiffel type open-return wind tunnel, composed of an inlet, a tranquilising chamber with a honeycomb and a turbulence grid to damp the structures of the incoming flow, a contraction chamber, a test section, and a diverging part followed by the fan. Since the experiments of Laurence Vion [Vion, 2013], it had been moved to another building. The inlet, converging part, and motor had been changed. Consequently, a characterisation of the flow in the new configuration was carried out, and the corresponding results are presented in chapter 3. With the new engine, flow velocities varying continuously from 4 m/s up to about 45 m/s could be achieved. Two test sections were used in this work: the wooden test section, which Laurence Vion used for her experiments; and a new optical test section built for this thesis. This optical test section has eight transparent interchangeable windows (some are plexiglass windows and some are glass windows), allowing an easy optical access (see figure 2.1).

2.1.2. The "fixed" HTC5 model blade

Rotational speed Ω	106 $rad.s^{-1}$
Blade radius R_{tip}	2.134 m
Hub tip ratio $\frac{R_{hub}}{R_{tip}}$	0.35
Inflow Mach number at take-off	0.2
Take-off advance ratio J	0.96
Thrust coefficient τ	1.24
Power coefficient χ	1.92
Reynolds number Re_{prop} $(0.75\,R_{tip})$	7.0×10^6

Table 2.1. *Main characteristics of the HTC5 front blade geometry at full scale.*

The leading-edge vortex flow was investigated on a front rotor blade of the open rotor geometry HTC5 designed at ONERA. The main characteristics of the blade can be found in Table 2.1, and its form laws are plotted in figure A.1 in appendix A. More details on this geometry and the related operating parameters can be found at full scale in [Gardarein, 1991] and at scale 2/5 in [Delattre and Falissard, 2015, Vion et al., 2011]. In the following, both the blades at scale 2/5 and full scale will be considered, in order to take advantage of previous work. When the scale is changed, the rotational velocity is adapted so that the advance ratio, power coefficient and thrust coefficient remain independent of the scale. Thus, with a change of scale, the only varying dimensionless parameter is the Reynolds number Re_{prop}, which anyways remains of the same order of magnitude.

The experiments were carried out on a model blade, derived from the HTC5 geometry at a scale of 2/5. For practical reasons, the model blade did not rotate but was fixed on the side of the wind tunnel. Therefore, in the manuscript, this model blade will also be referred to as "fixed blade". In order to be representative of the behaviour of a rotating blade, the model blade was twisted with respect to the HTC5 geometry. The form laws of the model blade can be found in figure A.2 in appendix A.

Figure 2.1. *Wall-mounted blade in the S2L optical test section.*

A similitude preserving the dimensionless circulation distribution. The twist law of the model blade was chosen in order to keep the dimensionless circulation distribution of the rotating blade at take-off $\frac{\Gamma(z)}{\Gamma_{tip}}$ (where $\Gamma_{tip} = W_{tip}\, c_{tip}$) in spite of a uniform inflow. The circulation distribution $\Gamma(z)$ was extracted from elsA chorochronic simulations in an Open Rotor configuration. Thus this circulation distribution takes into account the induced effects from the neighbouring blades and from the downstream propeller.

The twist law of the fixed blade was determined in [Vion, 2013, Vion et al., 2011], using a trial and error method based on numerical simulations. Two methods were used to extract the circulation distribution from the resulting flow fields. The first consisted in integrating the velocity on closed contours based on the streamlines. In the second method, the circulation distribution was derived from the lift distribution using the Kutta-Joukowski theorem.

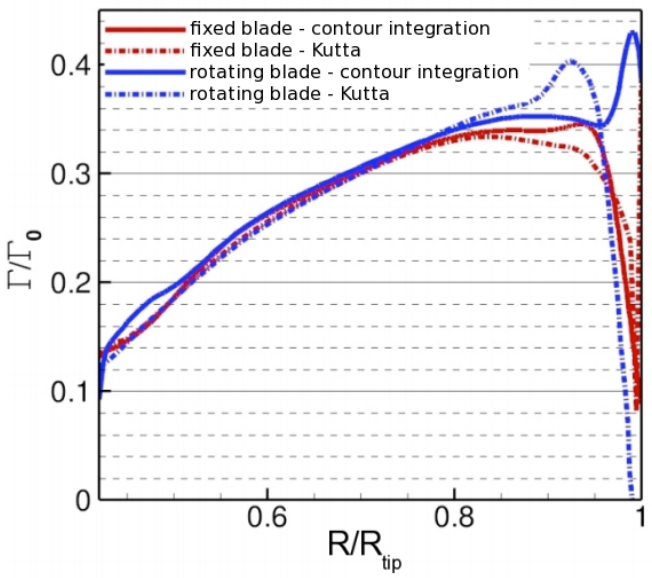

Figure 2.2. *Comparison between the dimensionless circulation distributions of the fixed and the rotating blade, from L.Vion [Vion, 2013]*

Figure 2.2 compares the dimensionless circulation distributions of the rotating and fixed blade, using the two extraction methods. The spanwise evolution of the circulation is typical of a propeller blade : due to the presence of the hub, the root circulation has a positive value, and the maximal circulation is reached close to the tip. The slope of the circulation distribution is well reproduced by the fixed blade up to $0.8R_{tip}$. Close to the tip, the differences can be explained by the fact that flow contraction is not accounted for in the fixed blade case. This will influence the topology of the tip vortex, and thus the circulation distribution. This effect becomes visible over $0.8R_{tip}$, as the leading-edge vortex starts to mix with the tip vortex. The profiles, chord distribution and sweep distribution of the model blade are unchanged with respect to those of the rotating HTC5 blade.

2.1.3. Pressure probes

Pressure sensors are classically used to measure average velocities at a given point in the flow. They can be associated to several types of probes, such as the Pitot tube, static pressure probe, or boundary layer probes. Rotating devices known as PSI, which cyclically survey several probes, were also used in this study. The probes can be placed on travel systems linked to MM4006 motors to scan the flow field.

In order to calculate the velocity, a static pressure p and a total pressure measurement p_0 are needed. For a better accuracy, a static temperature measurement probe T_0 can be added (compulsory in the case of a compressible flow). The velocity U_x (where x is the wind tunnel axis) can be expressed as : $U_x = f(p_0, T_0, p)$. Those quantities are measured using differential pressure sensors Druck UNIK 5000 1PSI D with given uncertainties yielding $\Delta p_0 = \pm 7.5$Pa, $\Delta p = \pm 8.5$Pa. In addition, $\Delta T_0 = \pm 0.5$K.

Using uncertainty propagation properties, and assuming that the measurement bias are inde-

pendent, the uncertainty associated to the axial velocity ΔU_x reads :

$$\Delta U_x = \sqrt{(\frac{\partial f}{\partial p_0})^2 \Delta p_0^2 + (\frac{\partial f}{\partial T_0})^2 \Delta T_0^2 + (\frac{\partial f}{\partial p})^2 \Delta p^2}$$

To comply with the conventions[1], the expanded uncertainties (i.e. $2\,\Delta U_x$) are displayed in Table 2.2, for several velocity regimes. For U_x in the order of 40 m/s, the expanded uncertainty with the chosen set of pressure sensors amounts to 1.5% of U_x.

Fan rotation velocity (rpm)	Axial velocity at test section inlet U_x (m/s)	Expanded uncertainty on U_x (m/s)	Expanded uncertainty on U_x (%)
200	8.3	2.3	27.9
400	17.4	1.1	6.45
600	26.4	0.76	2.89
800	35.5	0.60	1.68
1000	44.4	0.51	1.14

Table 2.2. *Expanded uncertainties on the axial velocity U_x measured by pressure sensors*

2.1.4. Hot wire anemometry

Just like pressure probes, hot wire anemometry consists in pointwise measurements. But, whereas pressure probes are mostly used for average measurements (as pressure fluctuations are damped in the vinyl cable connecting the probe to the sensor), hot wire anemometry is very sensitive to velocity fluctuations, and enables to draw spectra of the various scales existing in the flow.

A hot wire of type 55P11 is used in this study. It consists in a tungsten wire, with a diameter of 5 μm, welded between 2 electrodes spaced of 1 mm. The setup is linked to an electronic circuit comprising a Wheatstone bridge. The role of this bridge is to keep the wire at a constant temperature. When the flow velocity increases, heat losses through convection (and some conduction) are amplified around the wire. The voltage at the Wheatstone bridge, which will adapt to keep the temperature constant, is acquired over time.

Depending on the measurements, either a Dantec Streamline anemometer or a 55M anemometer is used. In order to measure a turbulence intensity, the hot wire is calibrated with respect to velocity measurements using pressure sensors. The velocity is measured using a pitot tube in the upstream and four static pressure probes scattered around the inlet plane of the test section. The velocities at the four points are averaged to give the reference velocity. A calibration law is prescribed: $U = (k\,(V^2 - V_0^2))^m$, where V is the voltage at the hot wire, U is the flow velocity, and V_0 the hot wire voltage obtained with still flow. The coefficients k and m are found optimising the least squares differences between the measurement points and the fitting law. The response time of the hot wire is checked and adjusted depending on the frequency of the phenomenon of interest, using a crenel signal generator.

[1] NF ENV 13005 norm, August 1999

2.1.5. Force balance measurements

Instead of pointwise measurements, a force balance provides integrated lift measurements on a given weighted surface. In the present thesis, a Kistler force balance of type 9254 was used. Put simply, a force balance is composed of a capacitive sensor associated to a signal conditioner. This sensor has a sensitivity expressed in pC/N, which must be prescribed depending on the range of the efforts to measure.

A typical measurement run is shown on figure 2.3. The force balance is set on before the wind tunnel. An offset is added on the signal in order to tune the zero. Then, the acquisition starts. After a few seconds, the wind tunnel is set on (1). When the desired velocity is reached and stable, a weight of 200 grams is applied on the lift component of the balance for a few seconds (2). After a short plateau, the wind tunnel is set off (3) and the velocity decreases gradually. When the initial state is reached again (4), and the constraints have relaxed, the measured lift force is not equal to zero. Indeed, the signal experiences a drift caused by the discharge of the capacitive sensor (due to earth-leakage currents). The drift is assumed to be linear with respect to time. In order to evaluate its slope in V/s, a 200 grams weight is placed again on the lift component (5).

The value of the lift is derived from this measurement run, taking drift correction into account.

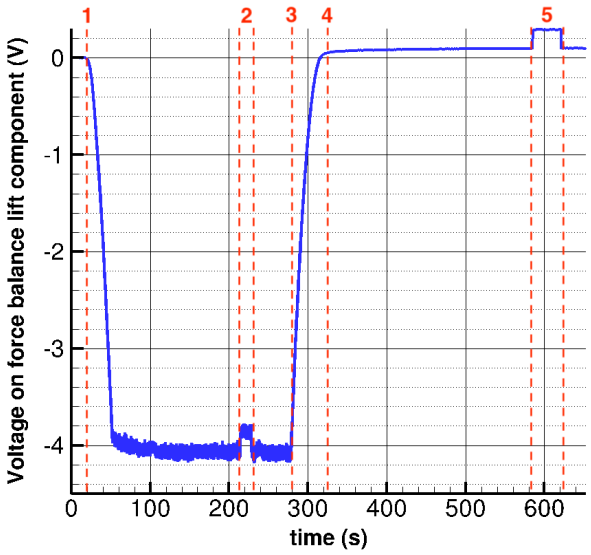

Figure 2.3. *Typical force balance measurement run*

2.1.5.1. Uncertainties and error sources

The main sources leading to uncertainties on force balance measurements are :

force balance misalignment Special care was dedicated to the placement of the force balance. Indeed, it must be perfectly vertical in order to avoid coupling between the three components of the force exerted on the blade. In this study, the angles of the balance with respect to the x and z axis were equal to zero, and the angle with respect to the y axis

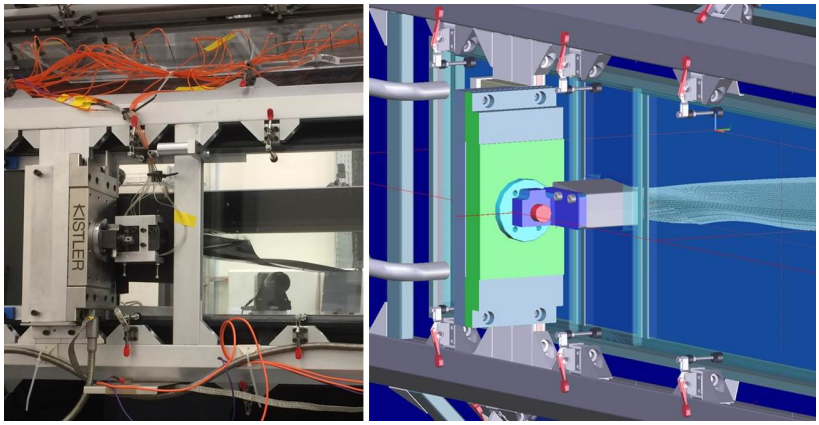

Figure 2.4. *Fixation of the blade on the force balance through the window of the test section*

was 0.1 degrees. Those values were measured using a clinometer with an uncertainty of 0.03 degrees.

signal quantification The signal coming from the sensor first goes to an amplifier, then the resulting signal in V/N is sent to a digital converter that will sample it in the range +/- 10 V. The uncertainty associated to the digital converter is due to the quantification of the signal and amounts to 2 mV.

sensitivity evaluation The lift component was calibrated on site using weighs up to 400 grams, carefully applying and removing them while acquiring the signal. Several runs of calibration were performed, leading to sensitivity values with a dispersion reaching 1.5% of the sensitivity.

setup relaxation Friction and relaxation phenomena in the weighing setup may also lead to measurement errors. Although the weighed part needs to be free from mechanical constraints, contacts between the weighed parts and the rest of the wind tunnel are nearly unavoidable. In order to attach the weighed element (inside the wind tunnel) to the force balance, there must be a hole in the test section (see figure 2.4). In order to prevent air leakage, this hole needs to be blocked - thick tape was used for this purpose, and placed carefully in order to avoid touching the blade. On the other hand, relaxation phenomena occur because a window of the test section needs to be taken out and replaced every time the blade position (or incidence) is changed. This causes residual constraints in the structure of the test section, that systematically affect the first measurement run of each sequence. Consequently, the first runs of each sequence were not taken into account.

Table 2.3 provides a summary of the sources of uncertainty and their magnitude.

2.1.6. Viscous oil visualisation

This technique is a visualisation technique highlighting wall friction lines. First, viscous oil is deposited on the surface of the model (in small drops or with a brush). When the wind tunnel is on, the oil will be rubbed by the flow, enabling to visualise wall friction lines (see for instance figure 4.1). The viscous oil classically consists in a mixture of pigments with two types of oil (oleic acid and gas oil were used in the present case). The viscosity of the mixture needs to be adapted depending on the Reynolds number of the flow.

cause	value	uncertainty on lift (N)
force balance misalignment	0.1 degrees (around y)	0.2% of lift ≈ 0.05 N
signal quantification	0.1% of measurement range (2 mV out of +/- 10V)	0.05 N
sensitivity uncertainty	1.5% of the sensitivity	up to 0.7 N
coupling		up to 0.2 N (according to the manufacturer)
repeatability		value dispersion ≈ 0.1 N

Table 2.3. *Uncertainties on force balance measurements*

2.1.7. Laser tomoscopy

Laser tomoscopy is also a visualisation technique. The flow is seeded with smoke particles, which are illuminated by a laser sheet in the region of interest. The movement of the illuminated particles is visualised using a high-speed camera. The acquired images can reveal flow structures such as turbulence, separations or vortices. This method is useful to understand the structure of the flow, especially to prepare further measurements.

In this work, the flow is seeded with white smoke created with a mixture of glycols and demineralised water (Martin Professional's Pro Smoke High Density) in a generator (Magnum-1800 fogger). In order to best visualise the structures, the seeding must be quite thick and inhomogeneous, which is why the smoke generator is generally placed just upstream of the plane of interest, in front of the wind tunnel inlet.

A picture of the setup is presented in figure 2.5, and its detailed description in Table 2.4.

Figure 2.5. *Setup used for laser tomoscopy*

2.1.8. Particle Image Velocimetry (PIV)

Like laser tomoscopy, Particle Image Velocimetry is a non-intrusive technique relying on the observation of seeded particles illuminated by a laser sheet. However, contrary to laser tomoscopy, it is a quantitative measurement tool that enables to recover the velocity field in a

plane (or volume in the case of three-dimensional or tomo PIV). The seeding must be as homogeneous as possible. Therefore, in this case the foggers are placed downstream of the wind tunnel, and the PIV is started once the hall is entirely filled with smoke to ensure homogeneity.

2.1.8.1. Principle of PIV

The laser sheet is positioned on the plane of interest. The laser is synchronised with the camera(s) in order to illuminate the seeded particles when an image is taken.

Each camera acquires two images closely spaced in time. These two images are classically called frame 1 and frame 2. The time is chosen such that particle displacement between the two frames is in the order of 5 to 15 pixels. Reconstruction algorithms look for the displacement field that maximises correlation between the positions of the particles on the two frames. Thus, the velocity field is recovered from a couple of images.

Two-components PIV (or 2C PIV) relies on one camera to acquire the two velocity components in the plane of interest. In order to get the velocity component normal to the plane of interest, two cameras are needed. This setup is called three-components stereoscopic PIV (3C stereo PIV). Both cameras are synchronised with the laser and acquire simultaneously the pair of images (thus four images are acquired in total). Typically in 3C stereo PIV, a 2-3 mm thick laser sheet is created. Indeed, the laser sheet has to be thin enough so that data acquisition is limited to the plane of interest, but thick enough in order to capture the velocity component normal to the plane.

If the time lag between the pair of images is reduced sufficiently, it is possible to perform Time-Resolved PIV (TR-PIV). Obviously, the choice of the PIV acquisition frequency f_{PIV} (corresponding to the frequency at which image pairs are acquired) must depend on the dynamics of the flow. The typical order of magnitude of f_{PIV} is the kHz. Specific high-speed lasers are used for this purpose.

The characteristics of the standard and TR-PIV setup used in this work are displayed in Table 2.4.

2.1.8.2. Calibration

As PIV is a quantitative measurement tool, calibration is necessary as soon as one camera is not placed perpendicularly to the imaged plane. Thus it is automatically the case if more than one camera is used. In such cases, the value of the magnification will vary over the images, and will be different from one camera to the other. Calibration consists in finding the "magnification fields" corresponding to a given setup. In other words, the aim is to find the transformation that links the coordinates on the camera CCD to those on the plane of interest. In order to do so, a sight with a calibrated pattern is placed at the plane of interest. It contains several points with known positions which are placed on two planes or levels (separated by 1 mm in the transverse direction). Images of this object are acquired with the cameras. The magnification fields for each camera are recovered using Afix, a pattern recognition software developed at ONERA.

	Standard PIV	Time-Resolved PIV	Tomoscopy
Laser	Nd:YAG (Dantec) 200 mJ/pulse	Nd:YLF LDY303 He (Litron) 22 mJ/pulse at 1 kHz	Millenia at 1.5 W + monomode fiber
laser sheet flaring angle	40 degrees	40 degrees	40 degrees
Camera(s)	2 HiSense 11M (Dantec) 12 bits with CCD matrix 4000 x 2672 pixels	2 Phantom V711 1280 x 800 pixels	1 Phantom V711 1280 x 800 pixels
Camera lenses focal length	60 mm (empty test section) 105 mm (shed vortex)	200 mm	200 mm
Acquisition frequency	2 Hz	0.1 - 10 kHz chosen : 3.725 kHz	continuous
Acquisition software	DynamicStudio Stereo PIV	DaVis 8.2.0	Phantom Camera Control (PCC)
Sight	Dantec 3D	Dantec Typ10	none

Table 2.4. *Description of laser setups*

2.1.8.3. Reconstruction

PIV reconstruction is the process enabling to recover the velocity field from the camera images. It is performed using the Folki-SPIV in-house software [Champagnat et al., 2011]. In order to recover the velocity field, the displacement of flow particles between the two laser pulses is analysed. The Lucas-Kanade algorithm minimises a criterion expressing the superposition of interrogation windows of a few pixels between the two images (frame 1 / frame 2). The minimisation is performed at several levels, the image at level n+1 being obtained replacing a group of 4 pixels in image n by a single pixel with the average gray level. This pyramidal resolution, treating coarser images first, enables the minimisation to converge, even for large displacements. The interrogation window size (in pixels) is an important parameter and its choice will detailed in section 4.2.2. A too large interrogation window, especially in the region of the LEV, would lead to under-estimated velocity gradients. On the other hand, if the interrogation window is too small, there is a greater chance of generating noise on the data. The magnitudes of the correlation peaks for each interrogation window pairs enable to create a correlation coefficient map. This map is used as a way to assess the quality of the correlation (which is influenced by the quality of the measurement and that of the reconstruction). Indeed, Champagnat et al. [Champagnat et al., 2011] shows that in the case of the Folki-SPIV algorithm, the quality criterion traditionally used in PIV (score) is equivalent to a classical correlation coefficient.

Pre-processing steps can be applied in Folki-SPIV in order to improve the quality of the images. Geometric masks enable to leave out some part of the image in order to orientate reconstruction (for instance, there is no point trying to find a displacement in walls). Average subtraction can help recover particles in zones that are excessively brightened by light reflections. Self-calibration enables to correct a potential misalignment between the sight and the laser sheet.

2.1.8.4. Uncertainty and error sources

Some of the main uncertainty and error sources include sight and laser misalignment, excessively low (or high) light intensity, peak locking, inaccurate calibration, optical defaults (diffraction through test section window) or bad choice of post-processing parameters.

Threfore an accurate PIV measurement is a matter of compromising.

2.2. Numerical methods

In order to allow comparisons with experimental data, and attempt at modelling vortex lift, various numerical methods were used in this work. In the following, those methods will be presented by increasing complexity.

2.2.1. The Polhamus method

This method was introduced in section 1.1.2, however, further details are given in this part, as this method will be referred to several times in the manuscript. As mentioned earlier, the Polhamus method provides an evaluation of integrated aerodynamic efforts due to the presence of LEVs, and is applicable to slender, thin, sharp-edged Delta wings. The results are very reliable for sweeps $\phi \geq 65$ degrees, and Polhamus considers an applicability zone for $\phi \geq 45$ degrees. This method is based on an analogy between the leading-edge suction force in a configuration without LEV (which can be easily estimated from potential theory on a flat plate) and vortex lift. Polhamus considers a representative profile on the Delta wing (see figure 2.6). The circulation around the profile, and the leading-edge suction force are calculated based on an analogy with potential flow around a flat plate in incidence, in a configuration without LEV. The only difference with 2D potential theory is that the induced drag D_i is taken into account.

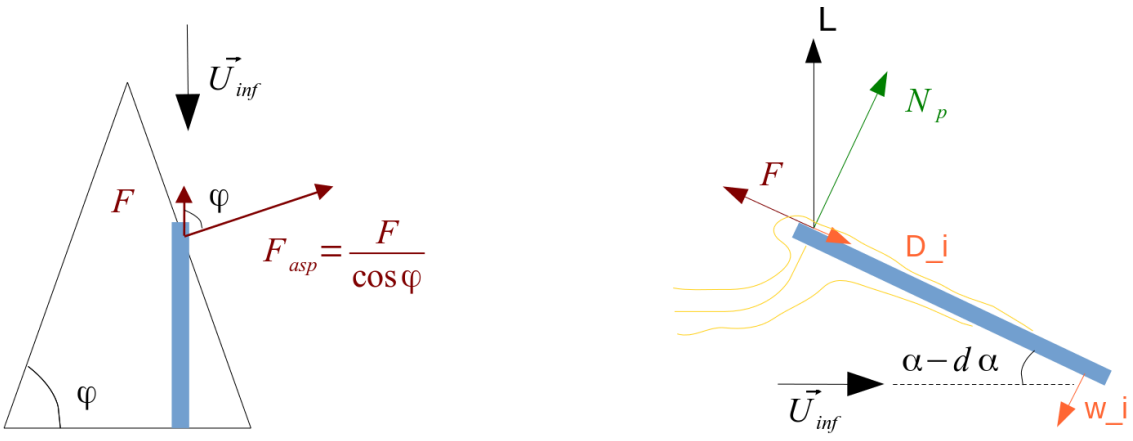

Figure 2.6. *Potential efforts on a Delta wing (at low incidence). Left : top view. Right : equivalent profile.*

The leading-edge suction force on the Delta wing is that on the representative profile F divided by $cos\,\phi$, where ϕ is the Delta wing sweep (see figure 2.6). The leading-edge suction analogy

consists in assuming that the leading-edge suction force will turn 90 degrees and be oriented normal to the wing surface on the suction side (see figure 2.7).

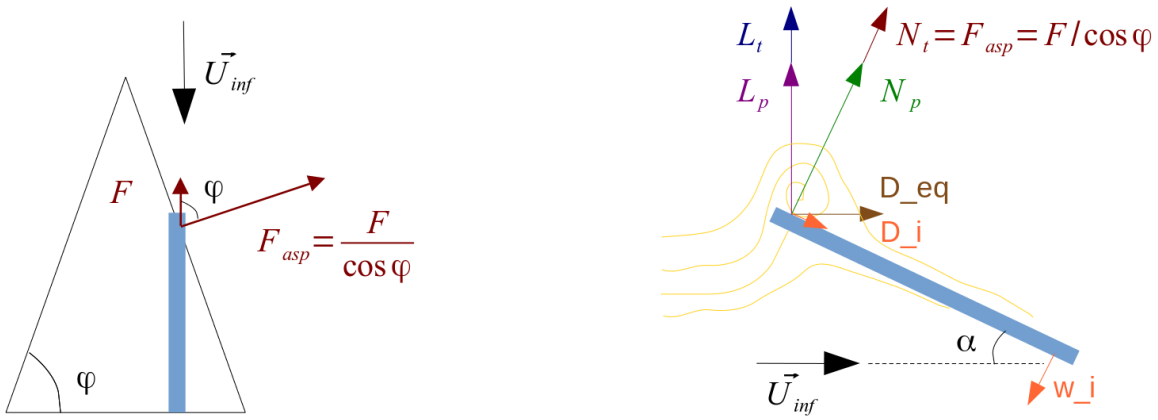

Figure 2.7. *Aerodynamic loads on the representative profile with attached flow (left) and in presence of the LEV (right) according to the leading-edge suction analogy*

The lift coefficient can be expressed as :

$$CL = CL_p + CL_v = Kp\,cos^2\alpha\,sin\alpha + Kv\,sin^2\alpha\,cos\,\alpha$$

where Kp and Kv can be evaluated from whole wing polars around zero lift incidence α_0 (where potential calculations are applicable) :

$$Kp = \frac{\partial CL}{\partial \alpha}\Big)_{\alpha_0}$$

$$Kv = \frac{Kp - Kp^2 Ki}{cos\phi}, \text{ where } Ki = \frac{\partial^2 CD_i}{\partial CL^2}\Big)_{\alpha_0}$$

The strength of Polhamus theory lies in the parallel between aerodynamic forces with and without LEV which allows to deduce efforts in a detached configuration from potential calculations in the corresponding attached configuration.

The following paragraphs will deal with classical 1D load calculation methods which enable to model spanwise variations. However, those methods do not account for vortex lift. In chapter 6, a 1D version of the leading-edge suction analogy will be developed, and coupled with a 1D load calculation method.

2.2.2. The Blade Element Momentum Theory (BEMT)

This section describes a 1D load calculation method, classically developed in the wind turbine and propeller literature. The Blade Element Momentum Theory (BEMT) stems from the 0D Rankine Froude theory. This theory models the propeller (or turbine) as an infinitely thin disk causing a pressure and velocity discontinuity. The axial and tangential velocity jumps at the propeller location are estimated using momentum and angular momentum conservation equations, before and after the propeller. Those velocity jumps will be referred to in the following as axial and tangential induced velocities, or in dimensionless form (non-dimensionalised by U_{inf}), as axial and tangential induction factors (a and a' on figure 2.8).

Therefore, the Rankine Froude theory expresses the thrust and torque on the propeller (or turbine) depending on the induced velocities. Glauert extended this theory to a 1D model, taking into account spanwise geometry variations. For this purpose, the disk modelling the propeller (or turbine) is decomposed into independent rings corresponding to various spanwise positions, and the Rankine Froude theory is applied to each of those rings (see figure 2.8). The corresponding thrust and torque, depending on induced velocities at spanwise position r are equated to formulas based on the local angle of attack, chord, lift and drag coefficients of the airfoil at position r. Thus, a fixed-point problem for the axial and tangential induction factors with a set on non linear equations is obtained. The equations are detailed in [Hansen, 2000] for the wind turbine case and [Rwigema, 2010] for the propeller case.

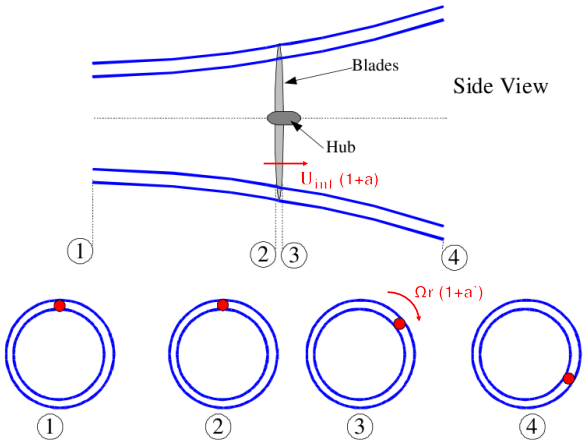

Figure 2.8. *Rotating annular streamtube used in the BEMT, for a wind turbine configuration. Source: [Ingram, 2005]*

One of the main hypotheses of this method lies in the assumption of independent spanwise sections. Therefore tip-loss corrections are used to account for some part of the 3D effects. The loads are multiplied by a tip loss factor, which is maximal at the foot and goes to zero at the tip. Reciprocally, for cases without hub it is possible to define a hub loss factor. [Branlard, 2011] interprets the tip loss factor as a ratio between the induced velocity with an infinite numbers of blades to that with a finite number of blades. Indeed, with a finite number of blades, a tip vortex will be formed and roll up in the wake, which will influence the induced velocities on the blade.

Prandtl was one of the first to investigate the impact of tip vortices on losses, both for a fixed wing and a propeller. He derived a formulation of the tip loss factor using a simplified representation of the wake. Indeed, he assumed that the wake consisted of a system of straight vortex sheets spaced according to the advance ratio in the axial direction (see figure 2.9), and determined the complex velocity in the wake using conformal mapping. Glauert integrated the induced velocity between two vortex sheets, which led to the expression of the tip loss factor widely used in BEMT codes, and usually called Prandtl tip loss factor.

Goldstein complexified this approach by assuming a screw surface in the wake, however, [Branlard, 2011] showed that the obtained tip loss factor was not far from the Prandtl tip loss factor. Several improvements of the tip loss factor were proposed (De Vries, Branlard 2012). In particular, [Shen et al., 2005a, Shen et al., 2005b] proposed a formulation ensuring non zero velocity at the tip, thus correcting a nonphysical aspect of the Prandtl tip-loss factor.

In order to improve the representativity of the BEMT, lit and drag coefficient corrections for

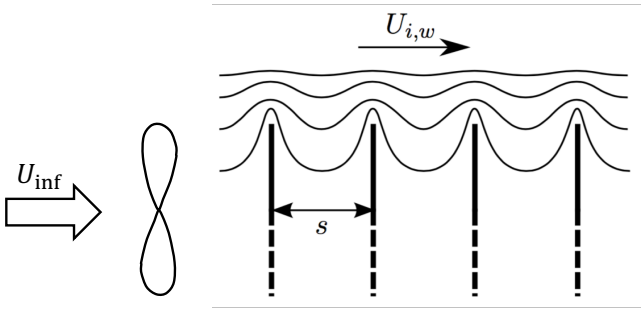

Figure 2.9. *Wake model with spaced vortex sheets. Source: [Branlard, 2011]*

rotational effects were proposed in the literature [Snel et al., 1994, Lindenburg, 2004]. Indeed, [Lindenburg, 2004] argues that rotational effects influence the lift coefficient on an airfoil. The article considers a wind turbine blade profile at high incidence, with detached flow at the trailing edge, and argues that the Coriolis force density is oriented chordwise towards the trailing-edge, with a tendency to delay flow separation. This reduces the effective angle of attack compared to a non-rotating case. Hence the idea to propose a polar correction taking into account the rotation velocity.

One of the difficulties of the BEMT lies in the convergence of the fixed point problem. Indeed, depending on the sign and values of the induced velocities, the behaviour of the propeller corresponds to different regimes : propeller, turbine, empirical, or propeller brake. Therefore the formulas to be used in the fixed point problem will change (see figure 2.10).

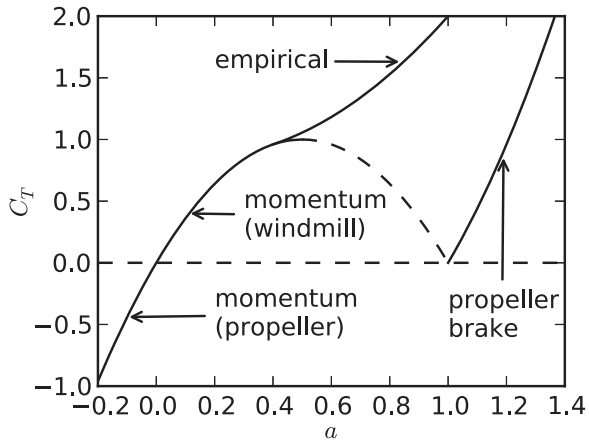

Figure 2.10. *Variation of thrust coefficient with axial induction factor and associated regimes. Source: [Ning, 2014]*

For instance, if the induced velocities are too high ([Hansen, 2000] mentions a threshold for axial induction factors above 0.4), the BEMT set of equations does not converge, and empirical laws are used. [Ning, 2014] proposes an algorithm for guaranteed convergence. First, the BEMT equations (as described in [Hansen, 2000]) are transformed into a system with only one unknown, and criteria are proposed to find the right solution range. Then, a fast root finding algorithm for non linear functions is applied.

To summarize, the BEMT is a very fast method enabling to calculate steady spanwise loading and efficiency for propeller blades, depending on advance velocity, rotation velocity, pitch angle and blade geometrical parameters. This method is still used for conceptual design phases,

especially for wind turbines. The main assumption is that of independent profiles. Various additions have been proposed to augment the BEMT and account for neglected physics. For instance, 3D effects can be accounted for using various types of tip loss and polar corrections, some of which are based on simplified wake models, and some are empirical. Another challenge lies in the existence of several solution ranges which can lead to convergence problems. The momentum propeller range, corresponding to the equations used classically, holds for a lightly loaded propeller assumption (which implies a rather low thrust coefficient, low wake contraction and distortion).

2.2.3. The lifting line theory

The other main 1D loading calculation method is the lifting-line theory. Its main asset compared to the BEMT is to take into account induced velocities from one profile to the other, which are calculated using the Biot-Savart law. This method applies to wings of high aspect ratio, or assimilated to high aspect ratio (meaning that the working part of the blade can be considered of high aspect ratio). Several lifting line theories exist, which will be presented in order of complexity.

Historically, the lifting line concept originated in the work of Prandtl, for a straight, thin wing and with high aspect ratio, which could be replaced by a lifting line with a circulation distribution corresponding to superposed horseshoe vortices (see figure 2.11). Using the Biot and

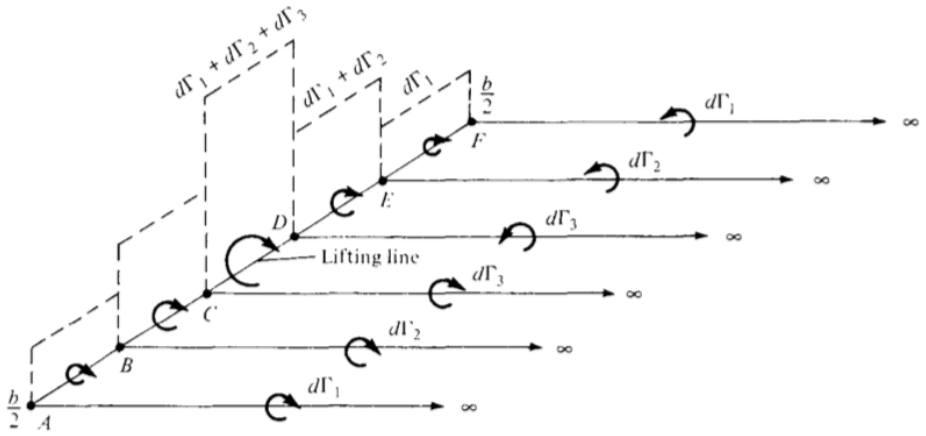

Figure 2.11. *Superposition of horseshoe vortices along the Prandtl lifting line. Source: [Anderson, 2007]*

Savart law, the velocity induced by each vortex and by the wake on the lifting line enables to estimate the downwash, thus the effective angle of attack at each spanwise position. Using thin airfoil theory (low thickness and low angle of attack), the lift coefficient is assumed to be linear with the angle of attack, with a factor of 2π. Finally, the lift is linked back to circulation using the Kutta Joukowsky formula. The Prandtl lifting line translates in a differential equation (presented in [Anderson, 2007]) where the unknown is the circulation distribution. This approach can be easily extended to higher angles of attack where the lift coefficient polar is non linear, by means of a numerical iterative procedure (also described in [Anderson, 2007]). The lifting line theory can also be complexified considering a free propagating wake (and the associated induced velocities), such as it is done in the PUMA ONERA code. Also, [Devinant and Gallois, 2002] states that this theory can be extended to curved wings by adding a sweep

correction to the inflow velocity at a given spanwise position. However the article shows that this does not consider all effects linked to sweep and curved lines. The lifting line theory based on Prandtl's approach reaches its limitations.

The other approach for the lifting line theory was pioneered by Van Dyke. The wing is viewed as a small perturbation in a perfect, incompressible and irrotational flow. The governing equation is thus the Laplace equation of the perturbation velocity potential, under the constraints of tangency at the wing, Kutta condition at the trailing edge, and zero pressure jump accross the wake. Under the same assumption of high aspect ratio, the various quantities are developed asymptotically, the small parameter being $\frac{1}{AR}$. The problem is solved in two "limit cases" : a lifting line of infinite span, and finite chord; and a line with infinitesimal chord and finite span. The resulting expressions for the velocity potential are matched using the Matched Asymptotic Expansions. Through this reasoning, Van Dyke recovered the Prandtl lifting line (at order 0).

The success of Van Dyke's approach based on matched asymptotic expansions boosted other researchers into finding extensions of the initial lifting line theory (which was only applicable to un-swept wings and steady flows). The most generalised expression of the lifting line theory is that of Guermond [Guermond, 1990], (extended to unsteady cases in [Guermond and Sellier, 1991]). This article proposed an asymptotic expansion for the circulation depending on the sweep, the lifting line curvature, and the spanwise variation of zero order circulation. [Devinant and Gallois, 2002] derives a numerical procedure where the asymptotic expansions of Guermond are included in an algorithm based on the Prandtl lifting line.

Although making less assumptions in the modelling of the induced velocities compared to the BEMT, the lifting line relies heavily on the assumption of high aspect ratio. In addition, the cases of swept and curved wings require more complex forms of the lifting line theory.

2.2.4. Lifting surface methods

As a consequence, lifting surface methods are recommended for application to low aspect ratio wings [Anderson, 2007]. Those are 2D methods, which provide access to the loading distribution on the wing surface.

Similarly to the lifting line case, the wing is viewed as a small perturbation in a potential flow. This small perturbation assumption enables to neglect thickness effects: the skeleton and the spanwise incidence variation are thus used to represent the wing.

The wing surface is decomposed into a vortex lattice. In figure 2.12, each square corresponds to a horseshoe vortex. The circulation of those horseshoe vortices must be determined such that the constraints of tangency to the wing surface (on prescribed control points) are verified. The wake is in the continuity of the lifting surface. The intensity is constant along a vortex filament at a given spanwise position in the wake. Several wake models (planar or free) can be considered. This potential flow calculation method is used in the TAGAZOU code developed at ONERA.

2.2.5. RANS simulations

Steady computations are carried out using ONERA's finite-volume elsA solver [Cambier et al., 2013]. The steady Reynolds-averaged Navier-Stokes (RANS) equations are solved in the com-

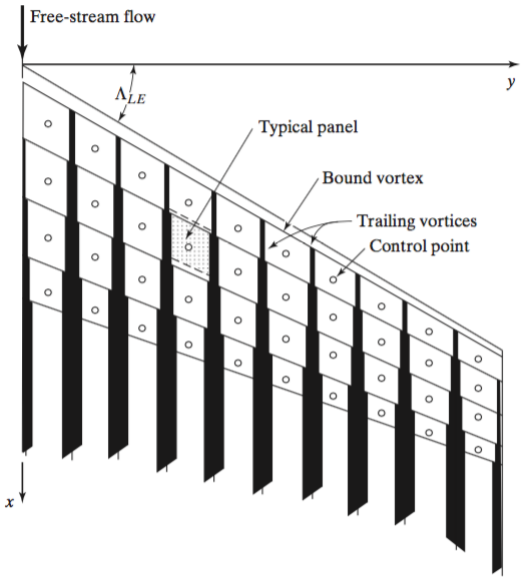

Figure 2.12. *Coordinate system, elemental panels, and horseshoe vortices for a typical wing planform in the vortex lattice method. Source: [Bertin and Cummings, 2014]*

pressible regime. The modelling of turbulence was accounted for using the Kok $k-\omega$ turbulence model [Wilcox, 1988, Kok, 2000]. [Wilcox, 1988] showed that $k-\omega$ models provide a better modelling of close-wall phenomena compared to $k-\epsilon$ models. However, a sensitivity to the boundary conditions was observed, which Kok [Kok, 2000] managed to limit thanks to a new set of diffusion coefficients. The Zheng limiter [Zheng and Liu, 1995] was also used to reduce the sensitivity of the model to the boundary conditions. In addition, the Menter Shear Stress Transport (SST) correction [Menter, 1994] was activated because it improves boundary layer modelling in the presence of an adverse pressure gradient by changing turbulent viscosity modelling close to the walls. It is thus particularly suited for the simulation of detached boundary layers. The same model was used in previous studies of transonic propellers [Vion, 2013, Delattre and Falissard, 2014, Delattre and Falissard, 2015, Delattre. et al., 2016].

The convective and diffusive fluxes were discretized using a second-order centered scheme with scalar artificial viscosity.

Some of the calculations were performed using a transition model, which will be detailed in chapter 4.

Structured meshes were designed either using the ICEM or the Cassiopée software. A specific Cassiopée code was designed to generate the detailed meshes surrounding the tested wing geometries. This tool first creates the skin mesh, then adds normal layers to it in order to automatically generate a refined mesh surrounding the blade. When several meshes were superimposed, the information transfer in the overlapping regions was accounted for using the Chimera method. The meshes and their characteristics, as well as the convergence characteristics will be detailed for each calculation in the course of the manuscript.

3

Definition of the experimental configuration

The objective of this chapter is to define the experimental configuration used to characterise the LEV on the fixed blade geometry designed by Laurence Vion. The first part deals with the re-qualification of the empty wind tunnel. Indeed, since Laurence Vion's experiments, it was displaced to a different building, its converging part was changed, and the optical test section was designed. The second part deals with the placement of the blade model in the wind tunnel. This step is especially important as Laurence Vion showed that the model blade was representative of the rotating configuration for a given position in the wind tunnel, and that blockage effects due to the test section influenced the generation of the leading-edge vortex.

3.1. Characterisation of the S2L wind tunnel

As the S2L wind tunnel was moved and some components replaced, it needed to be re-qualified before running the experiments. In particular, the wind tunnel was not placed at the centre of the hall, but much closer to the wall on the pilot right hand side. A characterisation of the wind tunnel was carried out in order to verify that its asymmetric position in the hall did not influence the flow in the test section. Also, it was necessary to check that the new contraction cone did not trigger flow separation. Finally, the turbulence intensity in the new configuration was measured. For this purpose, a first qualification campaign took place in the empty wooden test section.

The replacement of the wooden test section by the optical test section required to adapt the junction with the contraction cone. Indeed, the wooden test section had a circular cross section like the contraction cone, while the optical test section was octagonal. Further measurements (pressure distribution, boundary layer thickness, PIV velocity fields) were performed in the new test section to verify that the junction did not trigger flow separation, and that the change of test section did not have any major influence on the flow.

The wind tunnel was equipped with a Pitot tube and a static pressure probe placed at the end of the contraction cone to minimize disturbance to the flow (see figure 3.1), measuring the velocity at the test section entrance. Total temperature was measured by a thermocouple placed at the beginning of the contraction cone. In the following, the x axis is in the streamwise direction, y is the vertical axis, z is the horizontal axis from pilot right hand-side to left hand-side.

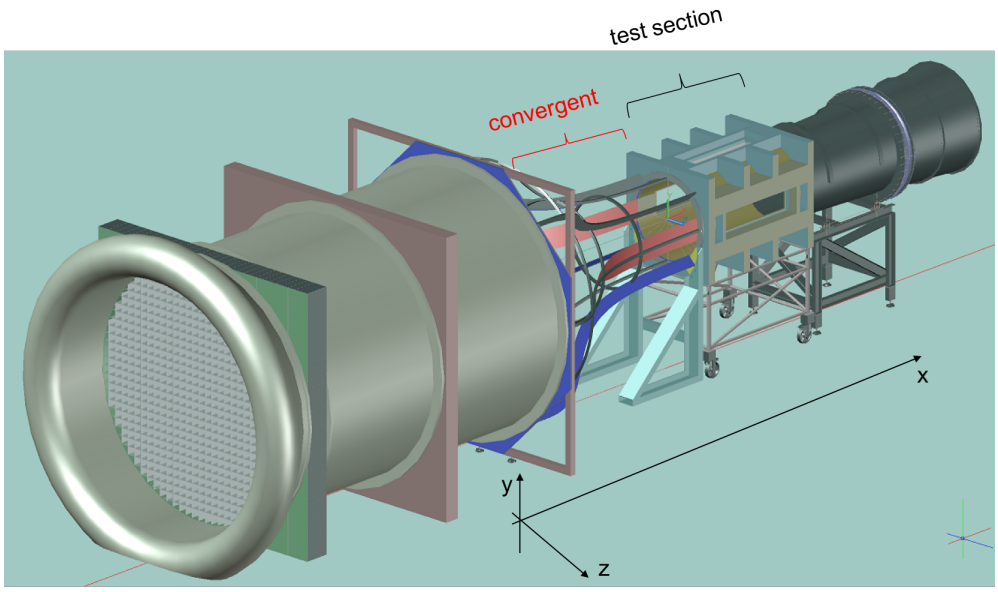

Figure 3.1. *CAO of S2L wind tunnel*

3.1.1. Average velocity field

In order to evaluate the homogeneity of the flow in the empty wooden test section, average velocity profiles were acquired using pressure sensors. A Prandtl antenna, mounted on a travel system in figure 3.2 was used to measure static and total pressure in the test section. The travel system consisted in 3 micro-controlled axes of type MM4006. At each point, the velocity was acquired at a frequency of 1 kHz during 6 seconds. Due to limitations in the range of the travel systems, an offsetting device was added. This increased the lever effect, causing the probe to oscillate. Thus the convergence of the average was verified on those points. The sounding of the flow was performed at the maximal rotating velocity of the fan which corresponds to $43,5m.s^{-1}$ in the test section.

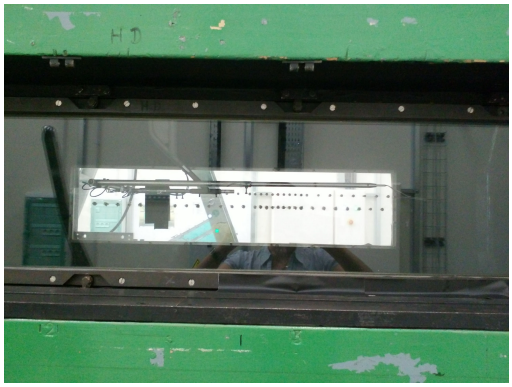

Figure 3.2. *Prandtl antenna mounted on the travel system in the wooden test section.*

Figure 3.3 displays a map of the average streamwise velocity differences in the test section, expressed in percentage of a reference streamwise velocity $\frac{\Delta U_x}{U_x} = \frac{U_x - U_{x,ref}}{U_{x,ref}}$. The streamwise velocity at the bottom of the test section serves as reference $U_{x,ref}$. This analysis shows that the flow accelerates as it progresses downstream. The divergence of the walls does not fully

compensate for the thickening of the boundary layer. The spanwise inhomogeneities are quite small, in the order of 1%. The most important inhomogeneity is caused by a positive vertical velocity gradient $\frac{\partial U_x}{\partial y}$. The maximal discrepancy along y amounts to 3% of the inflow velocity at 43.5 m/s.

A 2C PIV plane was acquired in the central part of the optical test section (see figure 3.4), revealing that the inhomogeneities in the optical test section were of the same nature. The results supported the fact that U_x increased on the centerline as the flow progressed downstream, and that a positive vertical velocity gradient $\frac{\delta U_x}{\delta y}$ existed. A possible explanation may be that the wind tunnel ingests a room floor boundary layer profile. Indeed, the entrance conditions are not axisymmetric because the wind tunnel is laid on the ground (see figure 3.1). However, this assumption could not be verified given the very low velocities involved on the wind tunnel entrance plane. At the maximal rotation velocity of the fan, the axial velocity in the test section was in the order of 44 m/s. The cross-section ratio between the entrance plane and the test section being about 9, the flow velocity in the entrance plane was in the order of 5 m/s. This velocity corresponds to a depression of about 10 Pa with respect to atmospheric pressure, which is the order of magnitude of the uncertainty of the available pressure sensors.

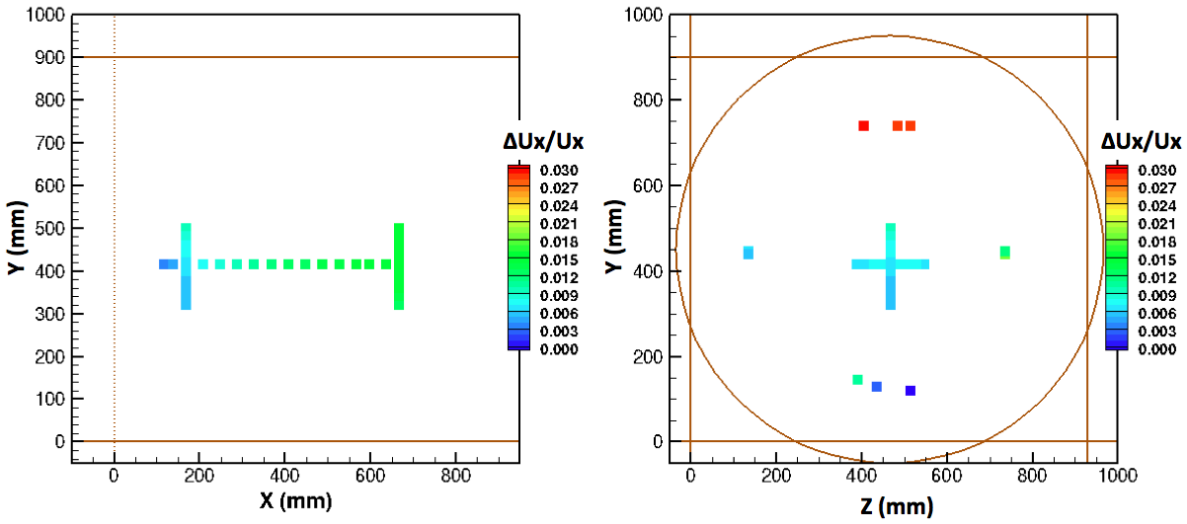

Figure 3.3. *Axial velocity field U_x in the empty wooden test section. Left : cut along the wind tunnel axis on the symmetry plane ($y = 450$ mm). $x = 0$ corresponds to the entrance plane of the test section. Right : transverse plane, at $x = 200$ mm. $z = 0$ corresponds to the right wall (pilot convention). The test section is materialised with brown lines.*

3.1.2. Boundary layer characteristics

In order to measure the boundary layer thickness, a traversing total pressure probe was attached to a micro-controlled axis mounted on the floor, outside of the test section (see figure 3.5). A static pressure probe tap was drilled in the floor. The boundary layer was probed at several points along the centerline of the test section floor. The same setup was used to probe the boundary layer in the wooden and optical test sections. The variations of the boundary layer thickness $\delta_{0.99}$, momentum thickness θ, displacement thickness δ_1 and shape factor h with respect to the distance from the entrance plane of the test section are presented in Table 3.1. The values of the shape factor clearly indicate a turbulent boundary layer.

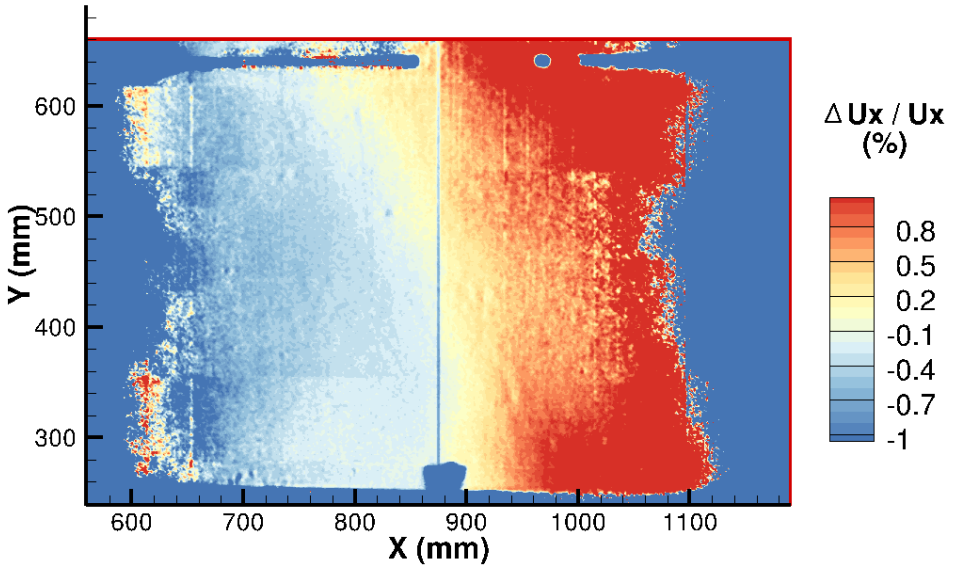

Figure 3.4. *PIV dimensionless streamwise velocity field* $(U_x - U_{x,ref})/U_{x,ref}$ *in the empty optical test section.* $U_{x,ref}$ *is chosen in the center on the bottom line of the image.* $x = 875mm$ *and* $y = 450mm$ *correspond to the center of the test section (in the streamwise and vertical directions respectively).*

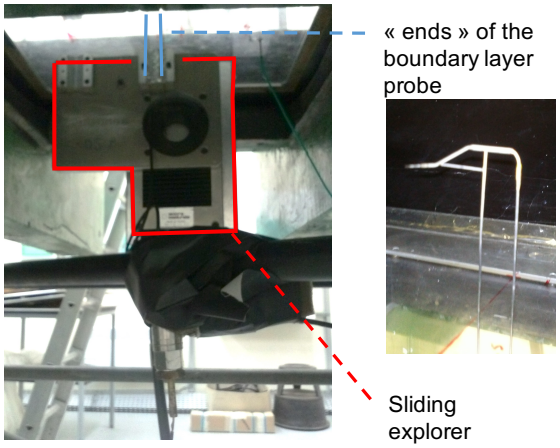

Figure 3.5. *Setup used to fix and move the boundary layer probe. Left : boundary layer probe in the test section. Right : setup with the micro-controlled axis fixed on the plexiglas floor. Holes in the floor enable the probe to slide easily.*

3.1.3. Turbulence level

The turbulence level in the wind tunnel was measured using a hot wire probe positioned at the center of the wind tunnel such as depicted in figure 3.6.

Before reaching the test section, the flow sucked into the wind tunnel passes through the honeycomb and the turbulence grid, then undergoes contraction. Therefore the residual turbulence level is very low in the test section. At the hot wire's terminals, those tiny velocity fluctuations result in voltage fluctuations in the order of the mV. Yet the acquisition system (INF) acquires data by quantifying them into "bites" of 0.6 mV^2. Consequently it was decided to increase the

[2]signals of amplitude comprised between -10V to 10V coded on 15 bites (+ 1 sign bite)

test section	x (cm)	U_{inf} (m/s)	$\delta_{0.99}$ (cm)	θ_1 (mm)	δ_1 (mm)	h
optical	41.5	38.5	1.66	1.8	2.4	1.32
optical	62.0	38.5	1.84	2.3	3.1	1.35
wooden	80.0	38.0	2.02	2.3	3.0	1.31
optical	130.0	38.5	2.42	2.8	3.8	1.34

Table 3.1. *Variation of boundary layer thickness $\delta_{0.99}$, momentum thickness θ_1, displacement thickness δ_1 and shape factor h with respect to the distance from the entrance plane of the empty test section x*

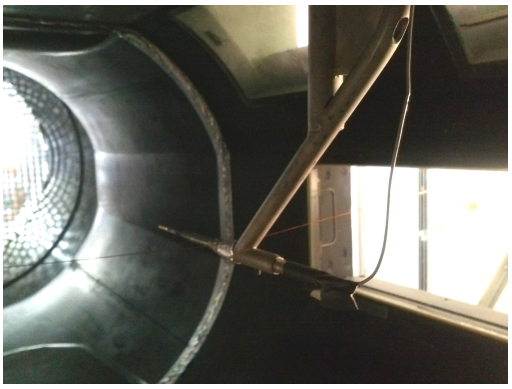

Figure 3.6. *Hot wire mounted on the travel system in the wooden test section. The stand is shrouded with wires in order to prevent vibrations.*

signal to noise ratio of those small velocity fluctuations.

The procedure consisted in amplifying velocity fluctuations. The chosen sampling frequency was 33 kHz. The continuous part of the hot wire signal was cut using a high pass filter at 10 Hz. A Krohn-Nite low pass filter with a cutoff frequency of 4kHz was used to avoid aliasing[3]. Then a gain was applied to this signal using an ANS amplifier. In this study a gain of 50 was chosen. Meanwhile, the average component of the signal was monitored at the same sampling frequency. The hot wire fitting law being non-linear, an asymptotic development at order one around the mean velocity was used to apply the fitting law to the fluctuating signal. The spectra calculating algorithm was the Fast Fourier Transform (FFT). The duration of the acquisition was chosen so that the spectral accuracy $\Delta f = \frac{f_a}{2n}$ (where n is the number of points used to calculate the spectra) was approximately equal to 1 Hz. 100 non-overlapping blocks of n points were considered. The acquisition thus lasted : $\Delta t = \frac{1}{f_a} \times n \times 100 \approx 100$ seconds.

Figure 3.7 features the spectral densities at 4 m/s and 38 m/s. Because of a defect identified later as the coupling of the Krohh-Hite filter and the StreamLine anemometer, the spectra were cut at 1 kHz.

The spectrum at 38 m/s features a peak at 56 Hz, corresponding to the rotor blade passing frequency (840 rpm multiplied by 4 blades), and its harmonics. The spectral densities decrease rapidly after 100 Hz with a slope close to $-\frac{5}{3}$. Another peak is present at 14 Hz, which corresponds to the rotor rotation frequency. This is the trace of the inhomogeneity of the 4 rotor blades. Therfore it is reassuring that this latter peak has a lower amplitude than the one at 56 Hz. Quite surprisingly, this 14 Hz peak was recovered for other inflow velocities (corresponding

[3]the slope of the filter has been characterised in this work to -24 dB per octave

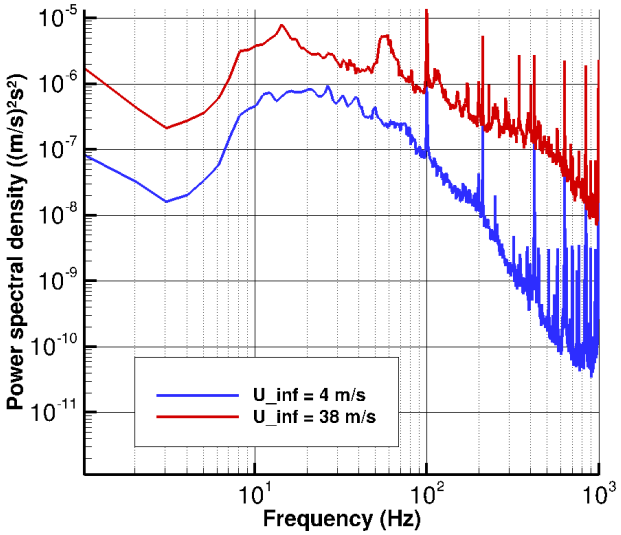

Figure 3.7. *Spectra of velocity fluctuations at the center of the empy test section at 4 and 38 m/s*

to 500 and 115 rpm). Suspecting that this frequency may be a structural vibration mode of the wind tunnel, vibration measurements were performed with an accelerometer at several fan rotation frequencies (115, 500 and 840 rpm). The results confirmed the presence of the 14 Hz vibration mode at all those frequencies. The amplitude of those vibrations was more important at 840 rpm, because the structural mode was excited by the blade rotation frequency. The peak at 100 Hz and its harmonics are caused by noise due to induced currents from the electric network.

Turbulence level measurements The turbulence level τ_u is equal to the standard deviation of the fluctuating signal u' divided by its average value U_{ave}:

$$\tau_u = \frac{\sqrt{\bar{u'^2}}}{U_{ave}}$$

The variance of u' is derived from the power spectral density $E(f)$:

$$\bar{u'^2} = \int_0^{+\infty} fE(f)d(ln(f))$$

Because of the defect on the StreamLine, the spectra exhibited nonphysical power spectral densities at frequencies higher than 1 kHz. Simply calculating the variance of the fluctuating signal would thus lead to an over-estimation of the turbulence level. Rather, frequencies above 1kHz were not taken into account in the evluation of $\bar{u'^2}$, because the energy carried by those high frequencies was quite low in reality (at least 2 orders of magnitude lower than the spectral densities from 10 to 100 Hz. Therefore :

$$\bar{u'^2} \approx \int_0^{10^3} fE(f)d(ln(f))$$

The calculated turbulence level for a fan rotating velocity of 840 rpm corresponding to 38.3 m/s, is $\tau_u = 0.035\%$, and is below 0.1%.

3.2. Blade placement

Given the wind tunnel characterisation presented in part 3.1.1, the axial velocity was more homogeneous along the horizontal direction. Thus, the model blade was placed horizontally, like in [Vion, 2013], its span covering about half of the wind tunnel diameter. Figures 2.1 and 3.8 depict the blade embedded in the optical test section.

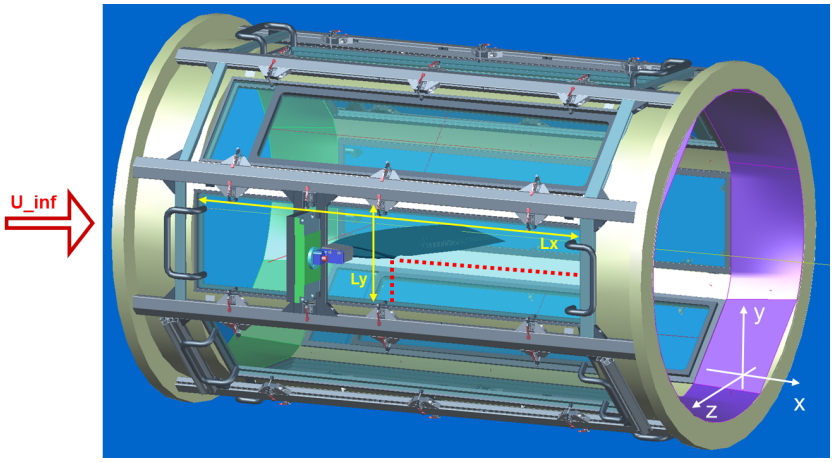

Figure 3.8. *CAO of model blade embedded in optical test section*

Special care was dedicated to the blade placement in the wind tunnel, to ensure compatibility with previous studies of [Vion, 2013] and with numerical simulations. Indeed, Laurence Vion showed that the model blade was representative of the turning case for a given incidence, and that blockage effects induced by the test section had to be taken into account to determine this value.

In [Vion, 2013], the blade was placed just at the entrance of the test section. In the present work however, the blade was placed further in the downstream (trailing edge located at $\frac{x_{blade}}{L_x} = 0.5$, where L_x is the length of the test section) in order to guarantee optical access to the leading-edge (see figure 3.9). The blade trailing edge is also placed at the center of the test section along y : $\frac{y_{blade}}{L_y} = 0.5$.

The displacement of the wind tunnel to a new hall, the change of major components such as the contraction chamber, the new test section of octagonal form and the change of blade position in the test section justify a careful assessment of the setup parameters. In particular, the model blade is now attached to the window of the test section, which is slightly diverging. This was not the case in the setup of Laurence Vion. In order to be representative of the turning case, the blade needs to be orthogonal to the inflow. Thus, the root section is placed at an angle with respect to the test section window (see figure 3.9). The setup parameters considered in the following are the angle of incidence α, and the orientation of the root section with respect to the test section window, noted ϵ in figure 3.9.

In the following the inflow velocity (measured at the entrance plane of the test section) was set to 36,0 m/s. Indeed, in those conditions, the static pressure probe 30 cm upstream of the blade apex (foremost point on the leading-edge) indicated 38,5 m/s, corresponding to the inflow velocity reported in Laurence Vion's experiments. In her experiments, the blade was placed just at the entrance of the test section, therefore much closer to the pressure taps monitoring the inflow velocity, and may have induced a blockage effect on them.

The incidence of the blade was monitored using a clinometer of type Clinotronic PLUS (Wyler) laid on a gauge designed to materialise the position of the blade at an incidence of 0 degrees. The uncertainty of the clinometer amounted to 0.03 degrees. The orientation of the root section with respect to the slightly diverging window of the test section (noted by the angle ϵ in figure 3.9) was also measured precisely using referenced wedges (with an uncertainty of 0.1 mm). In this part, we follow the convention used in [Vion, 2013] that a negative angle of attack corresponds to the leading-edge turned downwards compared to its position at an incidence of 0 degrees.

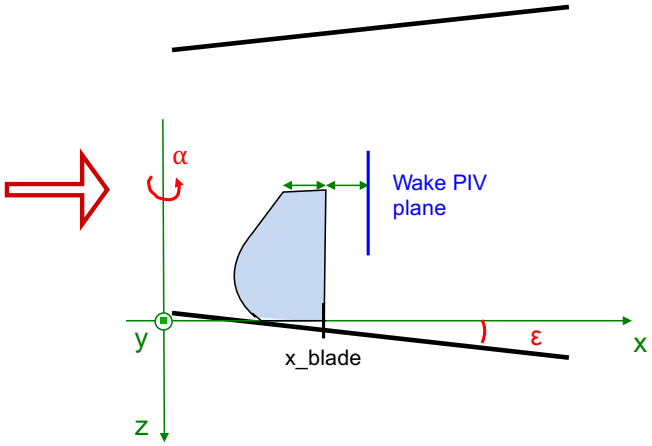

Figure 3.9. *Sketch of the blade positioning with respect to the side window of the test section, with the angles materialising the incidence α and the rotation around y axis ϵ*

3.2.1. Wall pressure distribution

The first idea to determine blade placement was to survey the pressure distribution variation on the blade surface with respect to incidence and compare the values to those measured by Laurence Vion. The model blade was embedded with 10 pressure taps [Vion, 2013], distributed along two lines on the suction side, at 50% and 80% of span, and one on the pressure side (see figure 3.10). The variation of the pressure coefficients Cp with respect to the incidence is compared with the measurements of Laurence Vion in Figure 3.11.

However, this figure demonstrates that most of the pressure taps were not sensitive to changes in incidence in the order of +/- 2 degrees. Only the one at 50% of span, closest to the leading edge, was found to be very sensitive. Therefore the initial idea was to place the model blade such that the Cp value on this probe would be the same as that measured by Laurence Vion for her reference position at an incidence $\alpha = -2.2$ degrees. However the experimental pressure coefficient value measured by Laurence Vion on this pressure probe was not reached in the tested incidence range.

This raised questions about the influence of the gap between the foot of the model blade and the window on flow topology over the blade. Indeed, this gap will trigger the shedding of circulation as a foot vortex. Therefore, the gap was filled, various types of scotch were tested to cover it, and the influence on the wall pressure coefficient was monitored, at $\alpha = -2.2$ degrees. This only affected the probe closest to the leading-edge at 80% of span, and the corresponding pressure coefficient varied in the order of 10%. Thus this did not help coming closer to the values of Laurence Vion.

In any case, because only one pressure tap was very sensitive to variations in angle of attack, those measurements were not conclusive regarding the position of the blade.

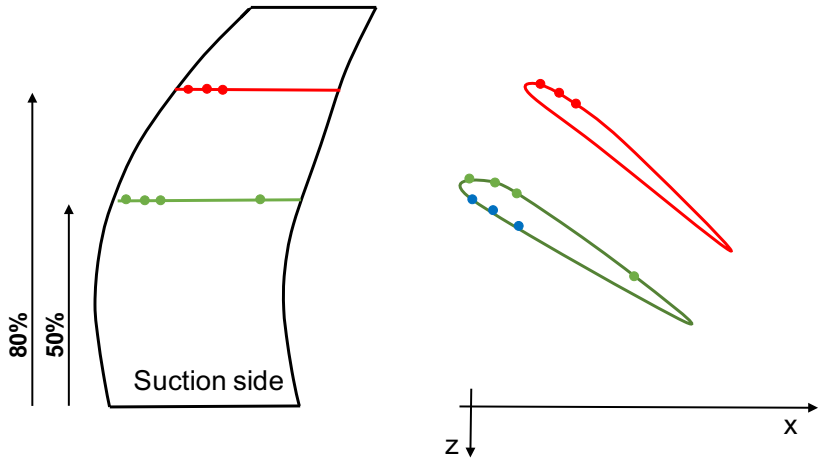

Figure 3.10. *Position of the static pressure probes on the model blade surface.*

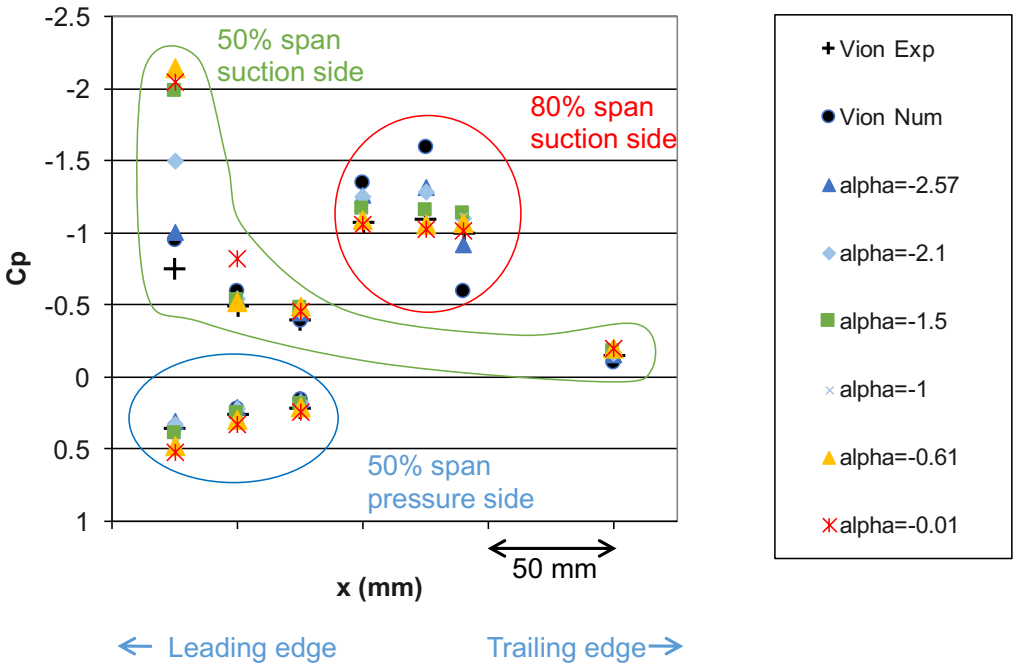

Figure 3.11. *Variation of wall pressure coefficients on the model blade Cp with respect to incidence α. The values are compared to Laurence Vion's experimental and numerical results with the blade at $\alpha = -2.2$ degrees.*

3.2.2. Force balance measurements

Therefore the idea was to monitor an integrated value such as the lift by means of force balance measurements. Managing to cover the foot gap while performing force measurements was problematic because of the contradictory needs to prevent foot vortex generation and avoid residual constraints affecting the measurement. Scotch of various thickness and elasticity were

tested, but it was finally decided that their influence on force measurements was too strong in each case which is why they were discarded in the following.

Force balance measurements were found to be much more sensitive to variations in incidence than wall pressure taps. As a consequence, the measurement of the lift was used as a means to assert the position of the blade in the wind tunnel. Lift variation with respect to the angle of attack of the blade is presented in figure 3.12.

As expected in the tested range of small angles of attack, the relationship between the lift and the angle of attack is linear. The measurement of Laurence Vion is represented on this graph by a blue triangle. The lift which Laurence Vion obtained for an angle of attack of -2.2 degrees was attained for $\alpha = -2.1$ degrees in our case. Consequently an angle of attack of -2.1 degrees was chosen in the following.

The value of the angle of the blade root with respect to the window is not reported in Laurence Vion's manuscript. It was thus necessary to quantify the sensitivity of the lift to a rotation around the y axis. The highest rotation along the y axis achievable with our setup was 0.62 degrees. The green circle on figure 3.12 represents the lift measured in this case ($\epsilon = 1.08$ degrees) for an angle of attack $\alpha = -2,2$ degrees. This shows that the impact of a rotation along the y axis is small compared to a change in incidence, which is encouraging in view of the comparison with the experiments of Laurence Vion. Thus, we have left the blade in the initial position ($\epsilon = 0.46$ degrees) which caused less constraints to the setup.

Figure 3.12 demonstrates the high sensitivity of the lift to the blade incidence and orientation along y axis, which gives confidence that the chosen blade position is representative of the case tested by Laurence Vion.

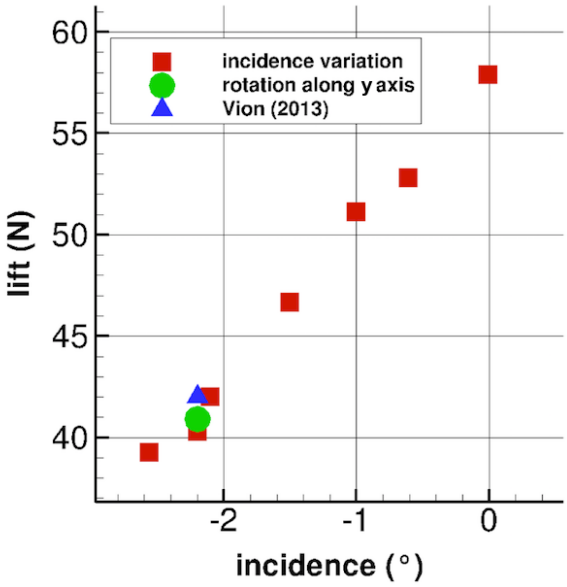

Figure 3.12. *Lift measured with respect to incidence on the fixed blade*

3.2.3. Shed vortex characteristics

Finally, the chosen position of the blade (with no cover on the foot gap) was validated thanks to a PIV plane in the wake. The characteristics of the shed vortex were compared to those reported in [Vion, 2013]. Therefore a 3C PIV plane was performed to observe the shed vortex in a cut at one tip chord length ($1\,c_{tip}$) downstream of the blade. Laurence Vion showed in her thesis that the vortex was not totally formed at $1\,c_{tip}$, and that it was easier to deduce the characteristics of the shed vortex further in the downstream (from 2 c_{tip} downstream of the blade). However, the main objective of this work being the observation of the leading-edge vortex, the blade was placed in the center of the wind tunnel in the streamwise direction to facilitate optical access to the leading-edge. Therefore the optical access in the wake was reduced, which barely allowed to survey the shed vortex at one tip chord in the downstream.

The setup used to acquire the 3C PIV plane is presented in figure 3.13. The standard PIV setup (presented in Table 2.4) was used. 2000 images were acquired to guarantee a converged average flow field. The spatial resolution of the PIV images obtained after reconstruction is 2 mm (which corresponds to an interrogation window of 31 pixels with the magnification factor associated to the image). As it is not useful to sample the images at a higher resolution than the spatial resolution, the images are decimated by 4 in order to facilitate post-processing.

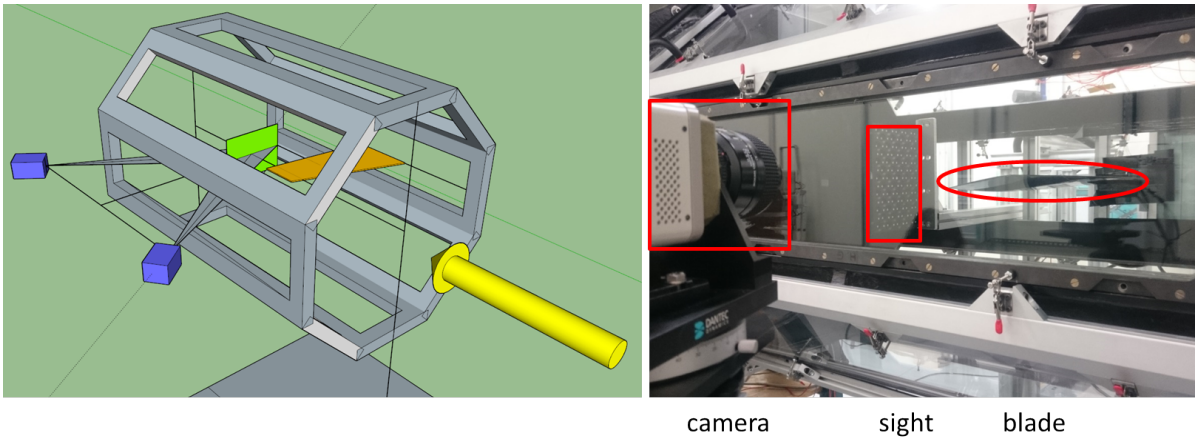

Figure 3.13. *Setup used for the plane in the wake. Left : sketch of the optical test section with the blade in orange, the laser sheet in green and the cameras in blue. Right : photograph of the setup with the sight instead of the laser sheet, pictures used for calibration.*

Laurence Vion showed that the shed vortex was subject to vortex wandering. This phenomenon has been investigated in [Jacquin et al., 2001] among others and consists in a wide band, low frequency displacement of the vortex along its mean position, with no distinctive frequency peak.

Thus, the vortex was re-centered before its characteristics were analysed, using the same procedure as Laurence Vion described in her thesis[4]. The center of the vortex on the instantaneous PIV images was tracked using the Gamma 2 criterion. This criterion, developed by [Graftieaux et al., 2001] is equivalent to a kinetic momentum barycenter. As it based on the topology on the velocity field, instead of punctual values or derivated values (such as the point with minimal axial velocity or maximal vorticity in absolute value), it is best suited for PIV images which may be impacted by noise. The Gamma 2 criterion relies on a square integration win-

[4]except that the tool was re-coded

dow of given size Nrr in pixels. A convergence of the average center coordinates with respect to Nrr is carried out to choose Nrr. Then, each instantaneous image is displaced so that the instantaneous centers are superposed. The average calculated on the intersection of all instantaneous images gives the re-centered vortex. The simple average of the instantaneous PIV images, without recentering, is referred to as uncentered vortex. The dimensionless vorticity and velocity along the axis of the re-centered and uncentered vortex are measured and compared to the results of Laurence Vion in Table 3.2. On the re-centered vortex, the higher central vorticity compared to the results of Laurence Vion can be explained by the higher resolution of the PIV images in the present study (2 mm versus 3 mm in the case of Laurence Vion). The circulation is evaluated by integrating the velocity square contours of increasing sizes and taking the asymptotic value (see figure 3.14). In our case, recentering does not affect the value of the circulation. Laurence Vion observed the same trend in the downstream, from $2c_{tip}$ onwards. All in all, the results indicate that the shed vortex characteristics compare reasonably well with those measured by Laurence Vion at the same location, and confirm that the model blade position in the wind tunnel is representative of the rotating case. They also confirm that the foot gap does not affect the value of the shed circulation, which is probably due to the fact that the circulation distribution is increasing along most of the span.

	Uncentered vortex		Re-centered vortex	
	present	Vion	present	Vion
Dimensionless central velocity $\frac{U_x}{U_{inf}}$	0.52	0.58	0.53	0.55
Dimensionless central vorticity $\lvert \frac{\omega_x\, c_{tip}}{U_{inf}} \rvert$	7.1	7.0	18.5	10.5
Dimensionless circulation $\lvert \frac{\Gamma}{U_{inf}\, c_{tip}} \rvert$	0.34	0.38	0.34	0.33

Table 3.2. *Comparison of the dimensionless characteristics of the shed vortex at one tip chord in the wake*

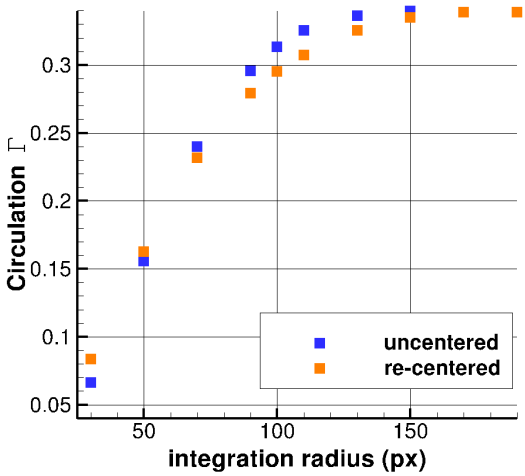

Figure 3.14. *Dimensionless circulation of the shed vortex at one tip chord in the downstream with respect to the integration radius in pixels*

3.2.4. Summary of the experimental setup

To summarise, the blade is placed on horizontally in the test section, its foot trailing edge point corresponding to the center of the test section (both along x and y). The angle of attack is set to $\alpha = -2.1$ degrees, and the angle of the foot section with respect to the window is set to $\epsilon = 0.46$ degrees.

As explained previously, the inflow velocity is fixed to 36 m/s at the entrance of the test section. Due to blockage effects created by the blade, this corresponded to 38.5 m/s ($\pm$0.6 m/s) on the static pressure probe on the top window, 30 cm upstream of the apex. This yielded an experimental Reynolds number based on the chord at $0.75\,R_{tip}$ (c=244 mm) $Re_{exp} = 4.4 \times 10^5$. The Reynolds number in the rotating Open Rotor case at full scale, also based on the chord and relative velocity at $0.75\,R_{tip}$ amounts to $Re_{prop} = 7.0 \times 10^6$. The impact of the Reynolds number on leading-edge separation for this kind of application still remains to be investigated. The following chapter focuses on the characterisation of the LEV on the model blade in this configuration.

4

Characterisation of the leading-edge vortex on the model HTC5 blade

The objective of this chapter is to characterise the leading-edge vortex on the model HTC5 blade, that is, define its characteristic dimensions, its core properties, and investigate its unsteady behaviour. This characterisation is performed both experimentally, using TR-PIV in the configuration described in chapter 3, and numerically using a RANS calculation in the same configuration. Here the experimental / numerical comparison is carried out with the objective of assessing the ability of RANS $k-\omega$ SST calculations to simulate the LEV. However, it is not the scope of this work to improve the numerical strategy in terms of schemes or turbulence models.

Before presenting the acquisition and post-processing parameters, the representativity of the fixed blade model is discussed. Although this subject was already covered in the thesis of Laurence Vion, new arguments to demonstrate the representativity of the fixed blade model were found in this work.

4.1. Representativity of the fixed blade model

The fixed blade model was validated through comparisons with RANS calculations of the rotating HTC5 blade. For this purpose, a complementary analysis of the reference configuration studied in Delattre [Delattre and Falissard, 2015] (rotating HTC5 case in Open Rotor configuration) was performed. The description of the numerical setup, parameters and procedure of this RANS calculation can be found in [Delattre and Falissard, 2015].

Friction line comparison

Figure 4.1 shows a reasonable qualitative agreement between friction lines obtained on the experimental model blade using oil flow visualisation, and friction lines given by RANS calculations of the rotating counterpart.

Indeed, in both cases, the first separation point, where the leading-edge vortex flow starts to form, corresponds to the apex (foremost point on the blade leading-edge). This point is noted as $D0$ in figure 4.2, which presents a schematic view of the oil flow visualisation. In both cases, the leading-edge vortex flow propagates along the leading-edge. Going up the span, the flow detaches at the leading-edge (see separation points $D1, D2, D3$ in figure 4.2) and reattaches further away in the downstream (see points $R1, R2, R3$ in figure 4.2). The reattachment lines

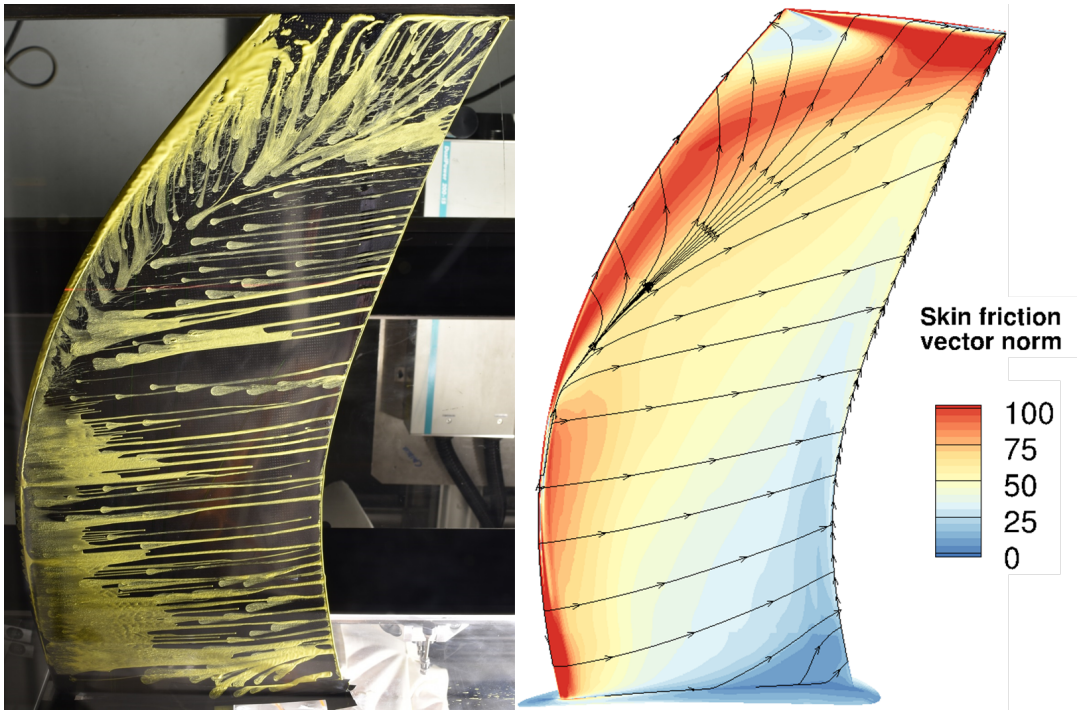

Figure 4.1. *Comparison between friction lines obtained from oil flow visualisation on the experimental fixed model blade (left) and friction lines on the numerical rotating case (right). The norm of the wall friction vector is displayed for the numerical case.*

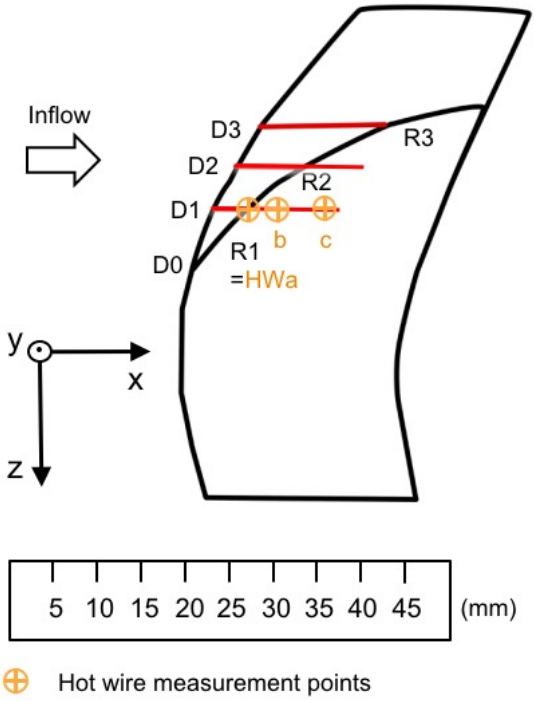

Figure 4.2. *Sketch of the friction lines on the model blade (drawn from figure 4.1) with location of the 3 planes investigated with TR-PIV (in red) and hot wire measurement points (HWa, HWb, HWc).*

are clearly discernible, and are in good agreement between experimental and numerical data. They show that the leading-edge vortex flow grows into a conical structure. Between the leading-edge and the reattachment line are friction lines indicating the recirculation of the flow next to the wall. For spanwise stations over 80% of span, the leading-edge vortex flow mixes with the tip vortex before it is shed into the wake.

The oil flow visualisation features an accumulation of yellow paint next to the leading-edge, close to the tip, which is typical of a detached or low skin friction area. This is in accordance with the lower norm of the skin friction vector in the corresponding zone for the rotating counterpart (see figure 4.1).

Order of magnitude analysis

Furthermore, following the analysis of [Garmann and Visbal, 2014], the importance of the rotation effects for the LEV dynamics was quantified. To do so, a comparison of the order of magnitudes of the force densities acting on the fluid was performed. Again, the reference calculation of [Delattre and Falissard, 2015] was exploited. The force densities were calculated at each point of the mesh using the classical expressions : Coriolis $\vec{f_{co}} = 2\,\rho\vec{\Omega} \times \vec{U_{rot}}$ where $\vec{U_{rot}}$ is the velocity vector expressed in the rotating frame; Centrifugal $\vec{f_{ce}} = \rho\Omega^2\vec{r}$ where $\vec{r}$ is the radial vector in the cylindrical set of coordinates; pressure gradient $\vec{\nabla}p$. The pressure gradient is calculated at each point of the mesh using finite differences.

The forces were first extracted at 75% of the tip radius. Indeed, the profile at 75% of tip radius is generally considered to be representative of the behaviour of the whole blade on open rotors, because the average centrifugal force on the blade is achieved at this location.

On the plane at 75% of the tip radius, the mid-point between the separation and reattachment lines is estimated from the friction lines (see figure 4.1, right). The force densities are extracted on a line normal to the blade surface at this point. For each force density, the L2 norm is computed and averaged on the first 10 mm close to the blade surface. Indeed, it will be detailed in the following that this represents the order of magnitude of the LEV's characteristic size.

Table 4.1 shows that the L2 norm of the average centrifugal and Coriolis force densities in the LEV at $0,75R_{tip}$ are one order of magnitude lower than the L2 norm of the pressure gradient. This supports the fact that the formation of the leading-edge vortex flow on this propeller blade is governed at first order by the pressure gradient effects. Of course, as mentioned in the literature review, part of the pressure gradient originates in the fact that the blade is rotating [Maxworthy, 2007]. Yet as pressure gradient effects are accounted for by the circulation distribution, the use of the fixed HTC5 model blade is justified.

Force density	Expression	Averaged norm in LEV
Pressure gradient	$\vec{\nabla}p$	1.8×10^6
Coriolis	$\vec{f_{co}} = 2\,\rho\vec{\Omega} \times \vec{U_{rot}}$	1.8×10^5
Centrifugal	$\vec{f_{ce}} = \rho\Omega^2\vec{r}$	7.1×10^4

Table 4.1. *Order of magnitude comparison of inertial and pressure gradient force densities. Data extracted on the mid-line (between the separation and reattachment lines), at 0.75 R_{tip}, and averaged in the first centimeter at the wall*

4.2. Choice of the PIV acquisition and post-processing parameters

Time-Resolved Particle Image Velocimetry (TR-PIV) measurements were performed on three cut-planes of the leading-edge vortex, normal to the blade, at at 67% (plane 1), 72% (plane 2), and 79% (plane 3) of span (see figure 4.2).

The setup is presented on figure 4.3. The cameras are placed with an angle of 40 degrees with respect to the normal to the laser sheet plane, so that the three velocity components of the flow field can be reconstructed with good accuracy. The laser sheet generation and displacement system was fixed above the test section (see figure 4.4).

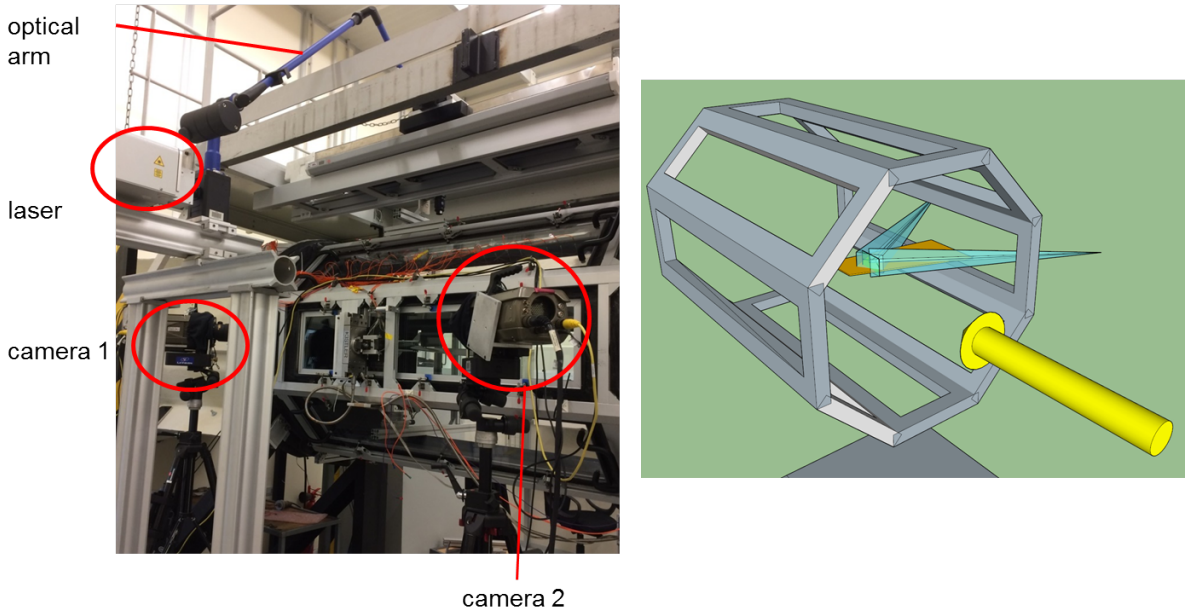

Figure 4.3. *Setup used for TR-PIV on the 3 planes normal to the blade*

Prior to the TR-PIV measurements, a laser tomoscopy was performed on each plane of interest (see figure 4.5). Those images enable an easy identification of the upper shear layer created when the flow detaches at the leading-edge. Indeed, the seeding density will be higher in the flow circumventing the leading-edge vortex flow. The distance between the upper shear layer and the blade surface is in the order of 10 mm, which corresponds to 4% of the average chord of the blade. This indicates that the leading-edge vortex flow is a very near-wall structure.

4.2.1. TR-PIV acquisition parameters

The choice of the TR-PIV sampling frequency was done considering that the Strouhal number is typically in the order of $St = 0.2$. Taking a characteristic height in the order of 10 mm as suggested by laser tomoscopy, and the inflow velocity in the order of 40 m/s, this gives a characteristic frequency in the order of 400-800 Hz. In order to choose the sampling frequency, it is also necessary to consider that the high speed laser enables to have a TR-PIV frequency up to 10 kHz, but at the expense of the energy per pulse. Indeed, the power of the laser varies with the acquisition frequency. It is maximal between 2 and 5 kHz, and at 10 kHz, it is in

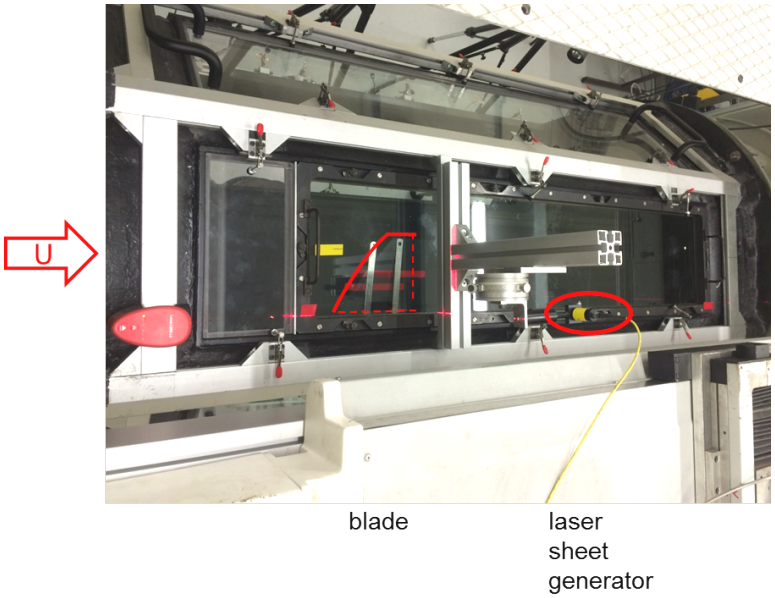

Figure 4.4. *Top view of the test section with the setup used to displace the laser sheet. The red marks are points of reference corresponding to the tested PIV plane*

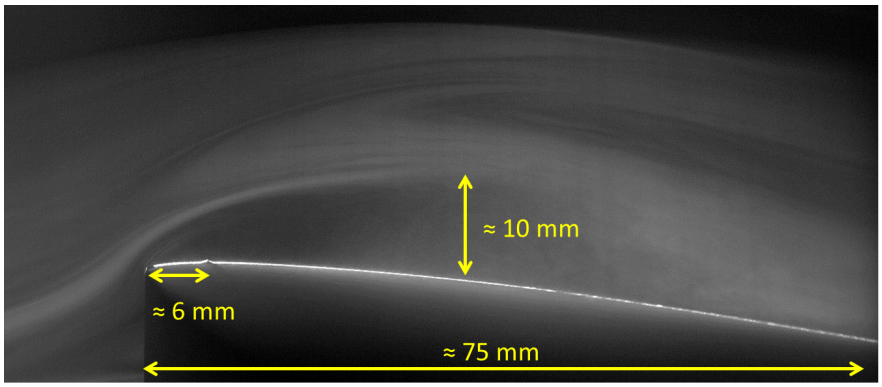

Figure 4.5. *Laser tomoscopy image on plane 2 (72% of span).*

the order of 60% of the maximal power. For instance, taking into account the higher flashing rate, the energy per pulse would be 75% lower at 10 kHz than at 4 kHz. Also, for data storage reasons, the size of the image needs to be reduced when the sampling frequency increases.

Finally the TR-PIV sampling frequency was set to $f_{PIV} = 3725$ Hz. This was seen as a good compromise between the need to capture unsteady phenomena up to 1 kHz, while keeping sufficient energy per pulse, and ensure that the images would be big enough to include the reattachment on the LEV on all planes.

Since the blade was coated with carbon fibres, the acquisition parameters were chosen carefully to avoid creating marks or cuts on the blade. 2000 images per run were found to be a maximal number given the sampling frequency and the energy per pulse required for a clear visualisation of the particles. In terms of time-resolved measurements, 2000 images correspond to a frequency resolution in the order of Δf =3.7 Hz. Several runs (from 12 to 24) of 2000 images each were acquired on each plane. Each run thus lasted around $500ms$ of physical time.

4.2.2. Post-processing parameters

As the laser tomoscopy indicated, the LEV is a very near wall structure. Treating such boundary layer structures with PIV is not straightforward. Indeed, close-wall reconstruction is hindered by the presence of light reflections. Also, the seeding density in boundary layers or vortex cores is typically lower than in the freestream. This complicates reconstruction, especially in such zones of high velocity gradients and possibly high vorticity. Consequently, special care was taken in the choice of the reconstruction parameters.

In the present work, four levels were considered, with 20 iterations in the minimisation algorithm. As pre-processing steps, geometric masks (on the blade profile), average subtraction and self-calibration were applied on the images. An analysis of the sensitivity of the correlation coefficient map to the size of the interrogation window was performed. In the following, the size of the interrogation window is noted $Nh \times Nl$ pixels, Nh being its height (in y direction), and Nl being its length (in x direction). A too large interrogation window, especially in the region of the LEV, would lead to under-estimated velocity gradients. On the other hand, if the interrogation window is too small, there is a greater chance of generating noise on the data. Due to the seeding density, the minimal interrogation window that was investigated was 7x7 pixels, so that it would comprise about three seeding particles. The maximal size was 15x30 pixels so that it would not be too big compared to the size of the LEV (approximately 100 pixels on plane 1, at 67% of span). 300 images were post-processed for several interrogation window sizes, and the resulting average flow fields and correlation coefficient maps were analysed.

The accuracy of the reconstruction was evaluated using the average correlation coefficient in the region of the LEV $s_{ave,LEV}$. This region is noted A in figure 4.6. The same procedure was performed in a region outside the LEV, and gave similar trends. The results of this analysis are presented in figure 4.7 for the PIV plane at 67% of span. Similar plots were obtained for the two other planes.

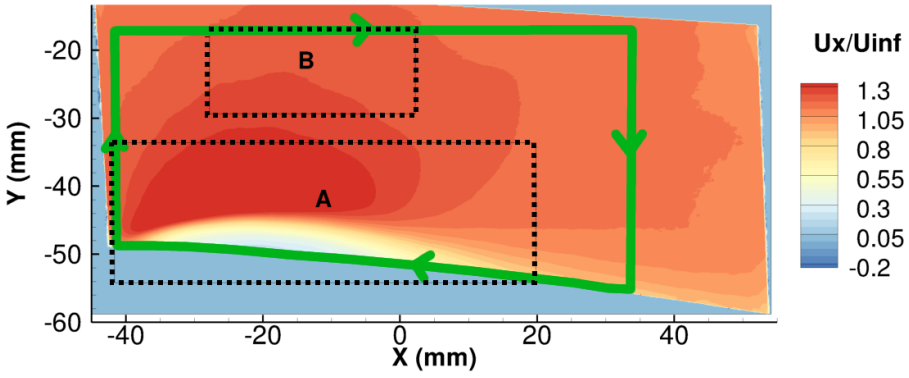

Figure 4.6. *Average dimensionless streamwise velocity U_x on plane 1 (67% of span) with contours and zones used in the study to calculate : (A) average correlation coefficient, (B) average standard deviation of velocity fluctuations, (green full line) circulation.*

In the tested size range, $s_{ave,LEV}$ increases as the size of the interrogation window decreases. However, the very high correlation coefficients obtained for interrogation windows which comprise less than three particles correspond to quasi-uniform flow fields which are not physical. Indeed, when the interrogation window is too small, the risk to wrongly associate an interrogation window from an image to the other is higher. For a given surface of the interrogation

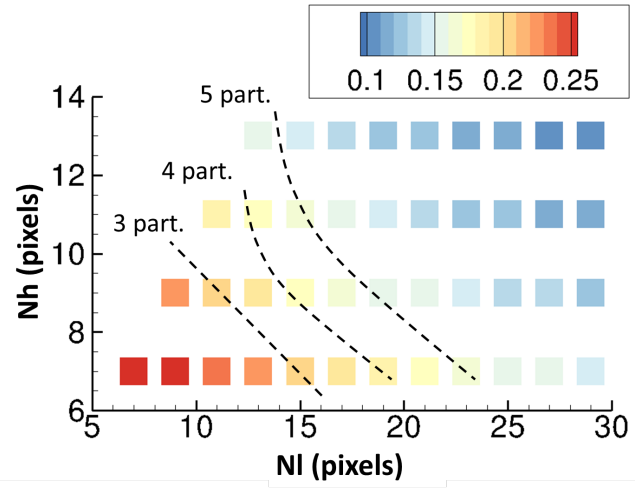

Figure 4.7. *Average correlation coefficient inside the LEV $s_{ave,LEV}$ with respect to the interrogation window length N_l (in x direction) and height N_h (in y direction). Dashed lines indicate the density of seeding particles in the interrogation window.*

window, $s_{ave,LEV}$ is higher if the window is rectangular. Indeed this shape fits better with the geometry of the flow field. It enables to best capture vertical velocity gradients (U_y component) while keeping enough seeding particles in the interrogation window to ensure a correct reconstruction. Consequently, an interrogation window of size 7x15 pixels was chosen in this study. Also, to verify the stability of the solution with respect to the interrogation window, the difference between the velocity fields obtained for two window sizes was expressed in percentage of the velocity at each point, and averaged over the zone of the LEV. For the windows containing at least three seeding particles, the discrepancies between the flow fields reconstructed with different window sizes were lower than 4% for all velocity components. The spatial resolution of the velocity fields is given by the size of the interrogation window, which corresponds to 0.40 mm×0.85 mm.

The average correlation coefficient in the LEV $s_{ave,LEV}$ for an interrogation window of 7x15 pixels is in the order of 0.2. This value corresponds to a suitable correlation quality, according to criteria applied at ONERA and described in [Champagnat et al., 2011]. Tools for a more precise assessment of the PIV uncertainties obtained with the Folki-SPIV algorithm are currently being developed at ONERA. Consequently, in the present study, an alternative way was used to evaluate the uncertainties linked to the reconstruction. In a zone where the flow is not turbulent, the velocity fluctuations will only be caused by the measurement and reconstruction process. Therefore the standard deviation of the velocity fluctuations averaged in a zone where the flow is the least turbulent should give an upper bound of the noise caused by the PIV.

This was performed on an average field obtained from 2000 snapshots. The convergence of the average with the number of snapshots was verified on the planes at 67% and 79% of span. Averaged flows over growing number of images (up to 4000) were computed. For each velocity component, the pixel-wise difference between two successive averages was divided by the reference velocity at this point. From 1400 images onwards, the mean pixel-wise difference was lower than 0.5% of the reference velocity at each point for all velocity components.

On each pixel, the norm of the velocity fluctuations was divided by the norm of the velocity.

This quantity was averaged on a zone noted B in figure 4.6, where the flow is likely to be the least turbulent. This zone is outside of the LEV and upstream of the wake of the LEV. Moreover, it has been spaced from the borders of the image which could be subject to more reconstruction errors. The analysis was performed at 67% of span, where the LEV is smaller. The average standard deviation of the velocity fluctuation norm was found to be in the order of 2.3% of the velocity norm.

4.3. RANS calculation setup

Because the observed LEV is very close to the blade surface, the dynamics are not easy to capture, neither using PIV, nor using RANS calculations. As a consequence, a RANS calculation of the flow around the fixed blade in the experimental setup was performed in order to allow a comparison with experimental data.

The computational domain is based on the exact geometry of the test section. However, to simplify the convergence process, the diffuser and converging parts of the wind tunnel were replaced by cylinders which prolong the geometry of the test section (see figure 4.8). The resulting "wind tunnel" mesh contained about three million points.

The mesh of the blade (in red in figure 4.8) amounted to eleven million points. The boundary layers around the blade are accurately discretized (y+ $\approx$ 0.1 at the blade surface, y+ $\approx$ 1 at the wind tunnel wall). Transfers between near-body and "wind tunnel" grids are accounted for using the Chimera method.

No-slip boundary conditions are imposed on wind tunnel walls and on the blade surface. Total pressure, total temperature, and the direction of the flow are prescribed at the inlet, while the output pressure is imposed at the outlet. The output pressure is chosen so that the lift and the streamwise velocity U_x at the location of the experimental static pressure probe (300 mm upstream of the apex) are in accordance with the experiment.

A calculation with a transition model was also carried out. Indeed, the laser tomoscopy image on figure 4.5 gives evidence that the flow detaches at the leading-edge, even before reaching the transition wire positioned 6 mm downstream of the leading-edge. This hints that flow separation may be laminar on the leading-edge. A calculation with a transition model was thus carried out in order to see if it would be more representative and give closer results to the experiment. The transition model used was a compressible AHD-Gleyzes model with a criterion to take into account cross-flows. The external turbulence intensity was set to 0.04%, in accordance with the value of the turbulence level which was measured in the empty test section (see chapter 3). The calculation was initialised to impose a laminar flow before it detached from the leading-edge. Moreover, a fully turbulent flow was prescribed at the trailing edge.

In all cases, the convergence of the solution was satisfying because all residuals decreased by at least 6 orders of magnitude.

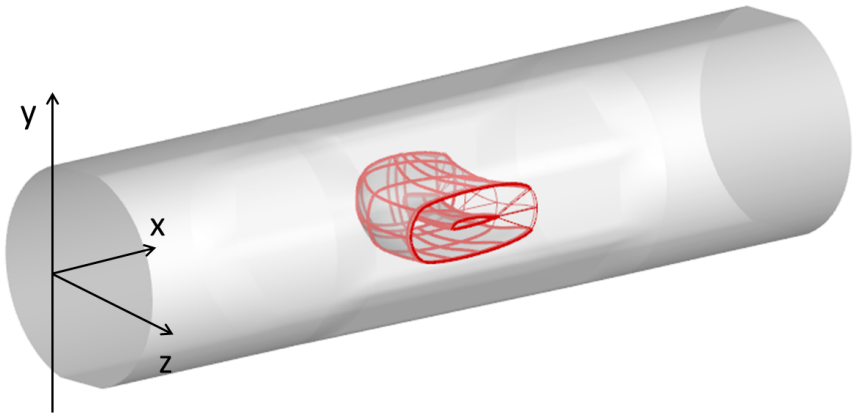

Figure 4.8. *Sketch of the computational domain used for RANS calculation of the fixed blade in the experimental configuration*

4.4. Characterisation of the leading-edge vortex flow

The TR-PIV measurements allowed to observe the three-dimensional separation bubble on three cut planes at given spanwise stations, with the objective of characterising this structure with respect to previously studied leading-edge vortices.

First, an analysis of the average flow fields will be carried out, in order to determine length scales and average core properties of the LEV.

The average flow fields at each spanwise location are presented in figure 4.9. The velocity in the chordwise direction (along x) is plotted for plane 1 (67% of span) and plane 3 (79% of span), while the velocity in the spanwise direction (along z) is plotted for plane 2 (72% of span). Note that the z axis is oriented from blade tip to root, so U_z is negative in the LEV, in accordance with the friction lines. Figure 4.9 shows a good qualitative agreement between experimental and numerical data. The velocity contours have similar shapes, both inside and outside the LEV.

On planes 1 and 3, the recirculation zone is not visible. It could be recovered on plane 2, though at the edge of the acquired velocity field. In fact, reconstruction is prevented in a region close to the surface of the blade, because the laser sheet impacting the blade creates an intense light reflection so that no seeding particle can be observed in this region. The position of the blade surface in the experiment is estimated from the calibration images and the position of the light reflection at the wall. This enables to place a cut of the blade profile (in white) on each image. The profiles are very thin, which is necessary to reduce profile drag in cruise conditions but easily triggers flow separation at take-off. The separation and reattachment points identified in figure 4.2 are indicated on each plane. On planes 1 and 3, the first acquired PIV data is respectively 0.8 and 0.4 mm away from the wall, while this distance goes up to 2 mm on plane 2. The difference is due to the position of the cameras, which were placed differently on each plane to reduce the halo caused by the illumination of the blade surface. Due to the twist of the blade on the sections around plane 2, one of the cameras was positioned with a more grazing angle, which made the light reflection zone appear bigger on the image. Because no particle was visible close to the wall where light reflections occurred, those zones were masked for PIV reconstruction. Consequently, on the average flow fields, the streamlines downstream

of the vortex follow the masked zone.

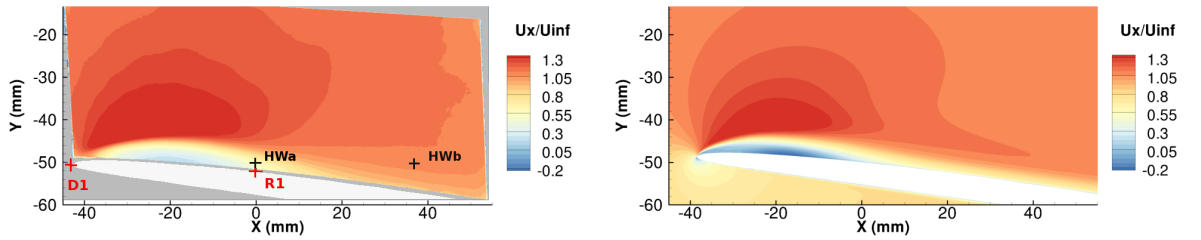

(a) Streamwise velocity field U_x on plane 1 (67% of span)

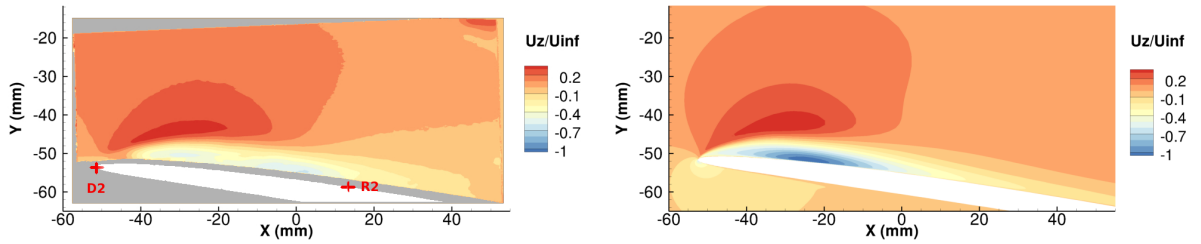

(b) Spanwise velocity field U_z on plane 2 (72% of span)

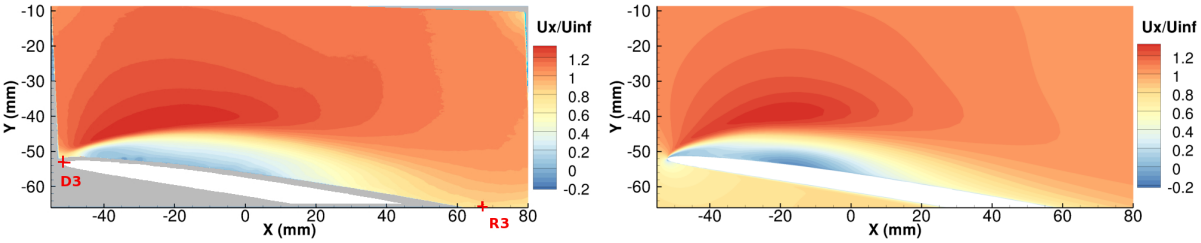

(c) Streamwise velocity field U_x on plane 3 (79% of span)

Figure 4.9. *Average velocity fields non dimensionalised with respect to inflow velocity U_{inf}. TR-PIV data (left) is compared with results of the RANS calculation of the experimental setup (right). The TR-PIV data is computed from 2000 snapshots.*

4.4.1. Evaluation of tools to characterise the scale of the leading-edge vortex

Defining length scales for the LEV on each cut plane is not straightforward, because it is not a streamtube isolated from the rest of the flow (as this can be the case for a laminar detachment bubble). Indeed, laser tomoscopy images shows that smoke penetrates the LEV, even though the seeding density is lower than in the mainstream. Also, the streamwise and spanwise velocities amount to about 40% of the inflow velocity. This is unlike the velocity magnitudes that can exist in laminar detachment bubbles, which can be nearly negligible and referred to as dead-air zones [Horton, 1968]. Indeed, according to the criterion developed by [Elimelech et al., 2013], the structure under investigation is really a LEV, and not a detachment bubble. Figure 4.10 shows that vorticity is maximal at the separation point rather than at the reattachment point.

As the reattachment line is clearly marked on the oil flow visualisation in figure 4.1, the distance between the leading-edge and the reattachment line on each plane was used as a characteristic distance of the length of the leading-edge vortex flow. In a similar way, the length of the LEV in the numerical case was measured using skin friction lines. Those results are presented in Table 4.2. The length of the LEV is well predicted by the RANS calculations (perfect match,

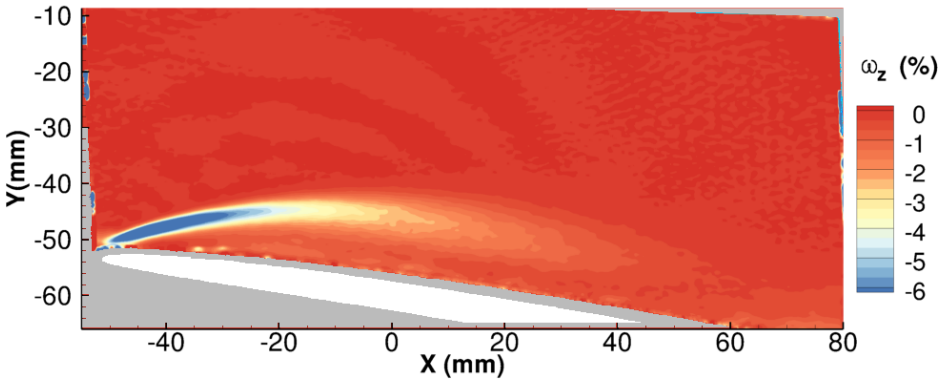

Figure 4.10. *Average field of dimensionless vorticity component normal to the plane ω_z computed from 200 snapshots on plane 3 (79% of span). The data is non-dimensionalised by $\frac{U_{inf}}{c_{tip}}$*

Plane position (% of span)	Experiment (oil) (mm)	RANS (wall friction lines) (mm)	RANS+transition (wall friction lines) (mm)
67 % (plane 1)	43 (± 2)	47 (± 1)	49 (± 1)
72 % (plane 2)	65 (± 2)	65 (± 4)	71 (± 4)
79 % (plane 3)	119 (± 10)	108 (± 20)	110 (± 30)

Table 4.2. *Length of the LEV on each cut plane.*

taking into account the error bars). The uncertainty linked to those measurements increased between plane 1 and 3, because the reattachment line was more difficult to discern as the LEV started to be influenced by the tip vortex.

In addition, a criterion based on the vorticity field ω_z was chosen to characterise the dimension of the bubble with respect to the y axis: $\max_{x \text{ in LEV}} y_m(x) - y_{wall}(x)$ with $\omega_z(x, y_m) = \min_{y \text{ in LEV}} \omega_z(x, y)$. This criterion, based on the maximal absolute value of the vorticity field ω_z, has a physical meaning because the top of the LEV consists in a region of high shear due to flow separation (see figure 4.10). Those characteristic dimensions on the three planes are summarised in Table 4.3. The uncertainties are derived either from the noise on the minimal vorticity profile (in the experimental case) or the size of the mesh cell (in the RANS case). RANS calculations underestimate the height with respect to the experiment. This is consistent with the higher velocities in the LEV core obtained for the numerical fields (see details in paragraph 4.4.2).

In figure 4.11, 200 laser tomoscopy images were superimposed, in order to give an idea of an average characteristic height. At the top of the LEV, the white zone indicates a high density of particles in average, because it is the trace of the flow circumventing the LEV. The distance of this zone to the blade surface can be a measure of the height. The uncertainty can be estimated by the thickness of this area. This criterion is qualitative, because laser tomoscopy is mainly used for visualisation purposes, so the camera's point of view is not calibrated. Nevertheless, the measurements are in reasonable agreement with the vorticity-based criterion. Both PIV and RANS methods show that the LEV is an elongated, close wall structure. Consequently, it is reasonable to validate those characteristics.

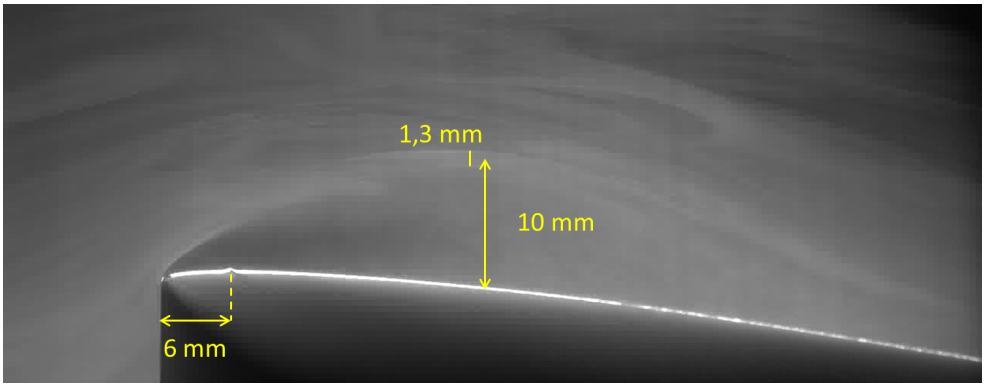

Figure 4.11. *Superposition of 200 laser tomoscopy images on plane 2 (72% of span). The images are acquired at 1 kHz.*

Plane position (% of span)	Experiment (tomoscopy) (mm)	(vorticity) (mm)	RANS (vorticity) (mm)	RANS+transition (vorticity) (mm)
67 % (plane 1)	6.0 (± 1)	5.8 (± 0.03)	(4.0 ± 0.3)	(4.0 ± 0.4)
72 % (plane 2)	10.0 (± 1.3)	8.0 (± 0.04)	(5.5 ± 0.5)	(5.5 ± 0.5)
79 % (plane 3)	12.0 (± 1.5)	10.7 (± 0.06)	(7.7 ± 0.7)	(8.3 ± 0.8)

Table 4.3. *Height of the LEV on each cut plane.*

4.4.2. Estimation of the core velocity

Thanks to the skin friction lines, it was possible to measure the angles θ between the axis of the LEV and each of the three planes, as follows. On the oil flow visualisation, the blade is assumed to be planar, which is a reasonable assumption given the low thickness and camber of the profiles. The axis of the leading edge vortex is assumed to be the mid-line between the detachment and reattachment lines, created by points P such that $x_P(z) = \frac{x_D(z)+x_R(z)}{2}$ and $y_P(z) = \frac{y_D(z)+y_R(z)}{2}$, where D belongs to the leading-edge (detachment line), and R to the reattachment line. Because the distance between the detachment and reattachment lines in the region of the 3 PIV planes is rather small compared to the camera field of view, it is reasonable to derive the position of the axis of the LEV without correcting the image by the camera point of view. Table 4.4 features the angles θ between the PIV planes and the LEV axis.

The velocity along the LEV axis was calculated from the streamwise and spanwise velocities: $U_{core} = U_x \cos\theta - U_z \sin\theta$. The value of U_{core} was extracted at the center of the LEV, defined as the point of coordinates $(x_m, y_m/2)$, where $\omega_z(x_m, y_m)$ is the maximal absolute vorticity in the shear layer. The value of U_{core} at this point is normalised with respect to the inflow velocity. In the numerical case, the same values of θ were used because the friction lines were in good agreement with the oil flow visualisation (as the measurement of the LEV length could show). The results are displayed in Table 4.4. The stated uncertainties are due to the propagation of the uncertainties in the measurement of θ. The values of the core velocity are over-estimated by the RANS calculations compared to the PIV. This is in accordance with the lower LEV heights reported in RANS, and would indicate that the vortex is more diffuse in the experiment. Given the uncertainties of the experiment (which are bound to be higher

Plane position (% of span)	Plane/vortex core angle θ (degrees)	Dimensionless core velocity $\frac{U_{core}(x_m,y_m/2)}{U_{inf}}$		
		experiment	RANS	RANS+transition
67 %	60 (± 1)	0.51 (± 3.5%)	0.70 (± 3.5%)	0.71 (± 3.5%)
72 %	50 (± 2)	0.51 (± 7%)	0.66 (± 7%)	0.65 (± 7%)
79 %	33 (± 2)	0.44 (± 7%)	0.62 (± 7%)	0.46 (± 7%)

Table 4.4. *Core velocity (along the axis of the LEV) on each cut plane.*

close to the blade surface) and the questionable reliability of RANS calculations for close wall structures, the discrepancy between the experimental and numerical results is not surprising. It is worth noticing, on the instantaneous velocity fields, that higher values of $\frac{U_{core}}{U_{inf}}$ can be found inside the LEV. However, the point where the maximum is attained changes from one snapshot to the other, which is why the LEV is more diffuse in average. This could indicate that the LEV is subject to vortex wandering in the experiment. As pointed by [Vion, 2013], the fact that vortex wandering is not accounted for by the present RANS simulations can lead to such discrepancies. This can explain the difference between experimental and numerical results.

Nevertheless, both methods indicate that the average core velocities do not exceed U_{inf}, while in the case of Delta wing leading-edge vortices, it can even reach $2\,U_{inf}$ [Payne et al., 1986]. The magnitudes of the core velocity are in reasonable accordance with the axial velocity profiles given in [Gursul et al., 2005] for a delta wing with 50 degrees of sweep and an angle of attack between 5 and 15 degrees. In that case, the LEV was also an elongated structure, where the velocity deficit typically varied between 25 to 60% of the inflow velocity.

4.4.3. Influence of the transition model

The RANS calculation with a transition model gives slightly higher values of the LEV length and height compared to the fully turbulent RANS calculation, and are thus slightly closer to the experimental results. It is worth noticing that the transition model improves more significantly the agreement with the experiment at 79% of span. The LEV is more diffuse than in the fully turbulent case and its core velocity has only 5% discrepancy compared to the experimental result (instead of about 40% for the fully turbulent calculation). The difference between the fully turbulent and transitional axial velocity flow fields is maximal in the shear layer, and amounts to about 10% of the inflow velocity. This is coherent with the fact that transition occurs in the shear layer. This result is supported by plots of the intermittency and the boundary layer shape factor on the blade surface (see figure 4.12). The intermittency is a value comprised between 0 and 1 used in the transition model. The flow is laminar when the intermittency is equal to zero. The intermittency field shows that a subsequent region of laminar flow exists between the blade root and the apex. For higher spanwise positions, the intermittency is equal to one. This indicates that the flow is either detached or turbulent. Figure 4.12b shows that the boundary layer shape factor is lower than 1.8 just downstream of the LEV which indicates that the flow is turbulent as soon as it reattaches downstream of the leading-edge vortex[5]. The mottled pattern near the trailing-edge is due to a failure of the BL

[5] a canonical turbulent boundary layer would have a shape factor in the order of 1.4

integral quantities prediction in the post-processing. This analysis supports the conclusions of [Schülein et al., 2012] that flow separation is the main trigger for transition to turbulence on propeller blades. The sketch proposed in this article to describe transition on propeller blades is displayed in figure 4.12c, and is in accordance with the previous RANS results.

Nevertheless, we can note that fully turbulent and transitional calculations are in relatively good agreement with each other on all planes, especially in view of the discrepancy with the experimental results. This can be explained by the fact that the flow quickly transitions to full turbulence when it reattaches. The following analysis of the unsteady behaviour of the LEV will enable to develop and support this assumption.

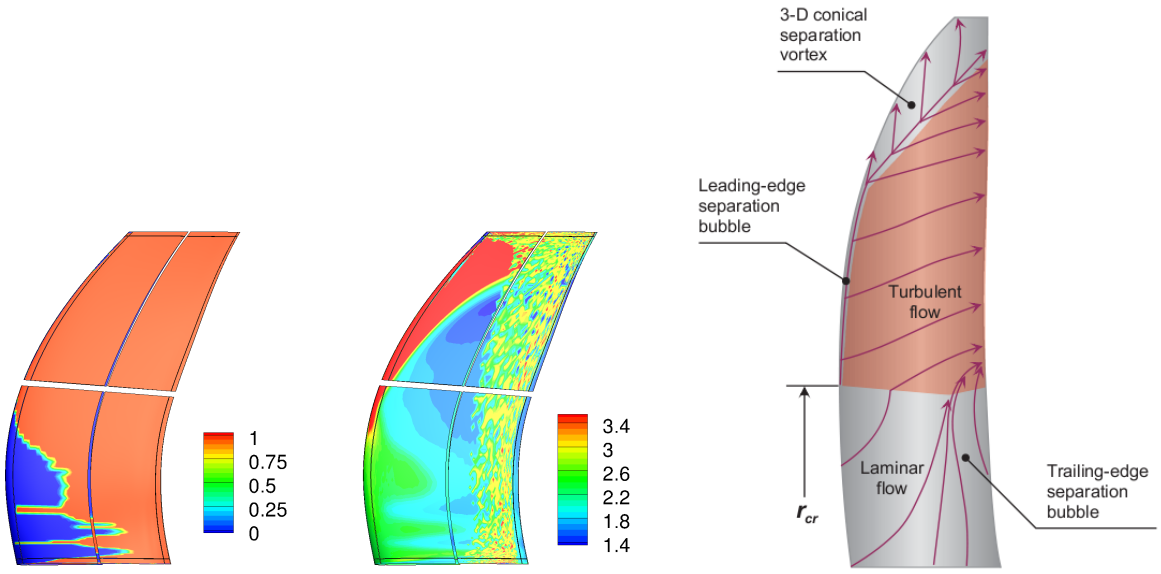

(a) intermittency

(b) boundary layer shape factor

(c) laminar to turbulent transition on a propeller blade. Source: [Schülein et al., 2012]

Figure 4.12. *Visualisation of transition on the suction side of the model blade and comparison with the results of [Schülein et al., 2012].*

4.4.4. Unsteady characteristics

Hot wire spectra in the LEV. In order to investigate the unsteady characteristics of the LEV, hot wire measurements were performed and were compared to TR-PIV data.

Hot wire measurements were carried out on planes 1 and 3, using straight 55P11 probes and a 55M hot wire anemometer from Dantec Dynamics. The sampling frequency was set to f_{hw}=41.6 kHz. No filters were applied on the signal, but the absence of aliasing was verified. The measurements were repeated at least two times at each location. 120 seconds of signal were acquired. Bartlett's method [Bartlett, 1948] was used to calculate the spectra. The signal was split into 76 non-overlapping blocks of 65536 points each. Then the spectra given by the Fast Fourier Transform on each block were averaged. Thus, the frequency resolution of the spectra is $\Delta f = \frac{f_{hw}}{65536} \approx 0.64Hz$.

Figure 4.13 shows the spectra obtained at three different locations along plane 1, represented

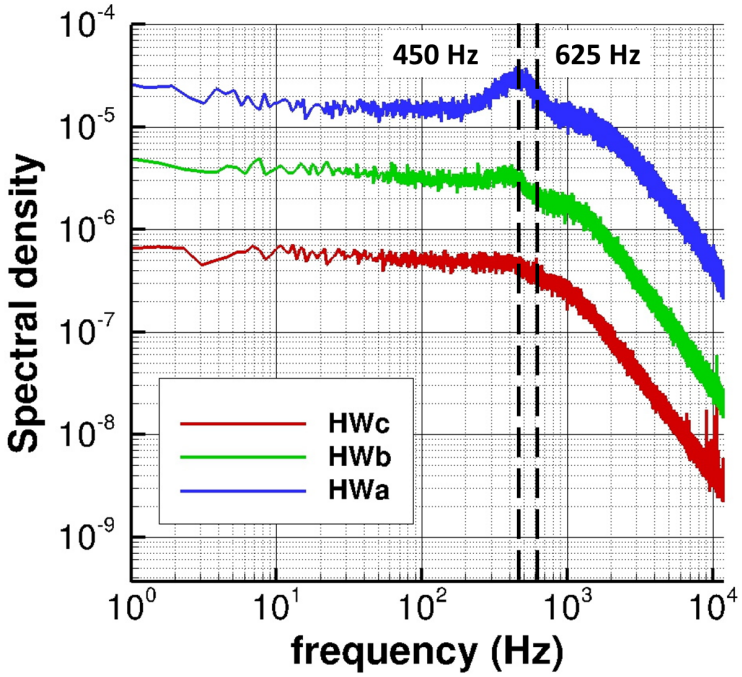

Figure 4.13. *Spectra obtained from hot wire measurements over the model blade (at points represented in figure 4.2).*

by points HWa, HWb, and HWc in figure 4.2 and 4.9. The hot wire was placed respectively at 2 mm, 5 mm and 15 mm of the surface at each of those points. While the signals were not filtered, the spectra showed no peak at frequencies higher than $\frac{f_{PIV}}{2}$, which confirms that the TR-PIV sampling frequency enabled to correctly solve the flow.

The spectra are characterised by a decrease in energy for high frequencies which is close to $\frac{-5}{3}$ law of Kolmogorov (but the slopes are not strictly equal because turbulence develops anisotropically due to the influence of the wall). For frequencies lower than $1kHz$, the spectra are rather flat except for a slight bump centered around a frequency of 450 Hz. This bump decays as the hot wire is moved away from the reattachment line, which seems to indicate that it is the signature of a phenomenon occurring in the LEV.

On plane 3, the spectra inside the LEV have similar characteristics. However the frequency corresponding to the bump varies between 300 and 500 Hz depending on the measurement point.

Determination of the associated mode using POD and Fourier transform The treatment of the TR-PIV images also enabled to recover this phenomenon. According to the method described in Chatterjee [Chatterjee, 2000], the three coordinates of the velocity were extracted on N points in the region of the LEV. Considering $N_t = 2000$ snapshots, the data was arranged in a matrix M of size $3N \times N_t$, each column corresponding to the description of one snapshot. The singular value decomposition of this matrix was performed such that $M = USV^T$, where U is a matrix of size $3N \times 3N$ giving an orthogonal basis of modes ordered according to the magnitude of their energetic contribution to the flow, S is a matrix of size $3N \times N_t$ containing the singular values associated to each mode, and V^T a matrix indicating

the temporal evolution of each mode.

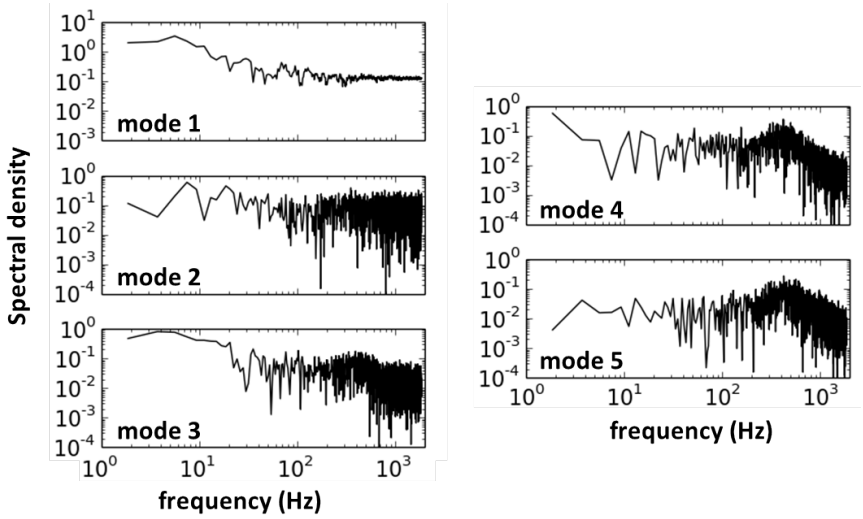

Figure 4.14. *Spectra for modes 1 to 5 drawn after POD decomposition from 10 sets of 2000 TR-PIV images on plane 3 (79 % of span).*

The POD gave more results on plane 3 where the vortex is the biggest, because the better resolution of the LEV enabled to decrease the signal to noise ratio.

A Fourier transform of the first 20 lines of V^T (corresponding to the first 20 modes) was performed on 10 sets of 2000 images. The spectra obtained from modes 4 and 5 were the first to exhibit a little bump such as was found in hot wire measurements (see figure 4.14). The bump is centered on a frequency of $400 - 500Hz$.

In figure 4.15, the streamwise velocity field plotted for mode 4 enables to identify that this mode is linked to the motion of the shear layer in the upper part of the bubble. This is consistent with the fact that this frequency is caused by an instability of the mixing layer due to the high shear existing in this region. The Kelvin-Helmholtz instability results in the shedding of small vortical structures in the downstream, as can be seen in figure 4.16.

A spatio temporal diagram was drawn from the TR-PIV images in order to show the vortex shedding phenomenon. A close-up on the first 50 images is presented in figure 4.17. Each band of the diagram corresponds to one snapshot. The tracer represents an average spanwise velocity profile $U_{z,ave}(x)$. Only the negative values of U_z are considered in the average:

$$U_{z,ave}(x) = \frac{1}{y_{max}/2 - y_{wall}(x)} \int_{y_{wall}(x)}^{y_{max}/2} max(0, -U_z(x,y))dy$$

On the graph, the time lapses between two vortex sheddings range between 6 and 8 images. 6 images would correspond to a frequency in the order of 625 Hz, and 8 images to a frequency in the order of 450 Hz. Those values are displayed in figure 4.13.

It is interesting to note that the vortex shedding phenomenon is a wideband phenomenon, as can be seen on the hot wire spectra and the spatio-temporal diagram. Moreover, the hot wire spectra in figure 4.13 show that the small secondary vortices produced by the shear layer instabilities are quickly damped in the downstream, because they quickly decay to turbulence

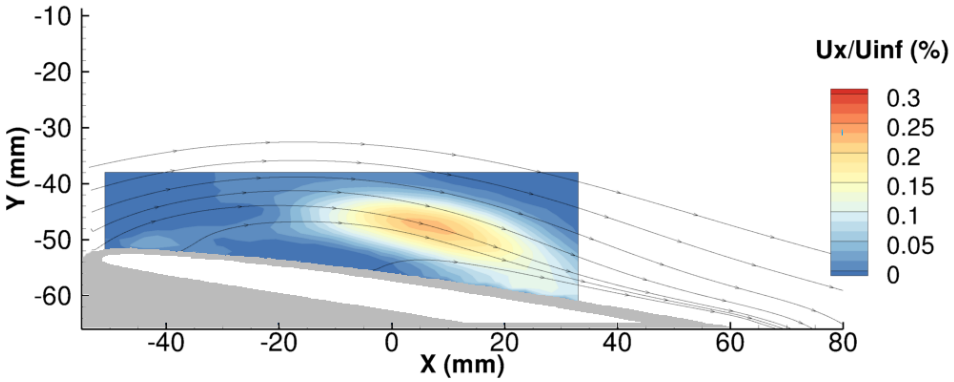

Figure 4.15. *Streamwise velocity field U_x (in m/s) of mode 4 and average (x,y) in plane streamlines on plane 3 (79% of span).*

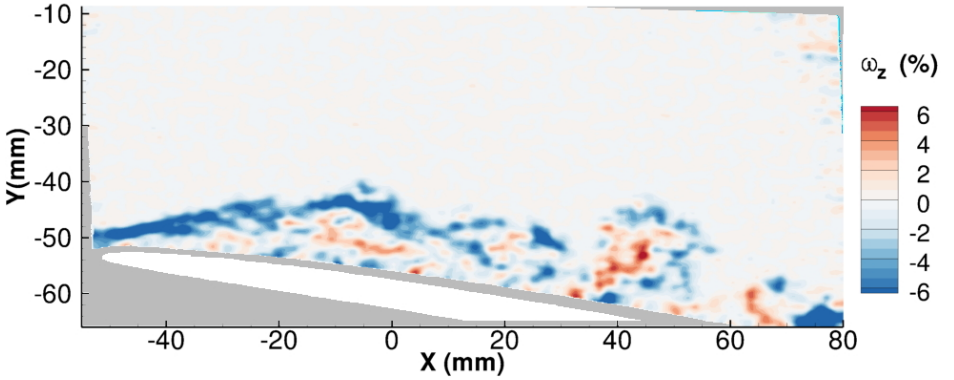

Figure 4.16. *Instantaneous field of dimensionless spanwise vorticity ω_z on plane 3 (79% of span). The data is non-dimensionalised by $\frac{U_{inf}}{c_{tip}}$*

(the locations of the hot wire measurement points Hwa, Hwb and Hwc are displayed in figure 4.2). In addition, the energy associated to this instability is somewhat limited. Indeed the most energetic POD modes related to it are mode 4 and 5. Spectra for POD modes 1, 2 and 3, corresponding to higher singular values, that is, contributing to a higher energy in the flow, do not exhibit the characteristic bump of this instability (see figure 4.14).

Characterisation of the impact of vortex shedding on the lift. In the framework of this study, the LEV is suspected to contribute to creating lift (thus thrust) on the blade. Thus, it seems worthwhile to examine the effect that this instability could have on the lift of the blade. In order to do so, the circulation was calculated on a contour enclosing most of the image (see figure 4.6). This contour was chosen so as to enclose most of the vorticity. The right hand side was left out because laser illumination in this region was less powerful, resulting in a lower correlation coefficient, especially on the instantaneous images. This was performed on 2000 snapshots, on plane 1. The average circulation and its standard deviation were calculated. The standard deviation of the circulation amounted to 3.4% of the average circulation. This has to be weighed against the 2.3% which characterised the standard deviation of the velocity norm in the least turbulent region of the flow. Even though this circulation is not the circulation around

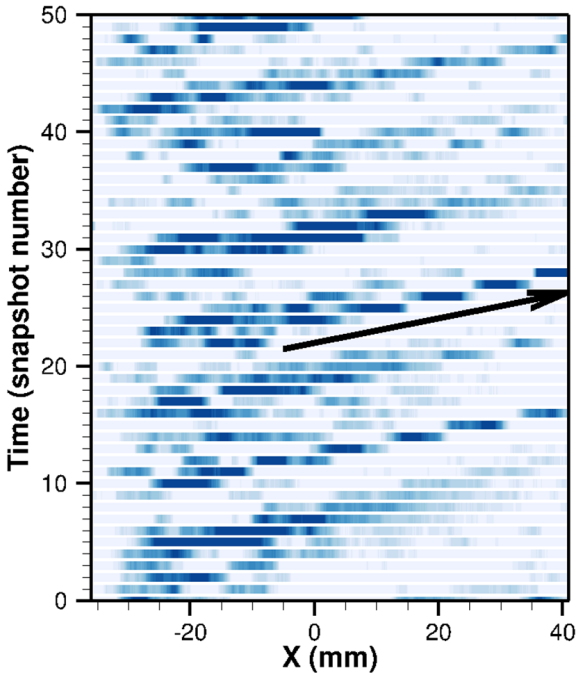

Figure 4.17. *Spatio temporal diagram drawn from plane 1 data, giving evidence of vortex shedding aft of the bubble. The tracer is* $U_{z,ave}(x) = \frac{1}{y_{max}/2 - y_{wall}(x)} \int_{y_{wall}(x)}^{y_{max}/2} max(0, -U_z(x,y))dy$. *Each color band corresponds to one snapshot.*

the blade profile, it is representative of that of the LEV. Thus, the impact of the unsteadiness on the efforts created on the blade can be considered to be quite low. The Kelvin-Helmholtz instability can be viewed as a second order phenomenon as far as the lift is concerned.

Also, it is interesting to interpret the representativity of fully turbulent and transitional RANS calculations in light of the unsteady characteristics of the flow. The fact that the flow quickly transitions to turbulence and that the instabilities correspond to a wide band phenomenon of relatively low amplitude indicates that the unsteady coherent structures are not strong and confined to a small region of the flow. This explain why fully turbulent RANS results provided a reasonable agreement with experimental data and were quite close to transitional RANS results, especially on the two first planes, at 67 and 72% of span.

Summary

The leading-edge vortex flow appearing on a low aspect-ratio propeller blade at take-off was characterised using TR-PIV and RANS calculations. The analysis was carried out on a fixed model blade with a circulation distribution that is representative of an HTC5 propeller at take-off. The use of the fixed blade is legitimized because keeping the dimensionless circulation distribution will account for the pressure gradient effects, which drive the physics of the LEV at first order. Although only one geometry was investigated, the circulation law considered in this study is generic for low-aspect ratio propeller blades.

The LEV was found to be a near-wall, elongated structure, with core velocities lower than the inflow (wake-like profile). The experimental and numerical shapes of the LEV have been

found in relatively good agreement. The friction lines match perfectly, but the LEV is more diffuse in the experiment. Transitional RANS calculations give only slightly different results from fully turbulent RANS calculations, except at 79% of span where they provide a better representativity. Fully turbulent RANS calculations still do a relatively good job at predicting LEV characteristics, because laminar to turbulent transition is driven by flow separation and full turbulence is quickly established downstream of the reattachment point.

Kelvin Helmholtz instabilities occur in the shear layer, which leads to the shedding of secondary vortical structures that are quickly damped in the downstream. This may trigger a flapping motion of the upper surface, leading the vortex core to move around its average location. This instability is found to be a wideband phenomenon, which does not seem to influence the circulation of the LEV at first order. The LEV can be considered as a quasi-steady structure with respect to the impact it has on the lift.

Both the elongated shape and the presumed wake-like structure of the flow enable to draw an analogy with leading-edge vortices on non-slender delta wings at low incidence. Indeed, while leading-edge vortices on slender delta wings exhibit a nearly circular region of high vorticity, they are more elongated for non-slender delta wings, and can be really close to the wing at low incidence [Gursul et al., 2005]. The values of the axial velocity in the core of the LEV in the experiment are in accordance with the axial velocity profiles given in [Gursul et al., 2005] for non-slender delta wing vortices.

This analogy with non slender delta wing vortices shows that it is reasonable to expect the leading-edge vortices on propeller blades at take-off to generate vortex lift. However, more circular leading-edge vortices with jet-like core velocity profiles will likely give a higher contribution to lift, although at the expense of take-off efficiency.

Therefore, the following chapter aims at estimating vortex lift on the HTC5 blade. Then, the objective will be to vary the blade geometry and functioning parameters, in order to determine the cost for vortex lift increase at take-off, and investigate if this would be of interest for aircraft engine propeller blades.

5

Estimation of vortex lift on the HTC5 blade

The aim of this chapter is to estimate the impact that the leading-edge vortex has on the lift of the HTC5 blade.

The panorama of the literature presented in section 1.1.2 indicates that the concept of vortex lift is not at all easy to define. Moreover, the methods existing in the literature were validated only for specific fixed wing geometries: slender Delta wings and derivatives, and thin rectangular wings. Those methods relied either on the slender wing assumption, or on the calculation of whole wing polars. Some authors state that vortex lift can be detected when the $CL(\alpha)$ polar ceases to be linear. However, in this work it was decided not to base vortex lift detection on the $CL(\alpha)$ polar of the fixed model blade, because variations in incidence on the fixed model blade would not have any physical meaning regarding the parallel with the rotating case. The remaining options to evaluate vortex lift consisted either in the study of the wall pressure distribution, or the use of a modelling approach. Those approaches will be covered respectively in the present chapter and chapter 6.

The study of the wall pressure distribution on the wing surface seems to be a relevant way to start investigating vortex lift, because the leading-edge vortex corresponds to a zone of enhanced depression (see figure 0.3 or figure 1.10). In this chapter, the idea is to highlight the presence of vortex lift, and attempt at evaluating its magnitude, directly through an analysis of fully turbulent RANS results, which were shown in chapter 4 to be reliable as far as the LEV characteristic dimensions are concerned.

First, an analysis of the wall pressure distribution on Delta wings will be presented. This leads to the method used to estimate vortex lift, which will be evaluated on Delta wings as a reference case. Finally, the vortex lift contribution on the HTC5 blade at take-off will be investigated using this tool.

5.1. Analysis of the wall pressure distribution on Delta wings

This section shows how the RANS pressure coefficients contours relate to the position of the LEV on the example of the Delta wing.

5.1.1. RANS calculation setup

The Delta wing geometry is build using NACA0006 profiles stacked on the trailing edge, with the appropriate chord law. NACA0006 profiles are chosen because they are thin and symmetric, in order to come closer to the flat plate hypothesis of [Polhamus, 1966]. In addition, those were the thinner profiles for which a detailed polar was available. The skin mesh can be visualised in figure 5.1. Half of the Delta wing is represented, the other half of the domain being accounted for by a symmetry condition. The computational domain is an extension of the skin mesh along the normals to the surface. Its radius extends to 20 times the maximal chord of the Delta wing. On the outer surfaces of the computational domain, far field boundary conditions are applied.

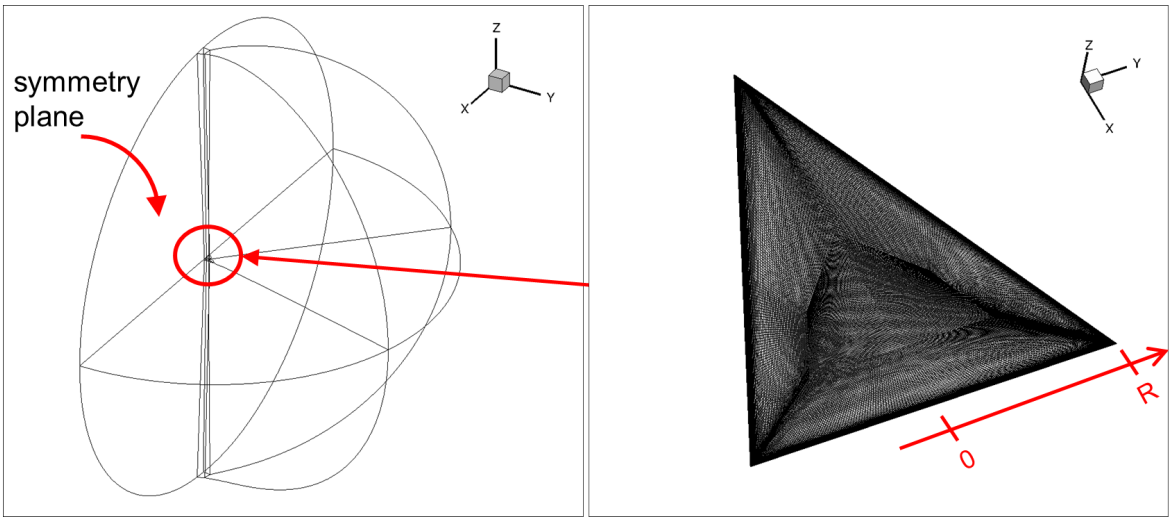

Figure 5.1. *Computational domain (left) and skin mesh (right) used for Delta wing calculations*

5.1.2. Extraction of pressure coefficient contours

The pressure field is extracted at the mesh nodes and interpolated on prescribed spanwise sections along the wing. The pressure coefficient Cp are calculated as such :

$$Cp = \frac{p - p_{inf}}{\frac{1}{2}\rho_{inf} W_{inf}^2}$$

where p_{inf}, ρ_{inf} are static pressure and density in the upstream (prescribed in the calculation) and $W_{inf}^2 = U_{inf}^2 + (\Omega r)^2$ is the relative incoming velocity at each spanwise position r.

In the following, the Cp profiles will be non-dimensionalised by the local chord so that each profile is drawn for $\bar{x} = \frac{x}{c(r)} \in [0, 1]$. To simplify further analysis, the Cp profiles were again interpolated on the same regularly spaced chordwise distribution, with 1000 points on the suction and pressure sides.

5.1.3. Link to leading-edge vortex position

Examples of pressure coefficient distributions from the RANS calculations described in section 5.1.1 are provided on Figure 5.8 for a Delta wing of 65 degrees sweep at 20 degrees angle of attack. The spanwise variation of the Cp profiles is presented on three graphs, spanning the wing from the central plane to the tip. The Cp profiles are represented by a line of the same colour on the picture of the blade with the friction lines and the friction vector norm distribution.

The suction side Cp profiles exhibit a bump which coincides with the position of the leading-edge vortex core. As the LEV moves towards the trailing edge and impacts more of the surface, the bump on the Cp profiles moves towards the trailing edge and is less peaked, with a lower maximal value. When the secondary leading-edge vortex is formed, a secondary bump, smaller in size, appears on the Cp profiles.

5.2. Development of a vortex lift estimation tool based on the wall pressure distribution

The aim of this section is to highlight the presence of vortex lift, and attempt at evaluating its magnitude, directly through an analysis of the RANS wall pressure distribution. As the bump on the Cp profiles is correlated to the position of the leading-edge vortex, a first assumption to evaluate vortex lift can consist in calculating the bump area. Indeed, without the leading-edge vortex, the Cp profiles on those lowly cambered airfoils would likely decrease monotonously between the leading-edge and the trailing-edge.

In order to detect the inflexion points surrounding the bump (A and B in figure 5.2), the suction side Cp profiles are fitted with a piecewise linear function f_{pw} in n pieces (n=4 or 6 depending on the case) using the least squares method (green curve on figure 5.2). Different values of the initial guess for the least squares optimisation are taken depending on the spanwise position.

Once the list of fitting points is found $(\bar{x}_i, \bar{y}_i)$, $i \in [1, n], \bar{x}_i < \bar{x}_{i+1}$, the fitting point with the maximal absolute value $(\bar{x}_{max}, \bar{y}_{max})$ is detected. Points A and B are defined as the surrounding points:

$$\bar{x}_A = \max(\max_{\bar{x}<\bar{x}_{max-1}} \bar{x}\,,\,0\,) \quad , \quad \bar{y}_A = Cp(\bar{x}_A)$$

$$\bar{x}_B = \min(\max_{\bar{x}_{max}<\bar{x}<\bar{x}_{max+1}} \bar{x}\,,\,1\,) \quad , \quad \bar{y}_B = Cp(\bar{x}_B)$$

Knowing the inflexion points, a "baseline" Cp profile Cp_{base} is defined, replacing the curve between A and B by a straight line (see red curve in figure 5.2). This choice for the baseline will be discussed in the following.

In the case of secondary vortices leading to several bumps, a slightly different procedure is adopted. The local maxima in absolute value of the Cp profile are detected and added to the list of fitting points. The "baseline" Cp profile is defined in a similar way as previously, by interpolating linearly in between surrounding points. The surrounding points are defined using a convexity criterion, as the points surrounding a convex portion of the Cp profile.

At each spanwise position, the difference between the Cp profile and the baseline profile is integrated, and multiplied by the local chord. This yields a spanwise "bump" lift coefficient

distribution $CL_{bump}(r)$.

$$CL_{bump}(r) = \int_{\bar{x}=0}^{1} \min(\,0\,,\,[\,Cp(\bar{x},r) - Cp_{base}(\bar{x},r)\,]\,)d\bar{x}$$

From this, we can calculate the contribution of the "bump" to total lift:

$$\frac{L_{bump}}{L_{tot}} = \frac{\int_r \frac{1}{2}\ \rho\ U_{inf}^2\ c(r)\, CL_{bump}(r)\ dr}{L_{tot}}$$

L_{tot} (and subsequently all integrated forces) is calculated by integrating the pressure field along the wing surface S_{wing}, considering the friction losses:

$$L_{tot} = \int_{S_{wing}} (p\,\vec{n} + \vec{f_v})\, dS_{wing} \cdot \vec{e_y}$$

where $\vec{f_v}$ is the friction vector. As can be verified in figure 5.3 or figure 5.4, the friction vector norm is negligible compared to the pressure field, which is in the order of $10^5\ Pa$ in the cases considered here.

For rotating cases, a specific feature is added in order to project the vortex contribution to lift on the thrust and torque directions. For this purpose, the components of the normal to the airfoil in each direction n_x, n_y, n_z are extracted on the same planes, and interpolated in the same way as the pressure coefficient profiles. This enables to project the pressure coefficient $Cp(\bar{x},r)$ values on the directions corresponding to the thrust and torque. For instance, the "bump" thrust coefficient τ_{bump} is expressed as:

$$\tau_{bump}(r) = \int_{\bar{x}=0}^{1} \min(\,0\,,\,[\,Cp(\bar{x},r) - Cp_{base}(\bar{x},r)\,]\,)\,\vec{n}(\bar{x},r) \cdot \vec{e_x}\, d\bar{x}$$

where $\vec{n}(\bar{x},r)$ is the normal to the suction side of the profile at spanwise position r and chordwise position $\bar{x}$.

At some spanwise stations, the detection of the inflexion points does not work properly, for instance due to a discontinuous f_{pw}. As a consequence, the profiles are filtered several times:

- suppression of zero values
- smoothing using a moving average on 2 points
- keeping local maxima of the spanwise vortex lift distribution

5.3. Comparative evaluation of the method in the case of Delta wings

The objective of this part is to examine if the "bump" contribution is a reliable estimation of vortex lift. For this purpose, the method described in section 5.2 is evaluated in the case of Delta wings, as it is one of the few cases where vortex lift has been modelled or quantified in the literature, using various approaches.

The literature survey in part 1.1.2 highlighted two main approaches for the definition of vortex lift. The first approach [Legendre, 1952, Brown and Michael, 1954, Brown and Michael, 1955,

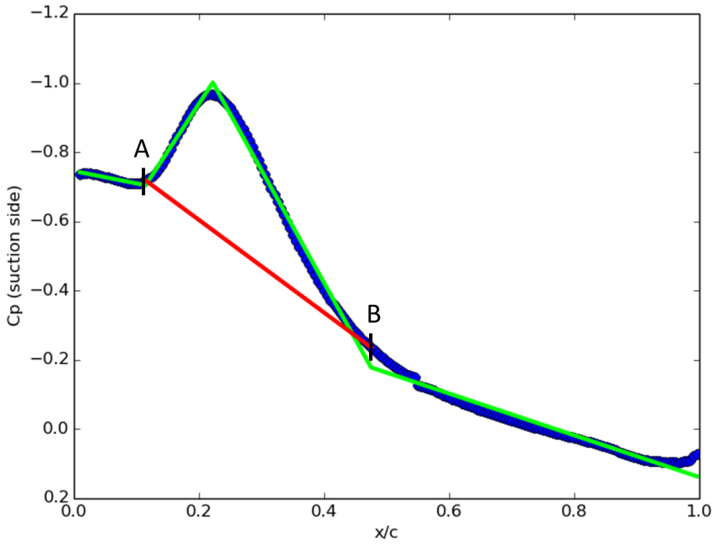

Figure 5.2. *Examples of pressure coefficient profiles (blue circles) with piecewise linear function fit (green) and baseline profile (red)*

Mangler and Smith, 1959] regards vortex lift as an addition to the potential flow solution around the wing and solves the problem analytically in 2D using the slender wing assumption. The second approach is the Polhamus approach [Polhamus, 1966], which states that vortex lift corresponds to the leading-edge suction force oriented normal to the suction side.

The decomposition between vortex lift and "non-vortex" lift provided by the first approach is interesting because it mirrors the concept that vortex lift is added on top of a baseline. This baseline is the potential solution for the attached flow around the wing. In previous work, the authors had to resort to the slender wing assumption in order to deduce an analytical solution of the potential flow around the wing plus the line vortex model. Here, the same reasoning is applied, except that the slender wing assumption is not needed. Indeed, the baseline will be evaluated thanks to potential calculations using the lifting surface method, and vortex lift is defined as the difference between the lift obtained from potential calculations and that obtained with RANS calculations.

Lifting surface potential calculations are a relevant "baseline" because they provide a solution with no trace of vortex lift. Potential theory is namely an inviscid theory, unable to capture flow separation, which gives the aerodynamic loading under the constraint of a fully attached flow. Moreover, the lifting surface method was chosen for its ability to take into account induced effects caused by the finite wing geometry in very low aspect ratio cases (which the lifting-line methods cannot perform). Because several variations of the lifting surface method exist, it is worth mentioning that the lifting surface potential calculations are carried out hereafter using TAGAZOU, the ONERA/ACI in-house software. As presented in chapter 2, this code is based on the wing skeleton and does not take the airfoil thickness into account. It consists in meshing the wing skeleton by an array of line vortices, whose circulation must be determined in order to verify tangency constraints at the wing surface. Again, the interest of this code is that it does not allow for the possibility of flow separation.

Another option could have been to run Euler calculations with elsA (ONERA finite volume

solver). Those simulations would also neglect viscosity, though Euler calculations are different from potential calculations in the sense that there is no irrotationality assumption. However, this option was discarded because the simulations would not converge in highly non-linear physical cases.

On the other hand, the Polhamus theory also provides an interesting basis for comparison, because the leading-edge suction analogy applies quite generally to slender Delta wings of high sweep.

The ratio of vortex lift (or CFD "bump" lift) with respect to total lift for several models is displayed in Table 5.1, in the case of a 65 degrees swept Delta wing at several incidences. This case was chosen because the Polhamus approach is reliable from 65 degrees of sweep. Vortex lift is evaluated from the following models:

from pressure distribution obtained in RANS calculations : application of the method described in section 5.2.

from potential calculations : $\frac{L_p - L_{tot,CFD}}{L_{tot,CFD}}$ where L_p is the lift obtained by potential calculations, and $L_{tot,CFD}$ the lift obtained using RANS calculations. L_p is calculated from the dimensionless spanwise circulation distribution given by TAGAZOU $\bar{\Gamma}(r)$ using the Kutta-Joukowsky formula $L_p = \int_r \bar{\Gamma}(r)\, c_{ref}\, \rho_{inf}\, U_{inf}^2$.

from the Polhamus theory : $\frac{Kv\, cos(\alpha)\, sin^2(\alpha)}{Kp\, cos^2(\alpha)\, sin(\alpha) + Kv\, cos(\alpha)\, sin^2(\alpha)}$, where Kp and Kv are the Polhamus coefficients, and α is the wing incidence.

Table 5.1 shows that the vortex contribution to lift increases with the angle of attack, for all the tested methods. The CFD and potential methods give lower results compared to the Polhamus method. Indeed, the "potential lift" as defined by Polhamus is, by definition, lower than the result of a potential calculation.

Incidence (degrees)	CFD Cp distribution (%)	Potential (%)	Polhamus (%)
10	4.3	6.0	21.0
15	9.6	10.6	28.8
20	11.2	14.8	35.5
25	12.2	15.1	41.3

Table 5.1. *Ratio of vortex lift to total lift in % for a 65 degrees swept Delta wing.*

This is illustrated by the reasoning below. Let us consider a Delta wing of sweep angle ϕ at an incidence α_* corresponding to the onset of flow separation at the leading-edge and vortex lift generation. For $\alpha = \alpha_*$, the potential lift according to Polhamus would be :

$$L_{pot}(\alpha = \alpha_*) = Kp\, cos^2(\alpha - \alpha_0)\, sin(\alpha - \alpha_0)\, \frac{1}{2}\rho_\infty U_{\inf}^2 S$$

where S is the Delta wing surface, $K_p = \frac{\partial CL_{tot}}{\partial \alpha})_{\alpha=\alpha_0}$ is the Polhamus coefficient for the corresponding Delta wing sweep, and α_0 is the zero lift incidence. For α slightly lower than α_*, the lift is fully potential and would amount to

$$L_{pot}(\alpha < \alpha_*) = CL_{tot}(\alpha)\frac{1}{2}\rho_\infty U_{\inf}^2 S$$

As the flow is still attached in this case, the incidence α can be assumed to be close to α_0. Within the limits of thin airfoil assumption, $CL_{tot}(\alpha)$ would be linear for α close to α_0. Thus, given the definition of Kp, the previous expression for the potential lift can be written as:

$$L_{pot}(\alpha < \alpha_*) = Kp(\alpha - \alpha_0)\,\frac{1}{2}\rho_\infty U_{\text{inf}}^2 S$$

If $\alpha - \alpha_0$ is small, the ratio between the potential lifts just before and after flow separation would be:

$$\frac{L_{pot}(\alpha = \alpha_*)}{L_{pot}(\alpha < \alpha_*)} \approx cos^2(\alpha - \alpha_0)$$

This reasoning indicates that potential contribution to lift according to Polhamus is lower compared to the result of a potential calculation. This is coherent with the higher values of vortex lift contribution found for the Polhamus method in Table 5.1. Also, it is worth noticing that the potential contribution to lift is discontinuous at $\alpha = \alpha_*$. Indeed, the leading-edge suction analogy induces a sudden change in the physical description of the phenomena, because the leading-edge suction force turns normal to the profile when flow separation occurs at the leading-edge.

The ratios in Table 5.1 obtained from the RANS calculations and the potential calculations are comparable. This indicates that the extraction of the "bump" on the Kp profiles using a "linear baseline" approximation is coherent from a physical point of view.

The spanwise distributions for those two cases are plotted in figure 5.3. The CFD RANS $\frac{dL}{dr}$ distribution is represented in blue, while the distribution obtained after the removal of the bump, called sectional baseline in the following, is displayed in dashed red. The potential calculation distribution is in green. Although the integrated vortex lift contributions were quite close in Table 5.1, the spanwise distributions of the potential calculation and the sectional baseline exhibit some differences. Up to 0.8R, the red curve is mostly on top of the green curve representing potential calculation data. However, this is partly compensated by the over-estimation of the lift distribution close to the tip for the potential calculations. The specific shape of the CFD spanwise lift distribution will be further discussed in chapter 6.

5.4. Application to the HTC5 fixed blade

The method described in part 5.2 is now applied on the HTC5 fixed blade case.

5.4.1. Analysis of pressure coefficient profiles

For this purpose, the RANS calculation described in section 4.3 is post-processed, and the corresponding pressure coefficient contours are displayed in figure 5.9. The spanwise variation of the Cp profiles is presented on four graphs, spanning the blade from foot to tip. For the sake of comparison, the apex Cp profile is pictured on all graphs. The Cp profiles are represented by a line of the same colour on the picture of the blade with the friction lines and the friction vector norm distribution.

The foot pressure coefficient contours are quite flat close to the leading-edge (1). Going up the span, the leading-edge suction peak becomes visible (2). After the apex, the base of the

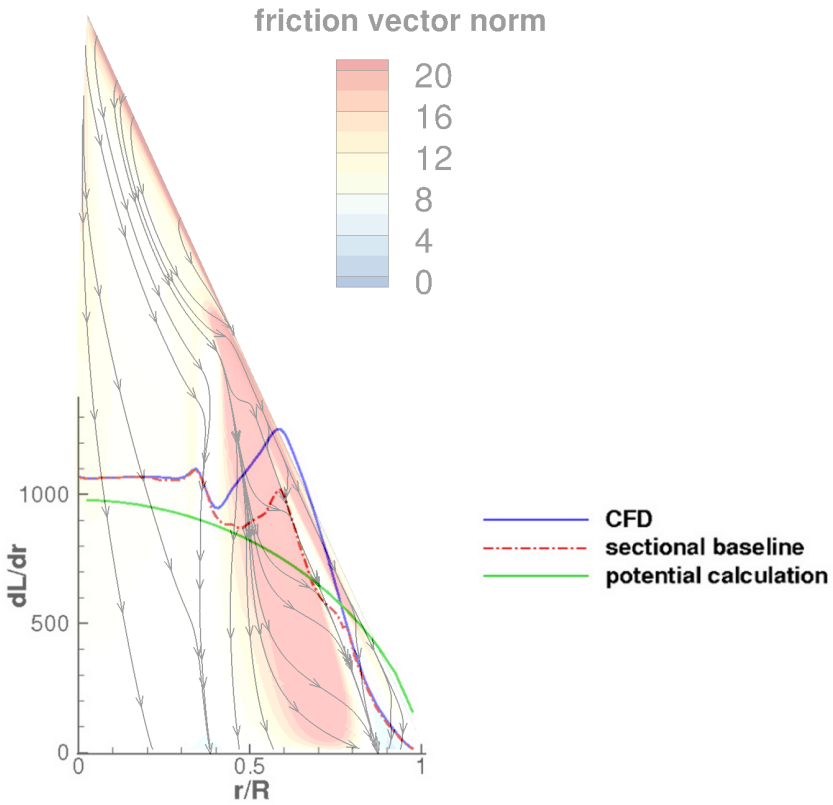

Figure 5.3. *Spanwise distribution of lift $\frac{dL}{dr}$ (in N/m) for a Delta wing of 65 degrees sweep at an incidence of 15 degrees, with superposed wall friction vector norm distribution*

peak gets larger and larger (3), then it "detaches" from the leading-edge (4). As it moves towards the trailing edge, the peak spreads and the maximal Cp value gets smaller. It is worth noticing that the higher pressure coefficients close to the leading-edge are associated to a slight decrease in pressure coefficient on the rest of the airfoil. As the leading-edge vortex approaches the blade tip, it migrates towards the trailing edge. The bump on the pressure coefficient thus extends towards the trailing edge until it influences most of the airfoil (4).

5.4.2. Estimation of vortex lift

The spanwise distribution of lift in the case of the HTC5 fixed blade is illustrated in figure 5.4. The total $\frac{dL}{dr}$ distribution is displayed in blue, while the dashed red line represents the sectional baseline. Figure 5.4 clearly shows that the bump contribution to lift increases as the LEV gets bigger and influences more of the surface. It starts to decrease when the LEV reaches the trailing edge. The spanwise integration of the bump contribution to lift amounts to 5% of the lift created by the blade.

In the case of the HTC5 fixed blade, only potential calculations can serve as a means of

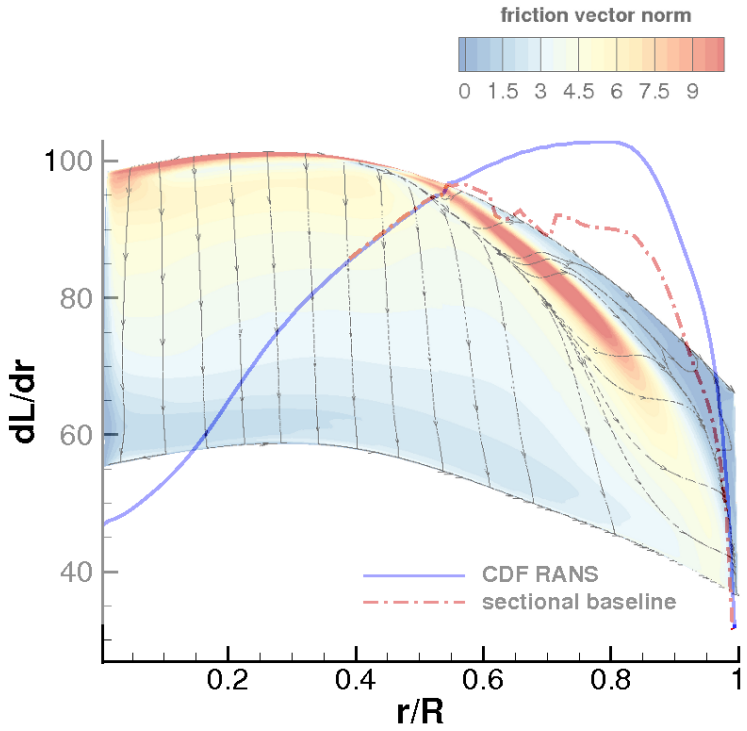

Figure 5.4. *Spanwise lift distribution $\frac{dL}{dr}$ (in N/m) including sectional baseline. The friction vector norm distribution and friction lines on the fixed blade are displayed in the background. The difference between red and blue lines represents the bump contribution.*

comparison, as the Polhamus theory is not directly applicable. A potential calculation was run with the TAGAZOU software. The fixed blade skeleton was deduced from the CAO. A symmetry condition at the fixed blade foot was applied to account for the wall window which is present in the RANS calculation. The comparison is displayed in figure 5.5 in terms of $\frac{dL}{dr}$.

The green line representing the spanwise potential distribution of $\frac{dL}{dr}$ is largely under the red line, which is the spanwise distribution after bump removal. The ratio of total lift in the potential calculation with respect to total lift in the CFD RANS calculation is equal to 74%.

The main difference between the green and blue curves is that the attached circulation (corresponding to the foot value of the circulation) is clearly lower in the potential calculation compared to the CFD. A possible explanation is that the potential calculation on the skeleton is not representative because the foot profiles of the HTC5 blade are too thick. Figure A.2, in appendix A, contains the spanwise form laws of the fixed HTC5 blade. Although the relative thickness of the HTC5 blade profiles is under 6% of the chord (which is the relative thickness used in the previous Delta wing calculations) on a large portion of the span (from 20% of the span up to the tip), the foot profile is 11.5% thick in order to provide sufficient lift (and thrust) in those low relative velocity zones close to the rotation axis.

In order to evaluate how airfoil thickness and symmetry impact the spanwise lift distribution, a RANS calculation of the fixed HTC5 blade with NACA0006 profiles was performed, at the same incidence $\alpha = -2.1$ degrees, and submitted to the same inflow velocity as the previous cases. All profiles of the HTC5 blade were namely replaced by NACA0006 profiles. Being thin and symmetric, the NACA0006 profiles enable to come closer to the description of the HTC5

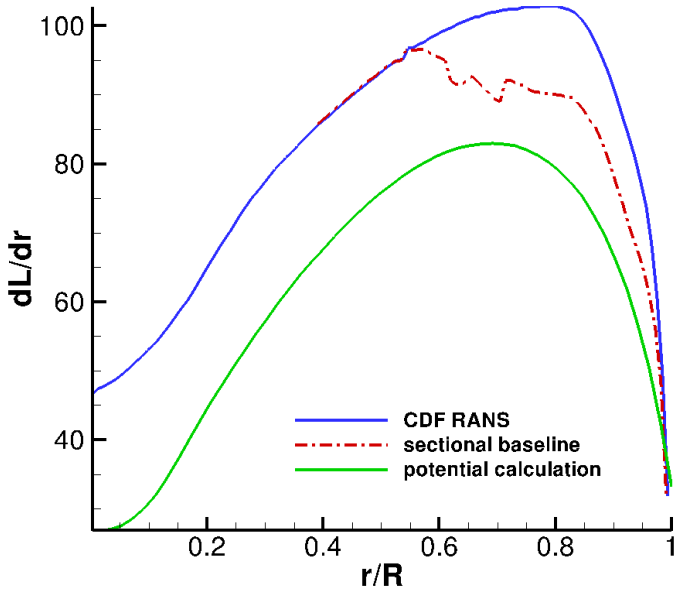

Figure 5.5. *Comparison of spanwise lift distribution $\frac{dL}{dr}$ (in N/m) on the HTC5 fixed blade, from potential calculations with lifting surface method and RANS calculations.*

blade skeleton. The blade mesh (in figure 5.6a) is embedded in a cubic computational grid (in figure 5.6b) with farfield boundary conditions on all sides except the one adjacent to the blade foot, where an inviscid wall boundary condition is imposed (in light blue in figure 5.6b). Indeed, the wall boundary condition on the blade foot is essential to accurately predict the foot circulation. The boundaries of the computational domain are spaced out from the blade by 10 times the span dimension in all directions. Classical wall boundary conditions (viscous) are applied on the blade surface. $y+$ is below one in the blade mesh.

The resulting spanwise lift distribution $\frac{dL}{dr}$ is plotted in orange on top of the previous ones in figure 5.7. It appears to be well below the levels of the blue curve, representing the RANS lift distribution on the "real" HTC5 fixed blade. This shows that the gap observed between CFD and potential calculation (green curve) is largely due to the the fact that airfoil thickness and camber are not taken into account in the potential calculation. Therefore, the potential calculation on the skeleton cannot be used as a baseline to evaluate vortex lift in the HTC5 case.

Moreover, the orange curve (RANS calculation on the HTC5 blade with NACA0006 profiles) is always on top of the green one (potential calculation), while their slopes are very similar, and their maximum attained at the same spanwise position. The slope similarity obviously owes to the similar blade geometries considered. However, this is also due to the fact that, even though the RANS calculation allows flow separation, the leading-edge vortex does not form of the HTC5 blade with NACA0006 profiles (as indicated by wall friction lines). In order to be representative of the skeleton of the fixed blade, the calculation with NACA0006 profiles was performed at the same incidence as the HTC5 fixed blade. From 20% of the span onwards, the relative thickness of the HTC5 profiles is below 6% (see figure A.2b in appendix A). Therefore, given the low incidences of the blade profiles, replacing them by thicker NACA0006

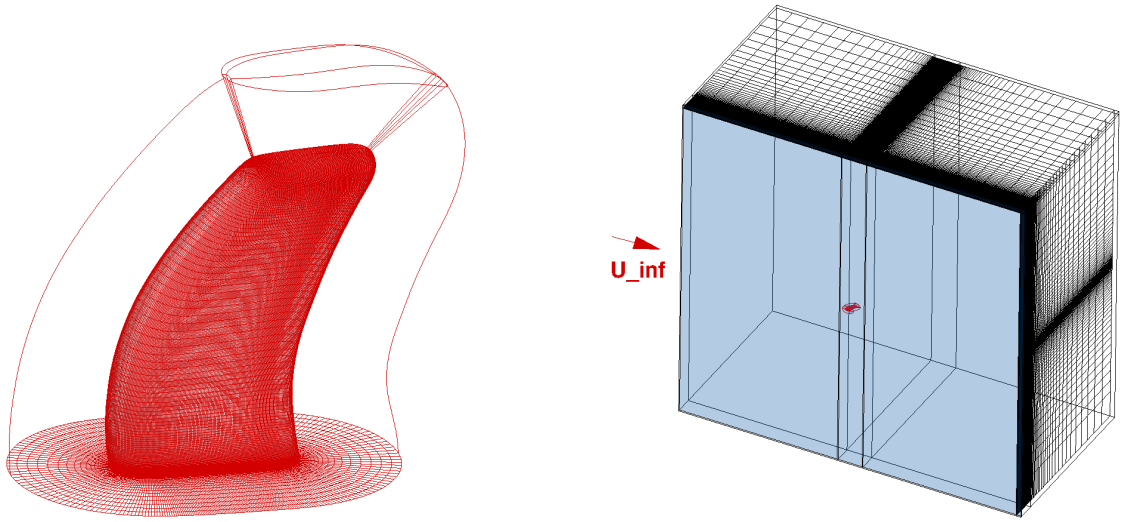

(a) Blade mesh (b) Computational domain

Figure 5.6. *Blade mesh and computational domain used for the RANS calculation of the fixed HTC5 blade with NACA0006 profiles. The blue surface represents the face with the invsicid wall boundary condition.*

may prevent flow separation. The discrepancy between the orange and green curves is likely caused by the relative thickness difference. In order to support this argument, the spanwise discrepancy between the two curves expressed in percentage of $\frac{dL_{CFD,NACA0006}}{dr}$ is compared to the difference in percentage between lift coefficients for a NACA0006 airfoil and a flat plate in the thin airfoil theory (equal to $2\pi\alpha$). Both are comparable, in the order of 5 to 10% along most the span.

In summary, the estimation of vortex lift on the HTC5 fixed blade to 5% of total lift is supported by the relevance of the vortex lift estimation method in the case of Delta wings, compared to other approaches. However it is difficult to provide means of comparison for the vortex lift contribution on the HTC5 fixed blade. Nevertheless, it is clear that the main interest of the vortex lift estimation approach proposed in this chapter is to compare vortex lift contributions obtained for different cases. Therefore it is legitimate to use the estimation method developed in this chapter for the sake of comparative studies.

5.5. Summary

To conclude, a method was proposed to deduce the vortex contribution to lift from RANS wall pressure distributions.

This method gives a satisfying evaluation of vortex lift in the case of Delta wings, which is close to the difference between the total lift in the RANS simulation and that in a potential calculation. Thus, this method seems to be physically grounded. The main advantage of this approach is that it can be used in comparative numerical studies, to determine the impact of a given parameter on vortex lift, such as will be performed in chapter 7.

The vortex lift estimation procedure was applied to the HTC5 fixed blade, and led to a vortex lift contribution in the order of 5% of total lift. The difficulty of providing relevant means of comparisons was discussed. The approach presented in this chapter enables to conclude that

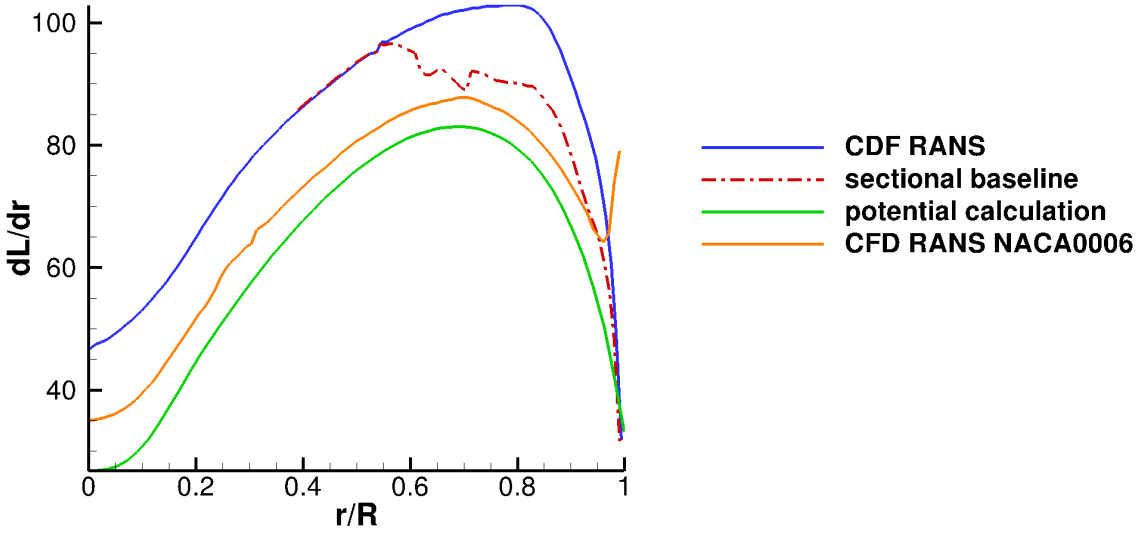

Figure 5.7. *Comparison of spanwise lift distribution $\frac{dL}{dr}$ (in N/m) on the HTC5 fixed blade, from potential calculations with lifting surface method, RANS calculations on the HTC5 fixed blade, RANS calculations on the HTC5 fixed blade with NACA0006 profiles.*

the LEV on the HTC5 blade produces vortex lift. It provides at least a lower bound of the vortex contribution to lift. More importantly, as was foreseen at the end of chapter 4, this chapter enables to confirm that the LEV contribution to lift on the HTC5 fixed blade is quite low (5%), when compared to that of Delta wing LEVs obtained with the same method (see Table 5.1).

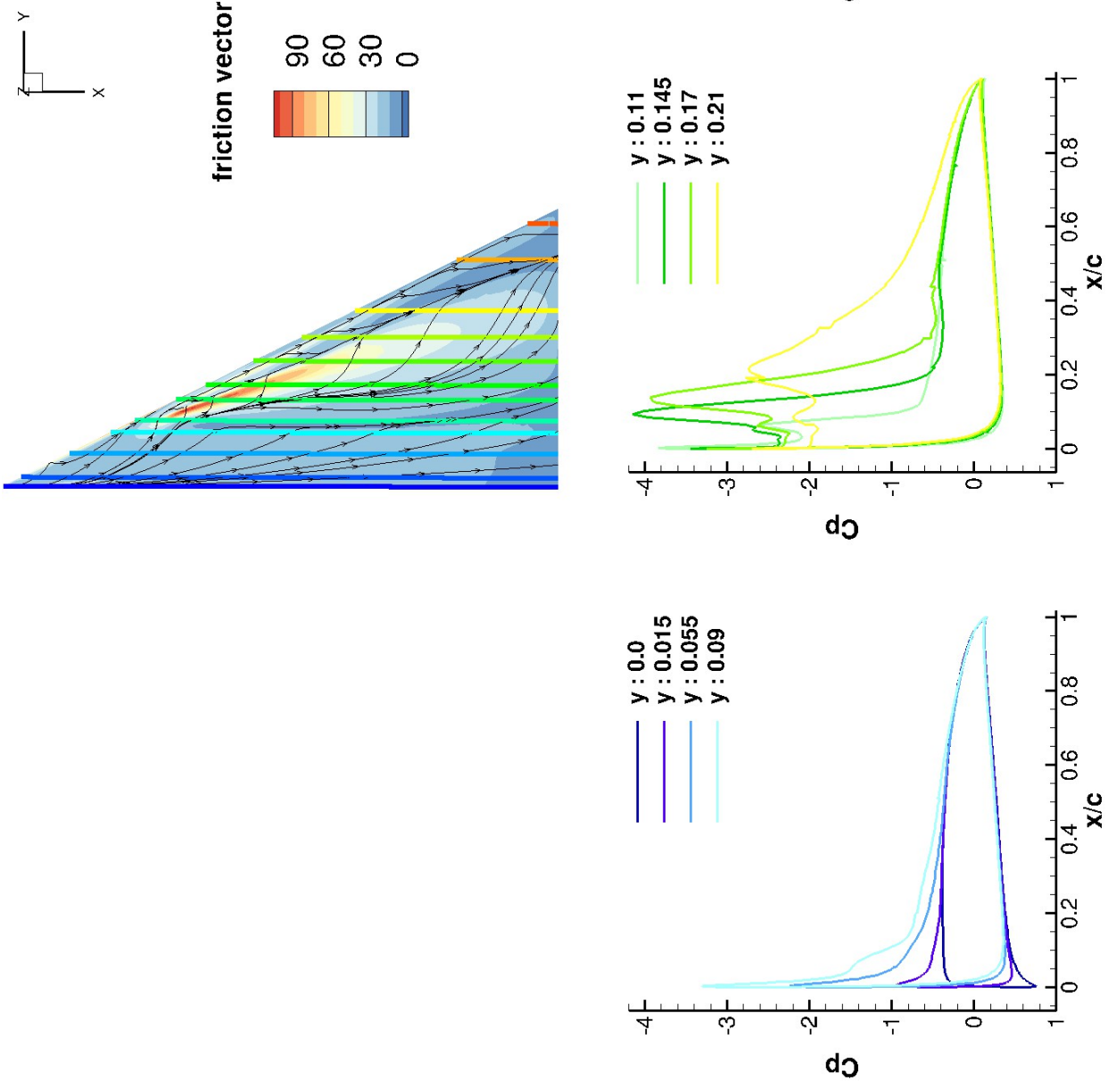

Figure 5.8. *Cp profiles extracted on a Delta wing of 65 degrees sweep at an incidence of 20 degrees.*

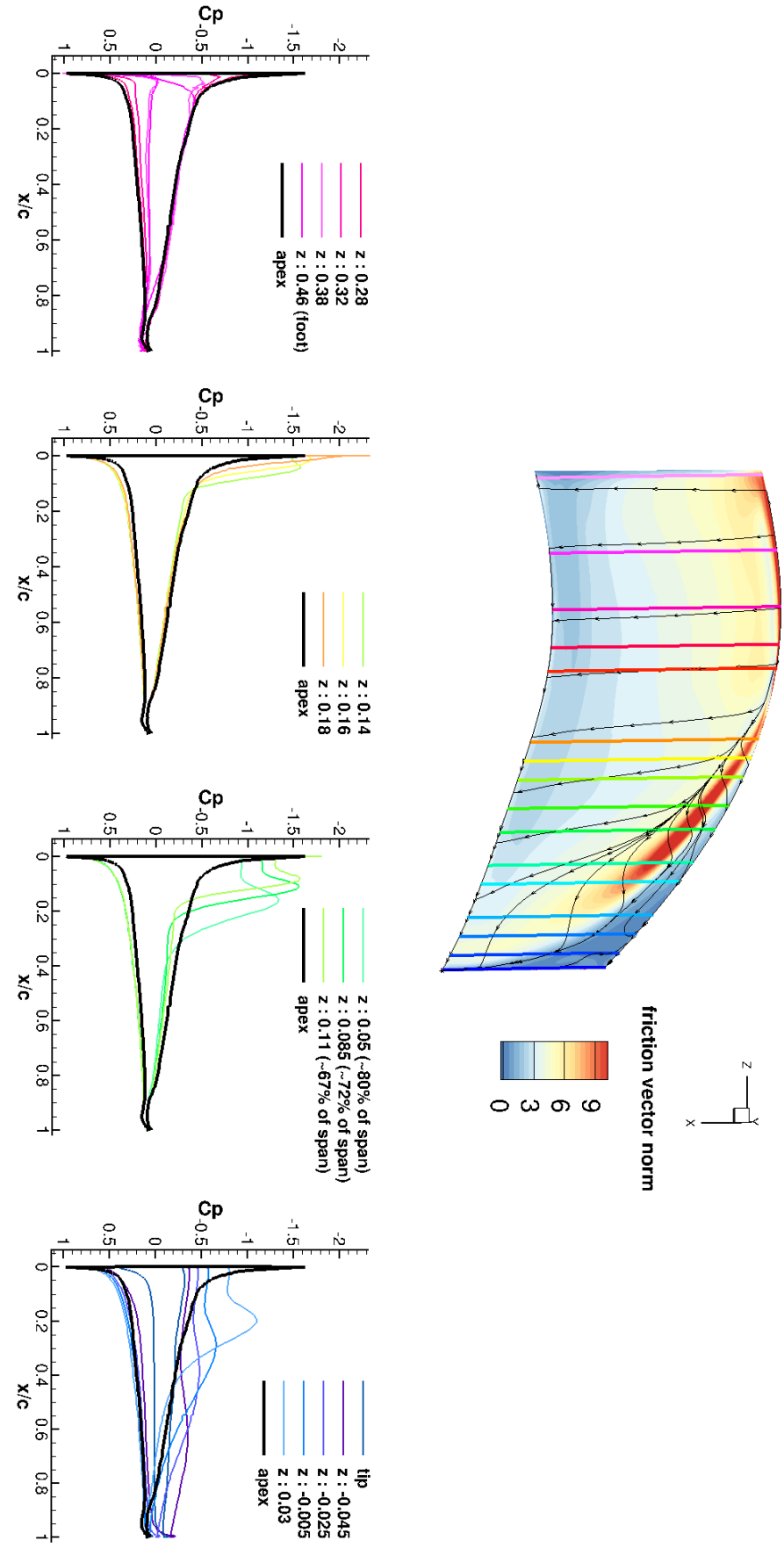

Figure 5.9. *Cp profiles extracted on the HTC5 fixed blade.*

6

Development of a 1D vortex lift model

In chapter 5, the leading-edge vortex on the HTC5 model blade was shown to generate vortex lift, using an approach relying on the post-processing of RANS results and the comparison with potential calculations. The present chapter focuses on developing a 1D (spanwise) vortex lift model, which could be easily compatible with fast 1D load calculation methods such as the BEMT or the lifting line method. The modelled vortex lift distribution would depend on spanwise distributions of geometrical parameters, such as sweep, chord, twist, relative thickness and the type of airfoil. The initial idea was indeed to include this model in a fast load calculation tool, in order to perform parametric studies for various geometries and operating conditions, taking into account vortex lift.

The vortex lift modelling approach is based on two starting points.

The first one is the Polhamus modelling approach. As explained in section 1.1.2, this is the most predictive approach existing in the literature, and it is easy to implement as well. However, the Polhamus model needs to be extended to wing geometries other than Delta wings of sweep $\phi \geq 65$ degrees, Delta wing derivatives, and rectangular wings. Also, it does not provide the spanwise lift distribution, but only an integrated value. Finally, this model relies on tabulated coefficients $Kp = \frac{\partial CL_{tot}}{\partial \alpha}\Big)_{\alpha=0}$ and $Kv = \frac{Kp - Kp^2 Ki}{cos\phi}$ where $Ki = \frac{\partial^2 CD_{i,tot}}{\partial CL^2}\Big)_{\alpha=0}$, which are deduced from whole wing polars around the zero lift incidence α_0.

Therefore, in order to build a 1D vortex lift model, the first idea consisted in developing a 1D formulation of Polhamus' model. For this purpose, the leading-edge suction analogy needed to be expressed into a "local" form, i.e. a form which would depend on the blade's characteristics at a given spanwise position. This implied in particular that a local form of the Polhamus coefficients Kp_{loc} and Kv_{loc} should be developed, which would depend on the airfoil polar instead of the whole wing polar.

The second starting point is the methodology developed in chapter 5, which gives access to spanwise vortex lift distributions. The spanwise evolution of vortex lift will be characterised on several cases to provide input for the spanwise vortex lift model.

The resulting 1D model will be evaluated on Delta wings of various sweeps ($20 \leq \phi \leq 90$ degrees), on the HTC5 fixed blade and on the rotating HTC5 in the configuration of a single propeller with 4 blades. This modelling effort enables to bring out the main physical mechanisms acting on LEV formation. In the following, the non-vortex part is referred to as "potential" part, using the vocabulary of [Polhamus, 1966]. By analogy, the sectional baseline issued from the algorithm developed in chapter 5 is also called "potential" part.

6.1. Development of a 1D formulation of the leading-edge suction analogy

The strategy adopted here to build a 1D model is to apply the leading-edge suction analogy at the level of the profile, i.e. at a given spanwise position r. This first implies to take into account the local incidence $\alpha(r)$ in the expressions of the lift coefficient, and the values of the Polhamus coefficients $Kp(r)$ and $Kv(r)$ corresponding to the local sweep angle $\phi(r)$:

$$CL(r) = CL_p(r) + CL_v(r) = Kp(r)\, cos^2\alpha(r)\, sin\,\alpha(r) + Kv(r)\, cos\,\alpha(r)\, sin^2\alpha(r) \tag{6.1}$$

In order to express the leading-edge suction analogy into a fully 1D form, the idea was that the Polhamus coefficients should not only depend on the local sweep, but also be based on the airfoil polar instead of the whole wing polar. Therefore, the aim of the following paragraph is to develop local expressions of the Polhamus coefficients, Kp_{loc} and Kv_{loc}, based on the airfoil polar.

6.1.1. Expression of Polhamus coefficients using the airfoil polar

Let us consider a finite wing before the onset of flow separation. In this configuration, the incidence α must be close enough to the zero-lift angle of attack α_0. For simplicity, we assume in the following that the airfoil is symmetric and that $\alpha_0 = 0$, without loss of generality. The attached flow hypothesis is not detrimental to finding Kp_{loc} and Kv_{loc}, as [Polhamus, 1966] showed that the values of Kp and Kv do not depend on the incidence. The strength of this model is namely that the loading under detached flow conditions can be deduced from attached flow conditions using the leading-edge suction analogy.

We consider the airfoil at a given position r along the span, with a local sweep $\phi(r)$, a local incidence $\alpha(r)$ and a chord $c(r)$, subject to the inflow relative velocity $W(r)$. In this section, all variables implicitly depend on r. In order to distinguish them from airfoil quantities, integrated or whole wing quantities will be referred to with the subscript tot.

6.1.1.1. Potential coefficient Kp_{loc}

We are looking for Kp_{loc} fulfilling a localised form of Polhamus' formula for lift. According to the Kutta-Joukowsky law, the lift on the airfoil at position r, dL verifies:

$$dL = \rho\,\Gamma\,W\,dr$$

where Γ is the profile circulation which according to the definition of Kp in [Polhamus, 1966] can be expressed as $\Gamma = \frac{1}{2}\,Kp_{loc}\,c\,W\,sin\alpha$. Therefore:

$$dL = \frac{1}{2}\rho\,Kp_{loc}\,W^2\,sin\alpha\,c\,dr \tag{6.2}$$

dL is expressed without the vortex lift term as we consider that the flow is attached.

Moreover, dL can be expressed using the airfoil's lift coefficient $CL_{airfoil}(\alpha, M)$:

$$dL = \frac{1}{2}\rho\,W^2\,cos^2\phi\,CL_{airfoil}(\alpha, M)\,c\,dr \tag{6.3}$$

Here, the lift is expressed using the inflow velocity corrected by the sweep $W cos\phi$. This expression implicitly assumes that most of the lift is created by the upstream portion of the chord, close to the leading-edge, and thus the "working part" of the swept wing can be viewed as a straight wing of higher aspect ratio in yawed inflow $W\,cos\phi$. This assumption is not valid for low aspect ratio wings, however it is used here for a 2D airfoil, considering that it is equivalent to an infinite wing with an extruded profile. Namely, the profile is considered to be independent from the other profiles (this assumption will be discussed in section 6.1.2).

After identification of equations 6.2 and 6.3 and simplification, we have :

$$Kp_{loc}\, sin\alpha = cos^2\phi\, CL_{airfoil}(\alpha, M)$$

Using a first order asymptotic expansion for the airfoil lift coefficient around α_0 reads :

$$CL_{airfoil}(\alpha, M) = \frac{\partial CL_{airfoil}(\alpha, M)}{\partial \alpha}\Big)_{\alpha_0} (\alpha - \alpha_0) + o(\alpha - \alpha_0)$$

Also, under the assumption that α is close to $\alpha_0 = 0$, $sin\alpha \approx \alpha$.

Finally we obtain :

$$\boxed{Kp_{loc} = cos^2\phi\, \frac{\partial CL_{airfoil}(\alpha, M)}{\partial \alpha}\Big)_{\alpha_0}} \tag{6.4}$$

6.1.1.2. Vortex lift coefficient Kv_{loc}

The identification of Kv_{loc} is achieved through the same kind of reasoning, considering the induced drag instead of the lift. The only source of drag on a finite wing in the potential flow formalism is the induced drag dDi.

dDi can be expressed using the profile circulation Γ as:

$$dDi = \rho \Gamma w_i dr$$

where w_i is the induced velocity at position r. On the other hand, the induced drag can be expressed using the induced drag coefficient CD_i :

$$dDi = \frac{1}{2}\rho W^2\, cos^2\phi\, CD_{i,airfoil}(\alpha, M)\, c\, dr$$

where $CD_{i,airfoil}$ is the induced drag coefficient at position r, which we denote by the subscript "airfoil" in order to differentiate it from the total induced drag coefficient integrated on the wing $CD_{i,tot}$. Identifying the two expressions for dDi reads :

$$\Gamma w_i = \frac{1}{2}\, W^2\, cos^2\phi\, CD_{i,airfoil}(\alpha, M)\, c$$

Using the expression for Γ used by Polhamus gives after further simplification :

$$Kp_{loc}\, sin\alpha\, w_i(r) = W\, cos^2\phi\, CD_{i,airfoil}(\alpha, M)$$

In analogy to [Polhamus, 1966], we introduce Ki_{loc}, such that $Kp_{loc} Ki_{loc} = \frac{w_i}{W\, sin\alpha}$:

$$Kp_{loc}^2\, Ki_{loc} = \frac{cos^2\phi}{sin^2\alpha}\, CD_{i,airfoil}(\alpha, M) \tag{6.5}$$

Under the same assumption as in section 6.1.1.1 that the behaviour of the 2D airfoil (infinite aspect ratio) can be assimilated at first order to that of a high aspect ratio wing, the induced drag coefficient is assumed to be proportional to CL^2. This result is valid for high aspect ratio wings with an arbitrary lift distribution, and demonstrated in [Anderson, 2007], from pages 335 to 338, using the lifting line theory and expressing the general circulation distribution as a Fourier series.

$$CD_{i,airfoil}(\alpha, M) = K\, CL^2_{airfoil}(\alpha, M) \tag{6.6}$$

with K a constant depending on the aspect ratio.

As the incidence α is assumed to be close to α_0, $CD_{i,airfoil}$ can be developed using the following Taylor expansion:

$$CD_{i,airfoil} = \frac{\partial CD_{i,airfoil}(\alpha, M)}{\partial \alpha}\Big)_{\alpha_0} (\alpha - \alpha_0) + CD_{i,airfoil}(\alpha_0) \; + \; o(\alpha - \alpha_0)$$

Moreover, $CD_{i,airfoil}(\alpha_0) = 0$ because for $\alpha = \alpha_0$, no lift is created, thus no tip vortices and no downwash generating induced drag. Considering $\alpha_0 = 0$ and expressing the partial difference term with $CL_{airfoil}$ gives:

$$CD_{i,airfoil} = \frac{\partial CD_{i,airfoil}(\alpha, M)}{\partial \alpha}\Big)_{\alpha_0} \alpha + o(\alpha) = 2K\, \frac{\partial CL_{airfoil}(\alpha, M)}{\partial \alpha}\Big)_{\alpha_0} CL_{airfoil}(\alpha, M)\, \alpha + o(\alpha)$$

Replacing $CL_{airfoil}(\alpha, M)$ by its Taylor expansion, we obtain at maximal order:

$$CD_{i,airfoil} = 2K \left(\frac{\partial CL_{airfoil}(\alpha, M)}{\partial \alpha}\Big)_{\alpha_0} \right)^2 \alpha^2 + \; o(\alpha^2)$$

Knowing that $Kp_{loc}(r) = cos^2\phi \, \frac{\partial CL_{airfoil}(\alpha, M)}{\partial \alpha}\Big)_{\alpha_0}$

$$CD_{i,airfoil} = 2K \left(\frac{Kp_{loc}}{cos^2\phi} \right)^2 \alpha^2 + \; o(\alpha^2)$$

Replacing $CD_{i,airfoil}$ in equation 6.5, and simplifying reads:

$$Ki_{loc} = \frac{2K}{cos^2\phi} \frac{\alpha^2}{sin^2(\alpha)}$$

Under the assumption that α is close to $\alpha_0 = 0$, $\frac{\alpha^2}{sin^2(\alpha)} \approx 1$. Finally, differentiating equation 6.6 two times gives :

$$\frac{\partial^2 CD_{i,airfoil}(\alpha, M)}{\partial CL^2_{airfoil}(\alpha, M)}\Big)_{\alpha_0} = 2K$$

Thus the local expression for Ki_{loc} is :

$$Ki_{loc} = \frac{1}{cos^2\phi} \frac{\partial^2 CD_{i,airfoil}(\alpha, M)}{\partial CL^2_{airfoil}(\alpha, M)}\Big)_{\alpha_0}$$

Around $\alpha = \alpha_0$, the drag coefficient can be expressed depending on the induced drag coefficient and on the profile drag coefficient at zero lift incidence $CD_{\alpha_0,airfoil}$ as:

$$CD_{airfoil} = CD_{i,airfoil} + CD_{\alpha_0,airfoil}$$

Therefore $\frac{\partial^2 CD_{i,airfoil}(\alpha,M)}{\partial CL^2_{airfoil}(\alpha,M)}\Big)_{\alpha_0}$ can be evaluated directly from the airfoil polar at position r as

$$\frac{\partial^2 CD_{i,airfoil}(\alpha,M)}{\partial CL^2_{airfoil}(\alpha,M)}\Big)_{\alpha_0} = \frac{\partial^2 CD_{airfoil}(\alpha,M)}{\partial CL^2_{airfoil}(\alpha,M)}\Big)_{\alpha_0}$$

Thus the local expression for Ki_{loc} can be simplified as :

$$\boxed{Ki_{loc} = \frac{1}{cos^2\phi}\frac{\partial^2 CD_{i,airfoil}(\alpha,M)}{\partial CL^2_{airfoil}(\alpha,M)}\Big)_{\alpha_0} = \frac{1}{cos^2\phi}\frac{\partial^2 CD_{airfoil}(\alpha,M)}{\partial CL^2_{airfoil}(\alpha,M)}\Big)_{\alpha_0}} \tag{6.7}$$

Kv_{loc} is deduced from Kp_{loc} and Ki_{loc} as:

$$\boxed{Kv_{loc} = \frac{Kp_{loc} - Kp^2_{loc}\,Ki_{loc}}{cos\phi}} \tag{6.8}$$

To conclude, in this section, local expressions of the Polhamus coefficients Kp_{loc} and Kv_{loc} were obtained depending on the polars of the airfoil at position r, around the zero lift incidence. It is worth noticing that the dependency to the local sweep angle $\phi(r)$ is explicit in those expressions.

Now that a formulation of the leading-edge suction analogy at the level of the airfoil is available, the next modelling step consists in accounting for three-dimensionality.

6.1.2. Building three-dimensionality

In the original Polhamus theory, three-dimensional effects are implicitly included in the original Kp and Kv, as they are deduced from whole wing polars. The reasoning of Polhamus is based on an equivalent profile of the Delta wing, whose circulation and induced drag depend respectively on Kp and Kv.

However, in the 1D formulation of the leading-edge suction analogy developed so far in part 6.1.1, no element is present to account for the three-dimensional behaviour of the leading-edge vortex. The reasoning relied extensively on the "2D" assumption on each profile, that is, the assumption that the profiles are independent. However, applying the expressions for Kp_{loc} and Kv_{loc} (equations 6.4 and 6.8) directly in a local version of the Polhamus formulas does not model the physical reality. For instance, let us evaluate equation 6.1 with the local formulations Kp_{loc} and Kv_{loc} replacing Kp and Kv along the span of a Delta wing. As the airfoil, incidence, and sweep angle are constant with respect to r, so are Kp_{loc} and Kv_{loc}, and the potential and vortex lift coefficients as well. The inflow velocity also being invariant along the span, the local lift would only depend on the chord variation. The ratio of vortex lift to potential lift would be constant along the span. However this is likely not the case. Indeed, given the conical form of the LEV, it is reasonable to assume that vortex contribution to lift will be lower on at spanwise positions where the LEV is still small, compared to more outward sections where it covers most of the chord. Thus, an alternative way is needed to account for three-dimensionality and model spanwise variations.

A first idea to account for three-dimensionality is to add extra degrees of freedom to the definition of $Kp_{loc}(r)$ and $Kv_{loc}(r)$. Therefore, cumulative factors $f_p(r)$ and $f_v(r)$ were added

to Polhamus' classical expressions as follows:

$$\boxed{\begin{aligned} CL_p(r) &= f_p(r)\, Kp_{loc}(r)\, cos^2\alpha(r)\, sin\,\alpha(r) \\ CL_v(r) &= f_v(r)\, Kv_{loc}(r)\, cos\,\alpha(r)\, sin^2\alpha(r) \end{aligned}} \tag{6.9}$$

where $f_v(r)$ can be interpreted as the percentage of the chord affected by the leading-edge vortex at position r.

In the following, the relevance of this formulation will be tested first on the Delta wing case. The main objectives are to determine the type of function of $f_p(r)$ and $f_v(r)$, and especially if they depend on the wing's geometric parameters (especially, on the sweep).

6.2. A first 1D model applicable to Delta wings

Knowing that the circulation of Delta wing leading-edge vortices increases linearly with span ([Renac, 2004]), a linear increase of $f_v(r)$ is tested at first approximation :

$$\boxed{f_v(r) = max(\,0\,,\, K\,\frac{r-r_0}{(R-r_0)^2}\,)\ ,\ K = 1.6} \tag{6.10}$$

where K is a constant, which will first be fitted based on comparisons with Delta wing cases, R is the Delta wing span, and r_0 the first detachment point along the span, which we assume for now to be the apex. The square at the denominator is added so that $\int_{r=0}^{R} \frac{r-r_0}{(R-r_0)^2}$ is of order one, which ensures that K is of order one.

On the other hand, we assume the potential contribution $CL_p(r)$ to gradually decrease with r. Indeed, when a LEV is formed, the leading-edge suction force turns and is counted as part of the vortex lift term. Thus, most of the lift created at the leading-edge is counted as vortex lift. The part corresponding to potential lift corresponds to the projection of the lift obtained in the attached case on the normal to the profile. This component being normal to the profile, its physical meaning lies in the pressure difference between the pressure and suction sides, leading-edge excluded. As the LEV impacts a greater part of the chord, the potential contribution (according to Polhamus' definition) should decrease. We assume at first approximation that $f_p(r)$ also has a linear spanwise evolution, but is decreasing along the span.

$$\boxed{f_p(r) = K' f_v(R-r)\ ,\ K' = 0.8} \tag{6.11}$$

In the following, the lift at a given position r, $dL(r)$ is evaluated independently from the other profiles:

$$dL(r) = \frac{1}{2}\,\rho W^2(r) CL(r) c(r) \tag{6.12}$$

where according to equation 6.9:

$$\begin{aligned} CL_(r) &= CL_p(r) + CL_v(r) \\ &= f_p(r)\, Kp_{loc}(r)\, cos^2\alpha(r)\, sin\alpha(r)\ +\ f_v(r)\, Kv_{loc}(r)\, cos\alpha(r)\, sin^2\alpha(r) \end{aligned} \tag{6.13}$$

This yields a spanwise lift distribution which can be integrated over the span to give the total lift, and in dimensionless form, yield the total lift coefficient:

$$L_{tot} = \int_r dL(r)dr$$

$$CL_{tot} = \int_r dCL(r)dr$$

6.2.1. Comparison of total lift coefficients

The total lift coefficient CL_{tot} given by the 1D model is evaluated with respect to experimental data from [Polhamus, 1966], the original Polhamus model, and CFD results, on Delta wings of various sweeps ($20 \leq \phi \leq 90$ degrees) and incidences ($\alpha = 5, 10, 15, 20, 25$ degrees).

The numerical results are obtained from RANS calculations with the same settings and parameters as described in section 5.1.1. The Delta wing is formed by stacked NACA0006 airfoils, in order to allow comparison with results from the 1D model. Indeed, the thinnest available NACA polar was that of the NACA0006 airfoil. The convergence of the calculations for $\phi \geq 40$ degrees was satisfying as the residuals decreased of at least 5 orders of magnitude. For $\phi = 30$ degrees, the convergence was more problematic. Indeed, all tested incidences correspond to a stalling configuration of the NACA006 airfoil, and the leading-edge vortex at this low sweep value was not strong enough to fully stabilise the flow. Therefore it was not possible to reach a steady RANS solution for all tested incidences with this sweep value. As the residuals' convergence was blocked, the results translated into oscillating aerodynamic forces. However in all cases, the average aerodynamic forces were converged, and the amplitude of the oscillations did not exceed 4% of the average value.

In the previous works of Polhamus, the global Kp and Kv coefficients were tabulated only for sweep values $\phi \geq 45$ degrees. In order to provide a comparison with the 1D model for lower sweeps, the Polhamus model was applied outside of the validity zone prescribed by Polhamus, which was limited to slender wings. In order to differentiate it from the original Polhamus model, the application of the Polhamus model for $\phi \leq 45$ degrees will be referred to as 0D model in the following. Therefore the Kp and Kv tables were extended to lower sweeps than those considered by Polhamus. For this purpose, RANS calculations of Delta wings with NACA0006 airfoils for sweeps $\phi = 10, 20, 30, 40$ degrees were performed at $\alpha = 0, 0.5, 1., 1.5$ degrees. At those small incidences, the convergence was satisfying for all cases (5 orders of magnitude decrease of the residuals). The symmetry assumption enabled to find a linear fit for $CL_{tot}(\alpha)$ and a quadratic fit for $CD_{i,tot}(CL_{tot})$ using seven fitting points. Euler calculations were carried out at first in order to take into account only induced drag $CD_{i,tot}$, thus guarantee the absence of viscous or friction drag. Nonetheless it was verified that Navier Stokes and Euler calculations led to the same value of $\frac{\partial^2 CD_{tot}}{\partial CL_{tot}^2}\Big)_{\alpha=0}$.

Figure 6.1 presents the variation of the total lift coefficient with respect to sweep, at incidences of 10, 15, 20 and 25 degrees. The black markers indicate the reference values, based either on the experimental results reported in [Polhamus, 1966], or on RANS results. The light red and light blue lines correspond respectively to the total lift coefficient CL_{tot} and its potential part, given by the application of the Polhamus model. The 0D model is represented by the dashed light red and light blue lines, in order to differentiate the sweep values lying outside of the validity zone initially prescribed by Polhamus (0D model). In the same manner, the red and blue dashed lines with markers respectively picture the total lift coefficient CL_{tot} and its potential part obtained with the 1D model.

First of all, we can notice that the reference experimental results of [Polhamus, 1966] and the reference RANS results are in good agreement. In addition, for $\phi \geq 65$ degrees, Polhamus predictions and experimental data are generally in very good agreement, for all tested incidences. As for the 1D model, it is also predictive in the high sweep range, regardless of the incidence. Finally it is particularly worth noticing that a single value of K and K' works for all tested incidences, in the high sweep range.

In the lower sweep range (for $\phi \leq 65$ degrees), the Polhamus model and its extension to ($\phi \leq 45$ degrees) overestimate total lift. This shows that the Polhamus model is not valid outside of the initial bounds tested by Polhamus. The predictions of the 1D model in the lower sweep range are more accurate for some values of the incidence. Yet more importantly, they feature a decrease in total lift which fits better to the RANS results and is physically more accurate than the 0D model at α =15, 20 and 25 degrees. Indeed, several authors [Hill, 1957, Wentz and Kohlman, 1971, Lee and Ho, 1990, Gursul et al., 2005] support that vortex contribution to lift would decrease with sweep (see part 1.1.2).

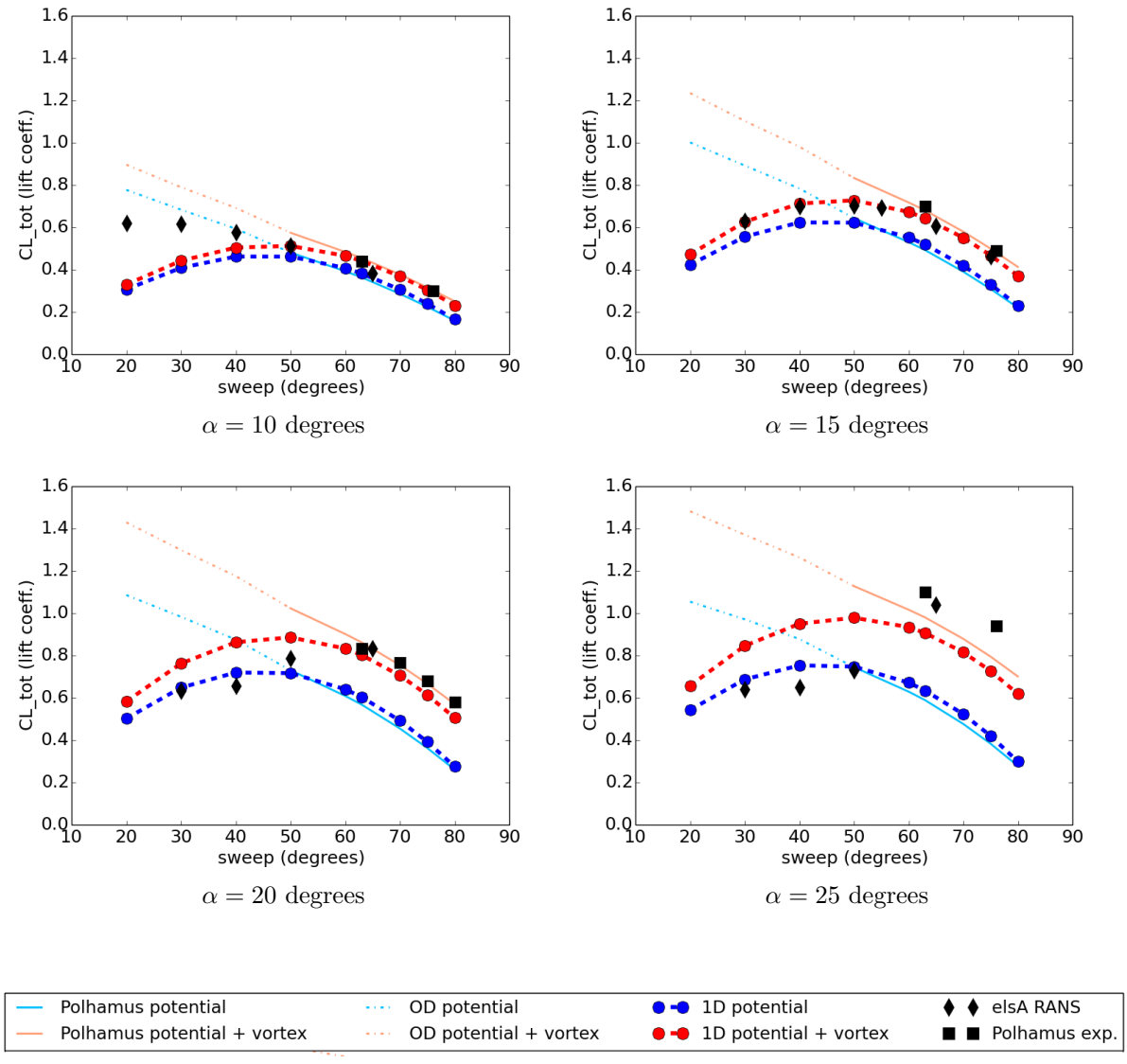

Figure 6.1. *Comparison of total lift coefficient CL_{tot} on Delta wings obtained through experiment, RANS, Polhamus model, 0D and 1D models. The 0D model consists in the application of the Polhamus model outside of the validity zone tested by Polhamus.*

Visualisations of Q-criterion flow fields may help understand the predictability challenge in the lower sweep range. Figure 6.2 shows that no proper LEV is formed for $\phi = 30$ degrees, whatever the incidence. In addition to the wing tip vortex, vortical structures close to the symmetry

plane can be observed but no conical structure following the leading-edge. For $\phi = 40$ degrees, a small LEV can be discerned at low incidences ($\alpha = 10$ and $\alpha = 15$ degrees), but it only impacts a small portion of the span and is quickly shed into the wake. At higher incidences, the same pattern as for $\phi = 30$ degrees occurs, which likely indicates a detached flow. Indeed, the sweep is not sufficient to generate a powerful enough leading-edge vortex to prevent stall at high incidences. For $\phi = 50$ degrees, a LEV appears at $\alpha = 10$, 15 and 20 degrees. For $\phi = 65$ degrees, a clear LEV characterises the flow whatever the incidence. Therefore the "low sweep range" seems to have a higher and higher upper bound as the incidence increases. For a given angle of attack, the more the sweep decreases, the more LEV formation is hindered. This trend is consistent with the observed discrepancies between the modelling and CFD in figure 6.1. As a consequence, the models' assumption that a LEV is generated in all cases is not validated, which explains their lack of predictiveness, especially at low sweeps.

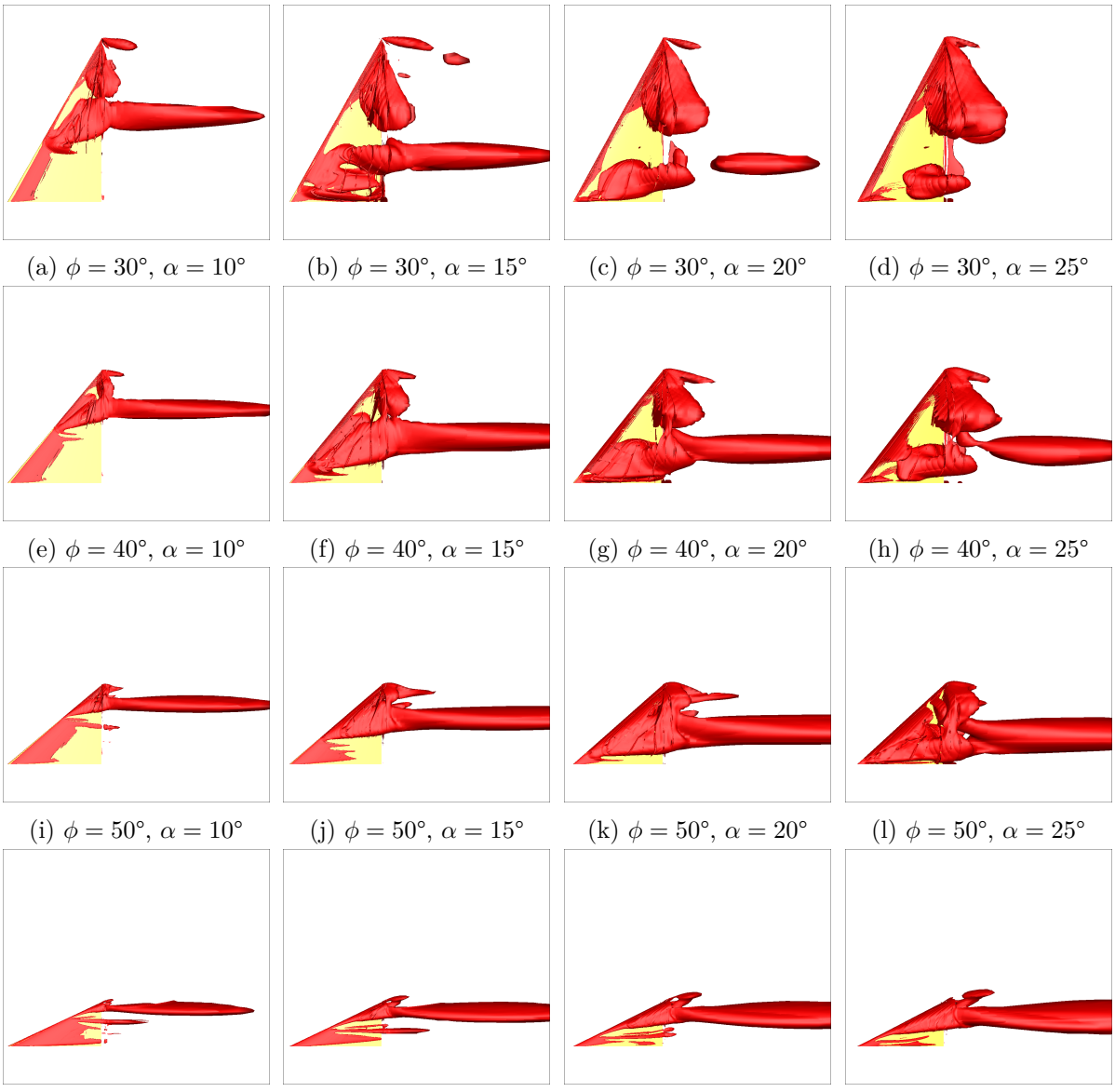

(a) $\phi = 30°$, $\alpha = 10°$ (b) $\phi = 30°$, $\alpha = 15°$ (c) $\phi = 30°$, $\alpha = 20°$ (d) $\phi = 30°$, $\alpha = 25°$

(e) $\phi = 40°$, $\alpha = 10°$ (f) $\phi = 40°$, $\alpha = 15°$ (g) $\phi = 40°$, $\alpha = 20°$ (h) $\phi = 40°$, $\alpha = 25°$

(i) $\phi = 50°$, $\alpha = 10°$ (j) $\phi = 50°$, $\alpha = 15°$ (k) $\phi = 50°$, $\alpha = 20°$ (l) $\phi = 50°$, $\alpha = 25°$

(m) $\phi = 65°$, $\alpha = 10°$ (n) $\phi = 65°$, $\alpha = 15°$ (o) $\phi = 65°$, $\alpha = 20°$ (p) $\phi = 65°$, $\alpha = 25°$

Figure 6.2. *Visualisation of Q-criterion iso-contours on the suction side of the Delta wing for various sweep and incidence angles (in degrees).*

Moreover, it is worth noticing that in most cases, the LEV does not appear at the apex but further away along the span, all the more so as the incidence is small. A leading-edge radius effect may contribute to this trend. Indeed, the Delta wing geometries were created using stacked NACA0006 airfoils, for a constant central chord. Being proportional to the chord, the leading-edge radius distribution decreases along the span. It is probable that for low incidences, the leading-edge radius close to the symmetry plane would be too large to allow the flow to detach.

In a nutshell, the proposed 1D extension of the Polhamus model with linear cumulative coefficients, is roughly as predictive as the original Polhamus model. The integrated lift coefficient values fit reasonably well to the experimental and RANS data for Delta wings of high sweep ($\phi \geq 65$ degrees) regardless of the incidence. For low sweeps, neither the 1D nor the 0D model manage to perfectly capture the RANS tendency. This can be explained by the fact that LEV formation was hindered at low sweeps, and the flow would detach completely in those cases above a threshold in incidence. At medium sweeps ($\phi \approx 50$ degrees), the 1D model is often closer to the RANS data than was the 0D model. In addition, the 1D model interestingly captures the tendency of vortex lift to decrease with sweep. Finally, it is worth mentioning that the 1D model is based solely on airfoil polars and fitting coefficients which do not depend neither on the sweep nor on the incidence.

The ability of the 1D model to give a reasonable prediction of the total lift coefficients shows that the assumption of a linear increase of the vortex lift distribution along the span enables to account for the aerodynamic effects of the LEV at first order.

6.2.2. Comparison of spanwise lift distributions

Now, the objective is to compare spanwise lift distributions given by the 1D model to those obtained through RANS calculations. We focus on the Delta wing at $\phi = 65$ degrees sweep, as it was shown previously that total lift was well predicted in this case. The comparison is depicted in figure 6.3a. The 1D model gives a linear spanwise distribution of $\frac{dL}{dr}$, which is expected as $CL(r)$ is linear with respect to the chord in the case of a Delta wing (see equations 6.13, 6.4, 6.8 and 6.7). However, this trend is very different from that of the CFD results, exhibiting more complex variations. Even though the total lift coefficients predicted by the 1D model were found to be in good agreement with CFD values in this case (see section 6.2.1), the corresponding spanwise variations of $\frac{dL}{dr}$ are not in accordance. In other words, the 1D model provides a reliable evaluation of the spanwise integral of $\frac{dL}{dr}$, but does not satisfactorily reproduce its spanwise distribution. This indicates that the 1D model is not of a sufficiently high order in terms of spanwise variation.

The CFD spanwise $\frac{dL}{dr}$ distribution is superposed with the wall pressure distribution field in figure 6.4, for the same case as depicted in figure 6.3a. This shows that the bump on the spanwise lift distribution starts from the spanwise position featuring the first reattachment lines (around r/R≈0.25). Then, the lift increases along the span because of the increasing portion of the chord with enhanced depression due to the conical development of the LEV. The lift distribution peaks at r/R≈0.45, after which the LEVs continue to expand but induce less depression over the chord, causing the decrease of the spanwise lift distribution. Also, the induced effects of the LEV on sections close to the symmetry plane compensate for the decrease of the chord and guarantee a constant lift distribution in this region.

Those effects are obviously not taken into account in the 1D model. First, we must stress

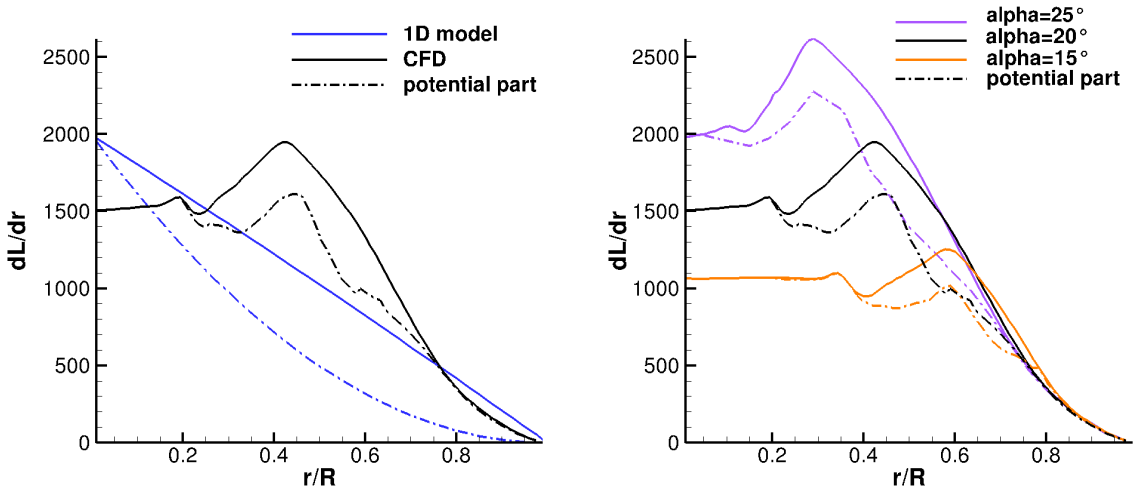

(a) $\phi = 65°$, $\alpha = 20°$ (b) $\phi = 65°$, varying incidence

Figure 6.3. *Spanwise distribution of lift $\frac{dL}{dr}$ (in N/m) for a Delta wing of 65 degrees sweep at various incidences, with vortex lift contribution evaluated from the Cp distribution*

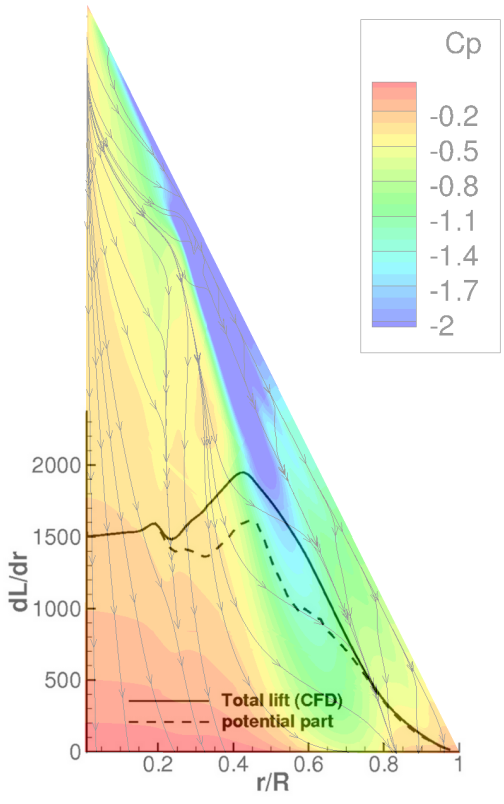

Figure 6.4. *Superposition of the spanwise distribution of lift $\frac{dL}{dr}$ (in N/m) with the wall pressure distribution and friction lines, on a Delta wing of 65 degrees sweep and 20 degrees incidence*

that the assumption of independent profiles which is used here does not allow to consider induced effects from other sections. Due to the low aspect ratios of Delta wings, the lifting line

method was not applicable. Therefore no 1D load calculation method would have been able to capture the induced effects. Ideally, the Delta wing case would require the use of 2D methods such as the panel method, which is not the objective of the present thesis. For now, there is only one way that the 1D model can account for three dimensional effects, or communication between profiles. This is via the proposed $f_v(r)$ and $f_p(r)$ cumulative functions, which can be tuned according to the CFD spanwise lift distribution to guarantee the right modelled lift distribution.

However, as explained previously, the onset of separation is not fixed at the apex, and depends on the incidence. This is also featured in figure 6.3b. As the incidence decreases, the detachment point appears further away along the span. Therefore, in order to provide an accurate modelling of the Delta wing case, the $f_v(r)$ and $f_p(r)$ functions would then have to depend on the incidence.

The interesting fact is that all incidences pictured in figure 6.3b are well beyond the stall incidence of the NACA0006 airfoil in a 2D (or non swept) configuration, which, according to the polar, is equal to 8.75 degrees. Therefore, the mechanisms which eventually lead to flow separation have a 3D component. At the moment, the understanding of flow separation mechanisms is not clear enough to provide a more accurate modelling of the spanwise vortex lift distribution in the case of Delta wings.

6.3. A 1D model for the HTC5 blade

This section aims at adapting the modelling tools developed in part 6.1 to the case of the HTC5 blade. Recall that this case is chosen because its circulation distribution and aspect ratio are representative of a propeller blade. First, let us characterise the spanwise evolution of vortex lift on the HTC5 blade using the procedure described in chapter 5.

6.3.1. Characterisation of vortex lift evolution

The spanwise evolution of vortex lift on the HTC5 blade will be characterised from the analysis of the wall pressure distribution in RANS calculations. This analysis was already performed in chapter 5 on the fixed HTC5 blade. The LEV would form at the apex and vortex lift would be detected shortly in the downstream, as soon as the LEV reached a minimal size. Vortex lift would increase along the span until the LEV reached the trailing-edge around 80% of span. The same analysis is carried out here on the rotating HTC5 blade, at scale 1, for various pitch angles.

6.3.1.1. Computational domain

The RANS calculations are performed in a 4-bladed, single propeller setup, with no hub. This configuration does not correspond to the counter-rotating configuration with 10 blades in the first row, which the HTC5 blade was designed for. However, its advantage is that it limits the effects of induced velocities by other blades (and eliminates the induced velocities from the downstream propeller). This simplified system allows an easier understanding of the impact of the leading-edge vortex on the blade's aerodynamics, while facilitating the calculation procedure and shortening calculation time.

The computational domain is displayed in figure 6.5. The general computational domain is a quarter cylinder, with periodic boundary conditions on lateral sides and far field boundary conditions on the circumference. A more refined computational domain around the blade is embedded in the general domain using the Chimera method. An additional Chimera level is used to handle the superposition of the blade mesh in the refined mesh.

The convergence of the solution is satisfying in attached flow cases (decrease of the residuals in the order of five orders of magnitude). However, in detached cases, a steady RANS solution cannot be found, which causes the residuals to oscillate on the two cases with the lowest pitch values, that is, highest incidence values. However, in all cases the convergence of the average forces is reached and the oscillations do not exceed 3% of the average value.

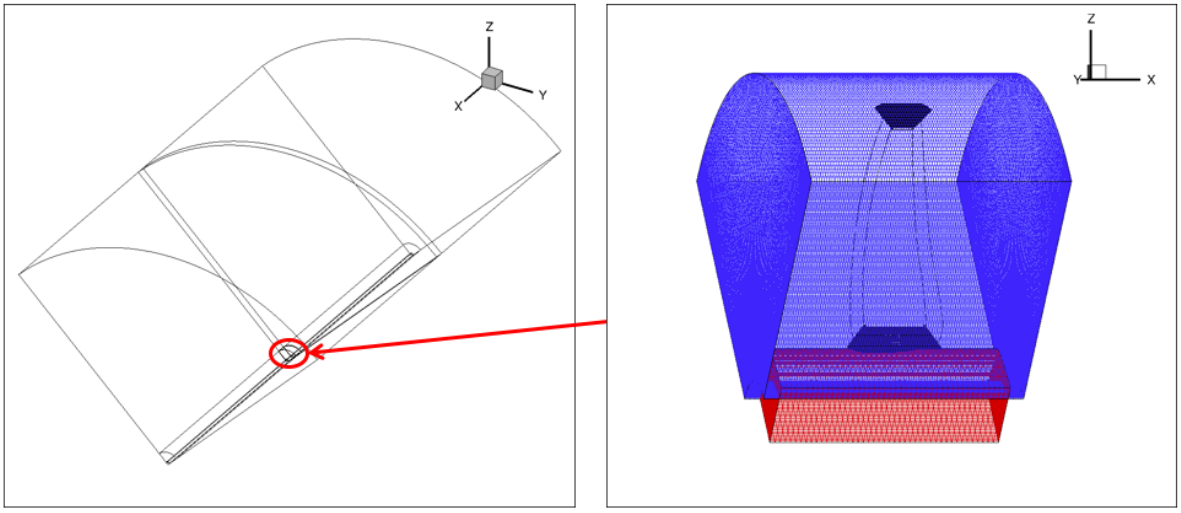

Figure 6.5. *Computational domain used for the 4 blade, single-propeller rotating configuration. Left : general computational domain. Right : Refined computational grid around the blade.*

6.3.1.2. Vortex lift evaluation

Vortex contribution to the aerodynamic forces is evaluated using the procedure described in chapter 5.

Figure 6.6 presents the superposition of the wall pressure field and friction lines with the spanwise lift distribution, for different pitch angles of the rotating HTC5 blade. The blade pitch angle at 70% of the tip radius is noted for reference (note that the working incidence of the blade profiles increases as the pitch angle decreases). Like in the fixed HTC5 case, or the Delta wing case, vortex lift rises shortly after the LEV detachment point, and starts to decrease when the LEV reaches the trailing-edge.

According to the friction lines, the point of first detachment corresponding to the birth of the LEV changes slightly with respect to the pitch. When the profiles work at higher incidence, the point of first detachment occurs closer to the root section. This trend is coherent with the behaviour observed on Delta wings. Also, the spanwise position where the LEV reaches the trailing-edge moves further towards the tip as the incidence of the profiles decreases. Nevertheless, it is worth noticing that the variability of those spanwise positions is much less marked than on the Delta wing case. The first detachment location varies in the order of 6% of the tip

radius R over 10 degrees of pitch variation in the rotating HTC5 case, while it is in the order of 40% of the Delta wing semi-span over the same incidence variation range (see figure 6.3b). Therefore, it should be easier to accurately model the spanwise lift distribution in the HTC5 case than in the Delta wing case.

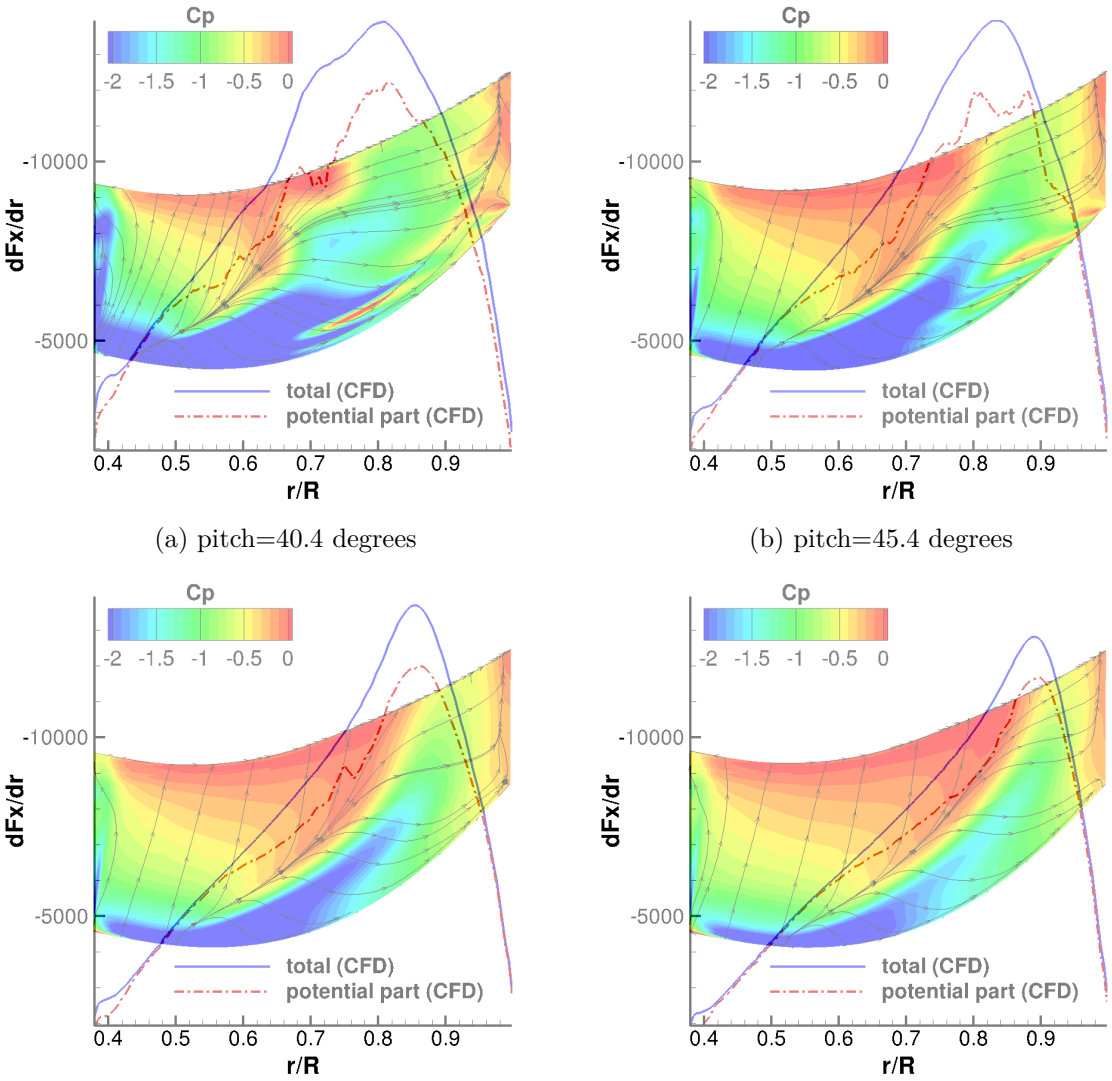

(a) pitch=40.4 degrees

(b) pitch=45.4 degrees

(c) pitch=48.0 degrees

(d) pitch=50.1 degrees

Figure 6.6. *Superposition of the spanwise distribution of thrust* $\frac{dFx}{dr}$ *(in N/m), including vortex contribution, with the wall pressure distribution and friction lines on the HTC5 blade with respect to the pitch angle at* $0.7R$.

6.3.2. Vortex lift modelling

Given that the pitch angle only has a slight influence on the spanwise positions corresponding to LEV formation (in the region of the apex) and LEV impact on trailing-edge, we consider at first approximation that vortex lift starts to be generated at the apex, for all pitch values.

6.3.2.1. Parabolic vortex lift model

The same expression for Kv_{loc} given by the 1D formulation of the leading-edge suction analogy in part 6.1.1 is used (see equation 6.8), with the cumulative function strategy (see equation 6.9). Only the function f_v is re-evaluated to best fit the vortex lift distributions extracted from CFD results.

According to the vortex lift estimation algorithm, it seems that a parabolic fit would be suitable to model the spanwise lift distribution. The following form is prescribed for f_v:

$$\boxed{\begin{array}{l} CL_v(r) = f_v(r)\, Kv_{loc}(r)\, cos\,\alpha(r)\, sin^2\alpha(r) \\ \\ f_v(r) = max(\,0,\, -4K''\frac{(r-r_0)(r-R)}{(R-r_0)^2}\,)\ ,\ K'' = 1.3 \end{array}} \tag{6.14}$$

considering that r_0 is the spanwise position corresponding to the detachment point (which we assume here to be the apex). Please note that in the case of a rotating blade, R is the tip radius, while it represents the span for a fixed wing. K'' is a constant which will be fitted with respect to the vortex lift distributions obtained from CFD. The value $K'' = 1.3$ was selected in the following. The maximum of $f_v(r)$ is obtained for $r = \frac{(r_0+R)}{2}$ which approximately corresponds to $0.8R$, that is, roughly the spanwise position where the LEV reaches the trailing edge. In the following, this parabolic vortex lift model will be compared to two other formulations.

6.3.2.2. Linear vortex lift model

This formulation is inspired from the previous section 6.1 on Delta wings. Indeed, it is also interesting to see how the 1D model used previously for Delta wings performs on the HTC5 case. As this model was accurate enough to allow for a reasonable prediction of total lift coefficients for various incidences and sweeps, we can therefore assume that it fits at first order to different types of LEVs, which is why it is also relevant to test it on the HTC5 case. Thus, a linear cumulative function is prescribed for $f_v(r)$, with the same slope as was fitted for Delta wings. The only difference introduced with respect to the 1D model used previously for Delta wings is that $f_v(r)$ is prescribed to decrease once the LEV has reached the trailing-edge, with the opposite slope. It was noticed that $f_v(r) = 1$ actually corresponded to $r \approx 0.8R$, which is consistent with the fact that $f_v(r)$ would model the portion of the chord covered by the LEV. Therefore :

$$\boxed{\begin{array}{l} CL_v(r) = f_v(r)\, Kv_{loc}(r)\, cos\,\alpha(r)\, sin^2\alpha(r) \\ \\ f_v(r) = \begin{cases} 1.6\,\frac{r-r_0}{(R-r_0)^2} & \text{if } r \leq r_{TE} \\ 1 - 1.6\frac{(r-r_{TE})}{(R-r_0)^2} & \text{if } r_{TE} \leq r \leq R \end{cases} \end{array}} \tag{6.15}$$

with r_{TE} defined as the location where $f_v = 1$.

6.3.2.3. Local application of the leading-edge suction analogy with the classical Polhamus coefficients

A last alternative would simply consist in applying the classical Polhamus model locally (see equation 6.1). The Kv values corresponding to the local sweep $\phi(r)$ are interpolated from the

values tabulated by Polhamus from whole Delta wing polars Kv. This procedure was applied for instance in [Thielicke et al., 2011].

$$\boxed{CL_v(r) = Kv(\phi(r))\, cos\, \alpha(r)\, sin^2\alpha(r)} \tag{6.16}$$

Those spanwise vortex lift models could also be used as an initialisation for the lifting line method, though this will not be tested in this work.

In order to evaluate those models with respect to reference CFD, the chosen load calculation method and the associated potential part description need to be stated.

6.3.3. Load calculation method

The vortex lift models will be coupled with the Blade Element Momentum Theory (BEMT). The implementation of the BEMT is explained in further detail in Appendix B. In a few words, the Shen tip loss correction [Shen et al., 2005b] is applied. A relaxation factor is used to foster the convergence of the BEMT iterative procedure. Also, an interpolation module was developed in order to interpolate (and extrapolate) in a database of symmetric NACA polars with respect to the incidence, airfoil thickness and Mach number.

The BEMT will enable to evaluate the effective angle of attack, together with the axial and radial induced velocities on each profile. It is based on an iterative procedure which stops when an equilibrium is reached between the momentum balance around the airfoil and the efforts acting on it. The concept of induced velocity enables to look at the flow around each airfoil in terms of a discontinuous discrepancy with the inflow conditions. Thus, three induced velocity components are necessary to describe the behaviour of the flow around the airfoil, in each direction.

On a rotating case, we can define the in-plane induced velocities, which are the axial and radial one, plus an out-of-plane induced velocity which would be a spanwise induced velocity. This last component is not taken into account in the BEMT (or only indirectly through the tip loss correction), as the profiles are assumed to be independent. Yet the iterative procedure of the BEMT still considers the two other components in order to find the effective angle of attack. Using both the axial and radial induced velocities as unknowns to the problem is equivalent to considering the effective angle of attack as an unknown [Ning, 2014].

However in a fixed case, the radial induced velocity is not defined. Thus, applying the BEMT while imposing zero rotation provides no leverage to find the effective angle of attack. Indeed, in the fixed case, the three induced velocities needed to define the flow would be the axial, spanwise and downwash (direction normal to the span).

This reasoning enables to highlight that if the BEMT is used, there needs to be a modelling discontinuity between the fixed and rotating cases. In other words, the BEMT allows to estimate the effective angle of attack in the rotating case without explicitly taking into account the three dimensional effects due to the velocities induced by other sections (or only via a tip loss correction). On the contrary, estimating the effective angle of attack in the fixed case requires the use of a method such as the lifting line method.

The scope of the present chapter is to provide the simplest possible model, aimed at formalising a physical characterisation of leading-edge vortex flows rather than achieving a predictive tool.

This motivated the choice of the BEMT as a load calculation model for the rotating case, and for reasons of coherence in the modelling, it was decided to make the same assumption of independent profiles in the fixed case, instead of using the lifting line method. Still it is necessary to account for the fact that the effective angle of attack α should be smaller than the geometrical angle of attack α_{geo} in the fixed case, because of the downwash caused by the tip vortices. For this purpose, we make the assumption that the lift coefficient $CL(\alpha)$ can be expressed depending on $CL(\alpha_{geo})$ as such:

$$CL(\alpha) = \frac{CL(\alpha_{geo})}{1 + \frac{CL(\alpha_{geo})}{\alpha_{geo}\pi AR}}\,\alpha_{geo}$$

where AR is the aspect ratio of the wing based on the average chord. This assumption is derived from an analytical result for a finite wing with an elliptical circulation distribution, which links the slopes of $CL(\alpha) = CL_{3D}(\alpha_{geo})$ and $CL(\alpha_{geo})$. Indeed, the downwash can be expressed analytically in this case, which enables to calculate the effective angle of attack. This result is demonstrated in [Houghton and Carpenter, 2003], page 284.

6.3.3.1. Potential part

In this paragraph, the potential part refers to the "non vortex lift" part. For the potential part, contrary to the Delta wing case, no cumulative function is applied. $CL_p(r)$ is deduced from equation 6.9 with $f_p(r) = 1$:

$$\boxed{CL_p(r) = Kp_{loc}(r)\,cos^2\alpha(r)\,sin\alpha(r)} \tag{6.17}$$

Applying the same cumulative function as the Delta wing case led the spanwise lift distribution to decrease too rapidly along the span. The increasing spanwise vortex lift distribution was not sufficient to maintain an increasing lift distribution along most part of the span. On the other hand, without cumulative function, the loading was found to be in satisfying qualitative agreement with the reference CFD. The reason why the cumulative function f_p was necessary for the Delta wing potential part, and not for the HTC5 case, is not clear. However, several hypotheses can be put forward to explain this fact:

1. The impact of the LEV on the spanwise lift distribution is somewhat different in the HTC5 case compared to the Delta wing case. In the HTC5 case, the LEV increases loading in a region where the loading was already high, while in the Delta wing case, it tends to homogenise the spanwise loading distribution, and to increase the loading in a region where it was previously low. It that sense, the LEV will more drastically modify the general aspect of the lift distribution in the case of the Delta wing.

2. Given the aspect ratio of both geometries, the assumption that the profiles are independent is more coherent in the HTC5 case than in the Delta wing case. Thus, the HTC5 case does not require as many cumulative effects. Actually, in the absence of LEV, the assumption of independent profiles (plus a tip loss correction) used by the BEMT would be quite reasonable. This is shown by the nice agreement between the BEMT and reference RANS calculations obtained close to the root, where no LEV is formed (see figure 6.9).

3. The local expression for the "potential part" of lift which is applied in the case of the HTC5 blade, $CL_p(r) = Kp_{loc}(r)cos^2\alpha(r)\,sin\alpha(r)$ where $Kp_{loc}(r) = \frac{\partial CL_{airfoil}(r)}{\partial\alpha}\Big)_{\alpha_0} cos^2\phi(r)$, can

be seen as an extension of the polar of the profile beyond the incidence corresponding to CL_{max}. Thus, it is well suited to the modelling philosophy of the BEMT. Beyond the incidence corresponding to flow separation, the polar is extended by considering a slope decrease (achieved by the multiplication by $cos^2\phi\, cos^2\alpha$) with respect to the linear part of the polar (which is given by the potential solution), in order to take into account the non linear effects which arise due to the appearance of the leading-edge vortex.

4. Recalling the studies presented in section 1.1.2 which relied on the slender wing theory, it would perhaps be physically more accurate to consider independent profiles along the chord direction (instead of the span direction) in the case of the Delta wing. However, the work of [Renac, 2004] who used the slender wing theory in order to find an explicit dependency of the Polhamus coefficients on the sweep, shows that for intermediate sweeps of the Delta wing, the slender wing theory is not verified anymore. The very low aspect ratios of Delta wings prevent any attempt to consider independent profiles for intermediate or low sweeps.

6.3.4. Evaluation of the 1D model

The 1D vortex lift models discussed in section 6.3.2 and the modelling strategy for the potential part described in section 6.3.3.1 are embedded in the load calculation method presented in section 6.3.3.

For $r \leq r_0$ (before the apex, which is assumed here to correspond to the onset of vortex lift generation), the classical BEMT is used, that is, the lift and drag coefficients corresponding to the effective incidence are simply interpolated from the polars. For $r_0 \leq r \leq R$, the leading-edge suction analogy is activated. The potential and vortex lift coefficients are evaluated using the models discussed in sections 6.3.2 and 6.3.3. The drag coefficient is evaluated as

$$CD = CL\, tan\, \alpha = (CL_p + CL_v)\, tan\, \alpha$$

according to the leading-edge suction analogy [Polhamus, 1968]. This formula is based on the assumption that induced drag is the main source of drag in the presence of the leading-edge vortex.

In the following, vortex lift models are numbered by increasing complexity: model 1 refers to the vortex lift model using the classical Polhamus coefficients (see equation 6.16), model 2 refers to the linear vortex lift model (see equation 6.15) and model 3 to the parabolic one (see equation 6.14).

Please note that the reference CFD values are obtained from calculations using the HTC5 profiles, while they are compared to the model results using NACA polars of the same relative thickness. Indeed, it was chosen to favour the use of detailed symmetric NACA polars (in terms of incidence variation) instead of the less detailed HTC5 polars available. As stated previously, on most part of the span, the relative thickness is actually very low (lower than 6% of the chord, from 20% of the span up to the tip, see figure A.1 in appendix A). Therefore, on most part of the span, the HTC5 and NACA profiles behave as very thin profiles. The $\frac{\partial CL_{airfoil}}{\partial \alpha}\Big)_{\alpha_0}$ and $\frac{\partial^2 CD_{airfoil}}{\partial CL^2_{airfoil}}\Big)_{\alpha_0}$ slopes around zero-lift incidence α_0 will thus be close to the values obtained for thin airfoil theory. At spanwise positions where the flow is detached, only polar slopes around zero-lift incidence are used, and the corresponding airfoils have a low relative thickness. Therefore the use of NACA polars instead of HTC5 polars will likely not be detrimental to the quality of the modelling.

However, in the foot region of the HTC5 blade, below 20% of the span, the relative thickness varies between 6% and 12%. This corresponds to a region where the flow is generally attached in the tested pitch range, so the whole incidence range of the polar is used (instead of only that around zero-lift incidence). Using symmetric airfoil polars instead of HTC5 polars affects the zero-lift incidence and therefore the load prediction in the foot region. However this error source should be limited because the HTC5 profiles are low-cambered profiles. In order to estimate it, the zero-lift incidence in absolute value, in the considered Mach number and relative thickness range is evaluated from the HTC5 polars. For root sections up to 20% of span, the Mach number is comprised between 0.25 and 0.33. The encountered values of zero-lift incidence for 6% and 9% relative thickness HTC5 airfoils at $M = 0.3$ amount to 0.7 and 0.65 degrees respectively (through linear interpolation in incidence of the available CL(α) values).

An interpolation/extrapolation module is used to estimate the polars for a given relative thickness from a database containing the NACA0006, NACA0008, NACA0010 and NACA0012 polars.

6.3.4.1. Evaluation on the HTC5 fixed blade

The spanwise vortex lift evolution given by the models is compared to the reference CFD results (using the vortex lift estimation method of chapter 5) in figure 6.7. Although the order of magnitude of the integrated lift values is recovered, the agreement between the CFD values and modelled spanwise lift distributions is not satisfying. Indeed, this is not surprising due to the fact that the induced velocities are not considered, as explained in part 6.3.3. However, the agreement between the model and reference CFD distributions should be improved on rotating cases, because the use of the BEMT should enable a more relevant determination of the induced velocities.

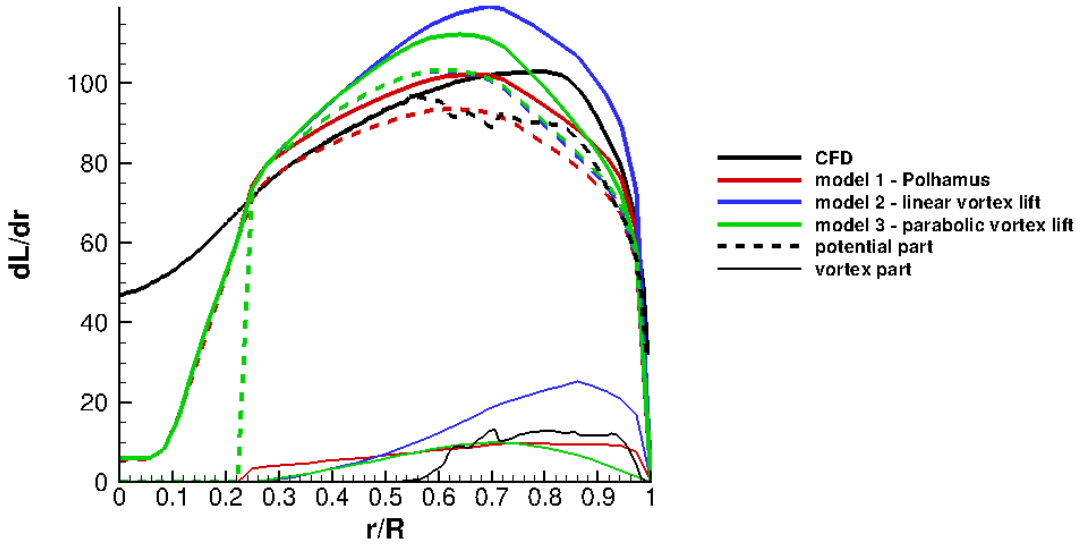

Figure 6.7. *Comparison between modelled and reference spanwise distributions of lift $\frac{dL}{dr}$ for the fixed HTC5 blade (in N/m). The reference vortex lift contribution is evaluated from the wall Cp distribution using the method described in chapter 5*

6.3.4.2. Evaluation on the rotating HTC5 case (full scale, 4 blades, single propeller, no hub)

The spanwise vortex lift evolution given by the models is compared to the reference CFD results (using the vortex lift estimation method of chapter 5) in figure 6.8.

Those plots show very well that the representativeness of the modelling could be increased if the variation with respect to the pitch of the spanwise positions corresponding to detachment and to the LEV reaching the trailing-edge were better modelled. Actually, it appears well on those plots that increasing the pitch (or decreasing the incidence of the profiles) roughly consists in shifting the detachment and maximal vortex lift points towards the tip.

Nevertheless, those plots also show that the models based on cumulative functions, and especially the parabolic vortex lift model roughly correspond to the slopes and maximal vortex lift values in the reference RANS calculations. In addition, it is worth noticing that those characteristics are quite reliably predicted with a 1D model based on a local application of the leading-edge suction analogy, with simple cumulative functions. The tested $f_v(r)$ only depend on the spanwise position and a constant which is fitted regardless of the pitch values.

In is interesting also to see that model 0 (which is based on the classical Polhamus coefficients), and model 1 (the linear model) give reasonable orders of magnitude of the vortex lift contribution, even though the slopes of the vortex lift distribution are not well captured.

The absolute values of the thrust distributions dFx/dr obtained by the models and the reference CFD are plotted in figure 6.9, in thick full lines. The "potential" and vortex components of thrust are also plotted on the same graphs, respectively in dashed and thin full lines. At a given position along the span, the thrust distribution suddenly shrinks. Then it catches up with the RANS profile quite nicely at the apex ($\frac{r}{R} = 0.56$). Indeed, in this region, the profiles work beyond the incidence corresponding to stall. This is due to an artefact of the BEMT, which does not take into account the induced velocities by the other profiles (including those where the LEV is present). As soon as the leading-edge suction is activated, at the apex, the thrust comes back to values which are close to those of the reference CFD. Therefore in order to calculate the integrated thrust and torque, the "stalled zone" is replaced by a linear interpolation between the values at $\frac{r}{R} = 0.42$ and $\frac{r}{R} = 0.56$.

The total thrust and efficiency given by the parabolic 1D model (model 3) are compared with those of reference CFD calculations in Table 6.1, for different pitch values. This demonstrates that the parabolic vortex lift model provides a fair estimate of total thrust and efficiency (integrated over the blade surface).

	pitch=40.4°		pitch=45.4°		pitch=48.0°		pitch=50.1°	
	model 3	CFD	model 3	CFD	model 3	CFD	model 3	CFD
total thrust (N)	13115	12233	11521	11370	10416	10550	9398	9772
efficiency	0.38	0.4	0.45	0.48	0.49	0.52	0.53	0.57

Table 6.1. *Comparison of total thrust and efficiency values obtained with the parabolic vortex lift model (model 3) with respect to CFD.*

Figure 6.8 depicts that with increasing pitch (or decreasing incidence) the spanwise position where the airfoil first stalls in the 1D model is displaced towards the tip. Actually, over the tested pitch range this displacement amounts to $0.06R$ (between $0.42R$ for a pitch of 40.4

degrees and $0.48R$ for a pitch of 50.1 degrees), which roughly corresponds to the displacement of the point where the flow first detaches (between $0.45R$ for a pitch of 40.4 degrees and $0.52R$ for a pitch of 50.1 degrees according to the friction lines in figure 6.6). Therefore, the position where the BEMT first gives a stalled result may be used as a criterion to activate the leading-edge suction analogy. This would be an easy perspective to account for the displacement of the onset of vortex lift with respect to the pitch.

The slopes of the thrust distribution (excluding the stalled part) are qualitatively well predicted in all cases. This indicates that the chosen modelling strategy captures the physical phenomena at first order. However, the spanwise distribution of the force in the direction corresponding to torque, dFy/dr, is further away compared to the reference CFD (see figure 6.10). dFy/dr is systematically over-estimated at the apex, and its slope is not well predicted. However, this default seems to come from the BEMT and the potential part modelling, rather than from the vortex lift model. Indeed, we can notice that the vortex contribution to dFy/dr qualitatively follows the reference CFD in the case with a pitch angle of 48 degrees, while the discrepancy on the modelled and reference dFy/dr is clearly non negligible.

6.4. Conclusion

This chapter dealt with the challenging task of setting up a 1D model for a 3D phenomenon.

In order to do so, the leading-edge suction analogy was expressed into a local form, leading to local values of the Polhamus coefficients based on the airfoil polar instead of the whole wing polar. The modelling methodology is based on the assumption of independent profiles, but corrects it by the use of cumulative functions. In the rotating case, this translates into the use of the BEMT load calculation method. The apex is assumed to be the onset of vortex lift. The leading-edge suction analogy is activated from this spanwise position onwards. Inboard of this position, the loads are calculated by interpolating in the polars' database. In order to account for 3D effects, the local Polhamus coefficients are assumed to depend on cumulative functions which vary along the span. The cumulative functions were fitted with respect to reference CFD data. Those reference results were extracted using the estimating procedure discussed in chapter 5. The 1D model provides a qualitative agreement with the CFD reference, which shows that it captures the main physical phenomena, at first order.

This modelling effort enabled to bring out several results regarding the characterisation of vortex lift :

- vortex lift increases with respect to spanwise position until the LEV reaches the trailing edge.
- cumulative functions are used to account for three-dimensional effects and communication between profiles. Those functions are only based on one fitted constant, thus do not depend neither on the local incidence, nor on the local sweep, but still enable to capture vortex contribution to lift at first order.

The modelling effort was carried out on three cases: Delta wings of various sweeps at various incidences, the fixed HTC5 blade, and the rotating HTC5 blade for various pitch values. It is interesting to pinpoint that a different modelling methodology had to be applied on those three cases, in particular regarding the potential part. However, those different strategies are not necessarily justified by differences in the physical mechanisms involved. Rather, they stem

from the fact that the present simple 1D model does not have enough degrees of freedom to encompass all those cases without changes in the modelling.

The major limitations of the present modelling strategy were identified as :

- regarding vortex lift : there is a lack of physical understanding regarding the onset of separation, especially its variability with incidence or pitch variation.
- the limitations inherent to the BEMT, which are due to the fact that not all induced velocities are considered. Those limitations may lead to an incorrect thrust over torque ratio, moreover, the induced effects from other profiles are not taken into account.

Therefore, as future perspectives, it would be interesting to implement the present vortex lift model in a generalised lifting line method [Guermond, 1990] (though this would likely not work for applications such as the Delta wing). On the HTC5 case, this would enable to distinguish the bias due to the vortex lift model from those induced by the load calculation method. In addition, the more accurate modelling of the induced velocities enabled by the lifting-line method would probably improve the prediction of the detachment point, as the induced velocities are also essential from the point of view of the prediction of flow separation.

Also, in order to improve the present 1D vortex lift model, a future step would consist in replacing the fitting constants by physical constants. This effort should start by a better understanding of the spanwise variation of LEV characteristic parameters, such as vorticity, circulation, core velocity, or characteristic size.

In a nutshell, the modelling effort provides interesting results from the point of view of the spanwise characterisation of vortex lift, as it captures the main physical phenomena. However, the limitations of the modelling and the fact that it has only been tested on a small number of geometries are such that the present 1D model is not validated enough to use for geometry parametric studies.

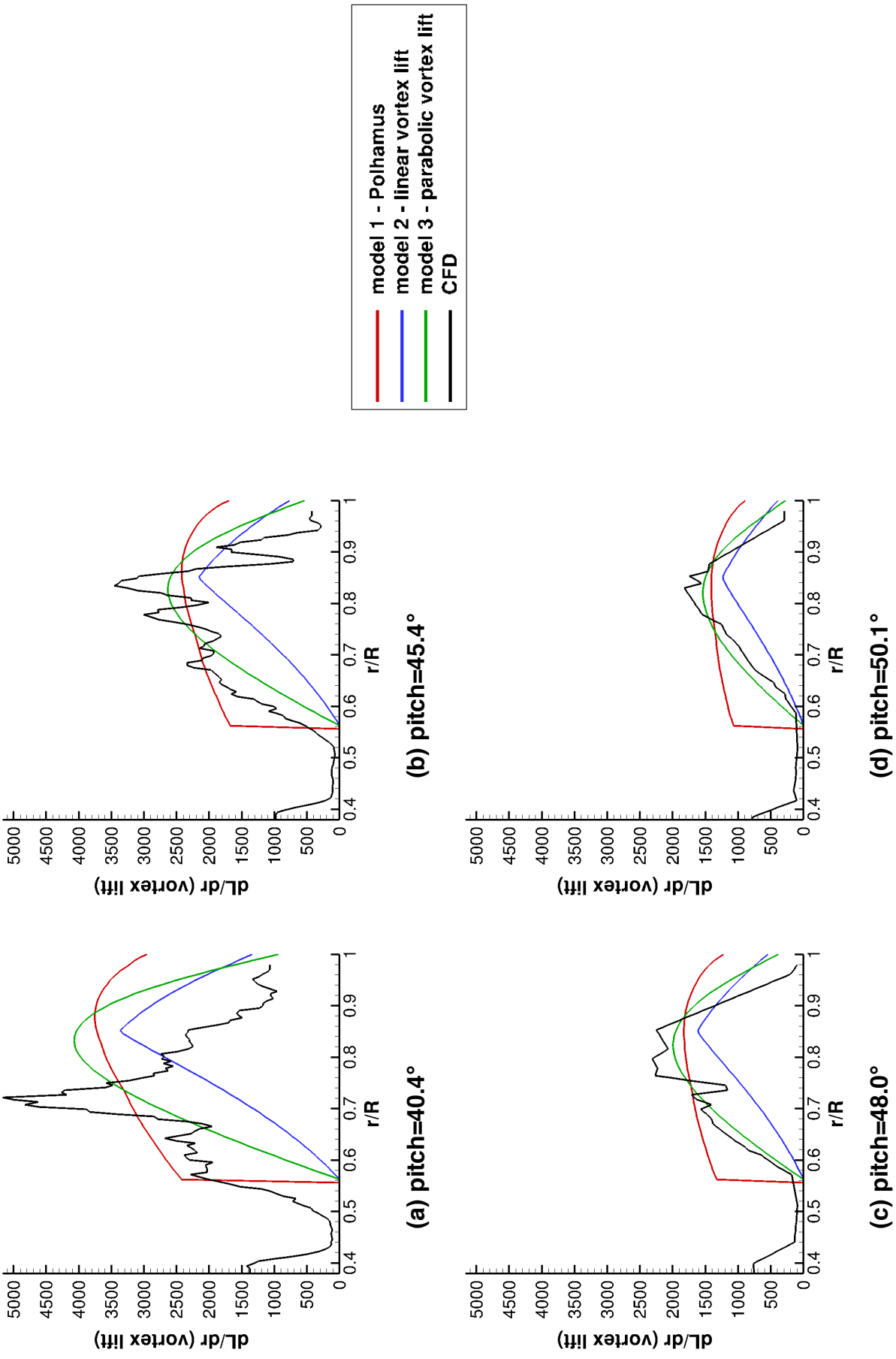

Figure 6.8. *Comparison of modelled spanwise vortex lift distributions with respect to CFD for various pitch values (in N/m).*

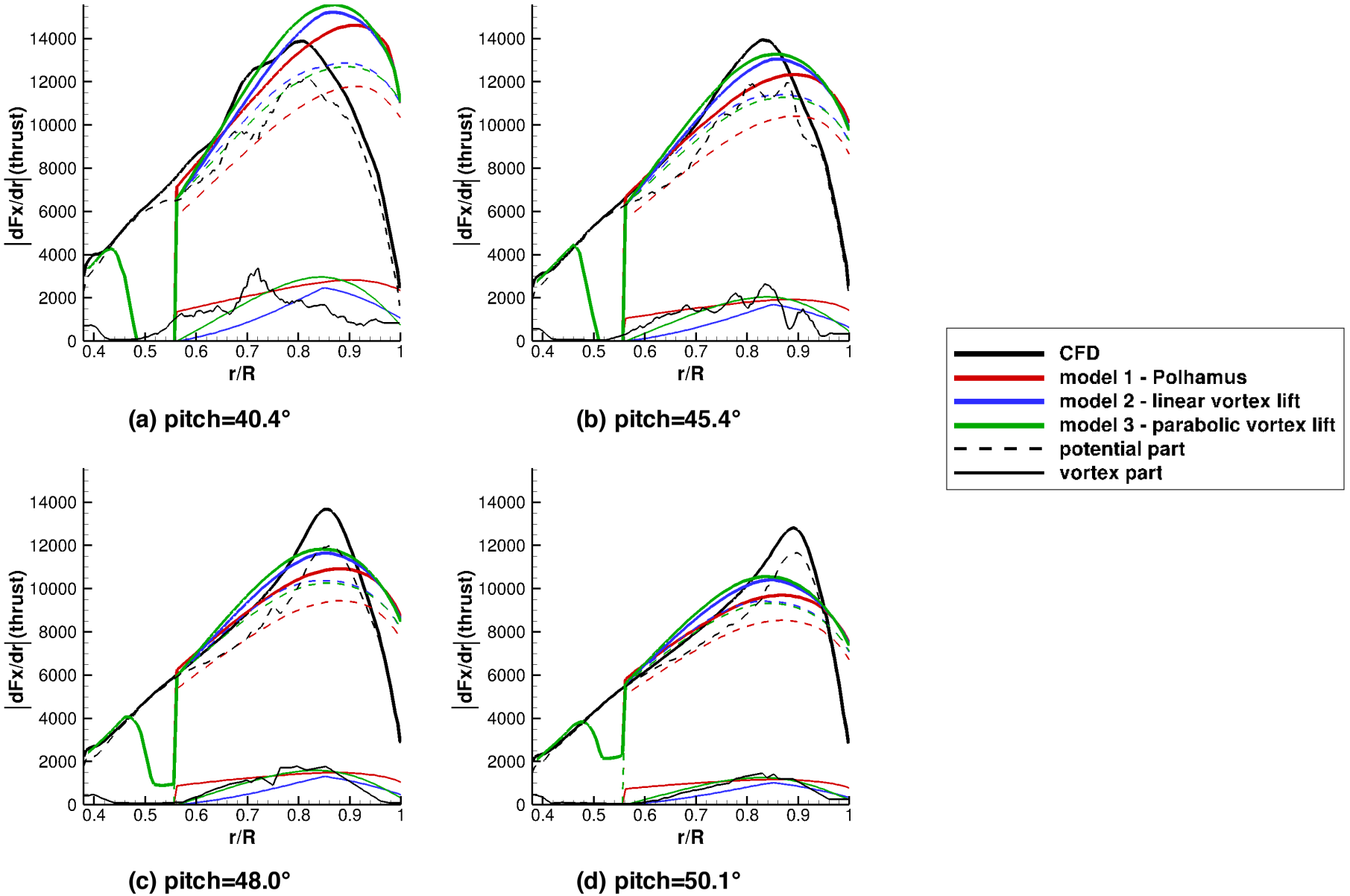

Figure 6.9. *Comparison of modelled spanwise distributions of* $|\frac{dFx}{dr}|$ *(absolute value of thrust component) with respect to CFD for various pitch values (in N/m). The "potential" and vortex contributions to thrust are displayed for each case.*

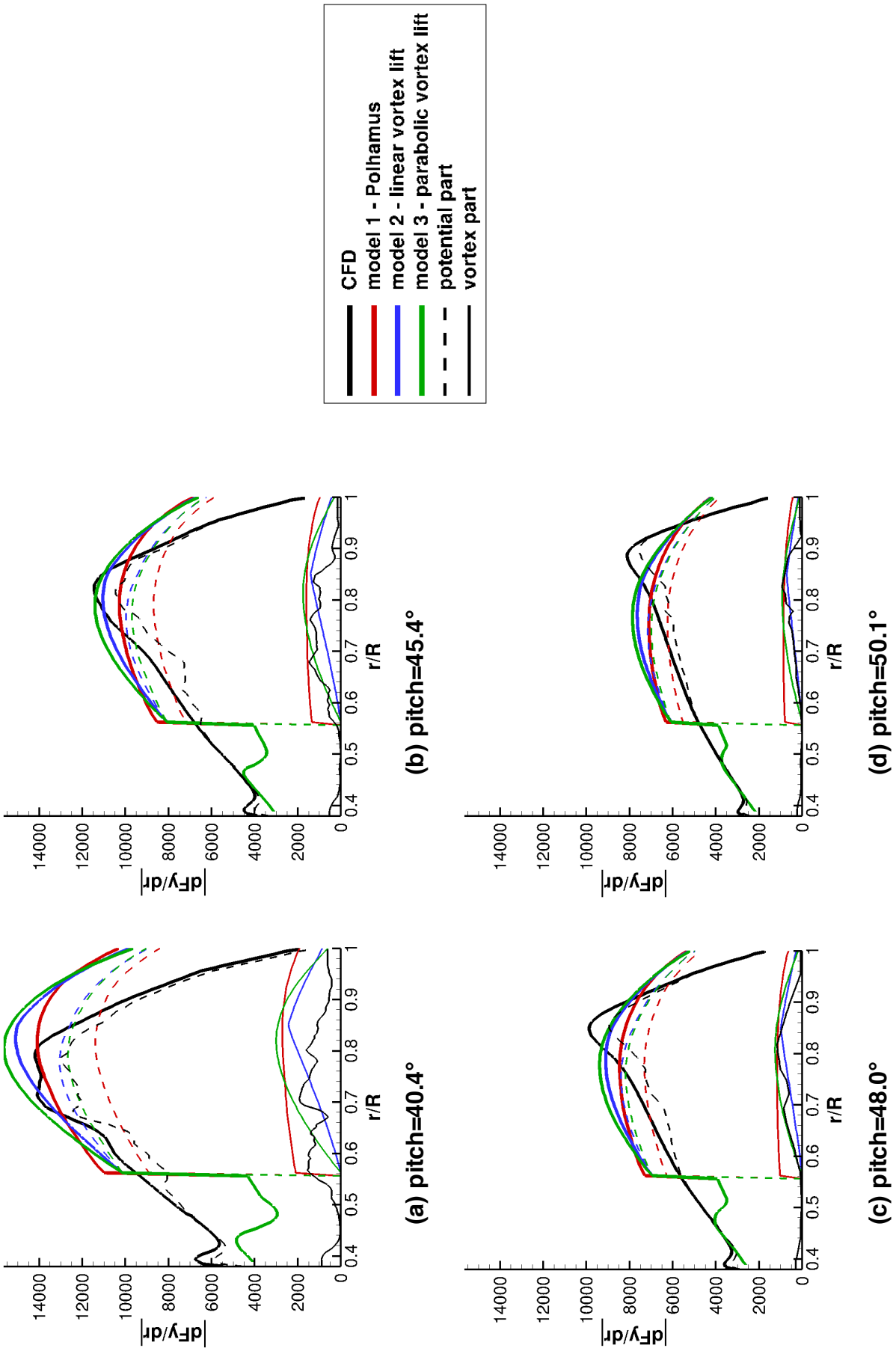

Figure 6.10. *Comparison of modelled spanwise distributions of* $|\frac{dFy}{dr}|$ *(absolute value of* Fy *component) with respect to CFD for various pitch values (in N/m). The "potential" and vortex contributions to thrust are displayed for each case.*

7

Evaluation of the interest of vortex lift enhancement at take-off

The objective of this chapter is to discuss the interest of vortex lift enhancement at take-off from an applicative point-of-view. On Delta wings, it is very clear that vortex lift comes along with an increase in drag. This chapter focuses on the consequences of vortex lift augmentation in a rotating case, and addresses how to most efficiently generate vortex lift.

By means of an exploratory study, the link between vortex lift and loss in efficiency, as well as the impact of the blade geometry on vortex lift generation will be addressed.

7.1. Discussion on the impact of vortex lift on efficiency in a rotating case, from the perspective of the leading-edge suction analogy

On a fixed case, the fact that the leading-edge suction force turns to be oriented normal to the profile causes an increase in lift together with an increase in drag, thus a systematic loss in efficiency. The drag is increased by $(Np + Nt)\, tan\, \alpha$ with respect to an attached case (where according to 2D potential theory, the drag is equal to zero).

In a rotating case, the efficiency η is based on thrust T and torque C: $\eta = \frac{U_{inf} T}{\Omega C}$. Given that the lift and drag projections on thrust and torque depend on the incidence angle, it is worth verifying whether the addition of vortex lift always decreases efficiency.

Let us consider a blade profile, at spanwise position r, as represented in figure 7.1. The leading-edge suction force F is represented (for a case without LEV). The leading-edge suction analogy consists in assuming that the projection of F normal to the sweep, $N_v = \frac{F}{sin\phi}$ turns in the presence of the LEV to be oriented normal to the blade.

Figure 7.2 presents the forces and resulting projections on thrust and torque, both with and without leading-edge vortex. The axial and radial induced velocities, noted respectively $a\, U_{inf}$ and $\omega r = -a'\, \Omega\, r$ are considered. The relative velocity is noted W. β is the angle between W and U_{inf}. The induced drag is taken into account through the induced velocities.

With leading-edge vortex, the forces applied on the profile are the resultant of the pressure forces normal to the profile N_p, and the force N_v linked to the leading-edge suction analogy.

Expressing the trust T_1 and torque C_1 in this configuration reads :

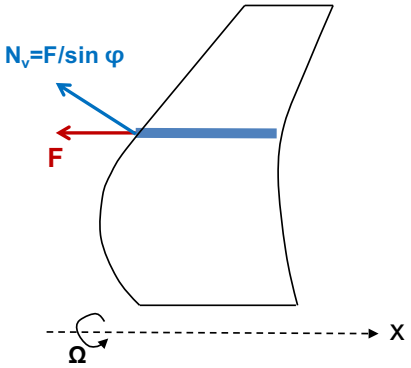

Figure 7.1. *Blade profile with the leading-edge suction force F (in absence of LEV) and the force normal to the blade caused by the LEV N_v*

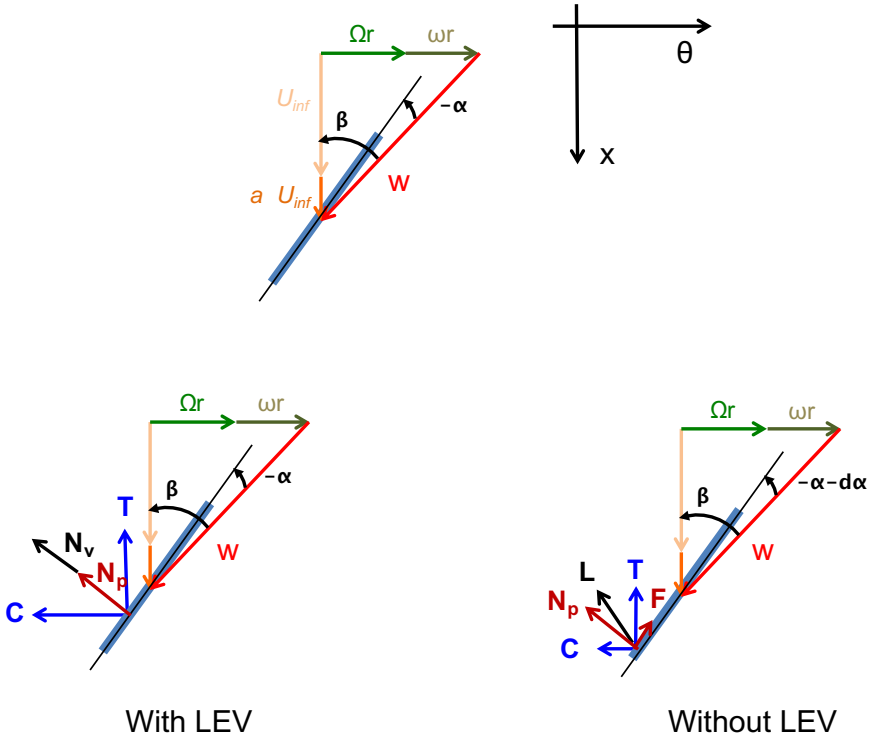

Figure 7.2. *Leading-edge suction analogy on a rotating case with projections on thrust and torque*

$$\begin{cases} T_1 = (N_p + N_v)\, sin(\alpha + \beta) \\ C_1 = (N_p + N_v)\, cos(\alpha + \beta) \end{cases}$$

Without leading-edge vortex, the forces on the profile are only the lift L, which can be decomposed into the resultant of the pressure forces normal to the profile N_p and the leading-edge suction force F. Using the same reasoning as [Polhamus, 1966], the leading-edge suction force F can be expressed as $F = N_v\, sin\phi$, as depicted in figure 7.2. Therefore the thrust T_2 and torque C_2 for a case without leading-edge vortex are :

$$\begin{cases} T_2 = N_p\, sin(\alpha+\beta) + F\, cos(\alpha+\beta) = N_p\, sin(\alpha+\beta) + N_v\, sin\phi\, cos(\alpha+\beta) \\ C_2 = N_p\, cos(\alpha+\beta) - F\, sin(\alpha+\beta) = N_p\, cos(\alpha+\beta) - N_v\, sin\phi\, sin(\alpha+\beta) \end{cases}$$

Let us compare the efficiencies obtained with LEV η_1 and without LEV η_2.

$$\eta_1 = \frac{T_1\, U_\infty}{C_1\, \Omega} > \eta_2 = \frac{T_2\, U_\infty}{C_2\, \Omega}$$

$$\frac{(N_p+N_v)\, sin(\alpha+\beta)}{(N_p+N_v)\, cos(\alpha+\beta)} > \frac{N_p\, sin(\alpha+\beta) + N_v\, sin\phi\, cos(\alpha+\beta)}{N_p\, cos(\alpha+\beta) - N_v\, sin\phi\, sin(\alpha+\beta)}$$

$$tan(\alpha+\beta) > \frac{N_p\, sin(\alpha+\beta) + N_v\, sin\phi\, cos(\alpha+\beta)}{N_p\, cos(\alpha+\beta) - N_v\, sin\phi\, sin(\alpha+\beta)}$$

$$sin(\alpha+\beta) > \frac{N_p\, sin(\alpha+\beta)\, cos(\alpha+\beta) + N_v\, sin\phi\, cos^2(\alpha+\beta)}{N_p\, cos(\alpha+\beta) - N_v\, sin\phi\, sin(\alpha+\beta)}$$

$$0 > \frac{N_v\, sin\phi\, cos^2(\alpha+\beta) + N_v\, sin\phi\, sin^2(\alpha+\beta)}{N_p\, cos(\alpha+\beta) - N_v\, sin\phi\, sin(\alpha+\beta)}$$

$$0 > \frac{N_v\, sin\phi}{N_p\, cos(\alpha+\beta) - N_v\, sin\phi\, sin(\alpha+\beta)}$$

$$N_v\, sin\phi\, sin(\alpha+\beta) > N_p\, cos(\alpha+\beta)$$

$$tan(\alpha+\beta) > \frac{N_p}{N_v\, sin\phi}$$

$$tan(\alpha+\beta) > \frac{N_p}{F}$$

Knowing that $\frac{N_p}{F} = tan(\frac{\pi}{2} - |\alpha|) = \frac{1}{tan(|\alpha|)}$, we obtain

$$tan(\alpha+\beta)\, tan(|\alpha|) > 1 \tag{7.1}$$

In order to verify this condition, $\alpha + \beta + |\alpha|$ would need to be higher than $\frac{\pi}{2}$. For a tractive propeller configuration, without resistive torque, β must be comprised between 0 and $\frac{\pi}{2}$ (excluded). The condition of equation 7.1 is never verified, which means that vortex lift systematically decreases efficiency for a tractive propeller configuration.

For a tractive propeller configuration, α has to be negative, with $|\alpha| \leq \beta$. Maximising the ratio $\frac{\eta_1}{\eta_2}$ therefore implies to maximise β, and set $|\alpha|$ as $|\alpha| = \frac{\beta}{2}$. Maximising β means increasing the rotation velocity for a given advance velocity, that is, decreasing the advance ratio. In short, a LEV always lowers efficiency for a tractive propeller configuration, but decreasing the advance ratio enables to come closer to the efficiency reachable in attached flow conditions.

7.2. Influence of blade functioning and geometrical parameters on vortex lift

The influence of the blade functioning and geometrical parameters on vortex lift generation and efficiency is tackled in this part, using RANS calculations and the vortex lift estimation method developed in chapter 5. In order to direct this parametric study, it was decided to compare cases at iso-thrust, both at take-off and in cruise condition.

7.2.1. Definition of target thrust

The configurations corresponding to take-off and cruise in terms of Mach number, total pressure p_0 and temperature T_0 are the same as those referenced in [Delattre and Falissard, 2014], and noted in Table 7.1.

For the HTC5 full propeller at take-off (containing $B = 10$ blades), the thrust coefficient is equal to $\tau = 1.22$ according to [Delattre and Falissard, 2014], the rotational speed is $n = 16.8$ (at full scale), and the thrust ratio between upstream and downstream propellers is $\sigma = 1.05$. The target thrust at take-off for a blade of the first row at full scale is $T_{TO} = \frac{1}{B(1+\sigma)}\tau\rho n^2 D^4 = \frac{1}{B(1+\sigma)}\tau\frac{p_0}{r_c T_0}n^2 D^4 = 6612N$. In the following this value is assimilated to $7000N$. Similarly, the target thrust in cruise is equal to $T_{cruise} = 1994N \approx 2000N$.

	Take-off	Cruise
Mach number M	0.2	0.75
Total temperature T_0 (K)	297.6	228.7
Total pressure p_0 (Pa)	101325.0	30090.0

Table 7.1. *Take-off and cruise characteristics*

The RANS simulation procedure and configuration used previously in chapter 6 (4 blades, single propeller, no hub) are kept in this part. Of course, this simulated configuration is not representative of the Open Rotor configuration (with 10 blades in the first row), because the induced effects from the hub and the downstream row of blades are not taken into-account, and the induced effects from other blades are reduced. Thus the flow topology and the efficiency of the reference HTC5 blade achieving target thrust at take-off ($\approx$ 7000 N) in the simulated conditions do not correspond to those in the Open Rotor configuration. In order to achieve target thrust at take-off in the simulated conditions, the HTC5 blade functions at a different pitch than the reference configuration considered in the previous chapters, for which the fixed model blade was designed.

The residuals decreased in the order of five orders of magnitude in converged cases. In cases with large flow separation, the residuals did not manage to decrease of a sufficient order of magnitude. As mentioned before, the convergence of the RANS calculations is hindered when the flow is detached because of the appearance non-negligible unsteady effects, which translate into oscillations on the aerodynamic forces. Nevertheless, the aerodynamic forces are converged in average, and the amplitude of the oscillations is lower than 5% of the corresponding aerodynamic average value in all simulated cases.

7.2.2. Pitch variation

First, the rate of vortex lift increase with respect to efficiency decrease was evaluated in the rotating HTC5 case by varying the pitch angle. For this purpose, the RANS calculations presented in chapter 6 for the HTC5 front blade at take-off were exploited. Vortex contribution to lift and thrust was evaluated using the method described in chapter 5. The results are presented in Table 7.2 in terms of a percentage of total values. Note the pitch angle is measured as the angle between the streamwise direction and the blade profile, at 70% of the tip radius. The pitch angle definition in the present work is such that its variation direction is opposite to that of the incidence. It is clear that as the pitch decreases (ie. as the incidence of the profiles increases), total thrust rises and a higher part of it is generated by the LEV contribution. However, this is achieved at the expense of efficiency. The corresponding wall pressure distributions and friction lines enabling to visualise the LEV for the tested pitch values are plotted in figure 7.3.

	pitch=40.4°	pitch=45.4°	pitch=48.0°	pitch=50.1°
total thrust (N)	12233	11370	10550	9772
vortex thrust contribution (%)	12.4	10.6	9.1	7.2
vortex lift contribution (%)	17.5	16.4	15.2	12.4
efficiency	0.4	0.48	0.52	0.57

Table 7.2. *Aerodynamic forces and efficiency, including vortex contribution, on the HTC5 blade at various pitch values, at a rotational speed* $n = 16.8$

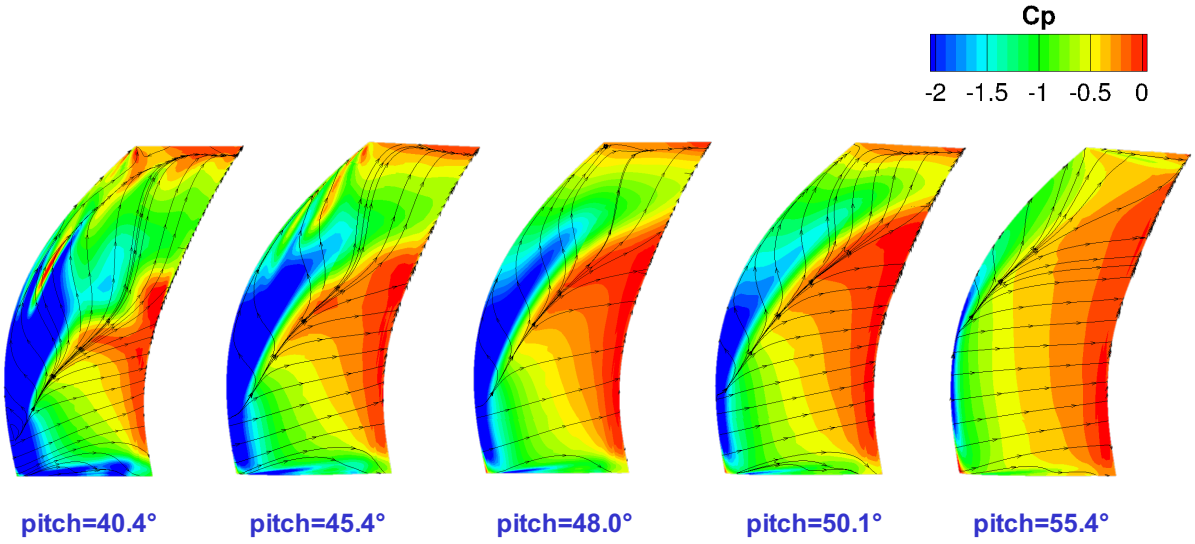

Figure 7.3. *Wall pressure coefficient and friction lines on the suction side of the HTC5 blade for different pitch values at take-off*

7.2.3. Rotational speed variation

The influence of the rotation velocity on the LEV and vortex lift was also investigated. Table 7.3 presents the variation of total thrust and efficiency, including vortex contribution, for the same pitch values as tested previously on the HTC5 blade, at a lower rotational speed $n = 13.3$.

	pitch=40.4°	pitch=45.4°	pitch=48.0°	pitch=50.1°
total thrust (N)	7078	6117	5392	4608
vortex thrust contribution (%)	13.0	10.2	5.9	2.9
vortex lift contribution (%)	18.2	14.2	8.4	4.5
efficiency	0.51	0.61	0.67	0.72

Table 7.3. *Aerodynamic forces and efficiency, including vortex contribution, on the HTC5 blade for various pitch values, at a rotational speed* $n = 13.3$

The target thrust at take-off is reached for a lower pitch value than for a rotational speed of $n = 16.8$. Indeed, for a lower rotational speed, it is even more necessary to count on vortex lift to generate the target thrust at take-off, which is why the profiles need to work at higher incidence. This appears very clearly in figure 7.9a and 7.9b, representing the superposed wall pressure distribution and spanwise thrust distribution on the HTC5 blade, for $n = 16.8$ and $n = 13.3$ respectively, at target thrust. Recall that in the simulated conditions (4 blades, single propeller, no hub), the HTC5 blade reaching target thrust at take-off functions at a higher pitch than the reference configuration considered in the previous chapters. This is why the friction lines indicate the absence of LEV in the reference HTC5 case considered hereafter. The LEV and associated depression on the suction side are much more prominent in figure 7.9b, for $n = 13.3$. Comparing red and blue markers in figure 7.5 provides another illustration of the same fact. In accordance with the results of [Zachariadis et al., 2013], decreasing rotation velocity and re-pitching the blade creates a bigger leading-edge vortex at iso-thrust. This leads to a lower efficiency in generating the same thrust. This can be related to the conclusion of part 7.1: the efficiency obtained in presence of a LEV is increased when rotational speed is increased (for a fixed advance velocity). In light of the above, rotational speed augmentation leads the LEV to reduce in size, which explains why the efficiency would get closer to that without LEV.

7.2.4. Influence of the blade geometry on vortex lift generation

After discussing the influence of the functioning parameters on vortex lift generation and efficiency, the aim of this part is to tackle the impact of the geometry. Blade geometries are compared under the constraint of iso-thrust at take-off and cruise. Depending on the geometry and the associated use of vortex lift at take-off, the target thrust will be attained for different efficiencies.

In the case of a change in geometry, it appears even more necessary to use a global criterion such as iso-thrust to perform comparisons. Indeed, it was attempted in this thesis to vary one shape parameter at a time and monitor its impact on the LEV topology and the aerodynamic characteristics. However, due to the strong coupling of the shape parameters, this approach did not enable to clarify which geometry changes were responsible for the changes in the behaviour of the blade. In other words, the physical phenomena around the blade are so coupled that it is not straightforward to find a set of dimensionless parameters which are independent from each other, and even more so for the LEV. Consequently, it seemed a better approach to allow any changes in the geometry provided that the result responded to the same applicative constraints, which the iso-thrust criterion could guarantee.

Another constraint on the tested geometries is that the foot radius and tip radius remain

unchanged compared to the HTC5 blade at full scale. The foot radius is maintained because we look for solutions with the same gas generator. Also, the tip radius is prescribed to be that of the HTC5 geometry in order to guarantee the same Reynolds number effects on the tested geometries, in accordance with the work of [Harbig et al., 2013].

All geometries are based upon stacked HTC5 profiles. The stacking axis is the vertical axis (along z) crossing the root profile in its middle. The spanwise thickness and twist distributions remain unchanged compared to the HTC5 case.

Reference geometry A: The reference is the HTC5 geometry.

Blade geometry B: The HTC5 chord law is simply multiplied by a factor of 0.6, which leads to a 40% blade surface reduction compared to the HTC5 case. The other form laws remain unchanged compared to the reference HTC5.

Blade geometry C: The HTC5 chord law is multiplied by a factor of 0.68, which leads to a 32% blade surface reduction compared to the HTC5 case. The other form laws remain unchanged compared to the reference HTC5.

Blade geometry D: The sweep is increased compared to geometry B. The chord law $c_D(r)$ is derived from the HTC5 chord law $c_A(r)$ as such :

$$c_D(r) = c_A(r)\,(1 - \frac{0.2\,r}{1 - r_{foot}})$$

The sweep law $dx_D(r)$ is prescribed as a spanwise shift of the profiles in the advance direction. It is deduced from the HTC5 sweep law $dx_A(r)$ as :

$$dx_D(r) = dx_A(r)\,(1 + \frac{0.6\,r}{1 - r_{foot}})$$

This leads to a 32% blade surface reduction compared to the reference HTC5 blade, just like case C.

The objective of this part is to show that vortex lift can help achieving the target thrust at take-off with a smaller blade surface, thus improving efficiency in cruise.

7.2.4.0.1. At take-off. The blades' behaviour at take-off is analysed first. Figure 7.4 pictures the tested blade geometries, at a rotational velocity $n = 16.8$. The wall pressure distribution and friction lines are featured for cases which correspond to target thrust (within ±4%). The total thrust, efficiency and vortex thrust contribution obtained for those geometries at take-off are presented in Table 7.4. Although their surface is lower, blades B, C and D are able to generate the target thrust at take-off. However they must rely on vortex contribution to achieve it, which is why their efficiency is reduced compared to the reference case. Comparing case B to cases C and D shows that this is even more the case as the blade surface is reduced.

In addition, it is worth noticing that a higher vortex contribution to lift and thrust is observed in case D compared to case C, while the corresponding efficiencies are very close. This seems to hint that the addition of sweep enables to generate vortex lift more efficiently.

This can be seen more clearly in figure 7.5 and 7.6 where thrust versus pitch and efficiency versus thrust polars are plotted, for a take-off configuration. Those graphs enable to distinguish more clearly the differences between cases C (purple dash) and D (green cross), which are at

iso-surface. Even though the aerodynamic performance of both cases are comparable, figure 7.5 shows that for a given pitch, case C produces a lower thrust than case D. Moreover, figure 7.6 shows that Case D reaches a given thrust with a slightly higher efficiency compared to case C.

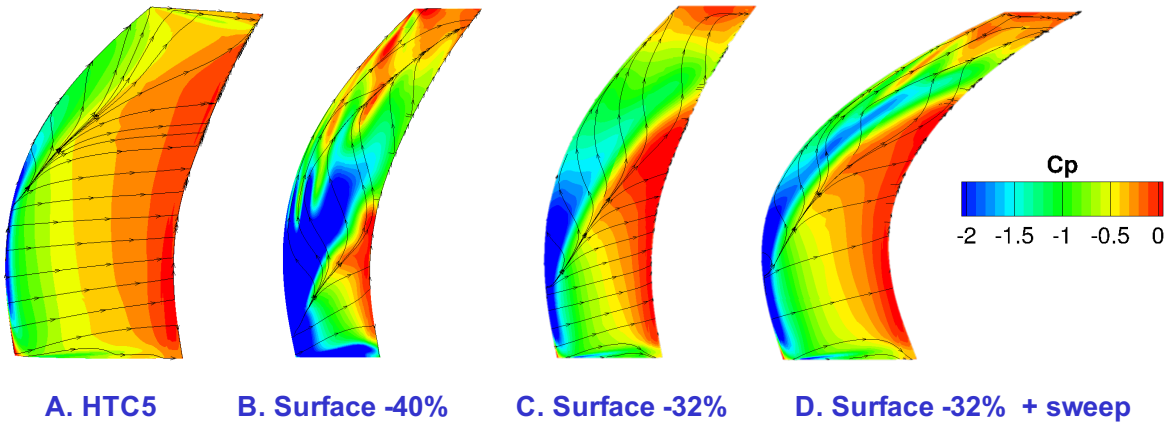

Figure 7.4. *Wall pressure coefficient and friction lines on the suction side of the tested blade geometries, at take-off, for* $n = 16.8$

	A. HTC5	B. Surface -40%	C. Surface -32%	D. Surface -32% + sweep
total thrust (N)	6910	7190	7124	7284
vortex thrust (%)	1.5	16.7	6.1	8.3
vortex lift (%)	2.4	22.6	10.6	14.8
efficiency	0.69	0.39	0.588	0.581

Table 7.4. *Comparison of aerodynamic forces and efficiency, including vortex contribution, at iso-thrust, in take-off configuration, for* $n = 16.8$

Increasing the sweep seems to help increasing efficiency at iso-thrust and iso-surface. A possible explanation is that for cases with higher sweep, the LEV manages to remain close the leading-edge on a longer portion of the span, and reaches the trailing-edge at higher spanwise positions. This will influence the aerodynamic forces: as it was observed in chapter 6, the spanwise lift distribution starts decreasing as soon as the LEV reaches the trailing-edge and leaves the blade.

Fig 7.9 illustrates this fact. The spanwise lift distributions obtained for cases B, C and D are depicted, and superposed with the wall pressure distribution, for various blades at iso-thrust. Blade B, of lower surface than cases C and D, relies on the presence of a huge LEV to generate target thrust at take-off. However, because the chord is short, this big LEV reaches the trailing-edge at a quite low chordwise position $\frac{r}{R} \approx 0.7$. For $r \geq 0.7$, the lift distribution starts decreasing. For cases C and D, the LEV stays close to the leading-edge for a longer portion of the span. The LEV reaches the trailing-edge at a slightly higher spanwise position in case D compared to case C.

The literature review in chapter 1 showed that the sweep played a less crucial role for LEV generation in a rotating case (compared to a fixed case). Here the role of the sweep is highlighted in the sense that it displaces further outward (towards the tip) the point where the LEV reaches the trailing-edge, and enables to more efficiently generate vortex lift.

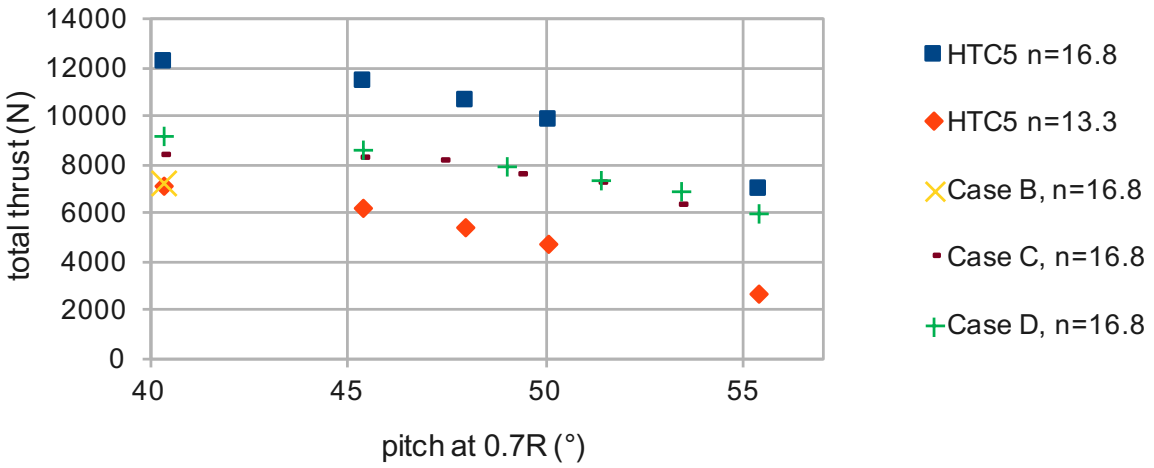

Figure 7.5. *Thrust with respect to pitch at take-off for tested cases*

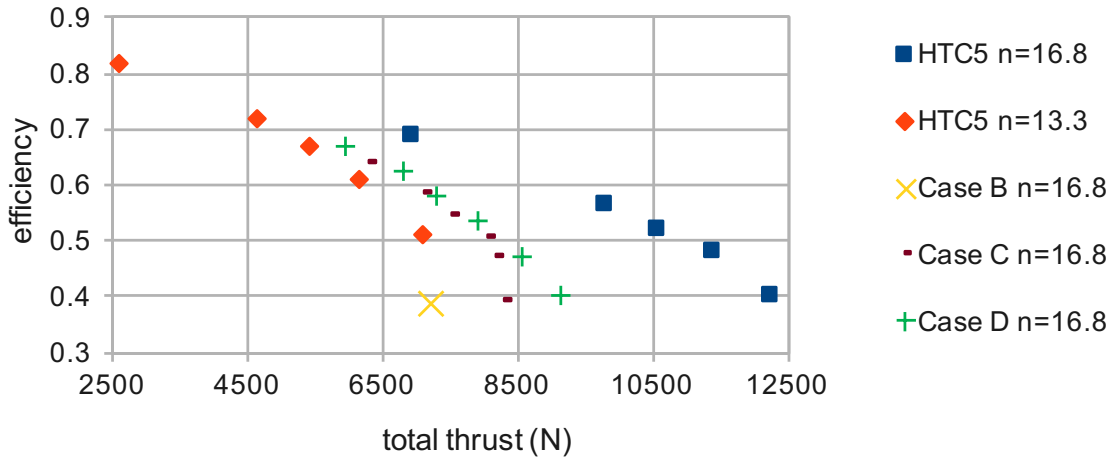

Figure 7.6. *Efficiency with respect to thrust at take-off for tested cases*

7.2.4.0.2. In cruise. Blade geometry concept D is evaluated in cruise with respect to the reference HTC5 case. The results are plotted in Figures 7.7 and 7.8. Due to the lower thrust needed in cruise, the incidence of the profiles is reduced compared to take-off, and no LEV appeared in neither case. Figure 7.7 shows that case D must work at a slightly higher pitch compared to the reference case in order to generate the same thrust. Indeed, case D has a lower surface, thus the profiles need to work at a slightly higher incidence in order to achieve the target thrust in cruise. However, figure 7.8 indicates that depending on the target thrust to reach, the fact that case D must work at a higher incidence is compensated by the fact that the drag is lower because of a lower chord. For the target thrust of 2000 N, the efficiency is one count higher in case D compared to case C.

Although the tested geometries were not optimised, this first study demonstrates the potential of relying on vortex lift to reach target thrust at take-off with a lower surface. Although the efficiency is reduced at take-off (in the order of 9 counts for case D), it can be increased in cruise (in the order of 1 count for case D). This could be interesting given the comparative duration of these operating phases. Further studies are needed to determine the applicability

of such concepts and evaluate the most promising geometries.

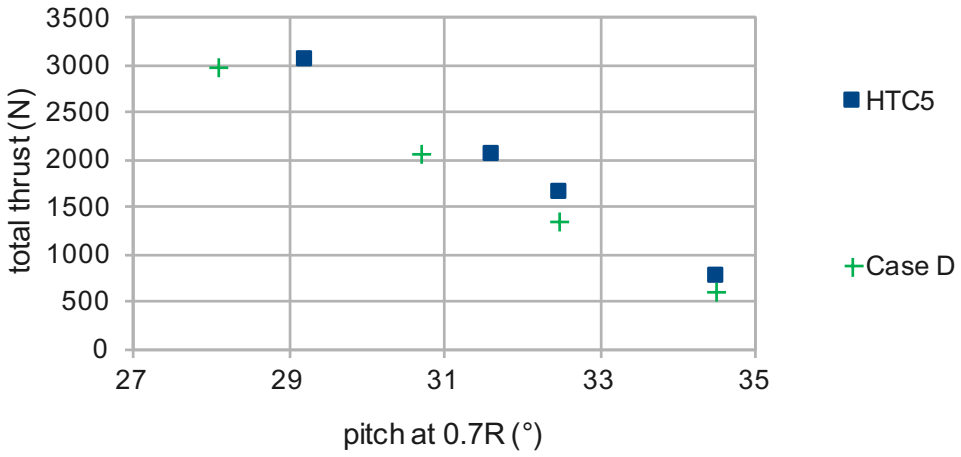

Figure 7.7. *Thrust with respect to pitch in cruise for tested cases*

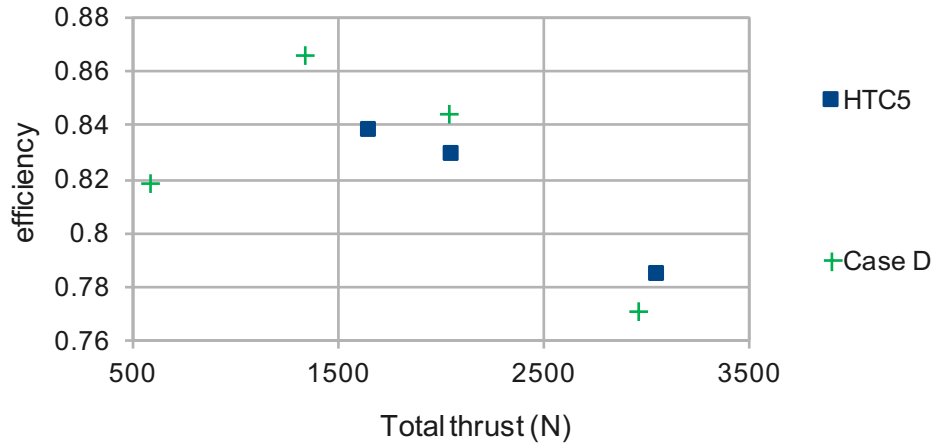

Figure 7.8. *Efficiency with respect to thrust in cruise for tested cases*

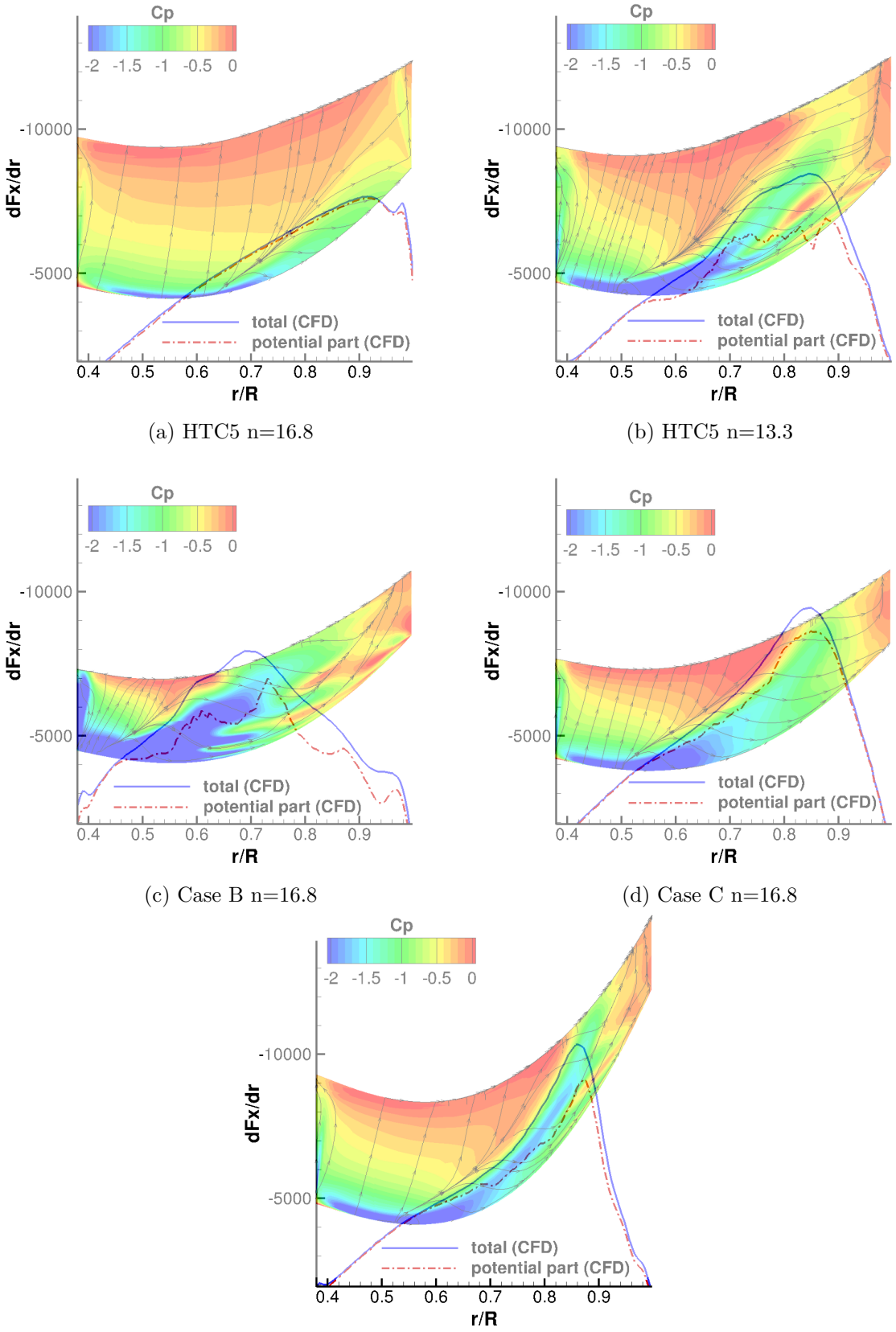

(a) HTC5 n=16.8

(b) HTC5 n=13.3

(c) Case B n=16.8

(d) Case C n=16.8

(e) Case D n=16.8

Figure 7.9. *Superposition of the spanwise distribution of thrust* $\frac{dFx}{dr}$ *(in N/m) with the wall pressure distribution and friction lines for different blade geometries at iso-thrust, at take-off*

7.3. Summary and perspectives

In a nutshell, the exploratory calculations performed in this chapter demonstrate the interest of vortex lift enhancement at take-off. Although vortex lift is generated at the expense of efficiency, it enables to achieve the target thrust at take-off with a blade of lower surface, which may therefore have a slightly increased efficiency in cruise. In addition, sweep enables to generate vortex lift with a higher efficiency. However, it is worth mentioning at this stage that geometry D is a proof of concept rather than an optimised blade geometry, which should also account for mechanical constraints. It would also be interesting to analyse its wake and shed vortex characteristics, in order to provide a first estimation of the acoustic performance of an Open Rotor configuration. The work of [Zehner et al., 2016] provides clues on this subject, as it covers the acoustic response of a blade of the downstream propeller impacted by Batchelor and Lamb-Oseen vortices. This study showed that the tangential and axial velocities of the impacting vortex influenced the frequency content of the noise level.

Another perspective would be to investigate whether forward swept blades (as opposed to backward swept blades tested until now) would generate a LEV forming close to the blade tip and progressing towards the root. This may be interesting from an acoustic point of view, because the spanwise lift distribution would then be more homogeneous. However, as mentioned in the literature survey, sweep is not the main parameter driving the formation of the LEV on a rotating case. Indeed, rotation alone is sufficient to provide an increasing circulation distribution along the span, which facilitates the appearance of the leading-edge vortex. Therefore, the twist would need to be adapted with respect to the HTC5 case, in order to compensate for the impact of rotation on the spanwise lift distribution.

Conclusion and perspectives

Summary and discussion of the main results of this thesis

First, this study enabled to characterise the LEV on a model blade whose circulation distribution was representative of the HTC5 propeller blade at take-off. In particular, the investigation focused on the LEV core characteristics. This constituted a step forward compared to previous studies on propeller blades, which either observed the LEV through RANS calculations, or experimentally using friction line visualisations. The need to characterise this structure was also justified by the assessed variability of LEV core topology depending on the sweep and incidence in the case of Delta wings, and the addition of extra LEV formation and stability mechanisms depending on the Reynolds number and the presence of rotation. The LEV on the model propeller blade was found to be an elongated, close-wall structure, with a wake-like core profile.

Meanwhile, the ability of RANS $k-\omega$ SST calculations to reproduce the characteristic dimensions and axial velocity in the LEV was assessed. In particular, the reattachment line obtained for fully turbulent calculations was found to be in perfect agreement with the experimental friction line results, taking into account the uncertainties of both methods. As for the other compared quantities, RANS calculations were found to give a satisfying agreement with the experiment, in the sense that they enabled to recover the main LEV core characteristics of interest in this study. In addition, the analysis of the time-resolved behaviour from instantaneous PIV images and hot wire measurements supported the fact that transition to turbulence was driven by flow separation. The Kelvin Helmholtz instability in the LEV upper shear layer was found to be a wideband phenomenon, which did not influence the circulation of the LEV at first order. The LEV can be considered as a quasi-steady structure with respect to the impact it has on lift.

The LEV on the model HTC5 propeller blade was found to contribute to lift, although this contribution was relatively low (5% of total lift). This finding was obtained thanks to an algorithm which was built to estimate vortex lift contribution from RANS wall pressure fields. This algorithm was validated by means of comparisons with other methods on Delta wing cases. The characteristics of the LEV as an elongated structure with a wake-like core suggest a similitude with Delta wing LEVs at low sweep and incidence, for which vortex lift is small according to the literature ([Hill, 1957, Wentz and Kohlman, 1971, Lee and Ho, 1990, Gursul et al., 2005]), therefore supporting the statement that vortex lift is limited on the model propeller blade.

Besides characterising the LEV topology and aerodynamic impact on the HTC5 blade at take-off, this thesis provides new results regarding vortex lift spanwise variation, and dependency on the blade's geometry and functioning parameters. Indeed, a 1D vortex lift model was developed, which takes into account spanwise geometric laws, inflow velocity and rotation velocity. Coupled to the Blade Element Momentum Theory (BEMT), this model satisfactorily predicts integrated aerodynamic characteristics, such as total lift, thrust or efficiency, both on the Delta wing case and the rotating HTC5 case. The spanwise vortex lift distribution is reasonably predicted in the rotating HTC5 case.

This 1D vortex lift model is based on the leading-edge suction analogy [Polhamus, 1966],

which was transformed to a profile-dependent version. One of the most promising results lies in the model's capacity to account for three-dimensional effects at first order, even though the induced velocities between profiles are not taken into account. This is performed by first making the assumption that the profiles are independent, then correcting it using cumulative functions which multiply the spanwise vortex lift distribution. Those cumulative functions have a prescribed linear or parabolic evolution with respect to the spanwise position, and only rely on a fitted constant which does not depend on the wing's working incidence. In the case of Delta wings, the fitting constant does not depend on the sweep either. The modelling approach developed in this thesis represents a step forward compared to the Polhamus model, and to studies which applied the leading-edge suction analogy directly at the profile level, using Polhamus coefficient tabulated for Delta wings [Thielicke et al., 2011]. Indeed, the present approach enables to better account for the blade's geometry and was shown to be more representative on the rotating HTC5 case.

On a more applicative note, this thesis puts forward that it could be interesting to take vortex lift into account for propeller blade's design. Although vortex lift always decreases efficiency for a tractive propeller blade, it reduces the blade surface necessary to generate target thrust at take-off. This can translate into a chord reduction, which enables to reduce profile drag in cruise, therefore allowing for higher cruise efficiencies, though at the expense of lower take-off efficiencies. This could be of interest considering the respective duration of both operating phases. In addition, sweep was found to more efficiently create vortex lift. This result enables to elaborate on the role of the sweep in a rotating case, where it is not essential to LEV generation, but rather helps generating vortex lift more efficiently. Preliminary blade concepts were presented to support these findings. The work presented in this thesis opens up new possibilities for the design of propeller blades.

Future work

In order to assess the interest of vortex lift enhancement at take-off on optimised geometries, it is clear that the parametric study presented in chapter 7 should be broadened and extended. In this context, it would be interesting to use the 1D modelling methodology developed in this thesis, in order to launch quick calculations yielding the aerodynamic performance of a given geometry, including the LEV contribution. Such a tool could even be encapsulated in an optimisation program, which would give the most promising blade shapes, while authorising flow separation at take-off.

However, in order to achieve this objective, the present vortex lift model should be improved first. Several improvement paths can be tested. First, an important limitation of the present model is that the velocities induced between profiles are not taken into account. Implementing the 1D vortex lift model in the generalised lifting-line method would likely increase the representativity of the predictions compared to CFD.

Second, the prediction of the LEV formation point is missing in the present model. For now, the onset of the LEV is assumed to be the apex. This assumption was taken because the BEMT lacks one degree of freedom, as it only considers two induced velocities out of three (one for each direction in space). Thus, there was little hope to accurately capture the LEV separation point, which is why an empirical criterion was used instead. Probably, the use of the lifting line method would enable to better predict the spanwise position where the LEV is formed, provided that an accurate flow separation criterion, depending on the profile, is added to the model (for instance the criterion of [Ramesh and Gopalarathnam, 2011, Ramesh et al.,

2012] could be tested).

Finally, the 1D vortex lift model would probably be more representative if the fitting constants in the cumulative functions were expressed in function of geometrical parameters or physical quantities. Achieving a "complete" model in this sense would probably require a better understanding of the link between the LEV characteristics and its contribution to lift. In this thesis, this link was evoked but remained mostly qualitative and based on the analogy between the LEV shape and its contribution to lift on Delta wings. It would thus be of interest to investigate how the LEV parameters such as its vorticity, its core velocity or the distance of its center to the wing surface impact its contribution to lift. The studies of [Slomski and Soleman, 1993, Ford and Babinsky, 2013] provide ideas to start with on this subject. The experimental data acquired in this thesis could also be used for that purpose, and could provide a better understanding of LEV propagation mechanisms by exploiting the correlations between the unsteady characteristics on the three surveryed planes.

A

HTC5 blade spanwise form laws

A.1. HTC5 blade (rotating)

In the case of the rotating HTC5 blade, R refers to the blade tip radius.

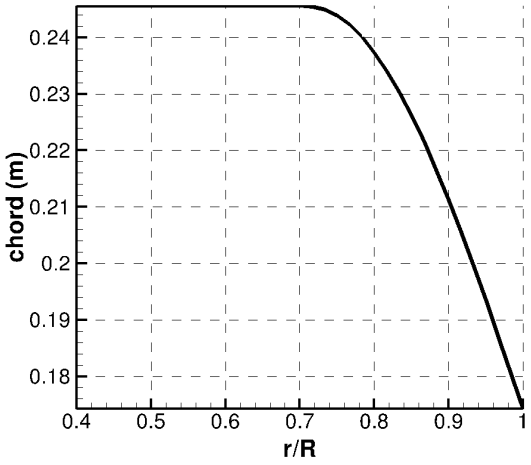

(a) chord law at a scale of 2/5

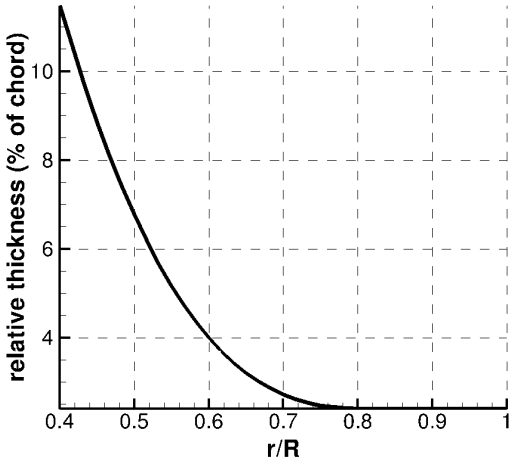

(b) relative thickness law

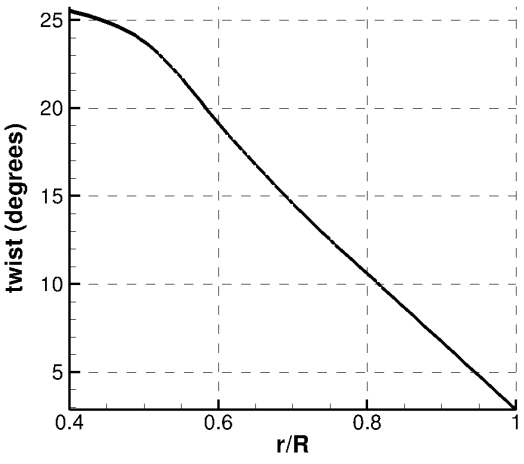

(c) HTC5 blade twist law

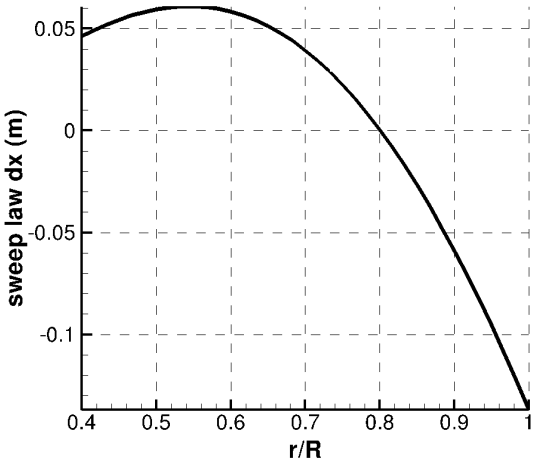

(d) sweep law (in terms of spanwise shift of the profiles in advance direction) at a scale of 2/5

Figure A.1. *Spanwise form laws of the rotating HTC5 blade. R refers to the blade tip radius.*

A.2. HTC5 fixed blade

The spanwise form laws of the HTC5 fixed blade are the same as those of the rotating blade, except for the twist. In the case of the HTC5 fixed blade, R refers to the span.

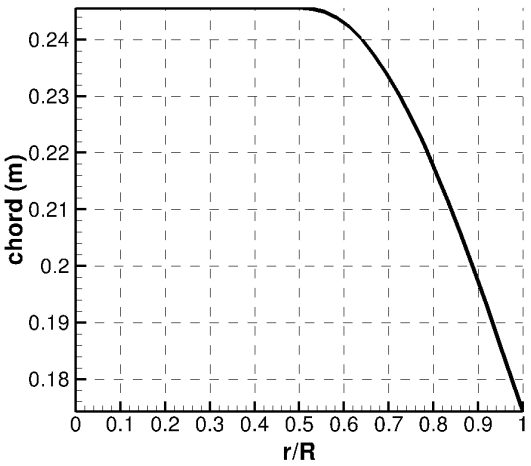

(a) chord law at a scale of 2/5

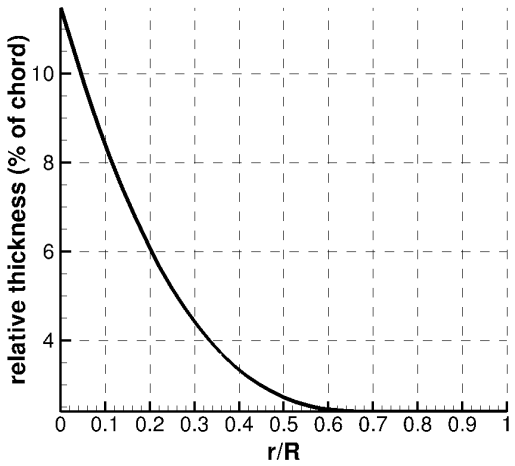

(b) relative thickness law

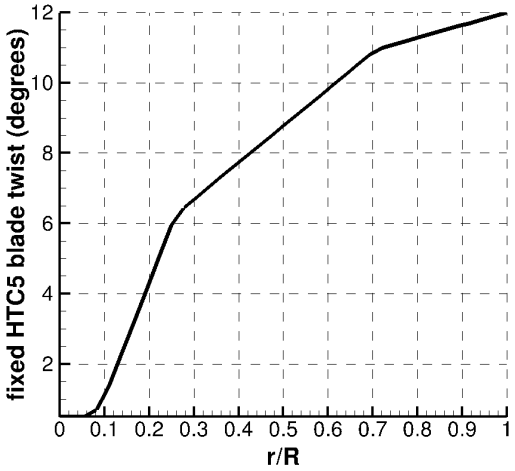

(c) fixed HTC5 twist law

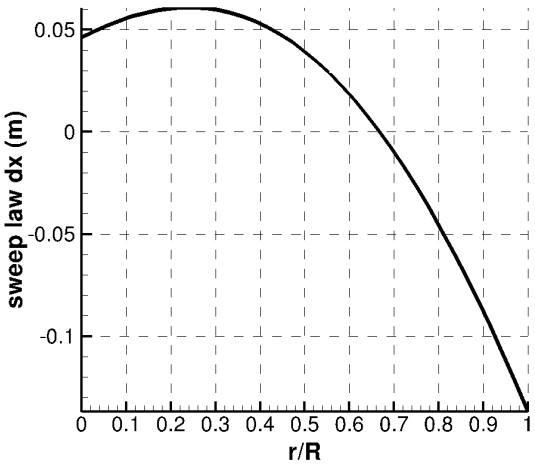

(d) sweep law (in terms of spanwise shift of the profiles in advance direction) at a scale of 2/5

Figure A.2. *Spanwise form laws of the fixed HTC5 blade. R refers to the span.*

B

BEMT implementation

The BEMT implementation used in chapter 6 is detailed in the following.

B.1. Inputs

The inputs to the program are :

- Inflow conditions: upstream Mach number, sound velocity in air, volumic mass, rotational velocity in rad/s
- Geometric parameters: span R, spanwise profile, thickness, chord, sweep and twist Θ laws, number of blades B, pitch angle Ψ
- Airfoil symmetric NACA CL and CD polars, for thickness values of 6%, 8%, 10%, 12% and 15% of chord
- Polhamus total (full Delta wing) Kp and Kv coefficient tables extended to low sweeps

B.2. Algorithm

First, the axial and radial induction factors are initialised to $a = 0$ and $a' = 0.001$ respectively. While a and a' are not converged (threshold lower than 0.01% of the difference), the following steps are taken. All variables are supposed to depend on the spanwise position r.

1. Calculation of the effective incidence α (see figure B.1).

   $$\alpha = \zeta - \beta$$

   where

   $$\beta = arctan(\frac{U_{inf}\,(1+a)}{\Omega r\,(1-a')})$$

   In the LPC2 formulation which is used in this work,

   $$\zeta = \frac{\pi}{2} - \Psi + \Theta$$

2. Evaluation of lift and drag coefficients CL and CD. For sections between the foot and apex $r \leq r_0$, they are interpolated from the polars. For $r \geq r_0$, they may be calculated

using various vortex lift models (see section 6.3.2). In any case, the lift and drag coefficients are divided by the Prandtl-Glauert factor $\sqrt{1-M^2}$ to account for compressibility effects.

3. Calculation of thrust and torque coefficients C_T and C_C.

$$C_T = CL\,cos\beta - CD\,sin\beta$$

$$C_C = CL\,sin\beta + CD\,cos\beta$$

4. Calculation of the Shen tip loss factor.

$$g = e^{-0.125\,(B\,\frac{\Omega\,R}{U_{inf}} - 21)} + 0.1$$

$$F = \frac{2}{\pi}\,arccos(e^{-g\,\frac{B\,(R-r)}{2\,r\,sin\beta}})$$

5. Re-evaluation of induction factors, taking into account a relaxation coefficient to foster convergence. This coefficient k was set to $k = 0.1$. Minimal and maximal bounds are given for the induction factors, $a_{min} = a'_{min} = -0.1$ and $a_{max} = a'_{max} = 0.4$. Indeed, it is known that the following formulas do not apply for induction factors with orders of magnitude which are too large.

$$a = max(\,a_{min}\,,\;min(\,a_{max}\,,\;a + k\frac{1.}{\frac{4\,F\,sin^2\beta}{\sigma'\,C_T} - 1} - a)$$

$$a' = max(\,a'_{min}\,,\;min(\,a'_{max}\,,\;a' + k\frac{1.}{\frac{4\,F\,cos\beta\,sin\beta}{\sigma'\,C_c} + 1} - a')$$

where σ' is the local blade solidity $\sigma' = \frac{B\,c}{2\,\pi\,r}$

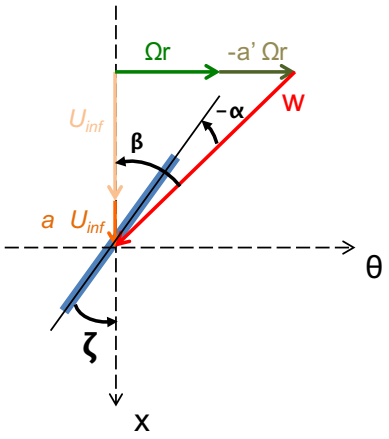

Figure B.1. *Schematic view of a blade profile with angles and induced velocities corresponding to the formulas used in the present BEMT implementation*

B.3. Multiple linear interpolations

Multiple linear interpolations are performed to evaluate lift and drag coefficients depending on the airfoil thickness, incidence and Mach number at spanwise position r. The polar derivatives, which are required for the 1D vortex lift model, are also calculated based on "linearly interpolated" polars.

C

Summary in French

Afin de garantir un bon rendement en croisière, les hélices rapides ont généralement des profils fins et peu cambrés, avec de la flèche en tête de pale. Au décollage, ces profils doivent travailler à forte incidence pour générer la traction cible, ce qui facilite le décollement de l'écoulement au bord d'attaque. La figure C.1 représente les lignes de frottement sur une pale d'Open Rotor de type HTC5 au décollage. On peut observer une zone de recirculation le long du bord d'attaque, entre l'apex et le bout de pale. C'est la trace d'une structure tourbillonnaire conique se formant le long du bord d'attaque.

Cette étude se fonde sur le constat que ce tourbillon de bord d'attaque est qualitativement similaire aux tourbillons de bord d'attaque d'ailes Delta (appelés aussi tourbillons d'apex d'aile Delta). Sur les ailes Delta, ces tourbillons exacerbent la dépression à l'extrados, donc contribuent à la portance [Hill, 1957, Wentz, 1968, Manie et al., 1978b]. Cette contribution, appelée portance tourbillonnaire, se fait toutefois aux dépens du rendement. Cette thèse a pour objectif de caractériser l'impact du tourbillon de bord d'attaque sur les performances aérodynamiques des hélices rapides au décollage afin d'en déterminer l'intérêt pour des concepts innovants de pale.

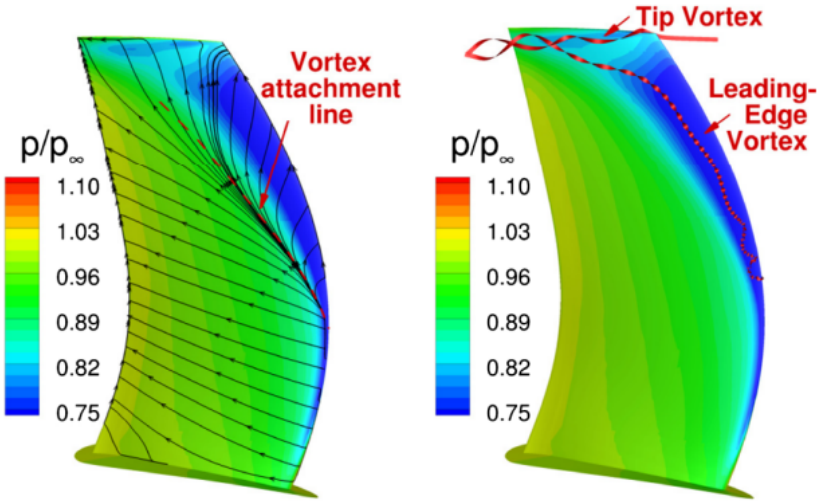

Figure C.1. *Champ de pression à la paroi et lignes de frottement pariétales sur une pale d'Open Rotor de type HTC5 au décollage. Source : [Delattre and Falissard, 2015]*

C.1. État de l'art sur le tourbillon de bord d'attaque

Dans un premier temps, l'étude bibliographique a permis de dresser un état de l'art des connaissances sur le tourbillon de bord d'attaque (TBA), afin de donner un cadre pour la caractérisation de la structure tourbillonnaire observée sur les hélices rapides.

Cette étude décrit la topologie de l'écoulement sur les ailes Delta en fonction de l'incidence, ainsi que sa sensibilité au nombre de Reynolds de l'écoulement amont et aux paramètres de forme de l'aile. Notamment, à forte flèche ($\phi \geq 65$ degrés), les tourbillons d'apex sont quasiment circulaires, avec des sur-vitesses dans le cœur. À même incidence mais pour des flèches moins élevées, ils sont plus allongés, proche paroi, et peuvent comporter des sous-vitesses dans le cœur [Gursul et al., 2005].

Portance tourbillonnaire. Plusieurs approches d'identification et de modélisation de la portance tourbillonnaire ont été proposées au cours du développement de l'aile Delta. Ces approches montrent que la portance tourbillonnaire n'est pas un concept clairement défini. En effet, ce concept implique que la portance créée par le TBA pourrait être isolée de la portance globale de l'aile. Autrement dit, il existerait une portance de référence à laquelle s'ajouterait la contribution tourbillonnaire. Toutefois, physiquement, cette référence n'a pas de raison d'être car on ne peut pas supprimer le TBA tout conservant les mêmes conditions d'écoulement amont et d'incidence. Deux approches principales pour définir la portance tourbillonnaire ressortent de la littérature. La première [Legendre, 1952, Brown and Michael, 1954, Brown and Michael, 1955, Mangler and Smith, 1959] considère que la portance tourbillonnaire s'ajoute au champ de pression donné par la solution potentielle de l'écoulement autour de l'aile. Le TBA est modélisé dans le formalisme des écoulements potentiels par un tourbillon linéique. Le problème est résolu analytiquement en 2D en utilisant l'hypothèse d'aile élancée. Comme la portance prédite par la théorie des écoulements potentiels est linéaire avec l'incidence, cette approche revient à identifier la portance tourbillonnaire avec la part non linéaire de la portance. La deuxième approche est celle de Polhamus [Polhamus, 1966], consistant à assimiler la portance tourbillonnaire à la force d'aspiration au bord d'attaque s'étant orientée perpendiculairement à l'extrados. Cette théorie s'applique plus largement aux ailes Delta de forte flèche ($\phi \geq 65$ degrés) que les théories fondées sur l'hypothèse d'aile élancée. Elle requiert l'utilisation de coefficients tabulés à partir de polaires d'ailes Delta de différentes flèches, mais dans lesquels la dépendance à la flèche n'est pas explicite. Cependant, la théorie de Polhamus sur-estime la portance tourbillonnaire pour des ailes de plus faible flèche. En effet, plusieurs études suggèrent que la part de portance tourbillonnaire devrait diminuer avec la flèche [Hill, 1957, Wentz and Kohlman, 1971, Lee and Ho, 1990, Gursul et al., 2005], bien qu'il n'existe pas à ce jour de modélisation explicite de la portance tourbillonnaire prenant en compte cette influence.

Influence de la rotation. Les tourbillons de bord d'attaque ont été peu étudiés sur les hélices rapides. Ils ont été observés au travers de simulations RANS [Zachariadis et al., 2013], ou visualisés expérimentalement à travers leurs lignes de frottement pariétales [Schülein et al., 2012, Vion, 2013]. Afin de comprendre l'effet de la rotation sur les caractéristiques et l'impact aérodynamique des TBA, on s'intéresse à des études appliquées aux ailes d'insecte (cas tournants à faible nombre de Reynolds $10^2 \leq Re \leq 10^4$). En effet, il est connu que les insectes utilisent les tourbillons pour générer de la portance [Sane, 2003], et ces mécanismes ont fait l'objet d'études récentes dans le cadre du développement de drones. Ces études montrent que la topologie des TBA sur les voilures tournantes est sensible aux mêmes paramètres que sur

les ailes Delta. Toutefois, d'autres paramètres spécifiques à la rotation s'y ajoutent [Lentink and Dickinson, 2009b], comme le nombre de Rossby, qui dépend du rapport d'avancement et de l'allongement de la voilure. En effet, les études sur les ailes d'insecte [Lentnik et al., 2008, Lentink and Dickinson, 2009a, Lentink and Dickinson, 2009b, Harbig et al., 2013, Garmann et al., 2013, Garmann and Visbal, 2014] soulignent l'influence de la rotation sur la formation et le maintien du TBA sur les voilures tournantes. Le fait que le TBA soit quasi-stationnaire au dessus de l'aile indique que la majeure partie de la vorticité est transportée le long du bord d'attaque jusqu'au bout de pale, ou détruite par interaction avec la vorticité de signe opposé dans la couche limite [Wojcik and Buchholz, 2014b]. La plupart de la vorticité n'est donc pas advectée vers le bord de fuite. Cela est lié à la présence d'un écoulement le long de l'axe du tourbillon. [Maxworthy, 2007] montre, en utilisant une approche théorique sur un modèle de tourbillon conique, que l'écoulement axial dans le cœur du tourbillon a deux origines qui s'additionnent : d'une part, la forme cônique du tourbillon, d'autre part les effets centrifuges causés par la rotation de la pale. [Garmann and Visbal, 2014] observe qu'à grand nombre de Reynolds, les efforts liés au gradient de pression sont majoritaires par rapport aux efforts d'inertie d'entraînement et de Coriolis dans le cœur du TBA. Les études de [Aono et al., 2007, Lentink and Dickinson, 2009b] semblent indiquer que le gradient de pression, lorsqu'il est présent à haut Reynolds $Re \geq 10^3$, est la principale cause de l'écoulement axial dans le cœur du TBA, donc de la formation et du caractère quasi-stationnaire du TBA. À bas Reynolds, ce sont plutôt des mécanismes liés aux forces d'inertie d'entraînement et de Coriolis tels que le pompage d'Ekman qui en seraient responsables. Ainsi, à plus grand nombre de Reynolds, les mécanismes de formation du TBA se rapprochent de ceux d'un cas fixe, au sens où les forces d'inertie liées à la rotation jouent peu dans la formation de l'écoulement axial le long de l'envergure.

La sensibilité de la topologie du cœur du TBA aux paramètres de forme et de fonctionnement dans le cas de l'aile Delta, et à la présence de rotation, justifient la nécessité de caractériser le TBA sur les hélices transsoniques rapides.

C.2. Principaux résultats de la thèse

C.2.1. Caractérisation du tourbillon de bord d'attaque sur une pale représentative

Dans un premier temps, on a caractérisé le TBA d'une pale dont la répartition de circulation en envergure est représentative d'une pale d'Open Rotor de type HTC5 au décollage. Cette pale est fixe et a été développée dans la thèse de Laurence Vion [Vion, 2013] afin de faciliter les expériences en soufflerie. Elle a les mêmes paramètres géométriques que la pale HTC5, mis à part le vrillage qui est adapté afin que la répartition de circulation adimensionnée en envergure soit conservée malgré le fait que la pale soit fixe. Dans cette thèse, l'utilisation de la pale fixe est justifiée car la répartition de circulation en envergure prend en compte les effets du gradient de pression. Or, le post-traitement d'un calcul RANS tournant de la pale HTC5 a confirmé que le gradient de pression était d'un ordre de grandeur supérieur aux forces d'inertie, donc déterminait au premier ordre la physique du TBA. Bien qu'une seule géométrie ne soit étudiée, la répartition de circulation considérée est générique et représentative d'une pale d'hélice rapide de faible allongement.

En particulier, l'étude s'est concentrée sur les caractéristiques du cœur du TBA. Trois plans

de PIV résolue en temps normaux à la paroi ont été effectués afin de visualiser le cœur du tourbillon de bord d'attaque à 67%, 72% et 79% d'envergure. Par ailleurs, un calcul RANS $k-\omega$ SST, puis un calcul RANS avec modèle de transition (AHD-Gleyzes) ont été réalisés dans les conditions expérimentales. La comparaison des champs PIV et RANS a montré que le TBA sur la maquette était une structure aplatie et proche paroi, avec des vitesses axiales plus faibles que l'écoulement amont (voir Figure C.2).

Par ailleurs cette étude a montré la capacité des calculs RANS à reproduire de façon satisfaisante les caractéristiques du TBA d'intérêt pour cette étude : ses dimensions caractéristiques et sa vitesse axiale. En particulier, la ligne de rattachement prédite par les calculs RANS tout turbulents est en parfait accord avec les résultats donnés par les lignes de frottement obtenues expérimentalement (en prenant en compte les incertitudes données par les deux méthodes). L'analyse des caractéristiques instationnaires à travers les instantanés de PIV et des mesures fil chaud montre que la transition à la turbulence est déclenchée par le décollement de l'écoulement au bord d'attaque. L'instabilité de Kelvin-Helmholtz présente dans la couche de mélange englobant le TBA est un phénomène large-bande, qui ne correspond pas aux modes POD les plus énergétiques de l'écoulement, et dont l'impact sur les variations de circulation du TBA est négligeable (celles-ci sont estimées à 3,4% de la circulation du TBA). Cela permet d'expliquer pourquoi les calculs RANS avec prise en compte de la transition donnent des résultats très peu différents des calculs RANS tout turbulents, sauf à 79% d'envergure où ils sont plus représentatifs. En effet, la turbulence s'établit rapidement en aval du point de rattachement.

La structure allongée du TBA, avec de faibles vitesses dans le cœur, permet de faire une analogie qualitative avec les tourbillons d'apex d'aile Delta à faible flèche et faible incidence. Or d'après la littérature, leur contribution à la portance serait plus faible que celle des tourbillons d'apex d'ailes Delta à forte flèche ([Hill, 1957, Wentz and Kohlman, 1971, Lee and Ho, 1990, Gursul et al., 2005]). Ainsi, on peut faire l'hypothèse que le TBA contribue à la portance, mais que cette contribution est relativement limitée sur la pale fixe HTC5.

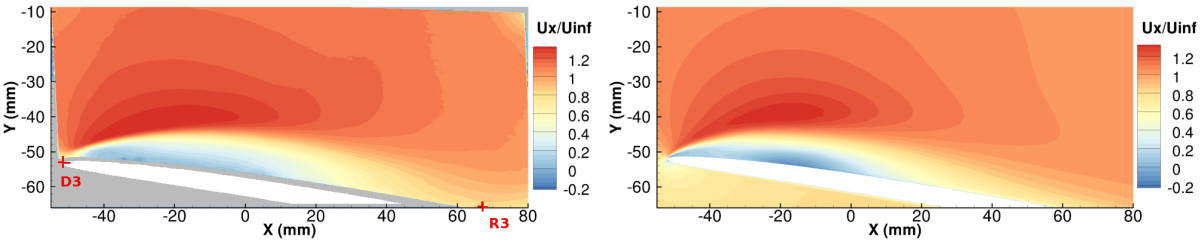

(a)

Figure C.2. *Champs de vitesse moyenne dans la direction de la corde U_x à 79% de l'envergure. Les grandeurs sont adimensionnées par la vitesse amont U_{inf}. Le champ PIV moyenné sur 2000 instantanés (à gauche) est comparé au champ RANS $k-\omega$ SST (à droite).*

C.2.2. Développement d'un algorithme d'estimation de la portance tourbillonnaire

L'étape suivante dans la démarche était donc d'estimer la portance tourbillonnaire sur la pale HTC5. Pour cela, un algorithme a été développé à partir des champs de pression pariétale issus de calculs RANS. Cet algorithme est fondé sur l'analyse des profils de coefficients de pression pariétaux Cp. En effet, la dépression induite par le tourbillon de bord d'attaque à l'extrados

se traduit par une "bosse" sur les profils de pression, corrélée à la position du tourbillon de bord d'attaque et à la surface impactée. L'idée était donc de relier cette bosse à la portance tourbillonnaire. Pour cela, il était nécessaire de définir une référence, c'est-à-dire, le profil de coefficient de pression que l'on obtiendrait en l'absence de TBA. L'hypothèse la plus immédiate consiste à repérer les points d'inflexion entourant la (ou les) bosse(s), et à définir la référence comme l'interpolation linéaire du profil de Cp entre ces points.

Cette hypothèse a été évaluée en appliquant l'algorithme au cas d'une aile Delta de 65 degrés de flèche à différentes incidences. En effet pour cette valeur de flèche, on dispose de plusieurs moyens de comparaison. Le premier est l'estimation de la portance tourbillonnaire réalisée par Polhamus. Le second découle de l'autre approche de définition de la portance tourbillonnaire, comme supplément au résultat donné par un calcul potentiel. Il s'agit en effet de réaliser un calcul de l'écoulement autour de l'aile en utilisant la méthode des panneaux, qui donnera une solution potentielle sans tourbillon de bord d'attaque. L'écart entre la portance donnée par ce calcul et celle obtenue par un calcul RANS est assimilé à la portance tourbillonnaire. La comparaison de ces différentes approches d'estimation de la portance tourbillonnaire est donnée dans le tableau C.1. L'algorithme utilisant les coefficients de pression pariétaux donne des résultats proches de ceux obtenus par application de la méthode des panneaux. Cela permet de valider le caractère physique de cette méthode. La différence entre les résultats donnés par l'application de la méthode de Polhamus et ceux donnés par la méthode des panneaux peut s'expliquer par la différence de définition de la portance tourbillonnaire dans les deux cas.

Incidence (degrés)	Cp CFD (%)	Potentiel (%)	Polhamus (%)
10	4.3	6.0	21.0
15	9.6	10.6	28.8
20	11.2	14.8	35.5
25	12.2	15.1	41.3

Table C.1. *Ratio de portance tourbillonnaire à la portance totale en % pour une aile Delta de 65 degrés de flèche.*

L'algorithme a été appliqué au cas de la pale fixe HTC5, et a donné une estimation de la part de portance tourbillonnaire de l'ordre de 5% de la portance totale. Cela confirme les hypothèses issues de la topologie du TBA caractérisée précédemment. L'avantage majeur de la méthode développée dans cette étude est qu'elle peut être appliquée à tout type de géométrie. Elle est donc particulièrement intéressante dans un contexte d'étude comparative.

C.2.3. Développement d'un modèle 1D de la portance tourbillonnaire

Après avoir caractérisé la topologie du TBA et son impact sur l'aérodynamique de la pale HTC5 au décollage, l'objectif était de tester de nouvelles géométries de pale. Un modèle 1D de la portance tourbillonnaire a été développé afin de proposer un outil rapide de calcul d'efforts prenant en compte les lois de description de la géométrie en envergure, la vitesse amont et la vitesse de rotation.

Le modèle de Polhamus a été exprimé sous une forme locale, dépendante du profil. Le coefficient

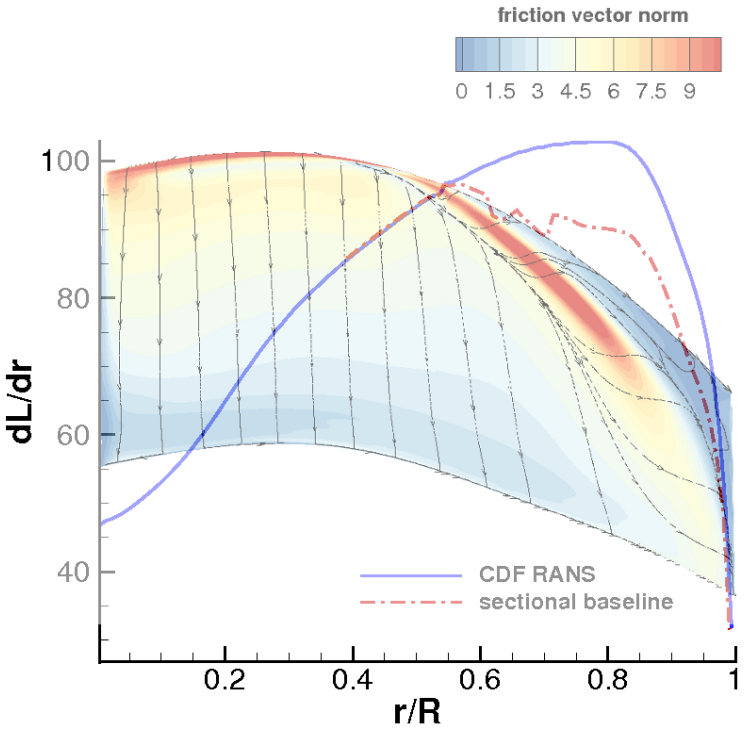

Figure C.3. *Distribution de portance en envergure $\frac{dL}{dr}$ incluant la part tourbillonnaire, superposée à la norme du frottement pariétal et aux lignes de frottement. L'aire entre les courbes rouge et bleue correspond à la part tourbillonnaire.*

de portance en présence d'un TBA s'écrit:

$$CL(r) = CL_p + CL_v = f_p(r)\, Kp_{loc}(r)\, cos^2\alpha(r)\, sin\alpha(r) \;+\; f_v(r)\, Kv_{loc}(r)\, cos\alpha(r)\, sin^2\alpha(r)$$

Cette forme locale dépend d'une expression locale des coefficients de Polhamus $Kp_{loc}(r)$ et $Kv_{loc}(r)$, calculés à partir de la polaire du profil $CL_{airfoil}$ à la position r.

$$Kp_{loc} = cos^2\phi\, \frac{\partial CL_{airfoil}(\alpha, M)}{\partial \alpha}\Big)_{\alpha_0}$$

où α est l'incidence locale, ϕ la flèche locale, M le nombre de Mach local, α_0 l'incidence de portance nulle du profil donné. Par ailleurs,

$$Kv_{loc} = \frac{Kp_{loc} \;-\; Kp_{loc}^2\, Ki_{loc}}{cos\phi}$$

où $Ki_{loc} = \frac{1}{cos^2\phi} \frac{\partial^2 CD_{airfoil}(\alpha,M)}{\partial CL^2_{airfoil}(\alpha,M)}$. L'hypothèse de profils indépendants est inhérente à la modélisation. Afin de prendre en compte les effets 3D liés au tourbillon de bord d'attaque, les coefficients de Polhamus locaux sont multipliés par des fonctions cumulatives $f_p(r)$ et $f_v(r)$ variant le long de l'envergure. Ces fonctions cumulatives sont définies à partir des données de répartition en envergure extraites à l'aide de l'algorithme d'estimation de la portance tourbillonnaire développé auparavant. En particulier, cela a permis de montrer que la portance (et sa part tourbillonnaire) augmentent le long de l'envergure depuis le point initial de décollement jusqu'à ce que le TBA atteigne le bord de fuite. Elles diminuent une fois que le tourbillon atteint le bord de fuite.

La modélisation a été réalisée sur trois cas : l'aile Delta à différentes flèches et incidences, la pale HTC5 fixe, et la pale HTC5 tournante pour différentes valeurs de calage. Dans chacun de ces cas, une modélisation légèrement différente a été appliquée, en particulier pour la partie potentielle. Ces différences sont dues au fait que la modélisation 1D ne permet pas suffisamment de degrés de liberté pour englober tous ces cas sans changer de modélisation.

Dans le cas de la pale HTC5 tournante, le modèle de portance tourbillonnaire développé est couplé à la méthode de l'élément de pale. On fait l'hypothèse que le point initial de décollement de l'écoulement est l'apex $r = r_0$. Entre le pied et l'apex ($r \leq r_0$), la méthode de l'élément de pale classique est appliquée, $CL(r)$ et $CD(r)$ étant calculés à partir de la polaire. Au-delà ($r \geq r_0$), le modèle 1D est utilisé pour calculer les coefficients aérodynamiques. Il prédit de façon satisfaisante les caractéristiques aérodynamiques intégrées, comme la portance, la traction ou le rendement, sur l'aile Delta (fixe) et sur la pale HTC5 tournante. Dans le cas HTC5 tournant, les fonctions cumulatives testées sont : $f_p(r) = 1$ et une évolution parabolique en envergure pour $f_v(r) = max(\,0,\, -4K'' \frac{(r-r_0)(r-R)}{(R-r_0)^2}\,)$, avec $K'' = 1.3$. La répartition de portance tourbillonnaire en envergure est en bon accord avec la référence CFD dans le cas HTC5 tournant.

L'approche présentée dans cette thèse représente une avancée par rapport au modèle de Polhamus, et par rapport aux études qui l'ont simplement appliqué au niveau du profil [Thielicke et al., 2011]. La modélisation choisie, avec prise en compte des fonctions cumulatives, permet de prendre en compte les phénomènes physiques principaux, au premier ordre. Un des principaux résultats est la capacité du modèle à prendre en compte les effets 3D au premier ordre, malgré l'hypothèse de profils indépendants.

Les principales limites de ce modèle sont :

- la prédiction du point initial de décollement (i.e. point de formation du TBA),
- les limites inhérentes à l'utilisation de la BEMT (dans laquelle les vitesses induites d'un profil sur l'autre ne sont pas prises en compte).

Dans le futur, il serait intéressant d'implémenter ce modèle de portance tourbillonnaire dans la ligne portante généralisée [Guermond, 1990] (bien que cela ne fonctionne pas pour des allongements aussi faibles que celui de l'aile Delta). La prochaine étape serait d'exprimer les fonctions cumulatives en fonction de paramètres liés à la géométrie de la pale ou de paramètres physiques du TBA, tels que la variation en envergure de sa vorticité, sa circulation, sa vitesse axiale, ou sa taille caractéristique.

En reproduisant les phénomènes physiques principaux, le modèle propose des résultats intéressants du point de vue de la caractérisation de l'évolution en envergure de la portance tourbillonnaire et de sa dépendance à la géométrie et aux paramètres de fonctionnement de la pale. Toutefois, étant donné ses limitations, et le fait qu'il n'ait été testé que sur un petit nombre de géométries, ce modèle n'est pas suffisamment validé en l'état pour être utilisé dans des études paramétriques.

C.2.4. Proposition de concepts de pale bénéficiant de la portance tourbillonnaire au décollage

D'un point de vue plus applicatif, cette thèse montre également l'intérêt que peut représenter la portance tourbillonnaire au décollage pour la conception de pales d'extrémité transsonique.

Différentes géométries ont été comparées à iso-traction au moyen de calculs RANS. La contribution du TBA à la portance et à la traction a été estimée à l'aide de l'algorithme développé précédemment. Bien que la portance tourbillonnaire soit générée aux dépens du rendement, elle permet d'atteindre la traction au décollage avec une surface alaire plus faible. Ainsi, cette pale peut atteindre un meilleur rendement en croisière. Par ailleurs, cette étude a montré que la flèche permet de générer de la portance tourbillonnaire plus efficacement à iso-traction et iso-surface. Un concept préliminaire de géométrie a été proposé, permettant d'atteindre la traction cible au décollage au prix de 9 points de rendement, pour un gain d'un point de rendement en croisière. Ces résultats sont prometteurs étant donné la durée comparative de ces phases de vol. Toutefois il reste à optimiser cette géométrie en prenant également en compte des paramètres de tenue mécanique. Il serait intéressant aussi d'analyser les caractéristiques du tourbillon de sillage de cette pale, afin d'obtenir une première estimation de ses performances acoustiques en configuration Open Rotor.

C.3. Perspectives

Afin d'évaluer l'intérêt d'augmenter la portance tourbillonnaire au décollage sur des géométries optimisées, l'étude paramétrique gagnerait à être prolongée et étendue à de nouvelles géométries. Dans ce contexte, il serait intéressant d'utiliser un modèle 1D de calculs d'efforts tel que celui développé dans cette thèse. Un tel modèle permettrait de lancer des calculs rapides afin d'obtenir les performances aérodynamiques d'une géométrie donnée en prenant en compte la part tourbillonnaire. Il pourrait être intégré dans un programme d'optimisation, qui donnerait les formes de pale les plus prometteuses, en autorisant le décollement au bord d'attaque.

Pour atteindre cet objectif, le modèle 1D de portance tourbillonnaire doit d'abord être amélioré. Une des limites majeures de l'outil de modélisation actuel concerne le fait que les vitesses induites d'un profil sur l'autre ne sont pas prises en compte. L'implémentation du modèle 1D dans la ligne portante généralisée devrait augmenter la représentativité des prédictions par rapport à la CFD.

Finalement, le modèle 1D de portance tourbillonnaire serait probablement plus représentatif si les constantes utilisées dans les fonctions cumulatives avaient une dépendance physique. Pour obtenir une modélisation "complète", une meilleure compréhension du lien entre les caractéristiques du TBA et sa contribution à la portance est nécessaire. Ce lien a été évoqué au cours de la thèse mais est resté qualitatif, et fondé sur l'analogie entre la forme du TBA et sa contribution à la portance sur les ailes Delta. Il serait donc intéressant de rechercher quelle influence sa vorticité, sa vitesse axiale, ou l'éloignement de son centre à la paroi ont sur la portance tourbillonnaire. Les études de [Slomski and Soleman, 1993, Ford and Babinsky, 2013] proposent un point de départ pertinent. En particulier, les corrélations entre les trois plans expérimentaux instationnaires acquis au cours de cette thèse pourraient être exploitées davantage et apporter un éclairage sur les mécanismes de propagation du TBA.

Bibliography

[Anderson, 2007] Anderson, J. (2007). *Fundamentals of Aerodynamics (4th edition)*. McGraw-Hill.

[Aono et al., 2007] Aono, H., Liang, F., and Liu, H. (2007). Near-and far-field aerodynamics in insect hovering flight : An integrated computational study. *Jornal of Experimental Biology*, 211:239–257.

[Bartlett, 1948] Bartlett, M. (1948). Smoothing periodograms from time-series with continuous spectra. *Nature*, 161:686–687.

[Beaumier, 2014] Beaumier, P. (2014). A low order method for co-axial propeller and rotor performance prediction. In *29th Congrees of the International Council of the Aerautical Sciences (ICAS 2014)*.

[Benjamin, 1967] Benjamin, T. (1967). Some developments in the theory of vortex breakdown. *Journal of Fluid Mechanics*, 28(1):65–84.

[Beom-Seok et al., 2002] Beom-Seok, K., Jeong-Hwan, K., Koji, K., van Rooij, R., and Young-Ho, L. (2002). 3d numerical predictions of horizontal axis wind turbine power characteristics of the scaled delft university t40/50 model. In *Fifth JSME-KSME Fluids Engineering Conference, Nagoya, Japan*.

[Bertin and Cummings, 2014] Bertin, J. and Cummings, R. (2014). *Aerodynamics for Engineers, 6th Edition*. Pearson Education Limites, Harlow, England.

[Birch and Dickinson, 2001] Birch, J. and Dickinson, M. (2001). Spanwise flow and the attachment of the leading-edge vortex on insect wings. *Nature*, 412(6848):729–733.

[Bollay, 1939] Bollay, W. (1939). A non- linear wing theory and its application to rectangular wings of small aspect ratio. *Zeitschrift für Angewandte Mathematik und Mechanik*, 19(1):21–35.

[Bousquet, 2008] Bousquet, J. (2008). Aérodynamique de l'hélice.

[Branlard, 2011] Branlard, E. (2011). Wind turbine tip-loss corrections: review, implementation and investigation of new models. *Master's thesis, Risø-DTU, Siemens Energy Inc.(available at DTU's library)*.

[Brown and Michael, 1954] Brown, C. and Michael, W. (1954). Effect of leading-edge separation on the lift of a delta wing. *Journal of Aeronautical Sciences*, 21(10):690–706.

[Brown and Michael, 1955] Brown, C. and Michael, W. (1955). On slender delta wings with leading-edge separation. Technical report, NASA Langley, TN-3430.

[Butoescu, 2011] Butoescu, V. (2011). A rotary wing system for micro air vehicle applications. part 1. *Incas Bulletin*, 3(3):23–33.

[Cambier et al., 2013] Cambier, L., Heib, S., and Plot, S. (2013). The onera elsa cfd software: input from research and feedback from industry. *Mechanics & Industry*, 14(3):159–174.

[Champagnat et al., 2011] Champagnat, F., Plyer, A., Besnerais, G. L., Davoust, S., Leclaire, B., and Sant, Y. L. (2011). Fast and accurate piv computation using highly parallel iterative correlation maximization. *Experiments in Fluids*, 50(4):1169–1182.

[Chatterjee, 2000] Chatterjee, A. (2000). An introduction to the proper orthogonal decomposition. *Current science*, 78(7):808–817.

[Delattre and Falissard, 2014] Delattre, G. and Falissard, F. (2014). Influence of torque ratio on counter rotating open rotor interaction noise. In *20th AIAA/CEAS Aeroacoustics Conference, AIAA AVIATION Forum*. Paper number AIAA 2014-2969.

[Delattre and Falissard, 2015] Delattre, G. and Falissard, F. (2015). Influence of torque ratio on counter-rotating open-rotor interaction noise. *AIAA Journal*, 53(9):2726–2738.

[Delattre. et al., 2016] Delattre., G., Falissard, F., Vion, L., and Jacquin, L. (2016). Open rotor interaction noise reduction through front rotor wake modification. *International Journal of Aeroacoustics*, 15(1-2):207–227.

[Devinant and Gallois, 2002] Devinant, P. and Gallois, T. (2002). Swept and curved wings: a numerical approach based on generalized lifting-line theory. *Computational mechanics*, 29(4-5):322–331.

[Earnshaw, 1961] Earnshaw, P. (1961). An experimental investigation of the structure of a leading-edge vortex. Technical Report Aeronautical research council reports and memoranda No. 3281, British ministry of aviation.

[Earnshaw and Lawford, 1964] Earnshaw, P. B. and Lawford, J. A. (1964). Low-speed wind-tunnel experiments on a series of sharp-edged delta wings. Technical report, ARC Reports and Memoranda No. 3424.

[Elimelech et al., 2013] Elimelech, Y., Kolomenskiy, D., Dalziel, S. B., and Moffat, H. (2013). Evolution of the leading-edge vortex over an accelerating rotating wing. In *Procedia IUTAM*.

[Ellington et al., 1996] Ellington, C., van den Berg, C., Willmot, A., and Thomas, A. (1996). Leading-edge vortices in insect flight. *Nature*, 384:626–630.

[Evans and Mort, 1959] Evans, W. and Mort, K. (1959). *Analysis of computed flow parameters for a set of sudden stalls in low-speed two-dimensional flow*, volume 85. National Aeronautics and Space Administration.

[Ford and Babinsky, 2013] Ford, C. P. and Babinsky, H. (2013). Lift and the leading-edge vortex. *Journal of Fluid Mechanics*, 720:280–313.

[Furman and Breitsamter, 2013] Furman, A. and Breitsamter, C. (2013). Turbulent and unsteady flow characteristics of delta wing vortex systems. *Aerospace Science and Technology*, 24:32–44.

[Gardarein, 1991] Gardarein, P. (1991). Calculs aerodynamiques des helices rapides transsoniques. In *28eme Colloque d'Aerodynamique Appliquee*, volume **1** of *ISL, Saint-Louis, France*, pages 1–3, Publisher address. Publisher Name.

[Garmann and Visbal, 2014] Garmann, D. and Visbal, M. (2014). Dynamics of revolving wings for various aspect ratios. *Journal of Fluid Mechanics*, 748:932–956.

[Garmann et al., 2013] Garmann, D., Visbal, M., and Orkwis, P. (2013). Three-dimensional flow structure and aerodynamic loading on a revolving wing. *Physics of fluids*, 25:932–956.

[Gersten, 1961] Gersten, K. (1961). Calculation of non- linear aerodynamic stability derivatives of aeroplanes. Technical Report Report 342, AGARD.

[Gordnier and Visbal, 1994] Gordnier, R. and Visbal, M. (1994). Unsteady vortex structure over a delta wing. *Journal of Aircraft*, 31(1):243–248.

[Gordnier and Visbal, 2003] Gordnier, R. and Visbal, M. (2003). Higher-order compact difference scheme applied to the simulation of a low sweep delta wing flow. In *41 st AIAA Aerospace Sciences Meeting & Exhibit, Reno, NV*.

[Gordnier and Visbal, 2005] Gordnier, R. and Visbal, M. (2005). Compact difference scheme applied to the simulation of low sweep delta wing flow. *AIAA Journal*, 43(8):1744–1752.

[Gordnier and Visbal, 2006] Gordnier, R. E. and Visbal, M. R. (2006). High-order simulation of low sweep delta wing flows using iles and hybrid rans/iles models. *AIAA Paper*, 504:2006.

[Gordnier et al., 2009] Gordnier, R. E., Visbal, M. R., Gursul, I., and Wang, Z. (2009). Computational and experimental investigation of a nonslender delta wing. *AIAA journal*, 47(8):1811.

[Graftieaux et al., 2001] Graftieaux, L., Michard, M., and Grosjean, N. (2001). Combining piv, pod and vortex identification algorithms for the study of unsteady turbulent swirling flows. *Measurement Science and technology*, 12(9):1422.

[Guermond, 1990] Guermond, J.-L. (1990). A generalized lifting-line theory for curved and swept wings. *Journal of Fluid Mechanics*, 211:497–513.

[Guermond and Sellier, 1991] Guermond, J.-L. and Sellier, A. (1991). A unified unsteady lifting-line theory. *Journal of Fluid Mechanics*, 229:427–451.

[Gursul et al., 2005] Gursul, I., Gordnier, R., and Visbal, M. (2005). Unsteady aerodynamics of nonslender delta wings. *Progress in Aerospace Sciences*, 41(7):515–557.

[Gursul et al., 2007] Gursul, I., Wang, Z., and Vardacki, E. (2007). Review of flow control mechanisms of leading-edge vortices. *Progress in Aerospace Sciences*, 43:246–270.

[Hansen, 2000] Hansen, M. (2000). *Aerodynamics of wind turbines*. Routledge.

[Hanson, 1985] Hanson, D. (1985). Noise of counter-rotation propeller. *Journal of Aircraft*, 22(7):609–617.

[Harbig et al., 2013] Harbig, R., Sheridan, J., and Thompson, M. (2013). Reynolds number and aspect ratio effects on the leading-edge vortex for rotating insect wing planforms. *Journal of Fluid Mechanics*, 717:166–192.

[Harvey, 1962] Harvey, J. (1962). Some observations of the vortex breakdown phenomenon. *Journal of fluid mechanics*, 14:585–592.

[Hemsch and Luckring, 1989] Hemsch, M. and Luckring, J. (1989). Connection between leading-edge sweep, vortex lift, and vortex strength for delta wings. *AIAA Journal of Aircraft*, 27(5):473–475.

[Hill, 1957] Hill, W. (1957). Experimental lift of low aspect-ratio triangular wings at large angles of attack and supersonic speeds. Technical report, NACA RM-A57117.

[Hoeijmakers, 1992] Hoeijmakers, H. W. M. (1992). Aspects of the modelling and numerical simulation of leading-edge vortex flow. In *IUTAM Symposium on Fluid Dynamics of High Angle of Attack*.

[Horton, 1968] Horton, H. (1968). *Laminar separation bubbles in two or three dimensional incompressible flow*. PhD Thesis, Queen Mary, University of London, London.

[Houghton and Carpenter, 2003] Houghton, E. L. and Carpenter, P. W. (2003). *Aerodynamics for engineering students*. Butterworth-Heinemann.

[Ingram, 2005] Ingram, G. (2005). Wind turbine blade analysis using the blade element momentum method. version 1.0. *School of Engineering, Durham University, UK*.

[Jacquin et al., 2001] Jacquin, L., Fabre, D., Geffroy, P., and Coustols, E. (2001). The properties of a transport aircraft wake in the extended near field - an experimental study. In *39th Aerospace Sciences Meeting and Exhibit Reno, NV, U.S.A.* AIAA paper 2001-1038.

[Kok, 2000] Kok, J. (2000). Resolving the dependence on freestream values for the k-turbulence model. *AIAA Journal*, 38(7):1292–1295.

[Kolomenskiy et al., 2014] Kolomenskiy, D., Elimelech, Y., and Schneider, K. (2014). Leading-edge vortex shedding from rotating wings. *Fluid Dynamics Research*, 46(3):031421.

[Lamar, 1974] Lamar, J. (1974). Extension of the leading-edge suction analogy to wings with separated flow around the side edges at subsonic speeds. Technical report, NASA Langley.

[Lamar, 1975] Lamar, J. E. (1975). Some recent applications of the suction analogy to vortex-lift estimates. Technical report, NASA Langley.

[Lambourne and Bryer, 1961] Lambourne, N. and Bryer, D. (1961). The bursting of leading-edge vortices - some observations and discussion of the phenomenon. Technical Report 3282, Report and Memorandum, Aircraft Research Council.

[Lawford and Beauchamp, 1961] Lawford, J. and Beauchamp, A. (1961). Low-speed wind-tunnel measurements on a thin sharp-edged delta wing with 70 degrees leading-edge sweep, with particular reference to the position of leading-edge vortex breakdown. Technical Report Tech. Note Aero. 2797, Royal Aircraft Establishment.

[Lee and Ho, 1990] Lee, M. and Ho, C.-M. (1990). Lift force of delta wings. *Appl. Mech. Rev*, 43(9):209–221.

[Legendre, 1952] Legendre, R. (1952). Ecoulement au voisinage de la pointe avant d'une aile à forte flèche aux incidences moyennes. *La recherche aéronautique*, 30:3–8.

[Lentink and Dickinson, 2009a] Lentink, D. and Dickinson, M. H. (2009a). Biofluiddynamic scaling of flapping, spinning and translating fins and wings. *The Journal of Experimental Biology*, 212:2691–2704.

[Lentink and Dickinson, 2009b] Lentink, D. and Dickinson, M. H. (2009b). Rotational accelerations stabilize leading edge vortices on revolving fly wings. *The Journal of Experimental Biology*, 212:2705–2719.

[Lentnik et al., 2008] Lentnik, D., Muijres, F. T., Donker-Duyvis, F. J., and van Leeuwen, J. L. (2008). Vortex-wake interactions of a flapping foil that models animal swimming and flight. *The Journal of Experimental Biology*, 211:267–273.

[Lepot et al., 2011] Lepot, I., Leborgne, M., Schnell, R., Yin, J., Delattre, G., Falissard, F., and Talbotec, J. (2011). Aero-mechanical optimization of a contra-rotating open rotor and assessment of its aerodynamic and acoustic characteristics. *Proceedings of the Institution of Mechanical Engineers, Part A: Journal of Power and Energy*, 225(7):850–863.

[Leuchter and Solignac, 1983] Leuchter, O. and Solignac, J. (1983). Experimental investigation of turbulent structure vortex wakes. In *4th Symposium on Turbulent Shear Flows*.

[Lim et al., 2009] Lim, T., Teo, C., Lua, K., and Yeo, K. S. (2009). On the prolong attachment of leading edge vortex on a flapping wing. *Modern Physics Letters B*, 23:357–360.

[Lindenburg, 2004] Lindenburg, C. (2004). Modelling of rotational augmentation based on engineering considerations and measurements. In *European Wind Energy Conference*.

[Lu et al., 2006] Lu, Y., Shen, G., and Lai, G. (2006). Dual leading-edge vortices on flapping wings. *J. Exp. Biol.*, 209:5005–5016.

[Maltby, 1968] Maltby, R. (1968). The development of the slender delta concept. *Aircraft Engineering and Aerospace Technology*, 40(3):12–17.

[Mangler and Smith, 1959] Mangler, K. and Smith, J. (1959). A heory of the flow past a slender delta wing with leading-edge separation. In *Proceedings of the Royal Society A*, volume 251, pages 200–217. Royal Society.

[Manie et al., 1978a] Manie, F., Rehbach, C., and Schmitt, V. (1978a). Etude d'une aile à flèche variable en écoulement sub ou transsonique. In *11e Congrès International des Sciences Aéronautiques*.

[Manie et al., 1978b] Manie, F., Rehbach, C., and Schmitt, V. (1978b). Study of a variable sweep wing in sub or transonic flow. In *International Council of the Aeronautical Sciences (ICAS)*. Number 81A14341 NASA Technical translation NASA TT-20117.

[Maxworthy, 1981] Maxworthy, T. (1981). The fluid dynamics of insect flight. *Annual Review of FLuid Mechanics*, 13:329–350.

[Maxworthy, 2007] Maxworthy, T. (2007). The formation and maintenance of a leading-edge vortex during the forward motion of an animal wing. *J. Fluid Mech.*, 587:471–475.

[Menke and Gursul, 1997] Menke, M. and Gursul, I. (1997). Unsteady nature of leading edge vortices. *Physics of Fluids*, 9(10):2960–2966.

[Menter, 1994] Menter, F. (1994). Two-equation eddy-viscosity turbulence models for engineering applications. *AIAA journal*, 32(8):1598–1605.

[Mitchell and Molton, 2002] Mitchell, A. M. and Molton, P. (2002). Vortical substructures in the shear layers forming leading-edge vortices. *AIAA journal*, 40(8):1689–1692.

[Nabawy and Crowther, 2017] Nabawy, M. and Crowther, W. (2017). The role of the leading edge vortex in lift augmentation of steadily revolving wings: a change in perspective. *Journal of The Royal Society Interface*, 14(132):20170159.

[Nelson and Pelletier, 2003] Nelson, R. and Pelletier, A. (2003). The unsteady aerodynamics of slender wings and aircraft undergoing large amplitude manoeuvers. *Progress in Aerospace Sciences*, 39:185–248.

[Ning, 2014] Ning, S. (2014). A simple solution method for the blade element momentum equations with guaranteed convergence. *Wind Energy*, 17(9):1327–1345.

[Ol and Gharib, 2003] Ol, M. V. and Gharib, M. (2003). Leading-edge vortex structure of nonslender delta wings at low reynolds number. *AIAA journal*, 41(1):16–132.

[Ozen and Rockwell, 2012] Ozen, C. and Rockwell, D. (2012). Flow structure on a rotating blade. *Exp Fluids*, 52:207–223.

[Pagan, 1989] Pagan, D. (1989). *Contribution a l'etude experimentale et theorique de l'eclatement tourbillonnaire en air incompressible*. PhD thesis, Paris 6.

[Pashilkar, 2002] Pashilkar, A. (2002). Surface pressure estimates for pitching aircraft model at high angles-of-attack. *Defence Science Journal*, 52(4):417.

[Payne et al., 1986] Payne, F., Ng, T., and Nelson, R. (1986). Visualization and flow surveys of the leading edge vortex structure on delta wing planforms. *Reno, NV, USA: AIAA*.

[Polhamus, 1966] Polhamus, E. (1966). A concept of the vortex lift of sharp-edge delta wings based on a leading-edge suction analogy. Technical note D-3767, NASA, Langley, Hampton, Va.

[Polhamus, 1968] Polhamus, E. (1968). Application of the leading-edge suction analogy os vortex lift to the drag due to lift of sharp-edge Delta wings. Technical note D-4739, NASA, Langley, Hampton, Va.

[Polhamus, 1971] Polhamus, E. (1971). Prediction of vortex lift characteristics by a leading-edge suction analogy. *Journal of Aircraft*, 8(4):193–199.

[Polhamus, 1969] Polhamus, E. C. (1969). Predictions of vortex-lift characteristics based on a leading-edge suction analogy. In *AIAA 6th Annual Meeting and Technical Display*. Paper Number AIAA 69-1133.

[Ramesh and Gopalarathnam, 2011] Ramesh, K. and Gopalarathnam, A. (2011). Augmentation of inviscid airfoil theory to predict and model 2d unsteady vortex dominated flows. In *41st AIAA Fluid Dynamics Conference and Exhibit*.

[Ramesh et al., 2012] Ramesh, K., Gopalarathnam, A., and Edwards, J. R. (2012). Effect of airfoil shape and reynolds number on leading edge vortex shedding in unsteady flows. In *30th AIAA Applied Aerodynamics Conference*.

[Renac, 2004] Renac, F. (2004). *Contrôle expérimental de l'écoulement tourbillonnaire sur une aile delta*. PhD thesis, Université Paris VI.

[Riou, 2009] Riou, J. (2009). *Etude et controle du decrochage d'ailes et gouvernes de missile en regime transsonique*. PhD thesis, Universite Paris 13.

[Roy, 1956] Roy, M. (1956). *Sur la théorie de l'aile en delta. Tourbillon d'apex et nappes en cornet*. La Recherche aéronautique.

[Rwigema, 2010] Rwigema, M. (2010). Propeller blade element momentum theory with vortex

wake deflection. In *Proceedings of the 27th Congress of the International Council of the Aeronautical Sciences, Nice, France, September*, pages 19–24.

[Saffman and Sheffield, 1977] Saffman, P. and Sheffield, J. (1977). Flow over a wing with an attached free vortex. *Studies in Applied Mathematics*, 57(2):107–117.

[Sane, 2003] Sane, S. (2003). The aerodynamics of insect flight. *Journal of experimental biology*, 206(23):4191–4208.

[Schülein et al., 2012] Schülein, E., Rosemann, H., and Schaber, S. (2012). Transition detection and skin friction measurements on rotating propeller blades. In *28th Aerodynamic Measurement Technology, Ground Testing, and Flight Testing Conference*.

[Shen et al., 2005a] Shen, W., Mikkelsen, R., Sørensen, J., and Bak, C. (2005a). Tip loss corrections for wind turbine computations. *Wind Energy*, 8(4):457–475.

[Shen et al., 2005b] Shen, W., Sørensen, J., and Mikkelsen, R. (2005b). Tip loss correction for actuator/navier-stokes computations. *Transactions of the ASME-N-Journal of Solar Energy Engineering*, 127(2):209–213.

[Simonich et al., 1990] Simonich, J., McCormick, D., and Lavrich, P. L. (1990). The role of leading edge vortex flows in prop-fan interaction noise. In *AIAA 13th Aeroacoustics Conference*.

[Slomski and Soleman, 1993] Slomski, J. and Soleman, R. (1993). Numerical simulation of vortex generation and capture above an airfoil. In *31st Aerospace Sciences Meeting*, page 864.

[Snel et al., 1994] Snel, H., Houwink, R., and Bosschers, J. (1994). Sectional prediction of lift coefficients on rotating wind turbine blades in stall. In *ECN-C–93-052*.

[Solignac and Leuchter, 1983] Solignac, J. and Leuchter, O. (1983). Etude expérimentale d'écoulements tourbillonnaires soumis à des effets de gradient de pression adverse. In *AGARD Symposium on Aerodynamics of Vortical Type Flows in Three Dimensions*.

[Sun and Wu, 2004] Sun, M. and Wu, J. (2004). Large aerodynamic forces on a sweeping wing at low reynolds number. *Acta Mechanica Sinica*, 20:24–31.

[Tangler, 2004] Tangler, J. (2004). Insight into wind turbine stall and post-stall aerodynamics. *Wind Energy*, 7:247–260.

[Thielicke et al., 2011] Thielicke, W., Kesel, A., and Stamhuis, E. (2011). Reliable force predictions for a flapping-wing micro air vehicle: A "vortex-lift" approach. *International Journal of Micro Air Vehicles*, 3(4):201–215.

[Torres and Mueller, 2004] Torres, G. E. and Mueller, T. J. (2004). Low-aspect-ratio wing aerodynamics at low reynolds numbers. *AIAA Journal*, 42(5):865–873.

[Usherwood and Ellington, 2002] Usherwood, J. and Ellington, C. (2002). The aerodynamics of revolving wings ii. propeller force coefficients from mayfly to quail. *Journal of Experimental Biology*, 205(11):1565–1576.

[Vaczy and Cormick, 1987] Vaczy, C. M. and Cormick, D. C. M. (1987). A study of the leading edge vortex and tip vortex on prop-fan blades. *Journal of Turbomachinery*.

[Vion, 2013] Vion, L. (2013). *Modification des tourbillons d'extremite d'helices contra-rotatives en vue d'une reduction des nuisances sonores*. PhD thesis, Ecole Polytechnique.

[Vion et al., 2011] Vion, L., Delattre, G., Falissard, F., and Jacquin, L. (2011). Counter-rotating open rotor (cror) : flow physics and simulation. In *20th French Mechanics Congress, Besancon*.

[Wentz, 1968] Wentz, W. (1968). Wind tunnel investigations of vortex breakdown on slender sharp edged wings. Technical report, NASA, CR-98737.

[Wentz and Kohlman, 1971] Wentz, W. and Kohlman, D. (1971). Vortex breakdown on slender sharp-edged wings. *Journal of Aircraft*, 8(3):156–161.

[Werlé, 1957] Werlé, H. (1957). Etude experimentale, au tunnel hydrodynamique, de l'ecoulement autour de l'aile delta aux faibles vitesses. Technical Report Note Technique 2/1859 A, ONERA.

[Werlé, 1959] Werlé, H. (1959). Etude experimentale, au tunnel hydrodynamique, de l'eclatement des tourbillons d'apex d'une aile delta aux faibles vitesses. Technical Report Note Technique 12/1859 A, ONERA.

[Werlé, 1960a] Werlé, H. (1960a). Sur l'éclatement des tourbillons d'apex d'une aile delta aux faibles vitesses. *La Recherche Aéronautique*, 74.

[Werlé, 1960b] Werlé, H. (1960b). Tourbillons d'apex d'ailes tres minces. Technical Report Note Technique 28/1859 A, ONERA.

[Werlé, 1961] Werlé, H. (1961). Tourbillons d'apex d'ailes delta et gothiques epaisses. Technical Report Note Technique 30/1859 A, ONERA.

[Wilcox, 1988] Wilcox, D. (1988). Reassessment of the scale-determining equation for advanced turbulence models. *AIAA journal*, 26(11):1299–1310.

[Wojcik and Buchholz, 2014a] Wojcik, C. and Buchholz, J. (2014a). Parameter variation and the leading-edge vortex on a rotating blade. *AIAA Journal*, 52:348–357.

[Wojcik and Buchholz, 2014b] Wojcik, C. and Buchholz, J. (2014b). Vorticity transport in the leading-edge vortex on a rotating blade. *Journal of Fluid Mechanics*, 743:249–261.

[Zachariadis et al., 2013] Zachariadis, A., Hall, C., and Parry, A. B. (2013). Contrarotating open rotor operation for improved aerodynamics and noise at takeoff. *Journal of Turbomachinery*.

[Zehner et al., 2016] Zehner, P., Falissard, F., and Gloerfelt, X. (2016). Aeroacoustic study of the interaction of a rotating blade with a batchelor vortex. In *22nd AIAA/CEAS Aeroacoustics Conference*, page 2999.

[Zheng and Liu, 1995] Zheng, X. and Liu, F. (1995). Staggered upwind method for solving navier-stokes and turbulence model equations. *AIAA journal*, 33(6):991–998.

[Zohar and Er-El, 1988] Zohar, Y. and Er-El, J. (1988). Influence of the aspect-ratio on the aerodynamics of the delta wings at high angle of attack. *Journal of Aircraft*, 25(3):200–205.

université PARIS-SACLAY

ÉCOLE DOCTORALE
Sciences mécaniques et énergétiques, matériaux et géosciences (SMEMAG)

Titre : Étude des écoulements tourbillonnaires de bord d'attaque sur les hélices rapides

Mots clés : tourbillon de bord d'attaque, PIV, portance tourbillonnaire, pales transsoniques

Résumé : Cette thèse concerne l'aérodynamique de pales d'extrémité transsonique. Ces pales sont conçues pour maximiser le rendement en croisière, tout en générant la traction requise au décollage. Elles ont des profils fins et peu cambrés, travaillant à forte incidence au décollage, ce qui peut entraîner l'apparition d'un tourbillon de bord d'attaque (TBA). Or ce TBA présente des similitudes avec les tourbillons d'apex d'aile Delta, connus pour leur capacité à générer de la portance tourbillonnaire. Cette étude consiste à examiner l'intérêt du TBA pour les performances aérodynamiques. La démarche a consisté dans un premier temps à caractériser la topologie du TBA sur une maquette représentative d'une pale d' Open Rotor, à l'aide d'essais PIV résolus en temps et de calculs RANS $k-\omega$ SST, et à evaluer la capacité de la simulation RANS à reproduire les caractéristiques d'intérêt pour cette étude. Un algorithme a été développé afin d'estimer la contribution de ce TBA à la portance à partir du champ de pression pariétal RANS. Ensuite, afin d'expliciter l'influence des paramètres géométriques et de fonctionnement de la pale sur la portance tourbillonnaire, un modèle 1D de la portance tourbillonnaire a été développé puis couplé à la méthode de l'élément de pale. Les premières comparaison de géométries à iso-traction ont montré que la portance tourbillonnaire permet de générer la traction requise au décollage avec une surface alaire plus faible. Ces résultats ouvrent de nouvelles perspectives pour la conception de géométries avec un meilleur rendement en croisière.

Title: Characterisation and aerodynamic impact of leading-edge vortices on propeller blades

Keywords: leading-edge vortex, PIV, vortex lift, transonic propellers

Abstract: This thesis deals with the aerodynamic properties of propeller blades. Those blades are designed to maximise cruise efficiency, while achieving the target thrust at take-off. Their thin, low-cambered profiles must work at high incidence at take-off, which may give rise to a leading-edge vortex (LEV). The topology of this LEV looks similar to Delta wing LEVs, which are known to generate vortex lift. the aim of this study is to explore the probable impact of the LEV on lift at take-off in order to reconsider propeller blade designs. The approach first consisted in caracterising the LEV topology on a model blade representative of an Open Rotor front blade, using both Time-Resolved PIV and RANS $k-\omega$ SST calculations. The comparison between both methods demonstrated the ability of RANS calculations to reproduce the LEV characteristics of interest to this study. Then, the LEV contribution to lift was evaluated thanks to an algorithm developed to estimate vortex lift contribution from RANS wall pressure fields. In order to explicit the influence of the blade's geometrical and functioning parameters on vortex lift, a 1D vortex lift model was developed and coupled to the Blade Element Momentum Theory. The first blade geometry comparative studies at iso-thrust showed that vortex lift enables to generate target thrust at take-off with a lower blade surface. This opens new perspectives for the design of blade geometries with enhanced cruise efficiency.

Université Paris-Saclay
Espace Technologique / Immeuble Discovery
Route de l'Orme aux Merisiers RD 128 / 91190 Saint-Aubin, France